Louisiana State University

LSU Scholarly Repository

Groundwater Flow With Heat and Solute Transport in Sedimentary Basins.

Guichang Lin
Louisiana State University and Agricultural & Mechanical College

Follow this and additional works at: https://repository.lsu.edu/gradschool_disstheses

INFORMATION TO USERS

GROUNDWATER FLOW WITH HEAT AND SOLUTE TRANSPORT IN SEDIMENTARY BASINS

A Dissertation

Submitted to the Graduate Faculty of the
Louisiana State University and
Agricultural and Mechanical College
in partial fulfillment of the requirements for the degree
of Doctor of Philosophy

in

Department of Geology and Geophysics

by
Guichang Lin
B.S., Jianghan Petroleum Institute, P. R. of China, 1983
Professional Degree, Colorado School of Mines, 1992
May, 1996

UMI Number: 9637788

UMI
300 North Zeeb Road
Ann Arbor, MI 48103

ACKNOWLEDGMENTS

This dissertation is also dedicated to the University of Petroleum, China, for her providing the opportunity for me to study in this country. Special gratitude goes to Professors Yiwei Zhang, Kezheng Lu, Yongkuang Yi, Chenglin Zhao, Shitong Du, Jimeng Lu, as well as many others.

Finally, my greatest thanks go to my wife, Zhuowei Chen, for her patient and inspirational support and the great effort of taking care of my new born son, Benjamin. Without her support, this dissertation would have been very difficult to complete.

TABLE OF CONTENTS

LIST OF TABLES

LIST OF FIGURES

ABSTRACT

Numerical experiments were undertaken to understand (1) heat and fluid transport in an uplifted foreland basin where fluid flow is driven by topographic gradient, and (2) effects of expulsion of geopressured fluids on the thermodynamic system in salt basins.

Thermal evolution of an uplifted foreland basin is strongly affected by thermal buffering of basement rocks. Thermal buffering by basement rocks does not permit constant heat flow along the sediment-basement contact, in contrast to many previous numerical studies. Ignoring basement effects can result in serious errors in temperature prediction, such as a false transient thermal pulse in the discharge area.

Carbonaceous sediments are common in many sedimentary basins in the Mid-continent of North America that developed during the Late Paleozoic. Thermal insulation by a low conductivity carbonaceous layer can result in high basin heat storage, lower fluid viscosities, high efficiency of heat transport and heat retention during the discharge of hot fluids. This is a possible mechanism for elevated temperatures associated with the formation of Mississippi Valley-type (MVT) ore deposits even under the continental mean of basal heat flow about 60 mW/m^2.

Expulsion of geopressured fluids along a fault zone can inject a large quantity of low salinity fluids into the overlying hydropressured sediments within a few hundred years, inducing fluid pressure and temperature anomalies in the overlying hydropressured sediments. The short term expelled hot and low salinity fluids are gravitationally unstable and can cause long term (>10,000 years) thermohaline convection in a salt basin.

Salinity analysis from SP logs and numerical simulation in South Eugene Island, Block 330 field suggest that the present fault zone in the Block 330 area may provide a permeable conduit to the deeper reservoirs (depth > 2000 m) immediately overlying the frictional failure zone. The shallow reservoirs (depth < 1600 m) are believed to be currently fault-sealed. Sediment compressibility can maintain excess fluid pressures and drive fluid

flow even thousands of years after fluid expulsion stops. Compressibility of sediments
may play an important role in the low decline rate of the production history in the study
area.

CHAPTER 1
INTRODUCTION

Groundwater flow is a common and important geological process in the Earth's crust. Large-scale fluid migration may reach depths of up to several kilometers, particularly in sedimentary basins where sediments are highly permeable and fluid flow is a dominant agent for heat and chemical mass transfer (e.g. Bethke and Marshak, 1990; Cathles, 1990). There are several major forces driving fluid flow through sedimentary basins. These include the gravity force related to topographic gradient, fluid pressure in excess of hydrostatic pressure, fluid buoyancy associated with temperature and salinity variations, and changes in stress fields associated with sediment compaction, erosion, and faulting (e.g. Toth, 1978). These forces vary spatially and temporally as the structural and hydrologic framework of a basin evolves.

In recent years, computer aided numerical simulations of groundwater flow have lead to a better understanding of fluid migration and its relationship to other geological processes. However, many problems remain unsolved. For example, the genetic relationship between regional groundwater flow system, basin tectonics, and stratabound ore mineralization is still poorly understood. The next two sections addresses this problem.

1.1. FLUID FLOW DRIVEN BY TOPOGRAPHIC RELIEF RELATED TO MVT ORE DEPOSITS

Mississippi Valley-type (MVT) ore deposits often refer to carbonate-hosted lead-zinc deposits found in the Mid-continent region of the United States and in Canada (e.g. Domenico and Schwartz, 1990). Numerical studies related to MVT ore deposits in recent years reveal that the topographic gradient caused by an uplifting foreland basin, can result in Darcy velocities on the order of meters per year (e.g. Bethke and Marshak, 1990; Deming and Nunn, 1991; Garven and Freeze, 1984b; Garven et al, 1993). This velocity is much higher than those generated by tectonic squeezing (Oliver, 1986), or

1

from compaction-driven flow from overthrust belts (e.g. Cathles and Smith, 1983; Bethke, 1985; Ge and Garven, 1989; and Deming et al., 1990). Although episodic discharge of overpressured brines (Cathles and Smith, 1983) from deep sediments can generate high flow velocities, the duration of expulsion in computer simulation where permeability is controlled by fluid pressure was found to be on the order of hundred years (Roberts and Nunn, 1995).

The high fluid flow velocity caused by the uplifting foreland basin can result in high rates of heat and chemical mass transport from deep sediments into the shallow discharge area. Even though lead-zinc sulfides can be formed in cap-rocks of salt domes in temperatures between 40 and 75 °C at depths around 500 meters (e.g. Saunders and Swann, 1994), it is generally recognized that the Late Paleozoic MVT lead-zinc deposits in the Mid-continent of North America were formed at temperatures 100-150 °C and at shallow depths (<1.5 km) (e.g. Sverjensky, 1986). This places very restrictive constraints on the formation mechanism for the MVT ore deposits. The required temperatures at such shallow depths can be obtained by topographically driven regional fluid flow (Garven and Freeze, 1984; Bethke and Marshak, 1990; and Garven et al., 1993) only under a limited range of geological conditions. These are (1) basal heat flow is much higher than the continent mean, (2) presence of a high permeability aquifer at depth, or (3) a narrow, deep basin geometry (Deming and Nunn, 1991). Furthermore, results from previous numerical studies (e.g. Garven et al., 1993) have shown that the high efficiency of heat transport usually results in high thermal gradients in the shallow discharge area, which is inconsistent with thermal gradients obtained from fluid inclusion studies (Rowan and Leach, 1989). Thus, it is necessary to seek an alternative hypothesis to explain the thermal mechanism for the formation of MVT ore deposits.

One of the purposes of this dissertation is to investigate a new mechanism for the formation of MVT ore deposits. Consequently, a study was undertaken which used

thermal insulation by low conductivity carbonaceous sediments. Carbonaceous sediments, such as coal and related mudstone, are characterized by thermal conductivities in the range of 0.25 to 1.0 W/m-K. These are much lower than that of other sedimentary rocks by a factor of 5 to 10 (Pollack, and Cercone, 1994). Thus, they can act as a thermal blanket retaining heat within basin sediments and cause anomalous thermal maturities at shallow depths. This mechanism is believed to be able to generate elevated temperatures at shallow depth required for the formation of MVT ore deposits even under basal heat flow of 60 mW/m^2.

Numerical simulation is a powerful tool for understanding and predicting different geological processes that are occurring or have once occurred in the Earth. This study is a significant improvement over previous modeling studies of MVT deposits, which assumed a lower thermal boundary condition of constant heat flow at the sediment-basement contact (Smith and Chapman, 1983; Garven and Freeze, 1984; Garven, 1985; Woodbury and Smith, 1985; Bethke, 1986; Bethke and Marshak, 1990; Person and Garven, 1992; 1994; and Garven et al., 1993). Such a basal thermal boundary condition does not allow sediments and basement rocks to dynamically exchange heat energy. Basement rocks act as a thermal buffer to affect temperature changes in basin sediments caused by surface geological processes, such as rapid groundwater flow, rapid sedimentation, uplift and erosion. Thus, it is necessary to quantitatively determine the consequence of the basement effect, so that a proper thermal boundary condition can be established for the thermal evolution of a foreland basin.

1.2. HEAT, SOLUTE AND FLUID MASS TRANSPORT IN SALT BASINS

Groundwater flow with heat and solute transport is complicated in a salt basin. This complexity is caused not only by salt tectonic activity, but also by diagenesis, and strong variations in physical properties of salt and sediments, the strong interactions between fluid pressure, temperature, salt concentration, and groundwater flow fields (e.g. Evans and Nunn, 1989). There are several mechanisms considered to be

responsible for driving groundwater circulation in salt basins. These include expulsion of geopressured waters, preferential salt dissolution near the top of domes, viscous drag from meteoric waters, and thermal effects related to geopressured flow and high thermal conductivity of salt (e.g. Evans and Nunn, 1989). All of these phenomena are strongly coupled to one another. Without modeling studies, observational data alone are unlikely to reveal which driving mechanisms are operative or dominant (e.g. Evans, 1989).

Groundwaters with high salinity result from dissolution of salt and solute transport, and are common in many salt basins. There are two ways for solute transport to occur, one is by diffusion and the other is by advection. Diffusion is chemical mass flux which is proportional to the gradient in concentration (e. g. Domenico and Schwartz, 1990). Whereas, advection is the chemical mass transport by fluid flow. Diffusion-controlled solute transport has been reported in the Mediterranean Sea (McDuff et al., 1978, Sayles et al., 1973), Red Sea (Whitmarsh, et al., 1974; Manheim, et al., 1974) and the Timor Trough off the coast of Northwest Australia (Cook, 1974). Vertical salinity profiles in diffusion-controlled cases are usually in the form of a continuous increase of Na and Cl in interstitial waters with depth (Ranganathan, 1988). Diffusion appears to be an important brine forming process where sediments are horizontal or dip very slightly, and where evaporite sources are located at depth (e.g. Ranganathan, 1988).

In areas of salt diapirs or sheets, advection or convection is the dominant mechanism for solute transport, because the salt structure creates topographic potential for density driven flow. The dissolution of salt increases the density of pore fluids immediately adjacent to the salt surface and cause these fluids to move downward. As the saline fluids move downward, low salinity fluids will replace them and interact with the salt surface. Thus the salt surface is continuously exposed to fluids with lower salinity, and dissolution continues. The details of density driven groundwater flow near salt domes are described in numerical simulations by Evans and Nunn (1989),

Ranganathan and Hanor (1989), Sarkar et al. (1995) and others. It was found that solute transport by density driven advection is much more efficient than by diffusion. Hanor et al. (1986) attributed the high salinity zone (salinity up to 150 g/L between depths 1 to 4 km) across the entire 320 km width of south Louisiana, to the dissolution of NaCl from numerous salt domes. They also found that salinity in the deeper shaly sediments, decreases with depth to values $\leq$ 50 g/L.

Galloway et al. (1991) similarly reported that fluid salinities range from about 10 wt% to 25 wt% in the hydropressured zone and from 5 wt% to 15 wt% in the geopressured zone in the Gulf of Mexico basin. They also found that the temperature gradient was higher in geopressured zone than in hydropressured zone. This was demonstrated in the USDOE/General Crude geothermal test well, where the observed temperature gradient increases from 1.0 to 1.5 °F/100 ft (0.018 to 0.027 °C/m) in the hydropressured zone to 1.8 to 3.5 °F/100 ft (0.033 to 0.064 °C/m) in the geopressured zone (Galloway et al., 1991). The depth to the top of the geopressured zone varies considerably depending largely on the amount of sandstone in the deep section. In areas of high sandstone content the top of geopressure is deep, and where shale is dominant, the top of geopressure can be shallow (Galloway et al., 1991). In South Texas, the top ranges from 2,100 to 3,600 m in depth, and in Louisiana it ranges from 2,700 to 5,500 m in depth.

Another purpose of this dissertation is to study the use of salinity as a tracer to understand the physical process of a short term expulsion of geopressured fluids through a permeable fault zone and its long term consequence on the groundwater system in a salt basin. Because NaCl diffuses very slowly through a porous medium, salinity is an effective tracer for groundwater flow. The expulsion of geopressured fluids into the overlying hydropressured zone can cause significant density inversions, when geopressured fluids are lower in salinity than hydropressured fluids. Density inversion can drive large-scale convective fluid flow, as is seen in the South Louisiana

salt basin (Hanor, 1987). Thus, fluid migration, caused by the expulsion of geopressured fluids, may play an important role in the thermal evolution, mineral diagenesis, and hydrocarbon migration in salt basins, even long after the termination of the expulsion.

In this study, salinity distribution is estimated from SP logs, using the technique developed by Bateman (1985), and used to document the migration of geopressured fluids along the Main fault zone in South Eugene Island, Block 330. A numerical simulation is applied to explain the salinity distribution and other observational data such as temperature and fluid pressure distribution in this area.

1.3. ORGANIZATION OF THIS DISSERTATION

Chapter 2 describes the theories and numerical representation of heat, solute and fluid flow used in this dissertation. Chapter 3 describes two numerical models of topographic driven flow in an uplifted foreland basin used to test the consequences of introducing different lower thermal boundary conditions. In one model, the sediment-basement contact is considered as the lower thermal boundary, in the other the lower thermal boundary is extended deep into the basement. Chapter 4 examines thermal insulation by low conductivity carbonaceous sediments on both instantaneously uplifting and gradually uplifting foreland basins to see if thermal insulation can generate the high temperature at shallow depths associated with the formation of MVT ore deposits. Chapter 5 explains the use of a simple geologic model with fully coupled heat, solute and fluid mass transport to study the short term expulsion of geopressured fluids along a fault and its long term effect on the thermohaline convection in a salt basin. Chapter 6 describes the salinity estimation of SP logs and documents the migration pathway of the geopressured fluids in South Eugene Island Block 330 field. Chapter 6 also describes a numerical study used to explain the estimated salinity field, and further explore the flow regime in south Eugene Island Block 330 area. Chapter 7 summarizes this dissertation.

CHAPTER 2
THEORIES AND MATHEMATICAL REPRESENTATION

To develop transport equations in a porous media requires the use of three

conservation equations: conservation of fluid mass, solute, and energy; and three

fundamental flow laws: Darcy's law, Fick's law, and Fourier's law (e.g. Evans, 1989).

These equations are all strongly coupled by terms involving groundwater velocity,

density, and viscosity.

Palciauskas and Domenico (1989) derived the equations representing the

conservation of fluid mass and momentum in material coordinates where fluid velocity

is computed relative to the deforming medium. The following derivations follows their

work and that of Roberts et al. (1996).

In a fixed coordinate system, conservation of fluid mass and solid can be

represented as

$$\frac{\partial(\rho_f \phi)}{\partial t} + \nabla \cdot (\rho_f \phi v_f) = 0 \tag{1}$$

and

$$\frac{\partial[\rho_s(1-\phi)]}{\partial t} + \nabla \cdot [\rho_s(1-\phi)v_s] = 0 \tag{2}$$

respectively, where ρ_f and ρ_s are the fluid and solid densities, v_f and v_s are the

fluid phase and solid velocities, t is time and ϕ is the porosity. The material derivative,

which follows the motion of the solid phase, is related to the derivatives in a fixed

coordinate system by

$$\frac{D\phi}{Dt} = \frac{\partial \phi}{\partial t} + v_s \cdot \nabla \phi \tag{3}$$

Applying (3) to (1) and (2) and assuming that the density of solid grains does not

change with temperature and pressure, yields:

7

$$\frac{D(\rho_f\phi)}{Dt} - v_s \cdot \nabla(\rho_f\phi) + \nabla \cdot (\rho_f\phi v_f) = 0 \tag{4}$$

and

$$\frac{D\phi}{Dt} = (1-\phi)\nabla \cdot v_s \tag{5}$$

The volume flux of fluid relative to the solid matrix, q is given by,

$$q = \phi(v_f - v_s) \tag{6}$$

Substituting (6) and the expression for $\nabla \cdot v_s$ from (5) into (4) and simplifying yields

$$\frac{\phi}{\rho_f}\frac{D\rho_f}{Dt} + \frac{1}{1-\phi}\frac{D\phi}{Dt} + \frac{1}{\rho_f}\nabla \cdot (\rho_f q) = 0 \tag{7}$$

If the fractional compression of the medium is small, $\partial z / \partial t \approx 0$, the material derivatives can be replaced by partial derivatives,

$$\frac{\phi}{\rho_f}\frac{\partial\rho_f}{\partial t} + \frac{1}{1-\phi}\frac{\partial\phi}{\partial t} + \frac{1}{\rho_f}\nabla \cdot (\rho_f q) = 0 \tag{8}$$

Following Domenico and Schwartz (1990), changes in porosity caused by changes in fluid pressure are related to the elastic properties of the matrix by

$$\frac{1}{1-\phi}\frac{\partial\phi}{\partial t} = \beta_p\frac{\partial P}{\partial t} \tag{9}$$

where β_p is the vertical compressibility of the medium and P is fluid pressure. It is also assumed that changes in fluid density are a linear function of temperature and independent of fluid pressure, or

$$\frac{\partial\rho_f}{\rho_f} = -\alpha_f dT \tag{10}$$

where α_f is the coefficient of thermal expansion of the fluid and T is the temperature. Substitution of (9) and (10) into (8) gives

$$-\alpha_f\phi\frac{\partial T}{\partial t} + \beta_p\frac{\partial P}{\partial t} + \frac{1}{\rho_f}\nabla \cdot (\rho_f q) = 0 \tag{11}$$

It is convenient to subtract the cold fresh water hydrostatic gradient from the pressure term, $P = P_{ex} + \rho_0 gz$, where P_{ex} is the excess fluid pressure, g is gravitational

$$-\alpha_f \phi \frac{\partial T}{\partial t} + \beta_p \frac{\partial P}{\partial t} + \frac{1}{\rho_f} \nabla \cdot (\rho_f q) = 0 \qquad (11)$$

It is convenient to subtract the cold fresh water hydrostatic gradient from the pressure

term, $P = P_{ex} + \rho_0 gz$, where P_{ex} is the excess fluid pressure, g is gravitational

acceleration, ρ_0 is the reference cold water density, and z is the elevation. Note that

excess fluid pressure is related to the more familiar equivalent freshwater head, h.

Again, assuming that fractional compression of the medium is small, $\partial z / \partial t \approx 0$, (11)

becomes

$$-\alpha_f \phi \frac{\partial T}{\partial t} + \beta_p \frac{\partial P_{ex}}{\partial t} + \frac{1}{\rho_f} \nabla \cdot (\rho_f q) = 0 \qquad (12)$$

According to Darcy's Law, the volume flux of fluid is

$$q = -\frac{k}{\mu} \nabla (P + \rho_f gz) \qquad (13)$$

where k is the intrinsic permeability of the medium and μ is the kinematic viscosity of

the fluid. Again subtracting the cold water hydrostatic gradient, (13) becomes

$$q = -\frac{k}{\mu} \nabla (P_{ex} + \rho_{ex} gz) \qquad (14)$$

where ρ_{ex} is the difference between the fluid density and the reference cold water fluid

density, $\rho_{ex} = \rho_f - \rho_o$. The first term in (14) represents fluid flow driven by spatial

variations in fluid pressure and the second term represents convective fluid flow caused

by fluid buoyancy. We solve for fluid flow by separating the non-convective (pressure

driven) and convective (buoyancy driven) contributions to (14). The non-convection

contribution, $q_{non} = - (k/\mu) \nabla P_{ex}$, is substituted into (12),

$$-\alpha_f \phi \frac{\partial T}{\partial t} + \beta_p \frac{\partial P_{ex}}{\partial t} - \frac{1}{\rho_f} \nabla \cdot \frac{k\rho_f}{\mu} (\nabla P_{ex}) = 0 \qquad (15)$$

while the solution for the convective contribution is obtained by solving

$$\frac{1}{\rho_f} \nabla \cdot (\rho_{ex} q) = 0 \qquad (16)$$

In two-dimensions, (17) can be solved for the convective component of fluid flux using the streamfunction, ψ defined as

$$q_{conv} = \nabla \times \psi \tag{18}$$

or, in terms of x, z component,

$$u = \frac{-\partial \psi}{\partial z}; \quad v = \frac{\partial \psi}{\partial x} \tag{19}$$

where u and v are the x and z components, respectively, of the convective fluid flux. From (14),

$$u = \frac{k_x}{\mu}\frac{\partial P_{ex}}{\partial x} \tag{20}$$

$$v = \frac{k_z}{\mu}[\frac{\partial P_{ex}}{\partial x} + \rho_{ex}g] \tag{21}$$

Cross differentiating and rearranging terms in order to eliminate P_{ex} gives

$$-\frac{\partial}{\partial x}(\frac{\mu}{k_z}v) + \frac{\partial}{\partial z}(\frac{\mu}{k_x}u) = g\frac{\partial \rho_{ex}}{\partial x} \tag{22}$$

or, using the stream function

$$\frac{\partial}{\partial x}(\frac{\mu}{k_z}\frac{\partial \psi}{\partial x}) + \frac{\partial}{\partial z}(\frac{\mu}{k_x}\frac{\partial \psi}{\partial z}) = -g\frac{\partial \rho_{ex}}{\partial x} \tag{23}$$

The total fluid mass flux is obtained by linearly combining the convective and non-convective contributions, or

$$q = -\frac{k}{\mu}\nabla \cdot p_1 + \nabla \times \psi \tag{24}$$

The conservation of thermal energy (e.g. Smith and Chapman, 1983) is

$$\rho_m c_m \frac{\partial T}{\partial t} - \nabla \cdot (K_m \nabla T) + q \cdot \nabla \rho_f c_f T = 0 \tag{25}$$

where ρ_m, c_m, and K_m are the medium's density, heat capacity, and thermal conductivity, respectively, ρ_f and c_f are the density and heat capacity of the fluid, and T is the temperature. The conservation of chemical mass (Domenico and Schwartz, 1990) is

$$\rho_f \phi \frac{\partial C}{\partial t} - \nabla \cdot D_E \nabla \rho_f C + q \cdot \nabla C = 0 \qquad (26)$$

where $D_E = \phi^2 D$, D is diffusion coefficient in fluid phase, and C is salinity.

The fluid density is computed as function of temperature, pressure, and salinity, using the empirical formulas developed by Phillips et al. (1983)

$$\rho(C, T, P) = 1000 (a_1 + a_2\chi + a_3\chi^2 + a_4\chi^3) \qquad (27)$$

where $\chi = c_1 EXP(b_1 C) + c_2 EXP(b_2 T) + c_3 EXP(b_3 P)$, C, T and P are the solute concentration, temperature, and fluid pressure respectively. Other constant parameters are list below

$a_1 = -3.033405$, $a_2 = 10.12816$, $a_3 = -8.750567$, $a_4 = 2.663107$,

$b_1 = -4.539 \times 10^{-3}$, $b_2 = -1.638 \times 10^{-4}$, $b_3 = 2.551 \times 10^{-5}$,

$c1 = -9.9559$, $c2 = 7.0845$, $c3 = 3.9093$.

Following Kestin et al. (1981), viscosity is calculated as function of C, T and P

$$\mu(C,T,P) = \mu(T,P) \sum_{i=0}^{4} \gamma C_m^i + \omega T(1 + e^{\sigma C_m})] \qquad (28)$$

where $\quad \mu(T,P) = \mu(T) \cdot (1 + 10^{-6} \cdot \frac{\beta_w P}{1000})$ \qquad (29)

and $\quad \beta_w = \sum_{i=0}^{4} \beta_i T^i$ \qquad (30)

where $\quad \mu(T) = 1002 \cdot 10^{\tau}$ \qquad (31)

and $\quad \tau = \dfrac{\sum_{i=1}^{4} \alpha_i (20 - T)^i}{96 + T}$ \qquad (32).

See Table 2.1 for the constant parameters α, β, γ, ω, and σ.

Eqs (15), (23), (24), (25) and (26) were converted into finite-element form (Baker and Pepper, 1991). Transient solutions to the resulting equations are obtained using the 2-D finite-element AKCESS.BASIN™ software package. In the present study, the solution to each equation is iteratively computed using a fully implicit, Newton-

Raphson technique. Fluid density and viscosity are updated after each iteration. In Chapters 5 and 6, equations (15), (23), (24), (25) and (26) are used. In Chapters 3 and 4, because the solute transport is not considered, Eq (26) is not used.

All simulations in this study use variable grid size. In areas where the pressure or salinity gradient is large, or the physical property of the media is discontinuous, more elements are used to increase the accuracy of results. Variable time step is also applied in all of these simulations. In the early stage of simulation when the system is relative unstable because of large pressure or salinity gradients inherited from the initial conditions, a small time step is used to ensure the accuracy. In the later stage of modeling when the system becomes stable, a large time step is used to increase the efficiency of calculations. In order to determine the grid size and time step suitable for a particular simulation, sensitivity tests in each model are run by changing the time step and grid size, until the interested results (e.g. temperature, salinity and pressure) do not change significantly. In other words, sensitivity tests are run until the results are not significantly dependent on time step and grid size. Then, the time step and grid size are chosen for the rest of simulations in that model.

TABLE 2.1. Coefficients for Eqs. 28 to 32
(e.g. Evans, 1989)

i	α	β	γ	ω	σ
0		-1.297	1.0	6.29×10^{-4}	-0.7
1	1.2378×10^{-3}	5.74×10^{-2}	8.16×10^{-2}		
2	-1.303×10^{-3}	-6.97×10^{-4}	1.22×10^{-2}		
3	3.06×10^{-6}	4.47×10^{-6}	1.28×10^{-4}		
4	2.25×10^{-8}	-1.05×10^{-8}			

CHAPTER 3
THERMAL BUFFERING BY BASEMENT ROCKS IN NUMERICAL SIMULATIONS OF BASIN-SCALE HEAT FLOW

3.1. INTRODUCTION

There have been many numerical studies of kilometer-scale heat and fluid transport in sedimentary basins. Some of these models have been used to explain the formation of Mississippi Valley-type (MVT) lead-zinc deposits in the North American Mid-continent (for example, Sharp, 1978; Cathles and Smith, 1983; Bethke ,1985; Garven and Freeze, 1982, 1984a, b; Garven, 1985; Bethke, 1986; Garven and Sverjensky, 1989; Ge and Garven, 1989; Bethke and Marshak, 1990, Deming et al., 1990; Deming and Nunn, 1991, Garven et al, 1993). These studies have supported the hypothesis that MVT ore deposits formed as a result of warm, saline fluids migrating through sedimentary basins and lead to the recognition that compaction of sediments results in flow velocities too low to efficiently transport heat by advection. Therefore, this is not a viable mechanism for MVT formation (Deming and Nunn, 1991).

Some of these studies (Garven and Freeze, 1982, 1984a, b; Garven, 1985; Bethke, 1986; Garven and Sverjensky, 1989; Ge and Garven, 1989; Bethke and Marshak, 1990, Garven et al, 1993) used constant heat flow at the sediment-basement contact as a lower thermal boundary condition and did not consider the basement as a part of the model. This type of boundary condition may cause problems in predicting temperature distribution and heat flux because of (1) heat refraction along the sediment-basement contact, and (2) thermal buffering by basement rocks in response to heat transport by fluid flow within the sediments.

Thermal conductivity of basement rocks is usually higher than that of overlying sediments, because basement rocks usually have lower porosity and contain less clay and carbonaceous materials. In some sedimentary basins underlain by igneous or metamorphic rocks, the thermal conductivity contrast between the sediments and

13

basement rocks can be significant. For example, thermal conductivities of sediments in the Ozark Plateau, Arkansas and Missouri, range from 1.42 to 2.69 W/m-K, whereas thermal conductivities of igneous rocks in the St. Francois Mountains range from 2.4 to 3.25 W/m-K (Meert et al., 1991). The buried Precambrian basement rocks of the North American Mid-continent are believed to have similar characteristics to those exposed in the St. Francois Mountain (Kisvarsanyi, 1980) and, therefore, should have similar thermal conductivities. Deming et al. (1990) pointed out that heat refraction along the basement-sediment contact can cause heat to preferentially flow into the more conductive basement rocks. They used a typical conductivity of 1.6 W/m-K for sediments and 3.2 W/m-K for basement rocks. Heat refraction can significantly increase surface heat flow at the basin flank (Figure 3.1). Similar refraction of heat within a basin may occur in the presence of large, lateral thermal conductivity contrasts, such as near the sediment-salt dome interface (O'Brien and Lerche, 1988; Evans and Nunn, 1989).

When topography is a major driving mechanism for regional flow associated with foreland uplift (Garven and Freeze, 1982, 1984a, b; Garven, 1985; Bethke, 1986; Garven and Sverjensky, 1989; Bethke and Marshak, 1990; Deming and Nunn, 1991), cold fluids driven downwards from the recharge areas can pick up a large amount of heat, which is efficiently transported along high permeable basal aquifers to the discharge areas. Thus, geothermal gradients in such basins are strongly effected by groundwater flow. This implies a difficulty in maintaining a constant heat flow along the sediment-basement contact. For example, in an uplifted foreland basin with a groundwater flow rate as high as 5.0 m/yr. along the basal aquifers (such as Garven et al., 1993), hot upward-flowing fluids can significantly decrease the temperature contrast between the sediments and basement rocks and reduce the upward heat flow from the basement into the basin.
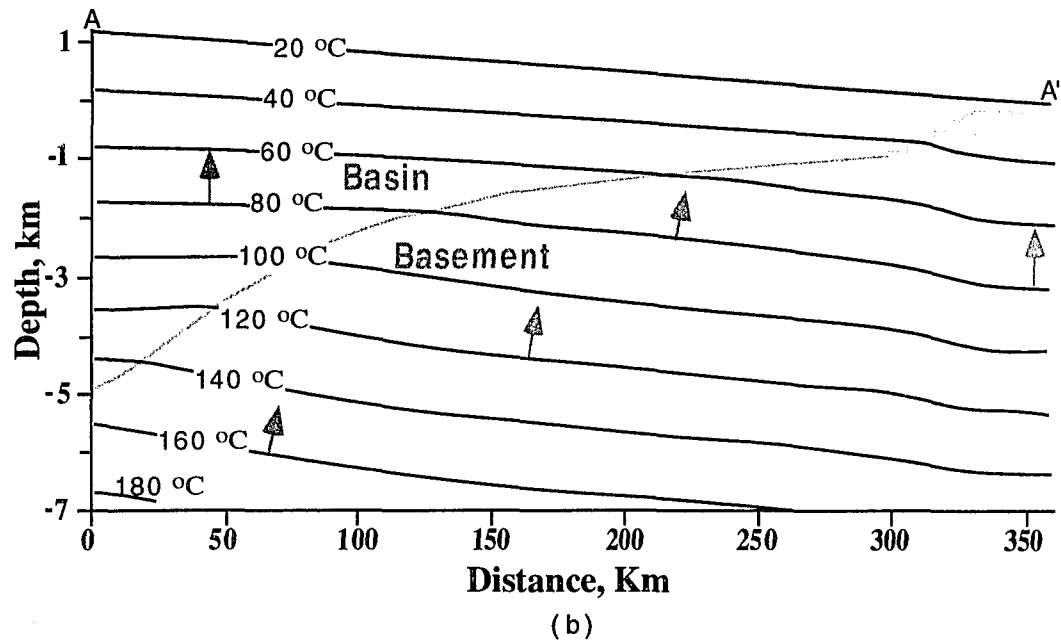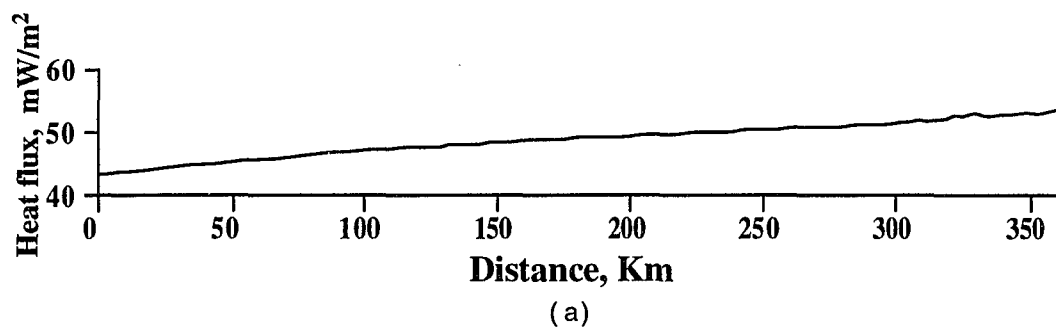
Figure 3.1 Surface heat flow (a) and temperature (b) of transient heat conduction calculated by the numerical model used in the study area. Arrows show heat rafraction from low thermal-conductivity sediments in the basin into surrounding basement rocks. See Figure 3.2 and Table 3.1 for the location of cross-section A-A', stratigraphy and for the details of rock properties.

Therefore, constant heat flow along the sediment-basement contact as the lower thermal boundary condition may cause under or over-estimation of the temperature field and heat flow within an uplifted foreland basin. Temperature is a important factor controlling many geochemical reactions such as organic matter maturation (e.g. Wood, 1988; Mackenzie and Quigley, 1988; Demaison, 1984) and mineral diagenesis (e.g. Sverjensky, 1986; Saunders and Swann, 1994; McManus and Hanor, 1993). Thus, it is necessary to precisely predict the temperature distribution in numerical simulations. The purpose of this study is to quantitatively determine the thermal consequences of introducing the basement section as part of the model and to understand the role which the basement plays in the thermal evolution of an uplifted foreland basin.

3.2. MODEL DESCRIPTIONS

The model profile is taken from Garven et al. (1993) for the simulation of southern interior flow systems. The cross-section cuts through the eastern half of the Arkoma Basin, along a transect that begins in the undeformed foreland north of Little Rock, Arkansas, extends northward over the Ozark dome, and terminates near the Missouri River, west of St. Louis (Garven et al., 1993; see Figure 3.2). The upper boundary of the model, which represents the water table, is idealized to have an uniform slope of 1.2 km over 360 km. Physical parameters used in this model are listed in Table 3.1. Units A and B have high permeabilities and are treated as basal aquifers. Units C and D are low in permeability and therefore treated as aquitards. I consider the igneous rocks in St. Francois Mountains as part of the basement. Because Garven et al. (1993) did not specifically describe the thermal conductivities of the sediments and igneous rocks, a typical value of 2.0 W/m-K for all the sediments and 2.9 W/m-K for the Precambrian basement rocks were used. These thermal conductivities are typical for the study area (Meert et al., 1991; Garven and Freeze, 1984b). See Garven et al. (1993) for details regarding the stratigraphy and lithology.
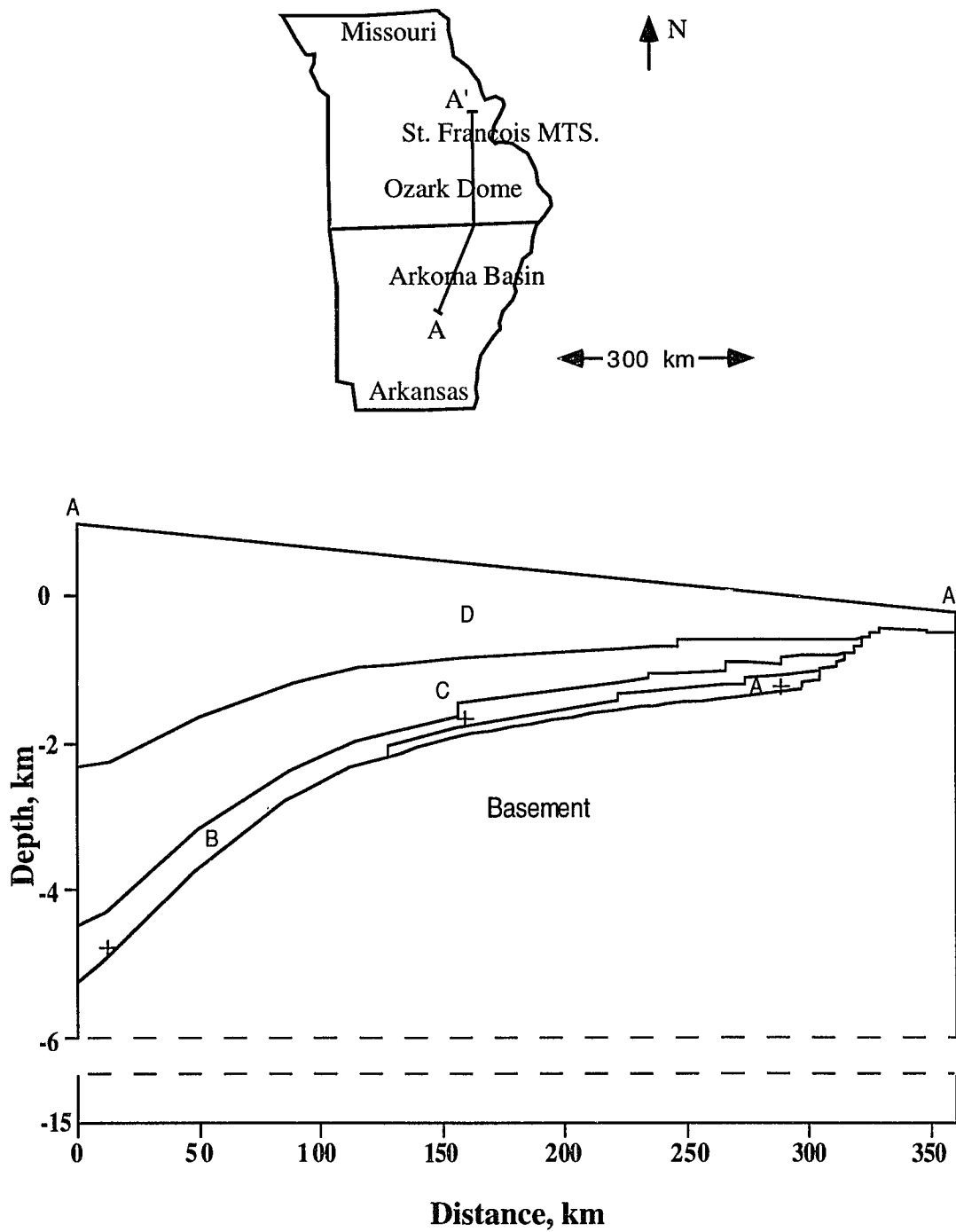
Figure 3.2. Hydrogeological model (modified after Garven et al., 1993). See Table 3.1 for parameters of Units A, B, C, D and the Basement rocks. The three cross marks show the locations of temperature variations with time shown on Figure 3.14.

The first model, no-basement model, does not include the basement and the lower thermal boundary condition is set at the sediment-basement interface. The upper part of the second model, with-basement model, is exactly the same with the first model, however, the lower thermal boundary of this model is extended far below the sediment-basement contact to a depth of 15 km (Figure 3.2). I assume that basement rocks are impermeable and have the same thermal conductivity of 2.9 W/m-K with those exposed in the St. Francois Mountains (Table 3.1).

TABLE 3.1. Model parameters
(see Figure 3.2 for the sections)

Sections	Horizontal permeability (mD)	Vertical permeability (mD)	Thermal Conductivity (W/m-K)	Porosity
Unit A	1.90×10^3	1.90×10^1	2.0	0.25
Unit B	9.50×10^2	9.50×10^0	2.0	0.20
Unit C	3.17×10^1	3.17×10^{-1}	2.0	0.10
Unit D	3.17×10^1	3.17×10^{-1}	2.0	0.10
Basement	0.0	0.0	2.9	0.01

Boundary conditions in both models are similar to Garven et al. (1993). In each of the models, temperature along the top (water table) was fixed at 20 °C and a constant heat flow of 66 mW/m^2, which is approximately the continental mean (Sclater et al., 1981) and lower than that used by Garven et al. (1993), was maintained along the lower base. There is no heat and fluid flow on the sides. Hydraulic head along the top boundary is linearly fixed corresponding to the water table elevation, with 12 MPa at the left end and 0 MPa at the right end.

Initial thermal conditions were steady state heat conduction (Figures 3.3a and 3.3b). Figure 3.4a shows the initial heat flow along the basement upper surface of the with-basement model and that along the lower boundary of the no-basement model,
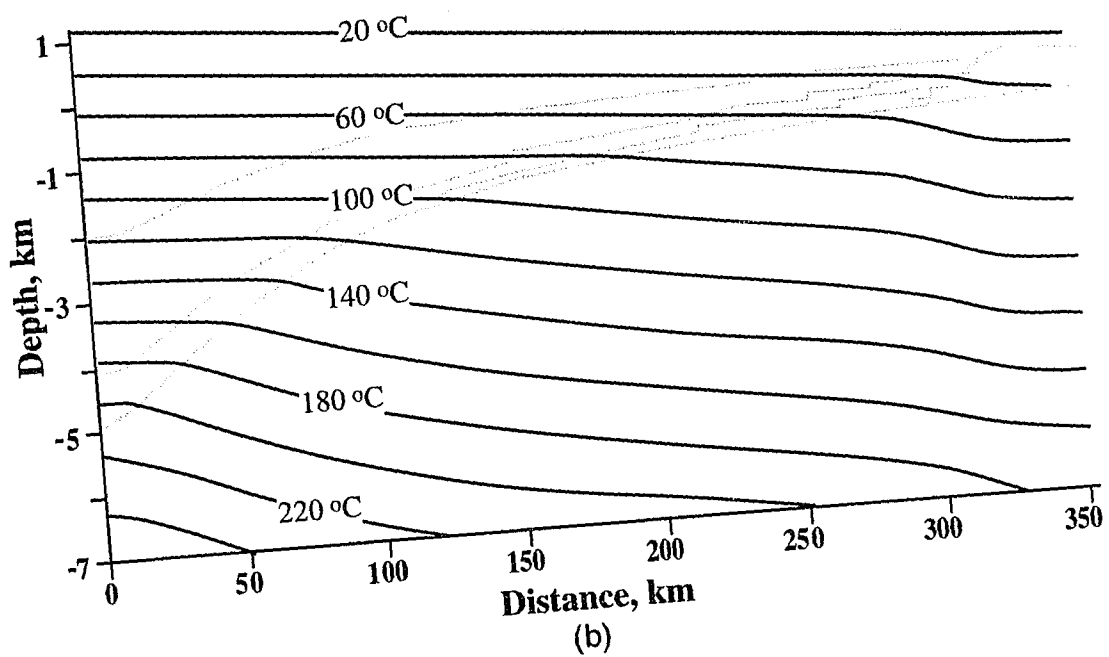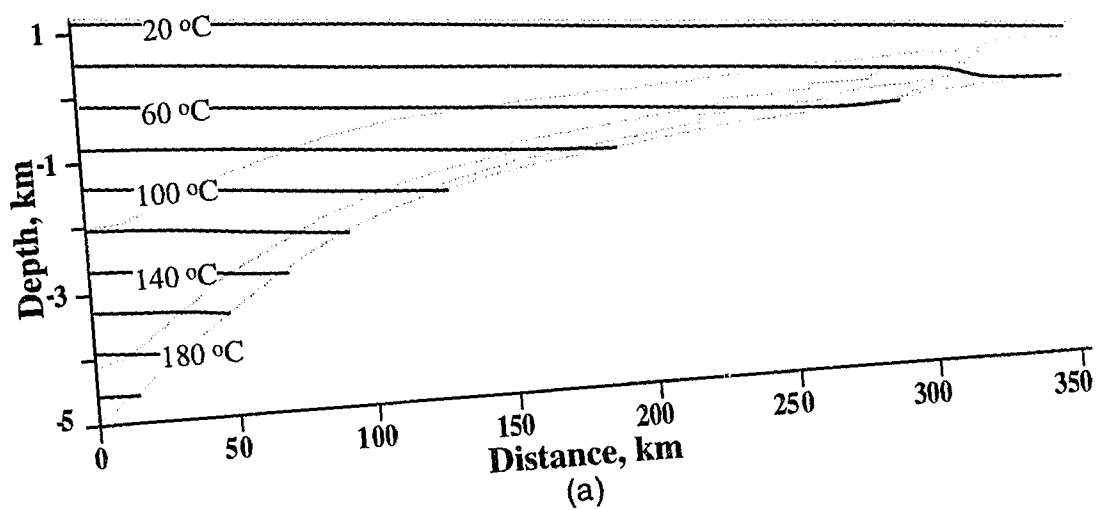
Figure 3.3. Initial temperature distribution of steady-state of heat conduction in no-basement (a) and with-basement (b) models.
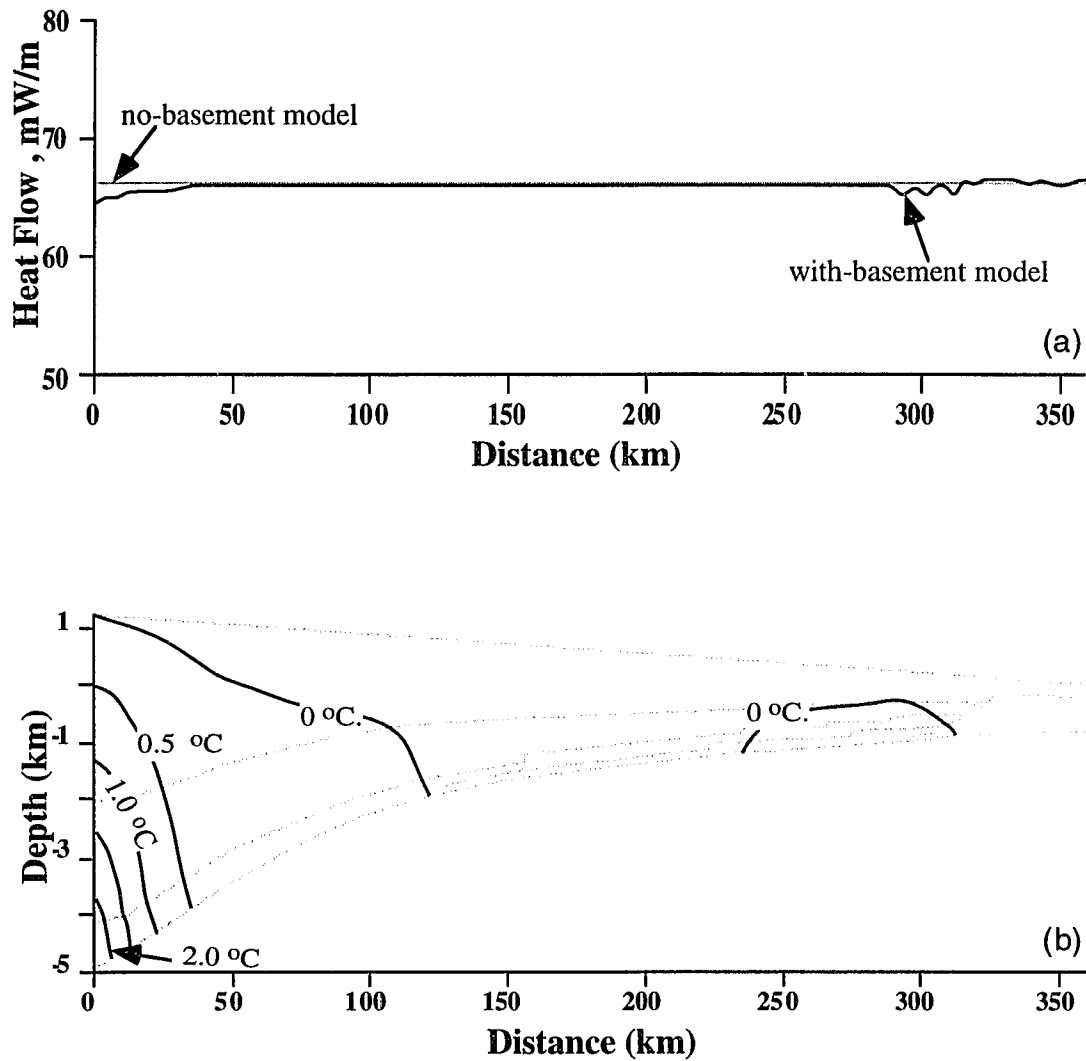
Figure 3.4. (a) shows initial heat flow along the sediment-basement contact in no-basement model (light line) and with-basement model (dark line); (b) shows the initial temperature difference between these two models.

respectively. Heat refraction along the basement-sediment interface causes slightly different in initial temperature between these two models. However, in most places the difference is less 0.1 °C and a maximum of 2.5 °C occurs in the bottom, left corner of the model (Figure 3.4b). The small difference between these two heat flow curves is caused by heat refraction along the basement top. Initial pressure conditions were taken from the steady state pressure diffusion.

The following simulations are transient cases. Governing equations used in this study are Eqs (15), (23), (24) and (25) in Chapter 2. Fluid density and viscosity are calculated using Eqs (27) and (28) in Chapter 2, respectively. In order to simplify the simulations, temperature was assumed to be constant (20 °C) for the fluid density calculation. Because these simulations do not consider the solute transport and the density variation with temperature, the hydrological system is relatively stable. Sensitivity tests in this study indicate that the simulations can use relatively large grid size and time step. The method for determining the grid size and time step is described in Chapter 2. In the very early stage of simulation, time step was set to be 1,000 years. The time step was gradually increased to 10,000 years at a modeling time of 500,000 years and then remained unchanged. The flow region is discretized with a finite element mesh containing 33 rows and 81 columns with variable element sizes in the no-basement model. In the with-basement model, because there is no fluid flow in the basement, I used a coarse finite element mesh with rows of 12 and columns of 81 to handle only heat conduction in the basement. The total number of nodes for the with-basement model is 45 x 81.

3.3. MODEL SIMULATIONS

3.3.1. Fluid flow

Figure 3.5a shows the groundwater flow field of the with-basement model at an elapsed model time of 1 Ma. Velocity fields are very similar in both models. The velocity arrows are shown with the same vertical exaggeration as the physical domain
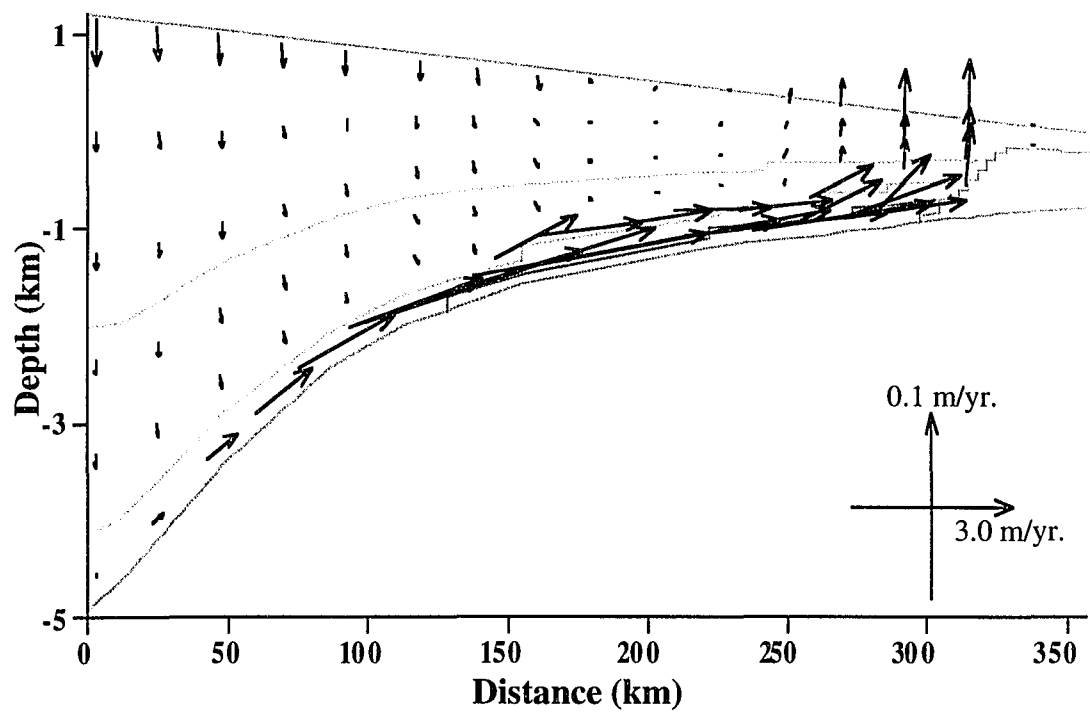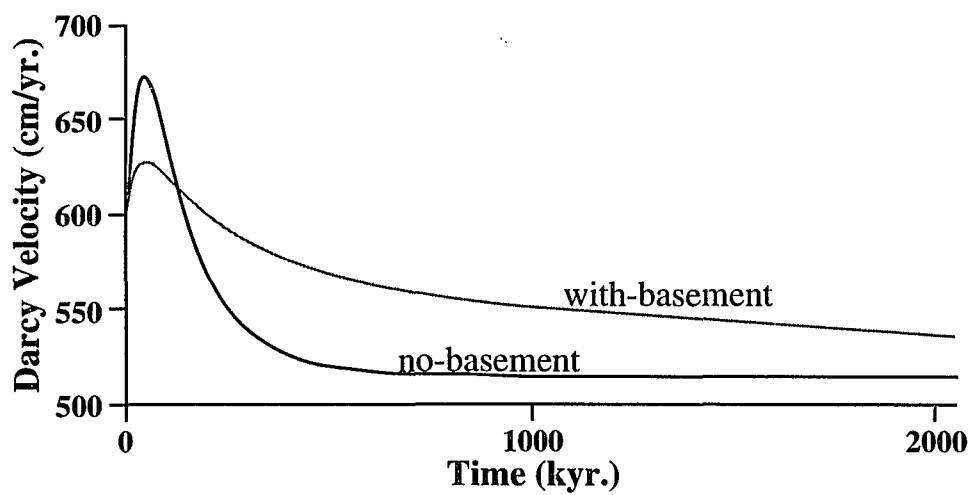
Figure 3.5. (a) shows the flow pattern at 1.0 Ma in with-basement model. This flow pattern is also similar to that in the no-basement model. (b) shows the variation of maximum Darcy velocity with time in both models

of the model basin. Thus, the arrows show the true direction of fluid flow. On the left

side of the model, fluids were driven by the topography gradient, flowing downwards to

recharge the basal aquifers, with a vertical flow rate of a few centimeters per year. In

the discharge area (on the right of the model), flow was upward from the basal aquifers.

Horizontal discharge Darcy rate in the aquifers can be as high as 5.0 m/yr., consistent

with Garven et al. (1993). In the middle region of the model, fluids are mainly flowing

horizontally.

The major differences in flow field between the two models are (1) the maximum

horizontal discharge velocity in the no-basement model was about 45 cm/yr. higher than

that in the with-basement model at an elapsed time of about 0.1 Ma; (2) Darcy velocity

in the no-basement model decreased more quickly than in the with-basement model;

(3) after an elapsed time of 0.2 Ma, Darcy velocity in the with-basement model became

higher than that in the no-basement model (Figure 3.5b).

These differences were primarily caused by thermal buffering by basement rocks in

the with-basement model, which I will discuss in the following section. The buffering

effect causes the sediments in the with-basement model to have a lower average

temperature in the early stage of modeling, but to maintain higher temperatures in the

later stage, compared to those in the no-basement model. Higher temperatures can

result in lower fluid viscosities and increase flow velocities. The rapid decrease in

Darcy velocity in the no-basement model also indicates that the system was losing heat

faster than the with-basement model.

3.3.2. Temperature field and heat flow at basement-sediment interface

The transient temperature distribution are quite different between the two models.

In each of the models, downward movement of fresh water from the recharge area has

cooled the sediments of the basin and, hence, pulled down the isotherms (Figures 3.6,

3.7 and 3.8). On the other hand, upward movement of hot fluids in the discharge area
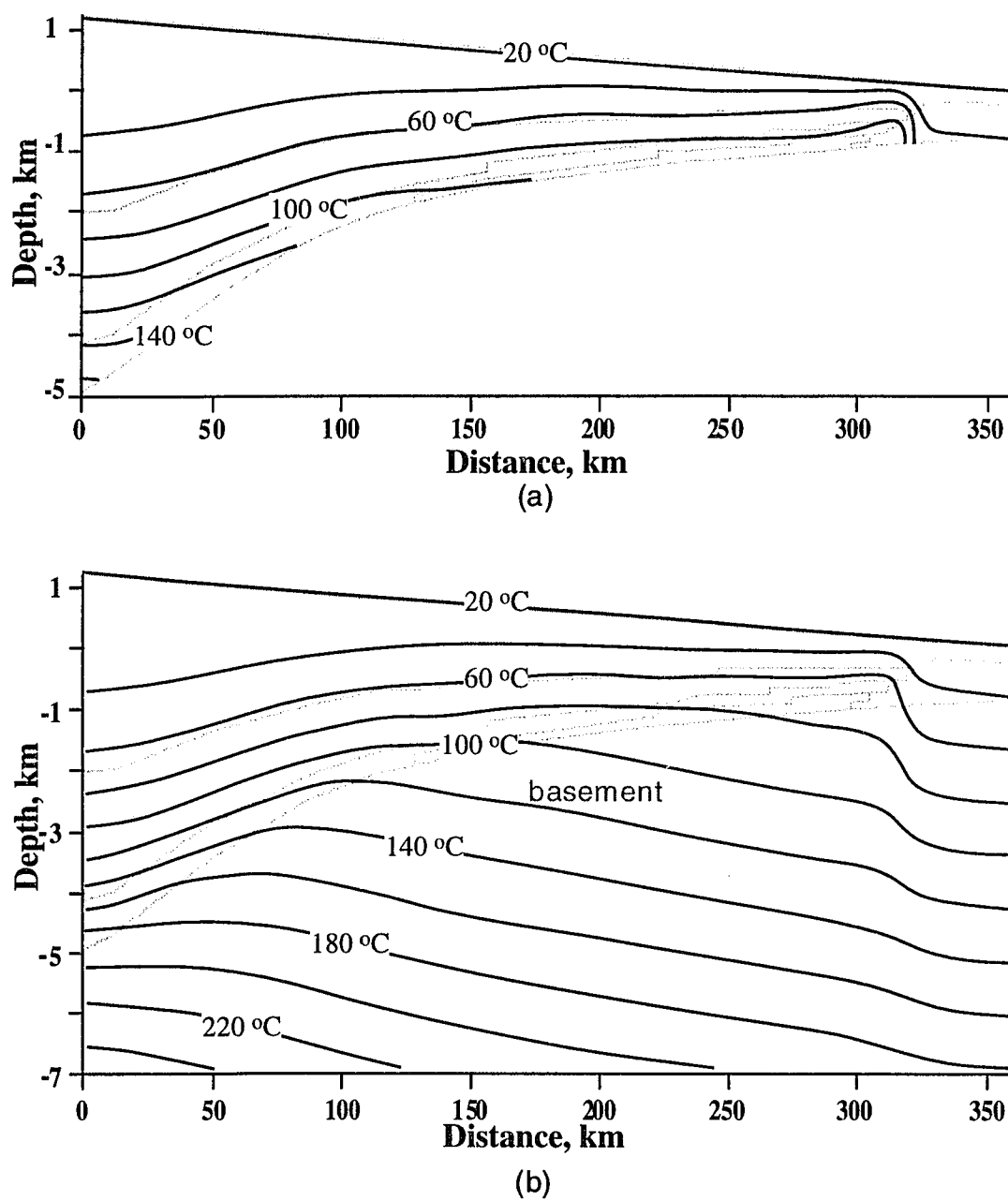
Figure 3.6. Temperature distribution at 0.1 Ma in (a) no-basement and (b) with-basement models. The light lines outline the stratigraphic units.
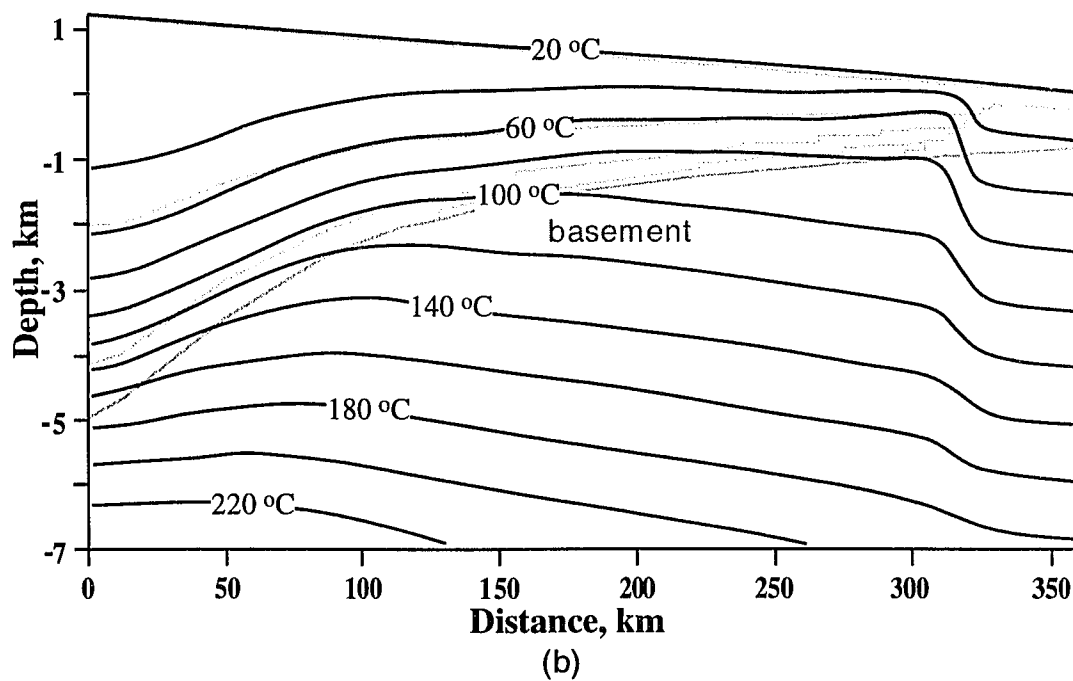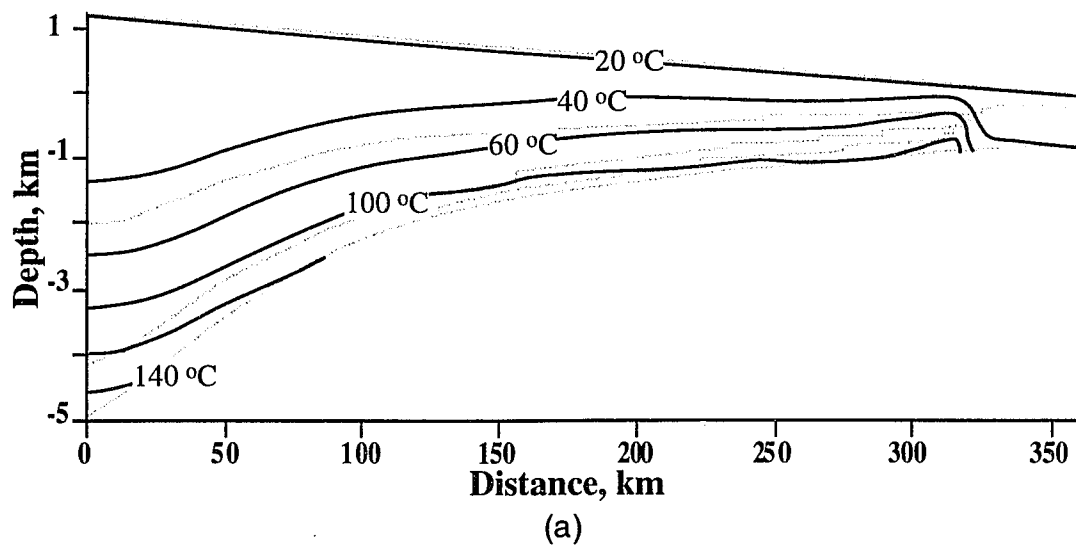
Figure 3.7. Temperature distribution at 0.2 Ma in (a) no-basement and (b) with-basement models. The light lines outline the stratigraphic units.
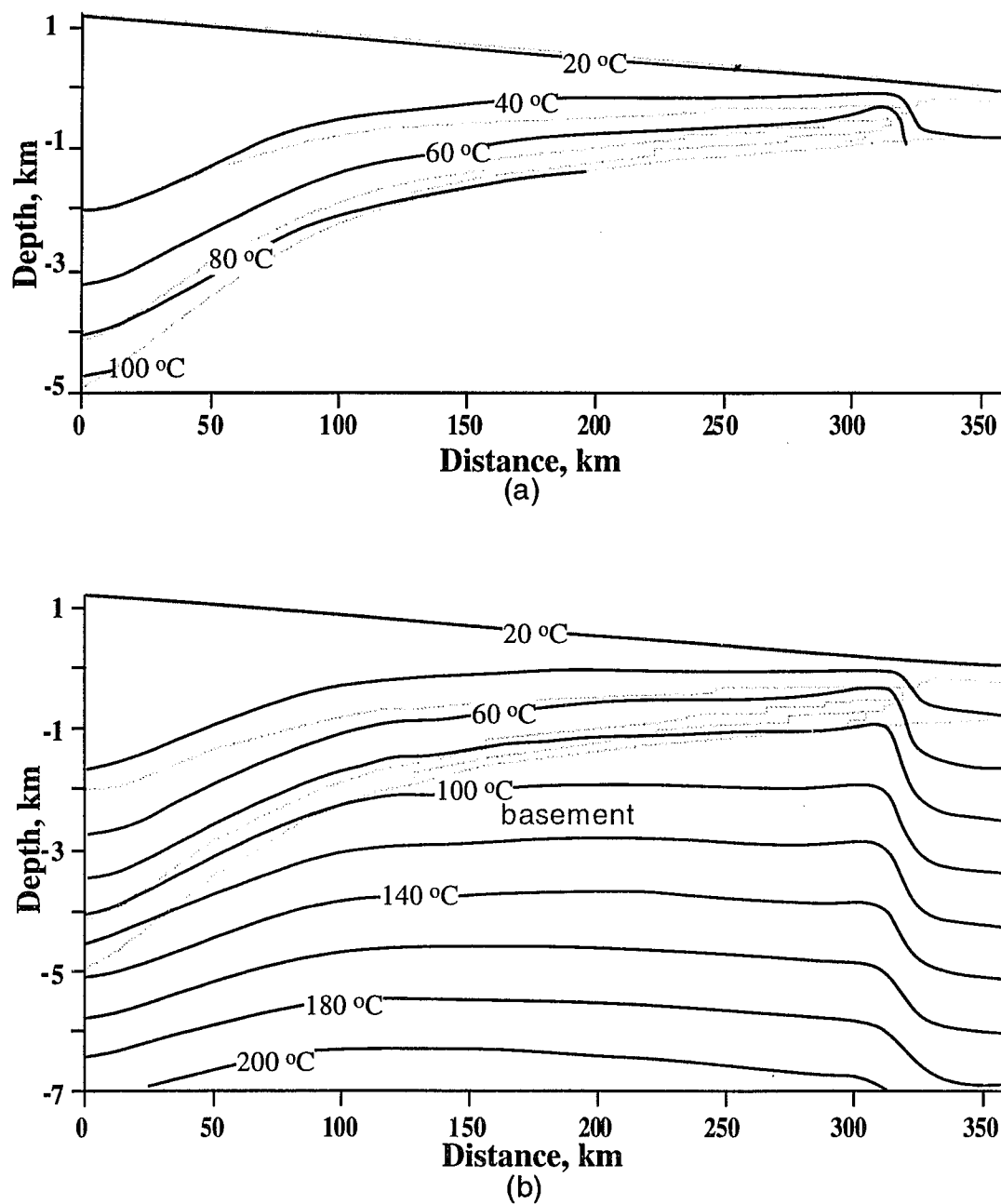
Figure 3.8. Temperature distribution at 1.0 Ma in (a) no-basement and (b) with-basement models. The light lines outline the stratigraphic units.

has warmed the shallow sediments and pulled up the isotherms in the discharge area (Figures 3.6, 3.7 and 3.8). The temperature changes caused by the dynamic flow systems are more obvious on the residual (current temperature minus initial temperature) temperature fields (Figures 3.9, 3.10 and 3.11).

In the early stage of simulation at 0.1 Ma, temperature increased about 40 °C in the discharge area and decreased about 40 °C in the sediments below the recharge area in the no-basement model compared to the initial temperatures; whereas in the with-basement model, temperature increased only about 20 °C in the discharge area and decreased about 25 °C in the sediments below the recharge area (Figures 3.9, 3.12 and 3.13). However, in the late stage of simulation, temperature variations in these two models are quite different. For example, at 1.0 Ma, temperature increased about 20 °C in the discharge area and decreased about 100 °C in the recharge area in the no-basement model. But in the with-basement model, temperature increased up to 30 °C in the discharge area and decreased about 80 °C under the recharge area (Figures 3.11, 3.12 and 3.13).

These differences are caused by the thermal effect of the basement rocks. In the with-basement model, heat lost by the downward flowing of cold waters and the upward flowing of hot fluids along the basal aquifers, was compensated by additional heat flow from the basement. In other words, cooling caused by the recharge of cold waters increased the thermal gradient between the deeper part of the basin and the basement rocks. Thus, heat flow increases along the left side of the basement surface to values much higher than those along the no-basement model base ($66 \ mW/m^2$), especially in the early stage of simulation (Figure 3.14). Even though heat refraction can cause heat to preferentially flow in the high conductivity basement rock, the large thermal gradients force more heat to flow vertically upward, which maintained higher temperatures in deep sediments below the recharge region. However, in the no-basement model, we always maintain a constant heat flow along the sediment-basement
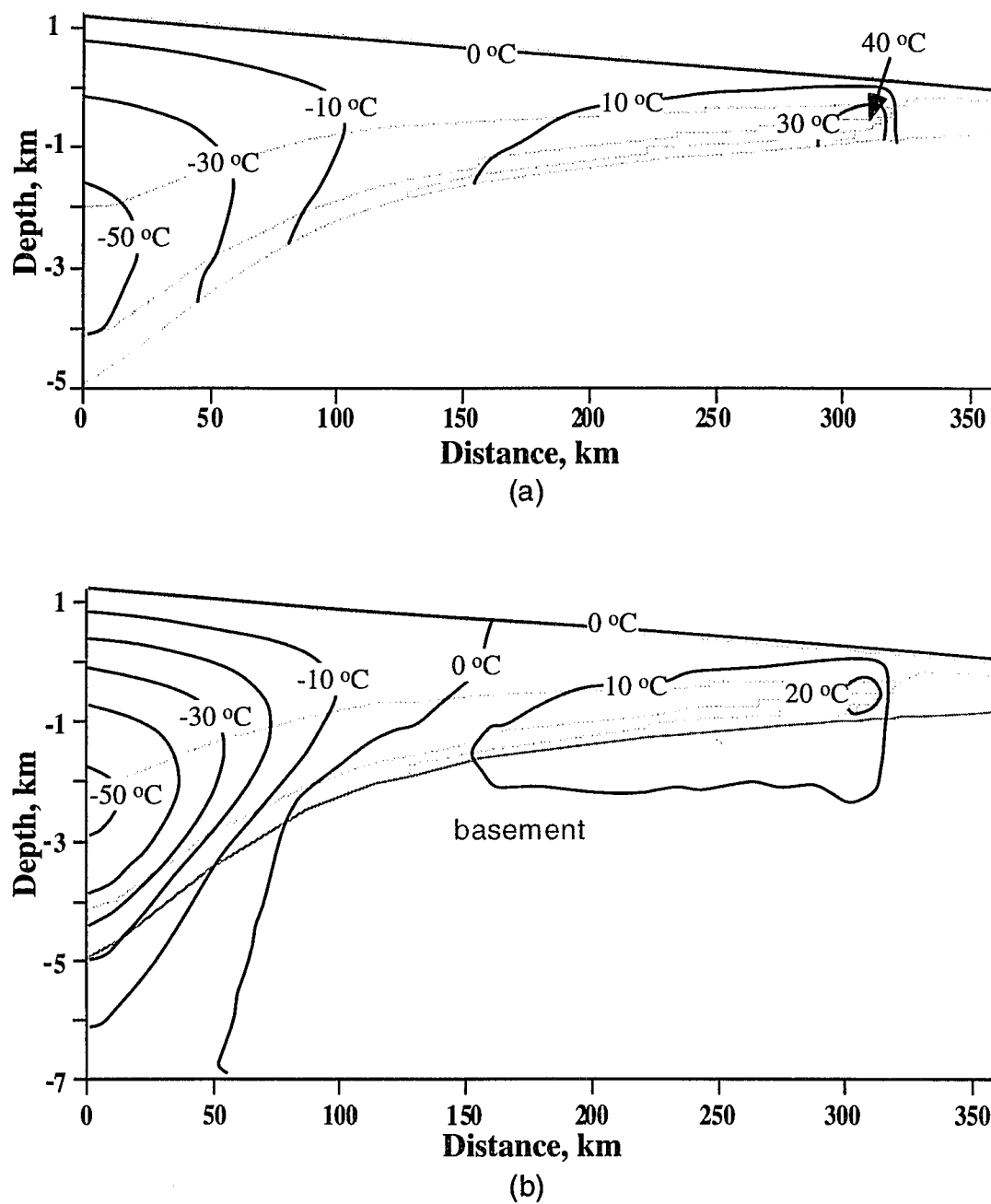
Figure 3.9. Residual temperature (T-To) at 0.1 Ma in (a) no-basement and (b) with-basement models. The light lines outline the stratigraphic units.

Depth, km

1

-1

-3

-5

0 °C

10 °C

20 °C

-10 °C

-30 °C

-50 °C

-70 °C

0   50   100   150   200   250   300   350

Distance, km

(a)

Depth, km

1

-1

-3

-5

-7

0 °C

0 °C

20 °C

-20 °C

-40 °C

-60 °C

basement

0   50   100   150   200   250   300   350

Distance, km

(b)
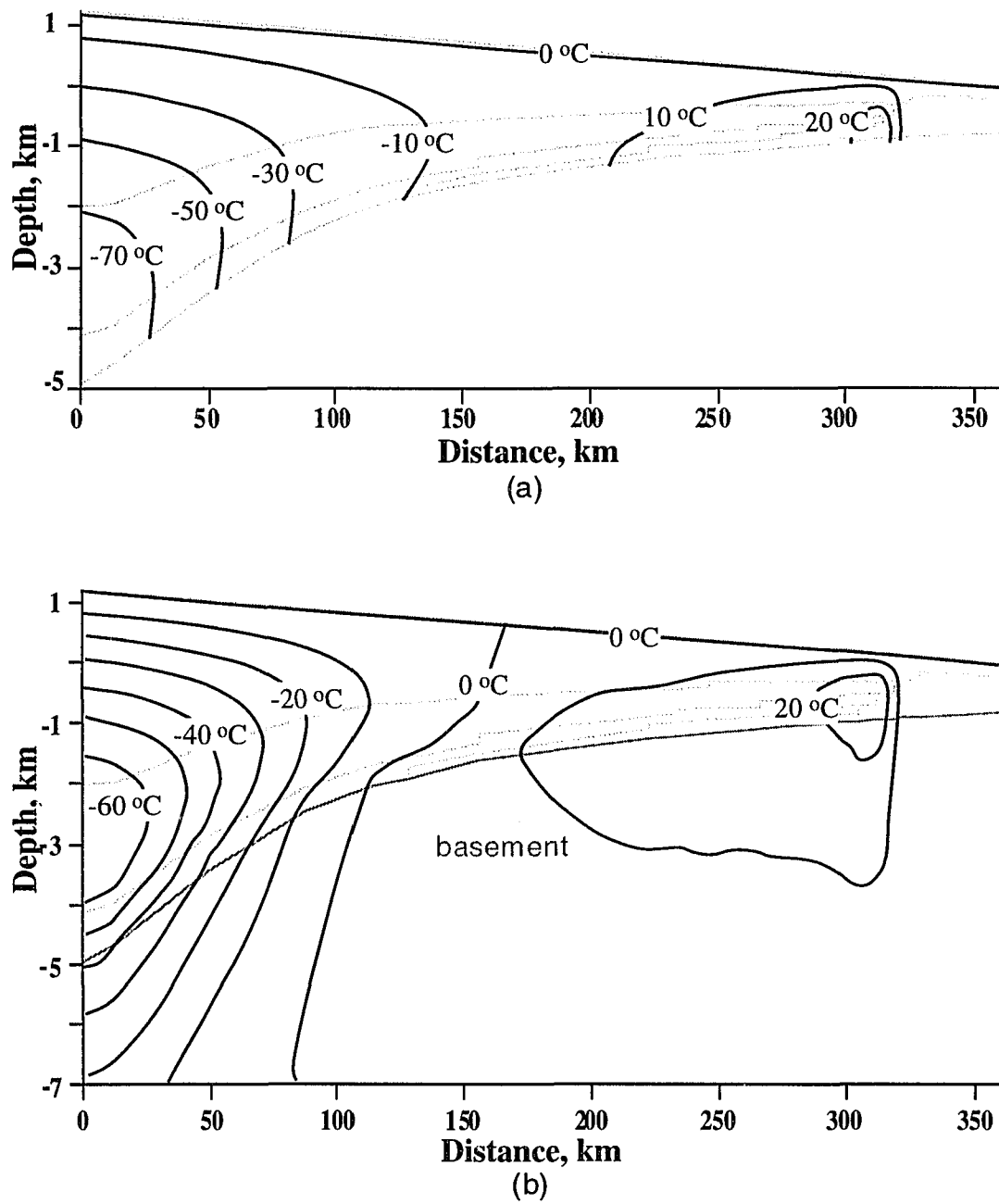
Figure 3.10. Residual temperature (T-To) at 0.2 Ma in (a) no-basement and (b) with-basement models. The light lines outline the stratigraphic units.
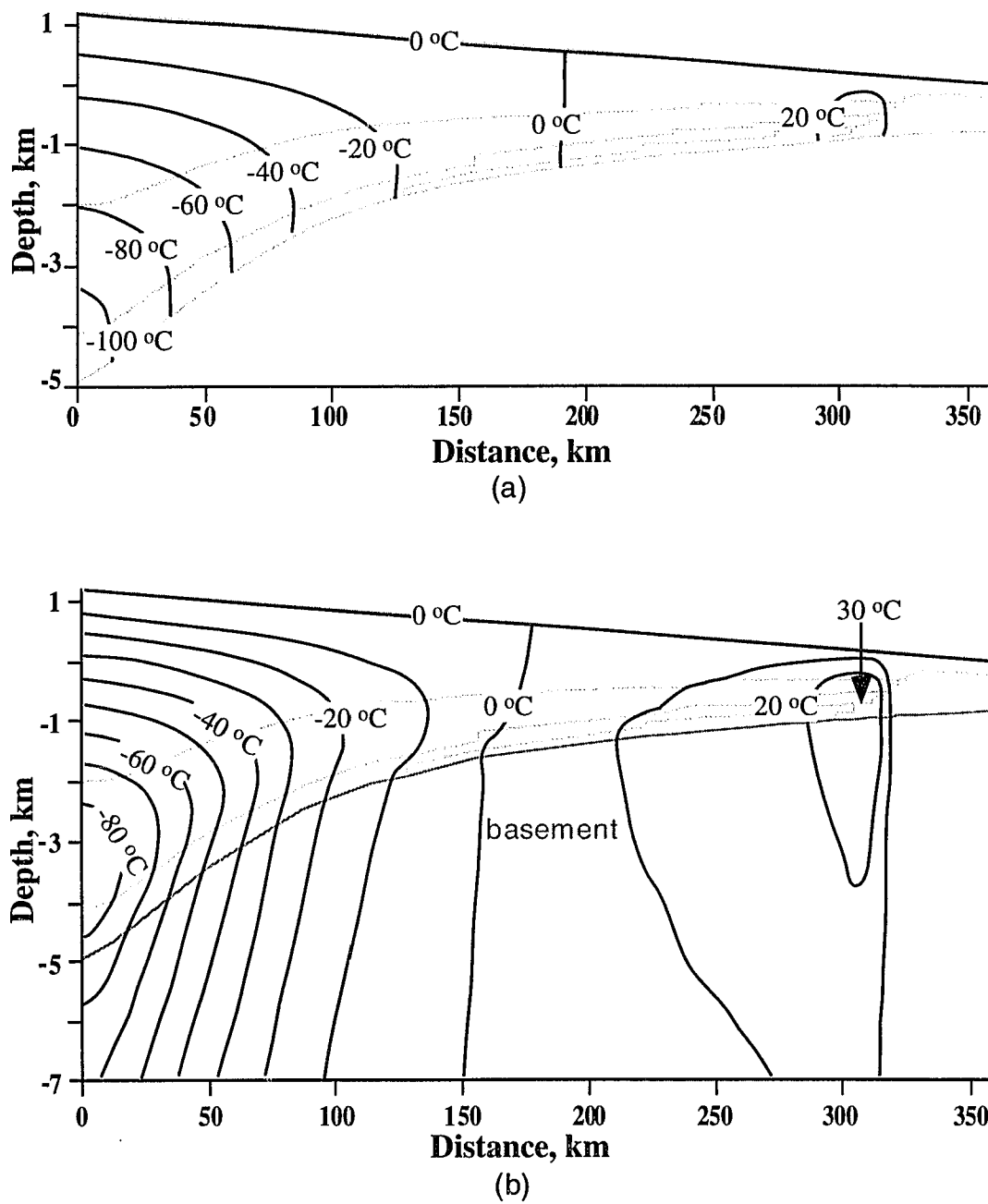
Figure 3.11. Residual temperature (T-To) at 1.0 Ma in (a) no-basement and (b) with-basement models. The light lines outline the stratigraphic units.
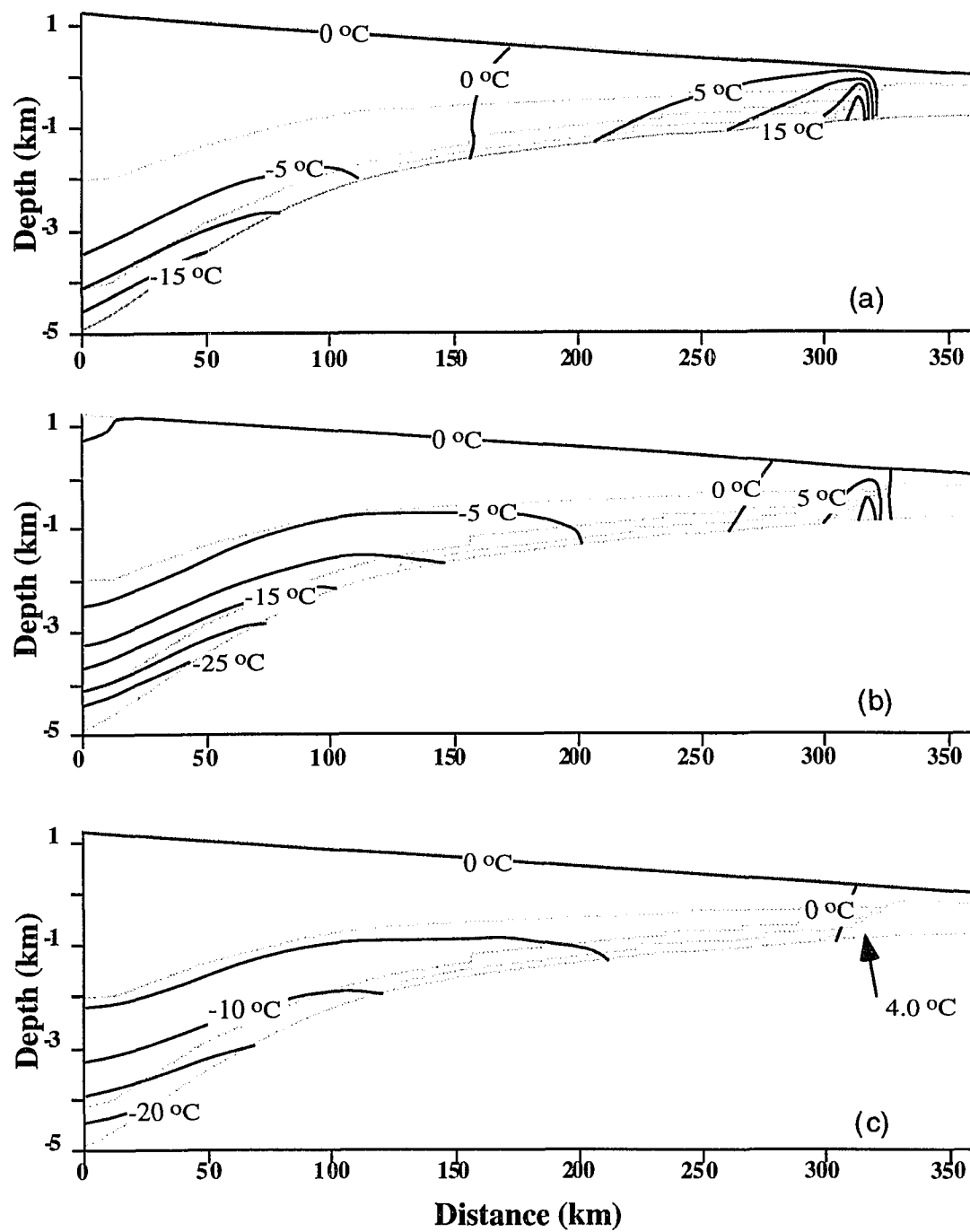
Figure 3.12. Temperature differences between no-basement and with-basement models at 0.1 (a), 0.2 (b) and 1.0 (c) Ma. The light lines outline the stratigraphic units.
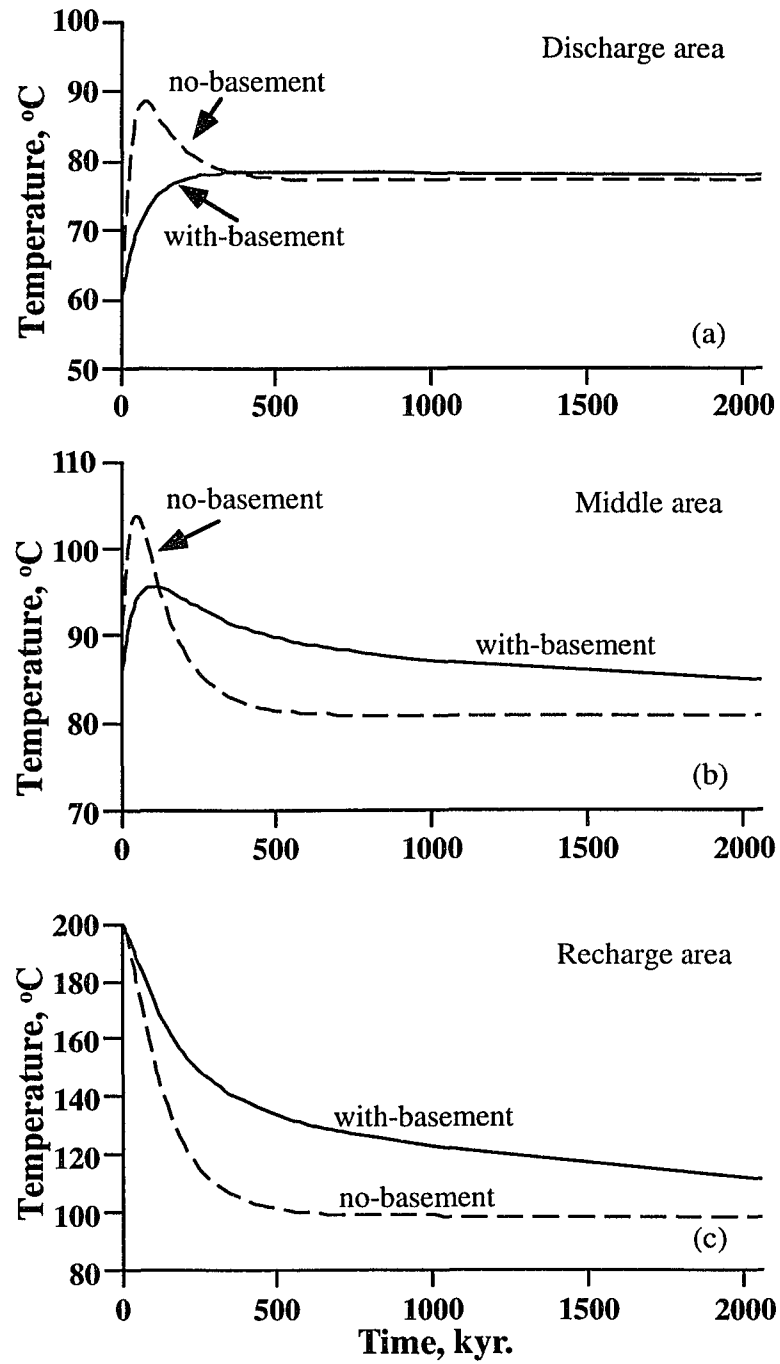
Figure 3.13. Temperature variation with time for both no-basement (dash lines) and with-basement (solid lines) in discharge area (a), in the middle of the basin (b) and below the recharge area (c). See the cross marks in Figure 3.2 for locations.

Heat Flow along Sediment-Basement Contact
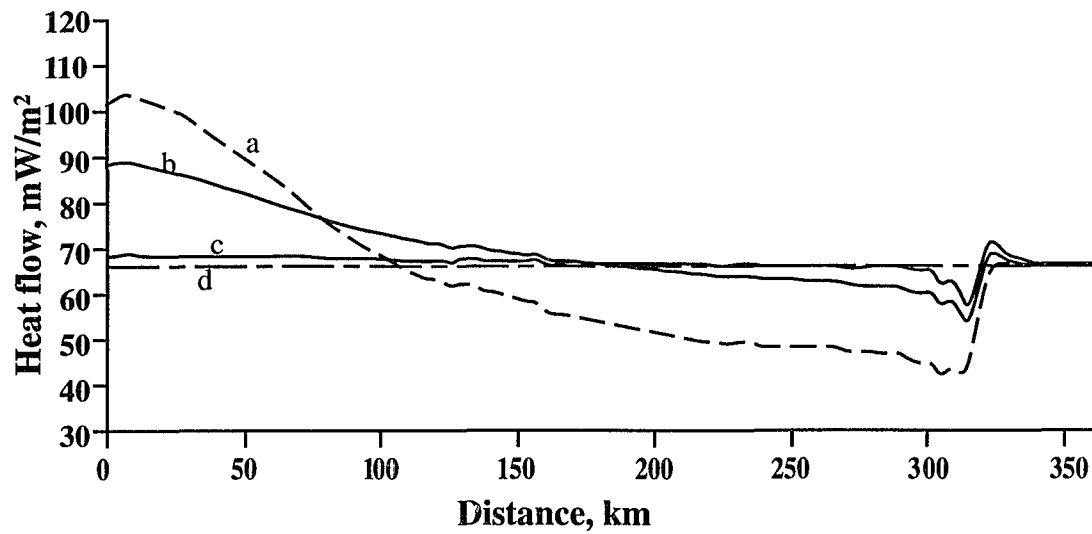
Figure 3.14. Heat flow along the sediment-basement contact at 0.2 (Curve a), 1.0 (Curve b) and 5.0 (Curve c) Ma in the with-basement model. Curve d is the heat flow along the sediment-basement contact in the no-basement model at all model times.

contact. Thus, the residual temperatures (absolute value) under the recharge area in the with-basement model are smaller than those of the no-basement model (Figures 3.9, 3.10 and 3.11).

In the discharge area, warming caused by the upward-movement of hot fluids along the basal aquifers has decreased the thermal gradient between the sediments and basement rocks. Thus, heat flow at the sediment-basement contact in the discharge area falls below the initial value of 66 mW/m^2 (Figure 3.14). This is why in the early stage of simulation, temperatures in the discharge area of the with-basement model are not as high as those in the no-basement model.

Temperature variations with time in shallow sediments of the discharge area, in the middle of basin, and in the deep sediments below the recharge region are shown in Figure 3.13. A very interesting phenomenon is the transient thermal pulse. In the discharge area, an obvious thermal pulse is observed in the early stage of simulation in the no-basement model, but not at all in the with-basement model (Figure 3.13a). In the middle of the basin, each of the models experienced a transient thermal pulse, but the amplitude in the no-basement model is much larger than in the with-basement model (Figure 3.13b). The transient thermal pulse observed in the no-basement model is consistent with that predicted by Garven et al. (1993). Temperature in deep sediments on the far left in both models always decreases with time, but temperature in the with-basement model decreases much slower than the no-basement model (Figure 3.14c), as discussed above.

The reason for the difference between the models is thermal buffering causes less heat to flow up from the basement into the overlying sediments in the discharge area. Less heat flux results in relative low temperatures in the discharge area. Heat energy represented by the thermal pulse carried upward by the fluid flow along the basal aquifers is partially offset by a decline in upward heat transport from the basement

rocks. Therefore, the transient pulse in the with-basement model is much smaller and eventually disappears in the discharge area.

Temperature increased 10 to 20 °C in the upper basement (Figures 3.9b, 3.10b and 3.11b). The major reason for this temperature increase is that a heat flow decrease from the basement rocks into the sediments in the discharge area (Figure 3.14) caused heat to accumulate in the upper basement. Thus, the temperatures increased in shallower basement rocks under the discharge area, while the temperatures of the deeper basement rocks remained unchanged (Figures 3.9b and 3.10b).

The basement acts as a thermal buffer, which keeps the cooling part of the basin warm and the warming part cool. Thermal buffering by basement rocks is also indicated by the variation of average heat flow at the basement-sediment interface. In the early stage of simulation (e.g. 0.2 Ma) when the whole basin was still hot, the basement provided less heat to the basin by decreasing the average heat flow at the interface to be lower than the basal heat flow. In the later stage of modeling (such as 1.0 Ma) when the basin is cool, more heat flowed from the basement into the basin, indicated by that the average heat flow at the sediment-basement interface is higher than the basal heat flow (Figure 3.14).

Although this buffering effect causes significant differences in the early stage of modeling, steady state results are similar. Identical temperature profiles along the sediment-basement interface in both models are attained at their approximately steady states (Figure 3.15). However, thermal buffering causes the with-basement model to take much longer (>5 m.y.) to attain steady-state conditions, whereas it takes less than 1 Ma for the no-basement model to achieve steady-state. Cooling and warming, respectively, below the recharge and discharge regions cause the temperature along the base of the with-basement model to be re-adjusted, in order to maintain the constant heat flow (not shown).
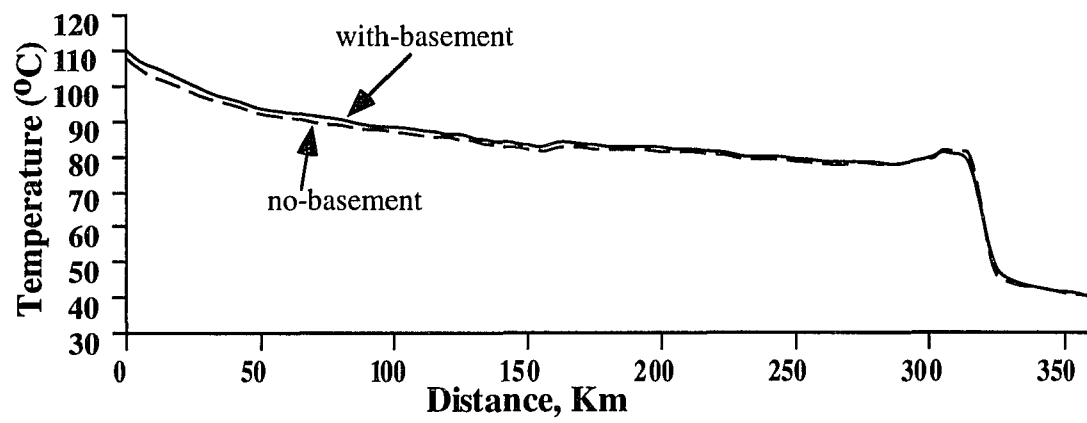
Figure 3.15. Temperature distributions at approximate steady-state along the sediment-basement contact in both no-basement (dash line) and with-basement (solid line) models.

3.3.3. **Surface heat flow**

Surface heat flow in each of the models is computed by considering only conductive component in the upper 2 nodes. Ignoring the advective component in heat flow calculations is to draw a comparison between model predictions and the usual convention (steady state conduction) used to estimate heat flow in geophysical field studies (e.g. Deming and Nunn, 1991). Surface heat flow in the recharge area does not change much with time and is about 50 mW/m² lower than the basal heat flow in both models (Figure 3.16). In the discharge area, however, maximum surface heat flow is about 330 mW/m² in the no-basement model and about 230 mW/m² in the with-basement model at 0.1 Ma. Both are much higher than the basal heat flow. Surface heat flow in the discharge area also significantly changes with time. In the no-basement model, surface heat flow decreases with time; whereas, in the with-basement model, surface heat flow increases with time (Figure 3.16). At 1.0 Ma, surface heat flow in the discharge area is very similar in both models.

High heat flow values in the discharge area are mainly caused by the high permeabilities of the basal aquifers and by the hydrological barrier of the impermeable igneous rocks such as those in the St. Francois Mountains (Figure 3.16). These curves, however, generally reflect that groundwater flow reduces heat flow in the recharge region and tremendously increases heat flow in the discharge area, and are consistent with results obtained by many other workers (e.g. Majorowicz and Jessop, 1981; Kilty and Chapman, 1982; Chapman, 1984; Majorowicz et al., 1984 and 1985b; Gosnold and Fischer, 1986; Gosnold, 1985 and 1990; Garven, 1989; Smith et al., 1989; Meert et al., 1991; Deming and Nunn, 1991).

In the discharge area of the no-basement model, the decrease in surface heat can be explained as heat energy initially stored in basin sediments, results in high temperature fluids discharged at the early stage, but with continuous recharge of cold fresh water and without a change in basal heat flow, the basin loses heat which eventually causes a

Surface Heat Flow at 0.1 and 1.0 Ma for Both Models
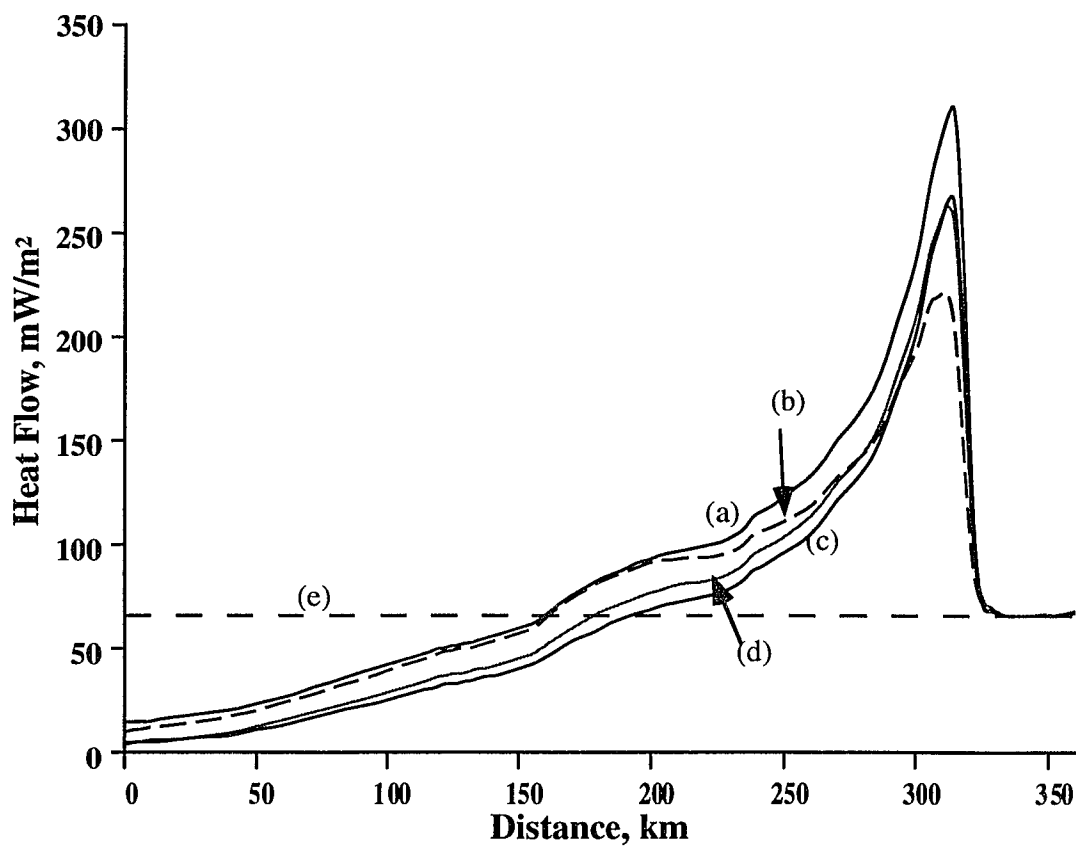
Figure 3.16. Both Curves (a) and (b) show the surface heat flow at 0.1 Ma in the no-basement model and with-basement model respectively; whereas Curves (c) and (d) are for surface heat flow at 1.0 Ma in the no-basement model and with-basement model respectively. Curve (e) shows the basal heat flow in both models.

decrease in surface heat flow. In the with-basement model, however, the buffering effect of the basement prevents the system from losing too much heat at the early stage, with the warming of basement rocks and with continuously higher heat flow at the basement top below the recharge region than that at the model base, surface heat flow in the discharge area is gradually increased. At 1 Ma, surface heat curves of both models are similar in the discharge area.

In the recharge area, there is little difference in surface heat flow between these two models. This is because the recharge surface is far above the basement top and cold water is continuously flowing downwards. Thus, basement rocks have little effect on surface heat flow in the recharge area.

Thermal buffering by basement rocks resulted in a lower average surface heat flow during the first 0.2 Ma of elapsed time (Figure 3.17). During that period, the maximum difference between the two models was larger than 10 mW/m^2. However, after 0.2 Ma, the average surface heat flow in the no-basement model quickly decreased to be less than that in the with-basement model. After a million years, the no-basement system had its average surface heat flow the same as the basal heat flow, and was in its steady state. Whereas, heat energy stored in basement rocks caused the average surface heat flow in the with-basement model to drop slowly. It took more than 5 Ma for the with-basement model to reach its steady state.

Surface heat flow in each of the models is higher than basal heat flow before the system reaches the steady state (Figure 3.17). This implies net heat loss from the basin in the both modes as indicated by the decreasing in average temperatures of the sediments. Non-conservative heat flow along the basin surface has been described by both modeling studies (e.g. Kilty and Chapman, 1982; Mojorowicz et al., 1985; Gosnold and Fischer, 1986; Forster and Smith, 1986; Smith et al, 1989; Deming and Nunn, 1991) and direct measurements of temperature and thermal conductivity in the field (Meert et al., 1991).

Average Surface Heat Flow Vs. Time
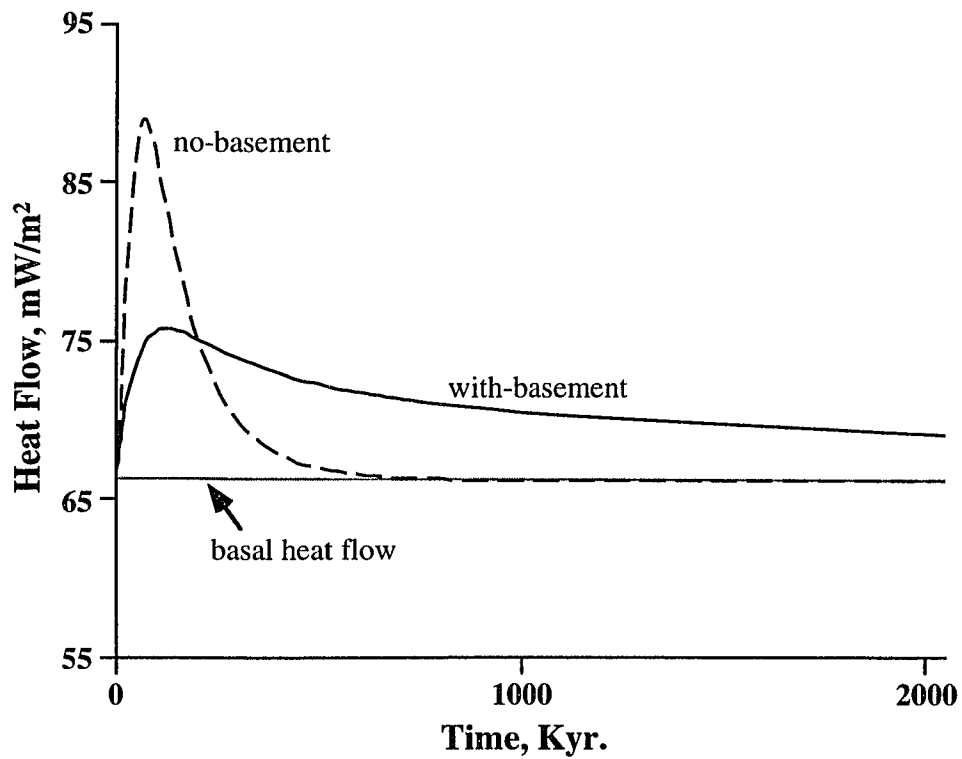
Figure 3.17. Average surface heat flow vs. time for both no-basement model (dash line) and with-basement model (solid line). The light line is the basal heat flow for both models.

3.4. DISCUSSION

The factors controlling thermal buffering by basement rocks in sedimentary basins, include topographic configuration, basin geometry, spatial variation in sediment properties and contrast of thermal conductivity between sediments and basement rocks. Topographic difference can be created by many geological activities, such as volcanism, subsidence, continental uplift and erosion. Topographic driven flow mechanism can generate Darcy velocities on the order of meters per year and efficiently transport heat along the sediment-basement contact (e.g. this study; Garven and Freeze, 1982, 1984 b; Garven et al., 1993; Deming and Nunn, 1991). This study indicate that the more efficient the lateral heat transport, the more important are the effects of thermal buffering by basement rocks. However, more sensitivity tests are needed, in order to further understand the relationship between the topographic gradient and buffering effect of basement rocks.

Slope of the sediment-basement contact also effects the thermal buffering by basement rocks. When the slope is steep, more heat, which is brought up by the fluid flow from deep sediments, flows laterally into the basement rocks in the early stage of modeling. Although the average slope of the sediment-basement contact in this model basin is less than 0.7^{o}, heat flow laterally back into the basement is observed (Figures 3.9b and 3.10b). A steeper sediment-basement contact increases heat refraction along the upper part of the basement. Thus, in a basin where the sediment-basement contact is steeper, thermal buffering by basement rocks can become more significant.

Is it possible for additional heat brought up by the fast movement of groundwater from deep basin along the basal aquifers to flow back to the basement? This study shows that this can occur in the discharge area and where the slope of the sediment-basement interface is large. Although basin sediments are never hotter than the basement rocks along a vertical line, calculations indicate that the lateral thermal gradient between basal sediments and the adjacent basement rocks (pointing to the

basement) was increased to about 0.35 °C/km at the time of 10 kyr., significantly higher than the initial value of 0.19 °C/km. The ratio of the horizontal thermal gradient to the vertical thermal gradient at the sediment-basement interface was elevated to 1.8×10^{-2}, much higher than the initial 8.4×10^{-3}. Therefore, in the early stage of the system's evolution, part of the heat transported by fluid flow can flow laterally back into the basement. In other words, part of the heat carried by fluids was used to heat the basement rocks. The lateral thermal gradient decreased after an elapsed time of 30 kyr.

The existence of the high permeability basal aquifers, immediately overlying the basement rocks in this model basin, is critical because it not only provides a conduit for fluid flow, but also directly connects the deep, hot zone of the basin and the shallow, cold discharge area.

In the deep part of the model basin, rapid recharge of cold fluids can result in fluid density overturn, which causes some fluids to move back into the deep sediments (not shown). This causes complexity in the present simulations. In order to simplify the simulations, The temperature effect on fluid density is ignored. However, because density driven flow is much weaker compared to the topographic driven mechanism in the present simulations, the results of this study are consistent with Garven et al. (1993).

A thermal conductivity difference between sediments and basement rocks can cause significant refraction of heat along the basement top (Figure 3.1; Deming et al., 1990). For example, this study has shown that thermal refraction alone can cause a heat flow difference as high as 10 mW/m^2 between the basin center and basin margin. For the basin conditions considered here, heat refraction is less important than the thermal buffering, and is considered as a secondary effect on thermal evolution of the basin. Heat refraction also occurs in many other cases, such as metamorphism of sedimentary rocks, salt diapirism, and in some basins rich in dolomites. Salt, dolomites and some metamorphic rocks such as quartzite, have higher thermal conductivities than sediments. Thus, they can act as conduits for heat transport. In all these cases,

especially when the slope of the interface between the high thermal conductivity rocks and surrounding sediments is large, such as that of a salt dome, heat conductive refraction alone may play a more important role in the thermal history of the sedimentary basins.

Many geochemical processes such as organic maturation and mineralization of economic ore deposits are strongly dependent on temperature. This study shows that ignoring basement effect can cause up to 20 °C over-estimation of temperature in shallow sediments in the discharge area and more than 30 °C under-estimation in deep sediments under the recharge area. Thus, spurious conclusions would be obtained if such temperatures were used to study the geochemical processes during the basin evolution . Therefore, it is necessary to consider all the above factors when doing numerical simulations of heat and fluid transport in a sedimentary basin. A convenient way to avoid errors from ignoring thermal buffering by basement rocks is to extend the lower thermal boundary far below the basement top, such as the 15 km depth used in the present study.

3.5. CONCLUSIONS

This study has shown that temperature fields in an uplifted foreland basin, where topographically driven recharge is the major driving mechanism for regional groundwater flow, are significantly effected by thermal buffering of basement rocks. Downward flow of cold fresh water causes a large thermal contrast between the deep sediments and basement rocks under the recharge area. This in turn elevates the heat flow across the sediment-basement interface. Upward flowing hot fluids in the discharge area, on the other hand decrease the thermal gradient between the shallow sediments and basement rocks and, hence, decreases the heat flow upward into the basin. In some places, where the slope of the sediment-basement interface is steep, additional heat brought up by the fast flowing groundwater along the basal aquifers, is conducted laterally back into the basement. Therefore, it is impossible to maintain a

constant heat flow at the sediment-basement contact before the system gets to steady state. Because basement rocks contain additional heat energy, it takes a much longer time (> 5 Ma) for the system to reach steady state.

Without considering basement rocks as part of the model, temperatures can be significantly over-estimated in the discharge area and under-estimated in the recharge region. Ignoring basement buffering also can cause other errors, such as a transient thermal pulse in the groundwater discharge region; incorrect prediction of fluid flow velocity in different stages of modeling. Thermal buffering by basement rocks also effects surface heat flow. With the warming up of basement rocks below the discharge area and with continuously high heat flow at the basement top below the recharge region, surface heat flow can gradually increase in the discharge area.

Ignoring the basement effect can cause errors in temperature prediction as high as 20 °C, which may result in completely different conclusions in studying geochemical processes such as organic matter maturation and mineralization of economic ore deposits. Thermal buffering by basement rocks makes it more difficult for a thermal transient regime to explain the mechanism for MVT ore deposits, which require high temperature (>100 °C) at shallow depths (< 1.5 km) (Sverjensky, 1986) in the discharge region.

CHAPTER 4
THERMAL INSULATION BY
LOW CONDUCTIVITY CARBONACEOUS SEDIMENTS:
AN IMPORTANT MECHANISM FOR FORMATION OF
MISSISSIPPI VALLEY-TYPE ORE DEPOSITS

4.1. INTRODUCTION

The migration of warm, saline water through the Appalachian basin and the North

American Mid-continent (Figure 4.1) has been inferred from the presence of Mississippi

Valley-type (MVT) lead-zinc deposits (Sverjensky, 1986), fluid inclusion studies

(Leach, 1979; Leach and Rowan, 1986; Coveney et al., 1987; Hearn et al., 1987;

Dorobek, 1989), widespread potassium alteration (Hearn and Sutter, 1985; Hearn et al.,

1987; Elliot and Aronson, 1987; Hay et al., 1988), remagnetizations (Jackson et al.,

1988; McCabe et al., 1989; McCabe and Elmore, 1989; Marshak et al., 1989; Lu et al.,

1990), hydrothermal alteration of coal (Daniels et al., 1990), and high degrees of

thermal maturity of organic matters that apparently can not be explained by maximum

estimates of eroded overburden (Johnsson, 1986) (cited from Deming and Nunn, 1991).

In recent years, many numerical models have been conducted to explain how the

migration of warm and saline fluids resulted in the formation of MVT ore deposits (e.g.

Sharp, 1978; Cathles and Smith, 1983; Bethke ,1985; Garven and Freeze, 1982, 1984a,

b; Garven, 1985; Bethke, 1986; Garven and Sverjensky, 1989; Ge and Garven, 1989;

Bethke and Marshak, 1990, Deming et al., 1990; Deming and Nunn, 1991, Garven et al,

1993). Fluid inclusion studies have provided the major quantitative constraint for these

simulations, that is MVT ore deposits were formed in high temperatures (>100 °C) at

shallow depths (< 1.5 km) (Sverjensky, 1986). Radiometric dating implies that

formation of Mid-continent MVT ore deposits are temporally related to the uplift of

orogenic belts and adjacent foreland basins during the late Paleozoic and early

Mesozoic (e.g. Garven et al., 1993). It is now accepted by many people that the MVT
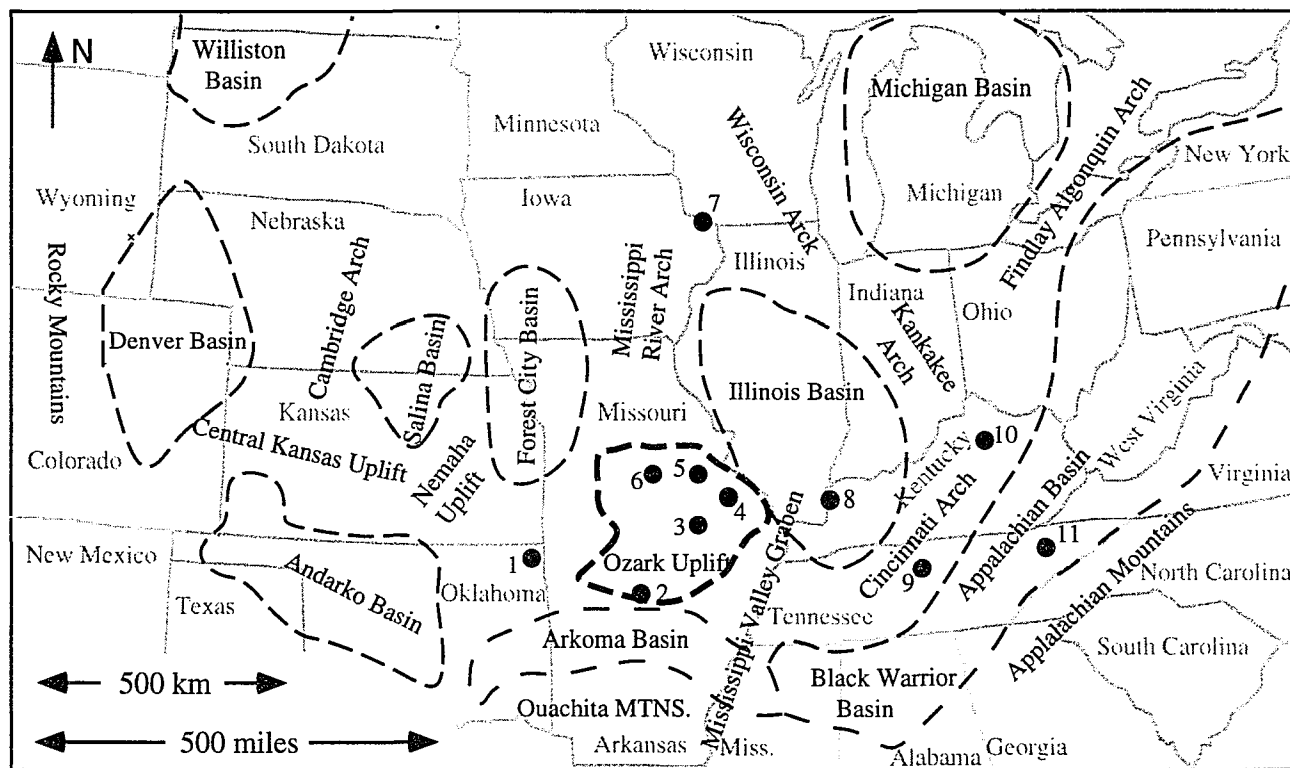
Figure 4.1. Location map of major sedimentary basins and Mississippi Valley-type ore deposits districts (the solid circles), including: (1) Tri-State, (2) Northern Arkansas, (3) Viburnum Trend, (4) Old Lead Belt, (5) Southeast Missouri Barite, (7) Upper Mississippi Valley, (8) Illinois-Kentucky Fluorspar, (9) Central Tennessee, (10) Central Kentucky, and (11) Eastern Tennessee. Redrawn after Garven et al., 1993.

ore deposits were formed as a result of warm, saline fluids migrating through sedimentary basins (e.g. Garven et al., 1993). It is also recognized that compaction of sediments does not result in flow velocities high enough to efficiently transport heat by advection and therefore may not be a viable mechanism for brine migration (Deming and Nunn, 1991), unless pore fluids can accumulate in geopressured zones which are periodically ruptured (Cathles and Smith, 1983).

However, one of the major difficulties in these modeling studies are assumptions regarding basal heat flow. For example, Deming and Nunn (1991) recognized in their study of a generic basin that in order to produce high temperature anomalies at shallow depths, it requires basal heat flow in the order of 100 mW/m^2, much higher than the continent mean of about 60 mW/m^2. The required values are high enough that the viability of topographically driven recharge as a mechanism to explain brine migrations may be contentious. Garven et al. (1993) applied constant basal heat flow values of 70 to 80 mW/m^2, to the simulations of foreland platforms of the Arkoma and Appalachian basins in North America. Even though high temperatures at shallow depths in the discharge regions were obtained, the temperatures were over-estimated, because the basement section was not considered as a part of their models. In the last chapter, it was pointed out that basement rocks of an uplifted foreland basin act as a thermal buffer, which strongly affects changes in the thermal regime caused by rapid fluid flow along basal aquifers. Ignoring the basement effects, the temperatures in the discharge regions can be significantly over-estimated as high as 20 °C in the early stage of uplift. Furthermore, in the Viburnum Trend, one of the major MVT ore deposit districts in southeastern Missouri, the vertical temperature gradient in the shallow sediments obtained by Garven et al. (1993) is about 150 °C/km, much larger than that (<25 °C/km within the Viburnum Trend area) obtained from fluid inclusions (Rowan and Leach, 1989). These difficulties are the motivation to conduct this study to seek an alternative

48

hypothesis to explain the mechanism for the high temperatures at shallow depths associated with the formation of MVT ore deposits.

Carbonaceous sediments, such as coal and related mudstone, prevailed in many sedimentary basins in the Mid-continent of the United States during the Late Paleozoic. Carbonaceous rocks are characterized by thermal conductivities in the range of 0.25 to 1.0 W/m-K, much lower than that of other sedimentary rocks, by a factor of 5 to 10 (Pollack and Cercone, 1994; also see Figure 4.2). Furthermore, surface or near surface organic matter has extremely low thermal conductivities. Most organic compounds have a thermal conductivity around 0.03 W/m-K (Handbook of Chemistry and Physics, 1995). Thus, organic matter, which consists of mostly organic compounds, should be also very low in thermal conductivity. Therefore, organic matter and carbonaceous sediments should act as a thermal blanket to retain heat within basin sediments. Many observations have shown the occurrence of high thermal maturities, as indicated by coal rank, vitrinite reflectance, conodont alteration indices, fission-track annealing histories, fluid inclusion homogenization behavior or other geological parameters, at the surface or at shallow depths of burial in many sedimentary basins in the world (e.g. Pollack and Cercone, 1994). Normal geothermal gradients can not produce the paleotemperatures suggested by these indicators at their current burial depths. These anomalous thermal maturities could be explained as consequences of former tectonic events involving significantly higher heat flow or large regional uplift and erosion. However, evidence for these tectonic events, such as stratigraphic constraints and magnetic and diagenetic overprints, are not always present. Pollack and Cercone (1994) successfully provided an alternative hypothesis to explain the anomalous thermal maturities, simply as a consequence of a relatively thin thermal blanket comprising low-thermal-conductivity carbonaceous sediments.

In this study, a two-dimensional finite element model of fluid flow and heat transport, has been used to study the insulation effect of a carbonaceous layer with low
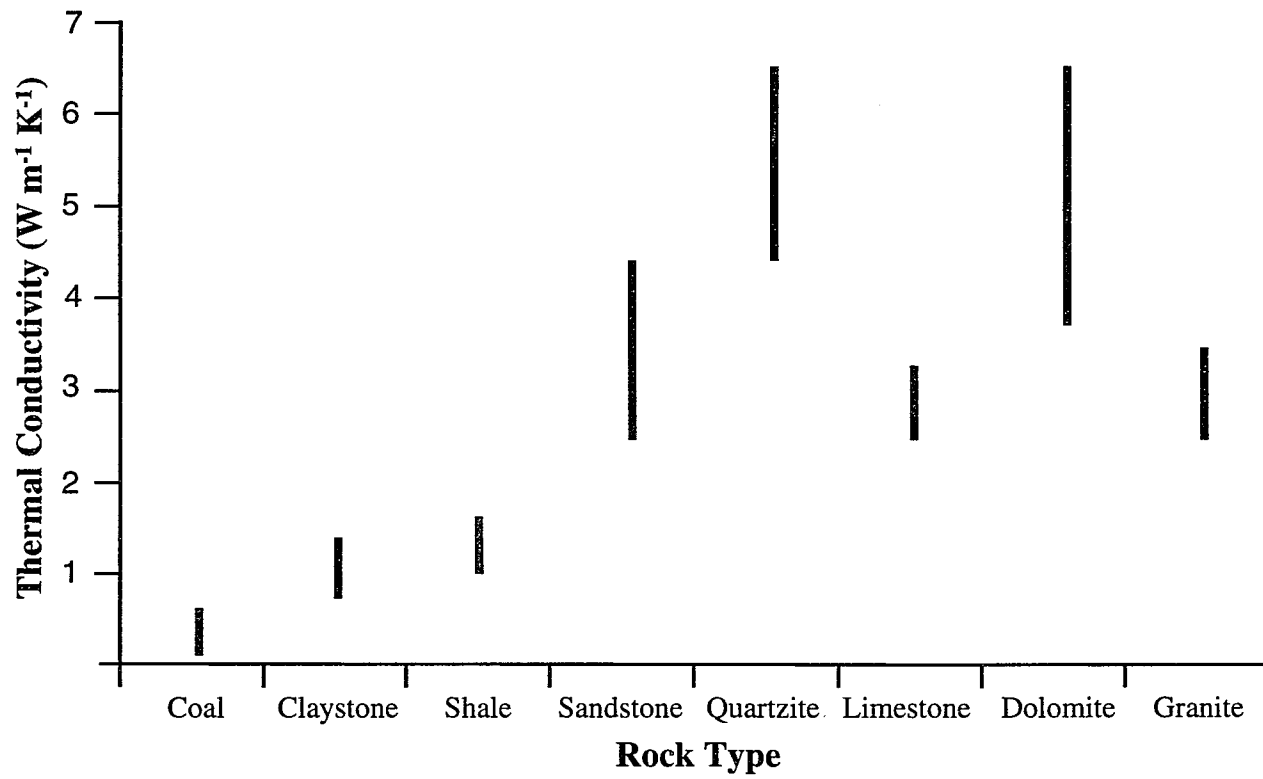
Figure 4.2. Thermal conductivities of different types of rocks (Blackwell and Steele, 1989).

thermal conductivity on the thermal evolution of an uplifted foreland basin and to

suggest its association with the formation of MVT ore deposits.

4.2. COAL DEPOSITS IN THE MID-CONTINENT OF THE UNITED STATES

Coal beds are common in many sedimentary basins surrounding the Ozark Dome,

one of the major MVT ore districts, indicating the enrichment of carbonaceous

sediments in the Mid-continent during the Carboniferous period. The tectonic history

of the Mid-continent of the United States has been well documented. A summary of

tectonic evolution related to brine migrations and ore formation in this region is

presented by Garven et al. (1993). Here only a brief review regarding the Late

Paleozoic stratigraphy is provided so that the geological significance of imposing a

carbonaceous layer to the models can be better understood.

In the Illinois Basin, which is located in the north-east of the Mid-continent

(Figure 4.1), the U.S. Geological Survey has estimated bituminous coal reserves in

Pennsylvanian rocks to be as high as 365 billion tons (Archer and Kirr, 1984). More

than 75 individual coal seams have been identified in this area ranging from a few tens

of centimeters to 5 meters in thickness over large areas (Figure 4.3). These rocks

underlie approximately 95,530 km^2 of Illinois, 16,827 km^2 of Indiana, and 16,569 km^2

of Kentucky. Coal deposits in this area are primarily confined to rocks of

Pennsylvanian age, although thin coal beds of limited extent have been found in Upper

Mississippi rocks. Lower Pennsylvanian rocks were deposited only in the southern

portions of the region; and in most places, progressively younger Pennsylvanian rocks

lie upon older Paleozoic rocks in northern Illinois (Willman et al, 1975). The majority

of Middle and Upper Pennsylvanian deposition occurred in transitional continental

environments such as alluvial and delta plains, distributary channels, marshes, and

swamps (Pryor and Sable, 1974). Several times, the delta platform was covered by

fresh-water coal swamps, and, as sea level rose, the swamps were flooded and black,

pyrite-bearing shales with beds of fossiliferous limestone were deposited. Many cycles
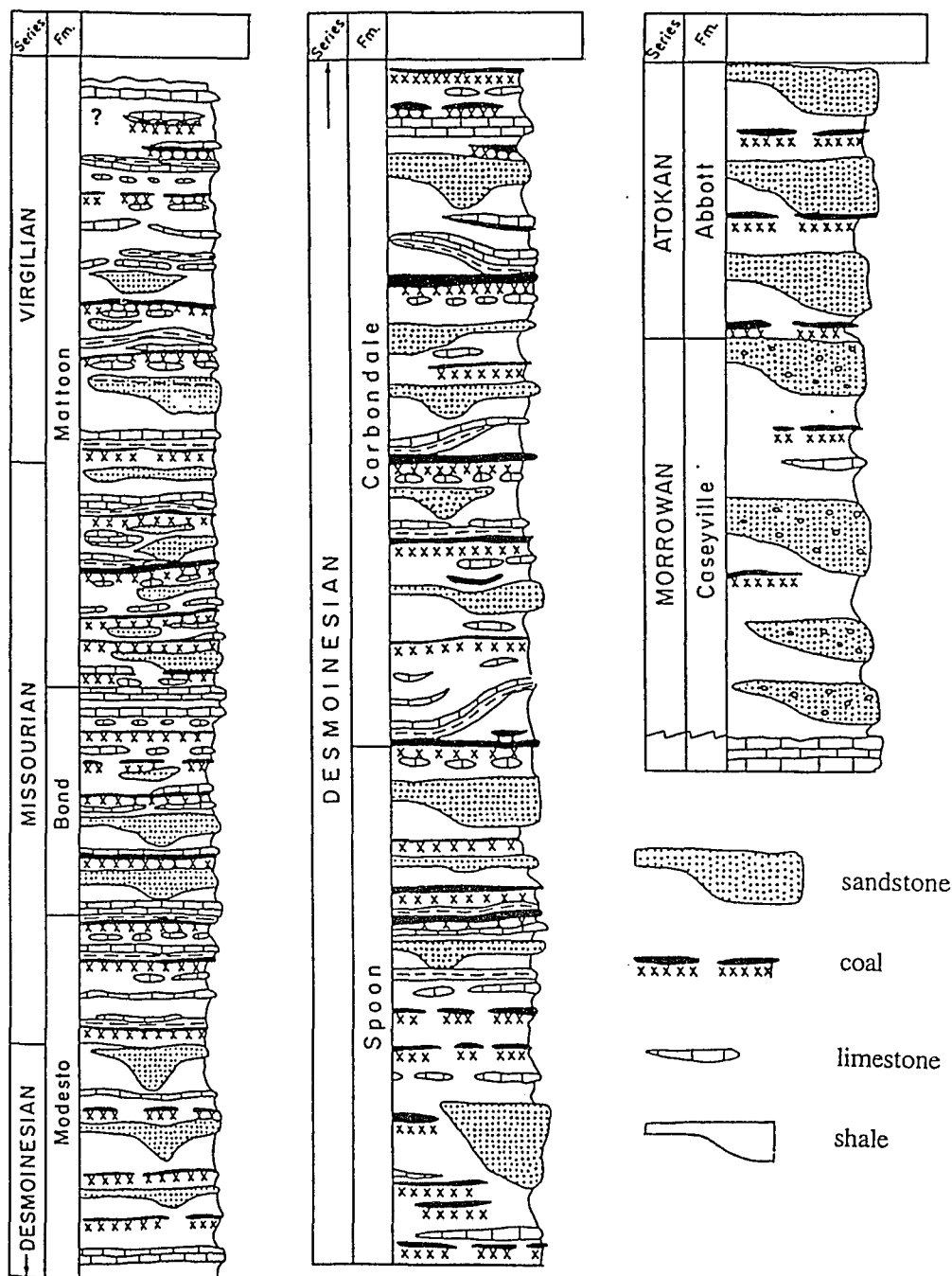
Figure 4.3. Stratigraphic column of sedimentary rocks in the Pennsylvanian period, showing the frequent coal beds in Illinois Basin. The total thickness in this column is about 800 meters. After Willman et al., 1975.

of deposition have been identified in the Pennsylvanian sequence. Each cyclothem
consists of sandstone, shale, limestone, and coal units arranged in a regular sequence
(Archer and Kirr, 1984). The greatest thickness of Pennsylvanian age rocks at present
in the Illinois basin is about 914 m. Coals make up only several percent of the total
Pennsylvanian section, a large portion of Pennsylvanian age rocks are carbonaceous
mudstone or limestone (Archer and Kirr, 1984).

The Black Warrior Basin is a triangular area in Mississippi and Alabama, bounded
by the Appalachian Mountains on the southeast and the Ouachita front on the southwest
(Figure 4.1). The major coalbeds were formed during the Carboniferous, a time when
the Black Warrior Basin was one of a number of rapidly subsiding basins in eastern
North America (Davis and Ehrlich, 1974). It represented the eastern shoaling of the
Ouachita trough (Graham et al, 1976) and was probably continuous with the Arkoma
Basin of Arkansas and Oklahoma along the Ouachita structural belt (Davis and Ehrlich,
1974; Graham et al., 1976). Most coals in the Black Warrior Basin are Pennsylvanian
in age, but some Mississippian coals occur in scattered locations. The Pennsylvanian
Pottsville Formation ranges up to 2743 m in thickness and overlies a thick sequence of
Mississippian deposits that grade from a cherty limestone at the base to shales and
sandstones at the top. The Pennsylvanian system is represented by the Pottsville
Formation and contains all the estimated 35 billion tons of coal resources in the basin
(Hewitt, 1984). Most of the coal is found in 20 seams forming seven coal groups.

The Arkoma Basin, located in the southern Mid-continent region (Figure 4.1), is an
elongated, linear east-west-trending basin covering an area of about 34,919 km^2 (Rieke
and Kirr, 1984). The deepest part of this basin is adjacent to the Ouachita Mountains
system, where the sedimentary column is estimated to be 9,144 m thick.
Pennsylvanian-age strata were deposited in deltaic environment in a rapidly subsiding
environment. Sediments of the Pennsylvanian Atokan and Desmoinesian series
comprise a typical coal-bearing molasse sequence where shallow marine, deltaic, and

fluvial conditions dominated (Garven et al., 1993). Sedimentation continued until Late
Pennsylvanian time, when the Arbuckle orogeny of southern Oklahoma took place.
This Late Pennsylvanian orogeny uplifted the Tishomingo anticline in south-central
Oklahoma, thereby separating the Arkoma depression from the Fort Worth Basin south
of the uplift. During Permian time, the Ouachita orogeny and erosion occurred. Within
this basin, extensive reserves of bituminous and some semianthracite coals are
contained in Pennsylvanian age rocks. The Oklahoma Geological Survey and the U.S.
Geological Survey have estimated that the total coal resource of this basin are 7.89
billion tons (Rieke and Kirr, 1984). More than ten individual coal seams have been
identified in this area. Individual beds range from 10 cm to 2 m in thickness.

Even though coal beds are common in many sedimentary basins in the Mid-
continent region, few coal beds have been found in the area of the Ozark Dome, one of
the major Mississippi Valley-type ore districts. The Ozark Dome borders the northern
fringe of the Arkoma Basin, and it developed probably as a result of the flexural related
stress relaxation that produced similar structural highs such as the Findlay, Kankakee,
Cincinnati, Nashville Domes, Pascola Arch and the Wisconsin Arch (Quinlan and
Beaumont, 1984). However, most of the arches and domes that separated various
basins in the Cambrian-Ordovician period were submergent or only intermittently
emergent (Thacker and Anderson, 1977). Beaumont et al. (1987) used a mathematical,
geodynamic model to simulate the relationship of the Alleghanian Orogeny to the
Permo-Carboniferous evolution of sedimentary basins in the Eastern Interior of North
America. They predicted that lithospheric flexure under loads by the Appalachian and
Ouachita orogens created more than 60 m of Lower Mississippian and more than 600 m
of Pennsylvanian sediments in the Ozark Dome region (Figure 4.4a). It is unlikely that
this area remained above sea level as suggested by McKee and Crosby (1979)
(Beaumont et al., 1987). Beaumont et al. (1987) compared the observed and model
maximum burial of coals that are now near the surface in the Mid-continent region, and

both of them show a maximum burial larger than 4300 feet in the Ozark Dome area.
These are consistent with model predictions (Beaumont et al., 1987) of the cumulative
load thickness for the Pennsylvanian and Permian and the cumulative erosion since the
Alleghanian Orogeny.

If these predictions are correct, it is very possible that a thick coal-bearing
carbonaceous sequence was deposited over the present Ozark Dome region during the
Carboniferous period. From the late Paleozoic or early Mesozoic to the present, the
Ozark uplift and surrounding region remained emergent and became part of the stable
western interior (Thacker and Anderson, 1977). The uplift and erosion have beveled
the stratigraphic profile so that only Pennsylvanian remnants still exist in Arkoma
Basin, Illinois Basin and Black Warrior Basin, where coals are preserved (Figure 4.4b).

4.3. MODEL DESCRIPTIONS

The model profile was derived from modification of a model profile used by Garven
et al. (1993) for the simulation of the southern interior flow systems. The model cross-
section cuts through the eastern half of the Arkoma Basin, along a transect that begins
in the foreland north of Little Rock, Arkansas, extends northward over the Ozark dome,
and terminates near the Missouri River, west of St. Louis (Garven et al., 1993; see
Figure 4.5). The basement section is considered as a part of the thermal model, because
it acts as a thermal buffer and strongly affects the thermal evolution of an uplifted
foreland basin (see Chapter 3).

Individual coal beds usually are heterogeneous and discontinuously distributed
(Figure 4.3). However, for a basin-scale simulation, the total thermal effect of many
individual coal beds can be approximated by a single continuously distributed
carbonaceous layer. Because this is a simulation of a paleo-hydrogeological system, it
is also necessary to consider the uncompacted carbonaceous sediments (e.g. peats).
Uncompacted carbonaceous sediments are thicker and usually have thermal
conductivities lower compared to coal, because they contain more organic matters, gas
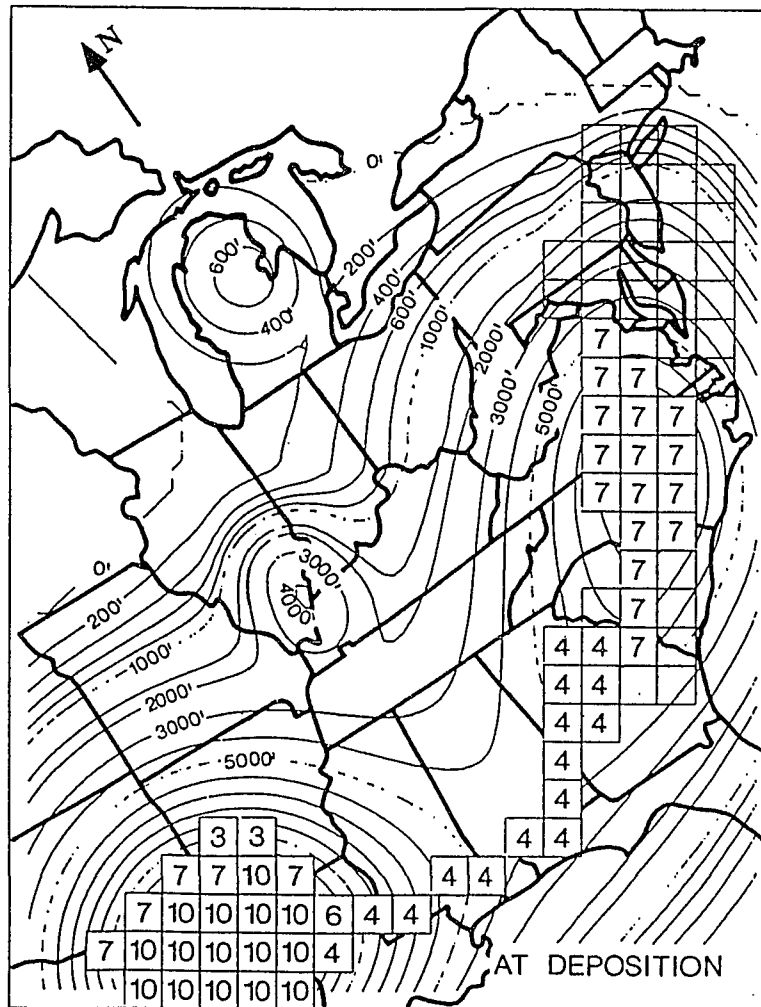
Figure 4.4a. Model predictions of the total deposition during the Pennsylvanian period. Note the numbers on the square blocks are the thickness of model thrust sheets in kilometers. Contour values are in feet. After Beaumont et al., 1987.
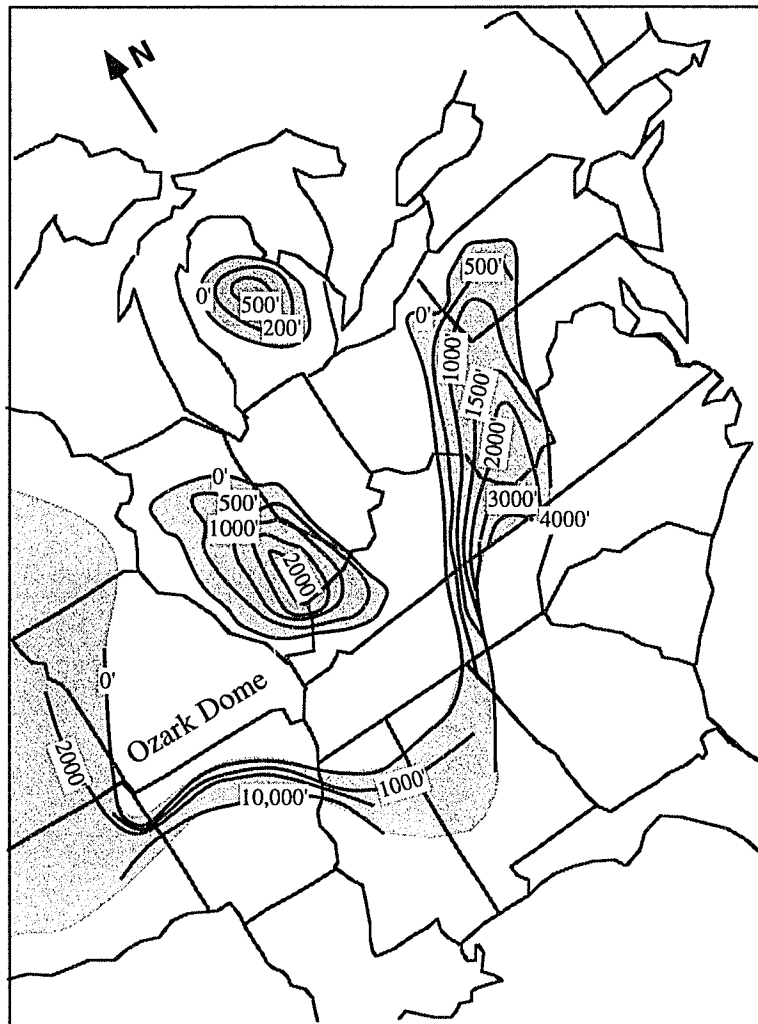
Figure 4.4b. Observational Pennsylvanian isopach. Contour values are in feet (Beaumont et al., 1987). The shadow areas show the approximately Carboniferous coal distributions in present day (from USGS Professional Paper, 853, Plate 16).
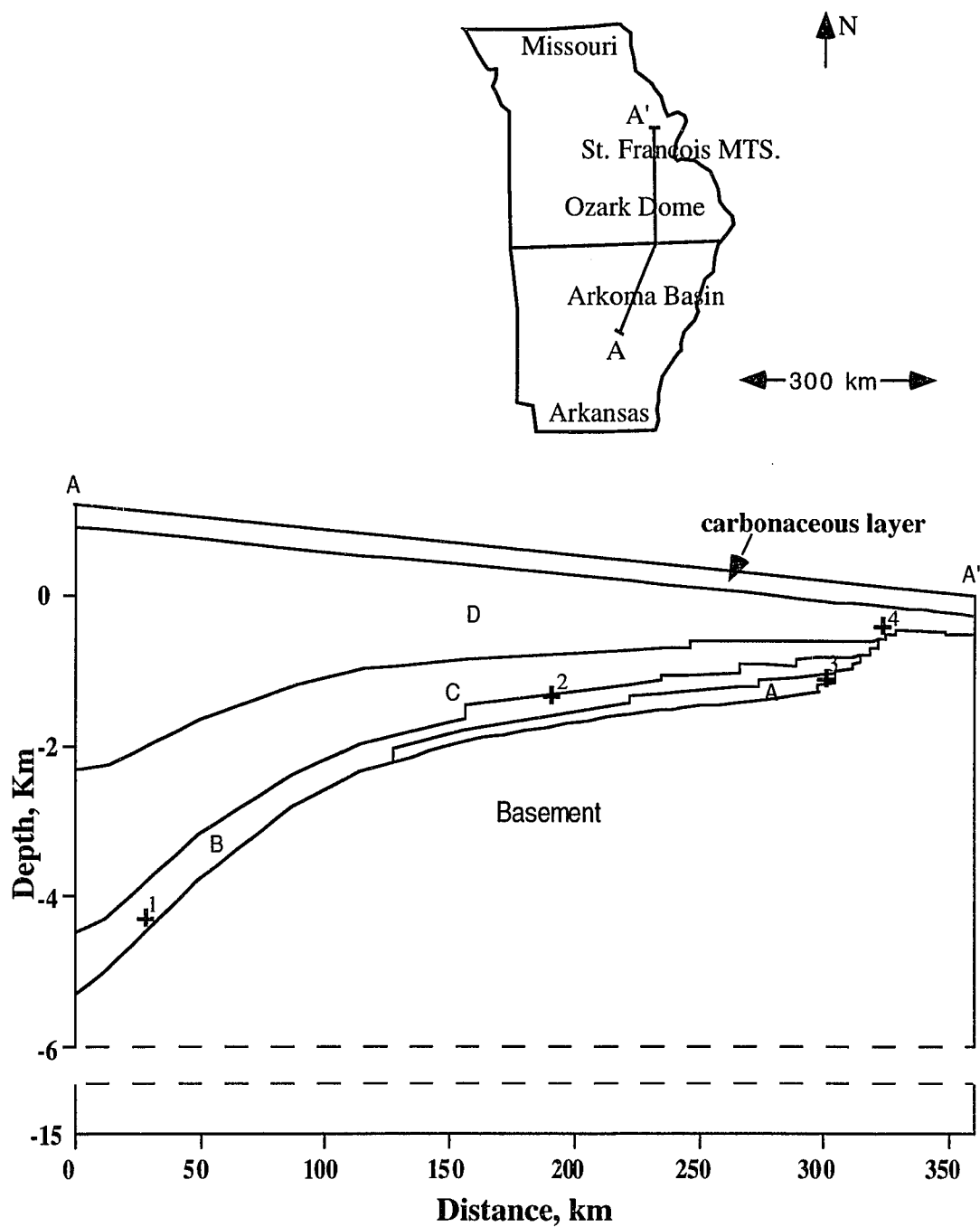
Figure 4.5. Hydrogeological model (modified after Garven et al., 1993). See Table 4.1 for the parameters of Units A, B, C, D, Basement and the carbonaceous layer. Cross-Marks 1, 2, 3 and 4 are the locations for temperature variation with time shown in Figure 4.12.

phases, and fluids. Because all the sediments deposited during the Carboniferous and Permian were removed by erosion since the early Mesozoic in the Ozark Dome area, the thickness and distribution of the carbonaceous sediments deposited during these periods are not available to this study. In this study, a uniform thickness of 300 m carbonaceous layer is assumed at the top of the models. Again, this layer represents the total thermal effect of all the carbonaceous sediments, including surface organic matters, uncompacted carbonaceous sediments and coal. This layer may represent a thicker section with higher thermal conductivity, containing other common sediments such as sandstone and shale.

Physical parameters that remain constant in most of the numerical simulations are summarized in Table 4.1. Layer Units A and B are highly permeable and treated as basal aquifers. Units C and D are low in permeability so that they are treated as aquitards. Because Garven et al. (1993) did not specifically describe the thermal conductivities of the sediments and igneous rocks in their article, I use a typical value of 2.0 W/m-K for all the sediments underlying the carbonaceous layer and 2.9 W/m-K for the basement rocks (including igneous rocks in St. Francois Mountains). These thermal conductivities are typical for the study area (Meert et al., 1991; Garven and Freeze, 1984b). See Garven et al., 1993, for details regarding the stratigraphy and lithology.

According to Deming (1995, personal communication), the average thermal conductivity of 500 coal samples in the Mid-continent region of U.S., is approximately 0.3 W/m-K. Other fine grain sediments, such as claystone and shale, have an average value around 1.0 W/m-K (Figure 4.2, Blackwell and Steele, 1989). Gaseous phases, such as oxygen, methane and air, have a thermal conductivity about 100 times smaller than sandstones or limestones (Bear, 1972). Thus, soil or rocks can have low thermal conductivity, if they are unsaturated. Furthermore, according to the Handbook of Chemistry and Physics, most organic compounds have thermal conductivities around

0.03 W/m-K. Thus, forests and other organic matter, which were once prevalent in the Mid-continent region during the Carboniferous period, may have resulted in a more effective thermal insulation. Therefore, the assumptions of thermal conductivities of the carbonaceous layer in the following cases are reasonable, if we consider all the above effects.

In order to better understand the thermal insulation effect, I introduce different thermal conductivities and permeabilities for the carbonaceous layer. In these cases (Case 0 to 4), I assume that the uplift occurred instantaneously. The upper boundary, which represents the water table, is idealized to have an uniform slope of 1.2 km over 360 km. To simplify the simulations, the thickness of the carbonaceous sediments was assumed to be constant, even though it is recognized that the Arkoma basin could have more carbonaceous deposition during the Pennsylvanian. I also developed a model to simulate the development of topography through time (Case 5).

Case 0: no carbonaceous layer on the top of the model basin

In order to better understand the thermal insulation by the carbonaceous layer, I first conduct a case, in which the top layer has the same physical properties as the underlying Unit D (see Table 4.1). The results from this case are very similar to those obtained in the with-basement model of the last chapter.

Case 1: low thermal conductivity carbonaceous layer

In this case, the carbonaceous layer has a thermal conductivity of 0.42 W/m-K. The permeability is also assumed to be the same as the underlying sediments (Table 4.1).

Case 2: high thermal conductivity carbonaceous layer

A thermal conductivity of 0.84 W/m-K is assigned to the carbonaceous layer and keep the same permeabilities with those in Case 1.

Case 3 : high thermal conductivity coal layer with low vertical permeability

A thermal conductivity of 0.84 W/m-K is again used in this case. Because compaction primarily reduces vertical permeability of sediments, the horizontal

permeability in Case 3 is assumed the same with Case 2, but vertical permeability decreases 10 times to a value of 0.0317 mD. The purpose of this case is to see the effect of decreasing advective heat transport on thermal anomalies at shallow depths in the groundwater discharge region.

Case 4: partial covering of carbonaceous sediments

In this case, it is assumed that the carbonaceous layer only covered the discharge region, the right half of the model basin. Thermal conductivity and permeability of the carbonaceous layer in this case are the same with those in Case 1. The reason for this simulation is that erosion in the high topography region may remove the carbonaceous sediments, which could be transported to the low topography areas and re-deposited. The Arkoma basin which is on the left of the model basin could have more carbonaceous deposits during the Ouachita and Appalachian orogenies. However, the further uplift of the foreland basin could remove most of the carbonaceous sediments in the left of the model basin. The main purpose of the case is to see how effectively the thermal insulation of the carbonaceous sediments retains heat during the discharge.

Case 5: increasing topography by uplifting

It is assumed that all physical parameters are the same as in Case 1, but with the simulated topography increasing through time. Uplift rates decrease linearly with distance from the fold-thrust belt, with the maximum rate of 1 mm/yr. (1 km/m.y.) at the left end of the model basin and minimum rate of 0 mm/yr. at the right end. According to Pinet and Souriau (1988), 1 mm/yr. is an average value for estimated uplift rates in active mountain chains. The water table corresponds to simulated topography at all time.

It is assumed that in each of the simulations, temperature along the model top (water table) was fixed at 20 °C. A constant heat flow of 60 mW/m^2, which is approximately the continental mean (Sclater et al., 1981) and much lower than that used by Garven et al. (1993), was maintained along the lower base at a depth of 15 km. There was no

fluid flow on both sides. In Case 1, 2, 3 and 4, hydraulic head along the top was linearly fixed corresponding to the elevation of the water table, with 12 MPa at the left end and 0 MPa at the right end. Initial thermal conditions were steady state heat conduction, characterized by the above mentioned thermal boundary conditions and without considering fluid flow for all of the cases (Figure 4.6). Similarly, initial pressure conditions were taken from steady state pressure diffusion, without considering fluid flow.

TABLE 4.1. Model parameters of rocks
(see Figure 4.5 for the sections)

Section	Horizontal permeability (mD)	Vertical permeability (mD)	Thermal Conductivity (W/m-K)	Porosity
Unit A	1.90×10^3	1.90×10^1	2.0	0.25
Unit B	9.50×10^2	9.50×10^0	2.0	0.20
Unit C	3.17×10^1	3.17×10^{-1}	2.0	0.10
Unit D	3.17×10^1	3.17×10^{-1}	2.0	0.10
Basement	0.0	0.0	2.9	0.01
Carbonaceous layer:				
Case 0	3.17×10^1	3.17×10^{-1}	2.0	0.10
Case 1	3.17×10^1	3.17×10^{-1}	0.42	0.10
Case 2	3.17×10^1	3.17×10^{-1}	0.84	0.10
Case 3	3.17×10^1	3.17×10^{-2}	0.84	0.10
Case 4	3.17×10^1	3.17×10^{-1}	2.0 and 0.42	0.10
Case 5	3.17×10^1	3.17×10^{-1}	0.42	0.10

The following simulations are transient cases. Governing equations used in this study are Eqs (15), (23), (24) and (25) in Chapter 2. Fluid density and viscosity are calculated using Eqs (27) and (28) in Chapter 2, respectively. In order to simplify the simulations, temperature was assumed to be constant (20 °C) for the fluid density calculation. Because these simulations do not consider the solute transport and the density variation with temperature, the hydrological system is relatively stable.

Initial Temperature Fields of Cases 0 and 1
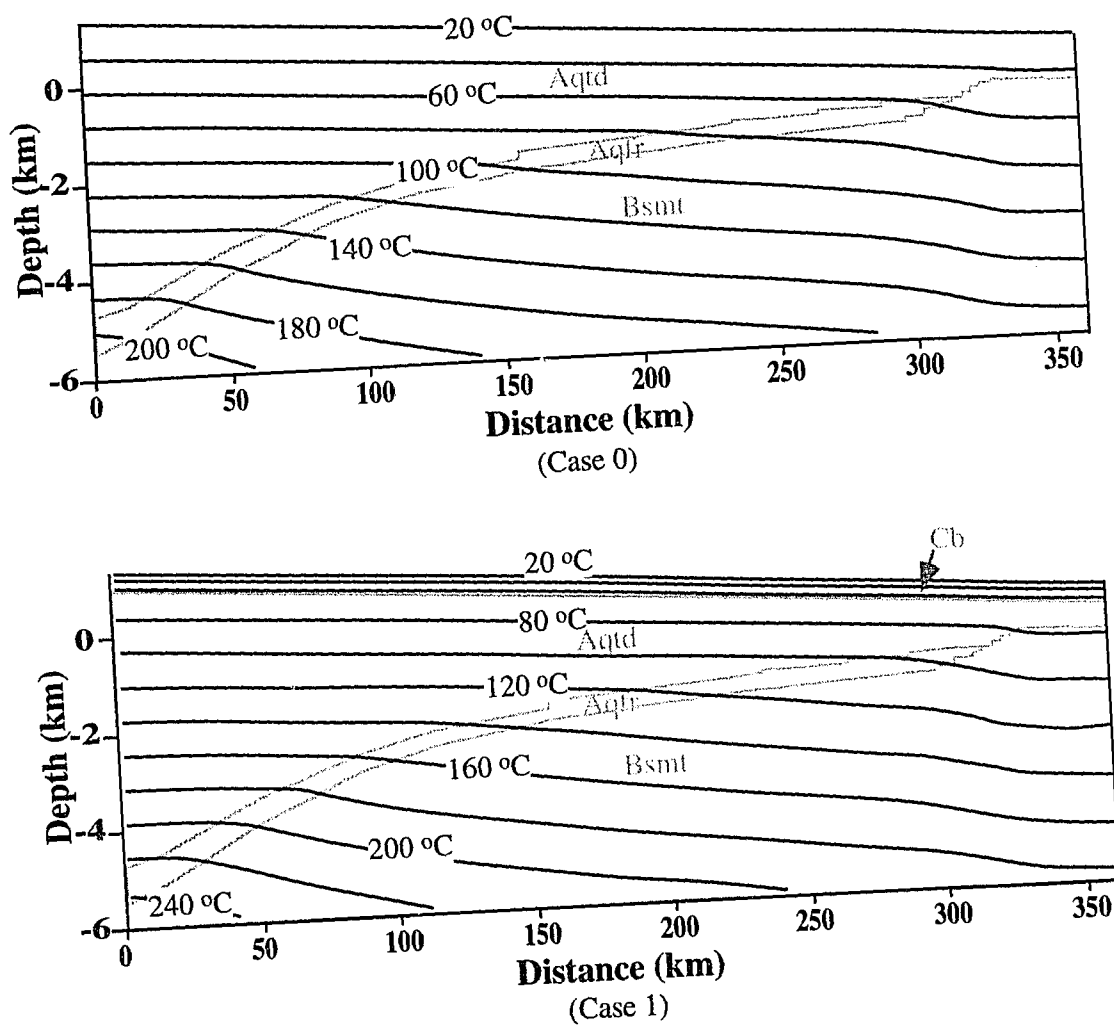
(Case 0)

(Case 1)

Figure 4.6a. Initial temperature of steady-state heat conduction in Case 0 (upper diagram) and Case 1 (lower diagram). The light lines outline the basement (Bsmt), aquifers (Aqfr, Units A and B), aquitards (Aqtd, Units C and D) and carbonaceous layer (Cb). See Table 4.1 for the stratigraphic properties.

Initial Temperature Fields of Case 2 and 4
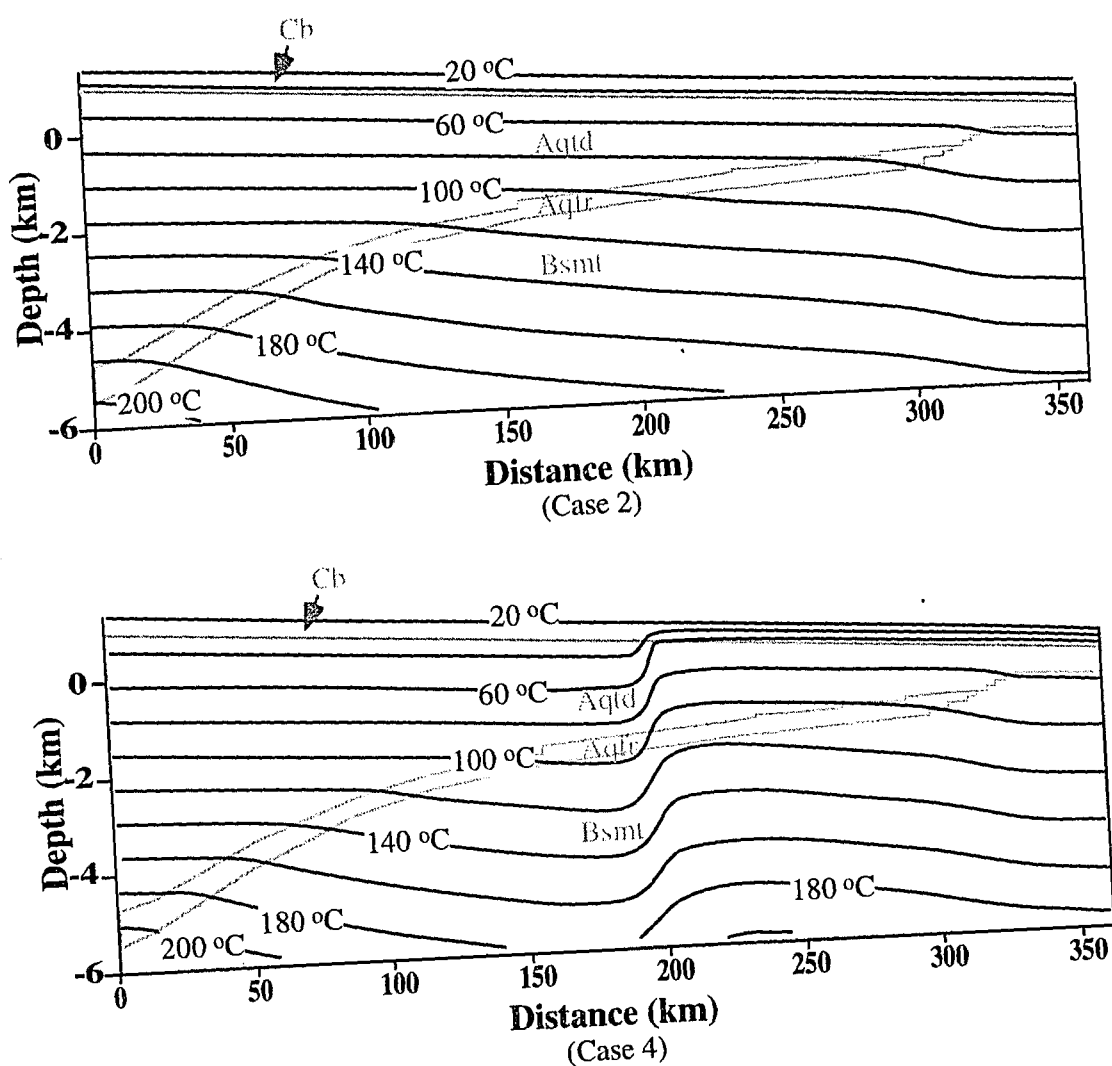
(Case 2)

(Case 4)

Figure 4.6b. Initial temperature fields of Case 2 (upper diagram) and Case4 (lower diagram). The light lines outline the basement (Bsmt), aquifers (Aqf, Units A and B), aquitards (Aqt, Units C and D) and carbonaceous layer (Cb). See Table 4.1 for the detail of stratigraphic parameters. Note that Case 3 has the same initial temperature with Case 2.

Sensitivity tests in this study indicate that the simulations can use relatively large grid size and time step, which do not significantly change the model results. In the very early stage of simulation, time step was set to be 1,000 years. The time step was gradually increased to 10,000 years at a modeling time of 500,000 years and then remained unchanged. I used a coarse finite element mesh with rows of 12 and columns of 81 to handle only heat conduction in the basement. The flow region is discretized with a finite element mesh containing 38 rows and 81 columns with variable element sizes. The total number of nodes in the model is 50 x 81.

4.4. MODEL RESULTS

4.4.1. Thermal gradients

Figure 4.7 shows the initial temperature variations with depth in Cases 0, 1 and 2. The low thermal conductivity of the carbonaceous layer causes sharp temperature gradients through the coal-bearing section. In Case 1, the thermal gradient is about 0.143 °C/m across the carbonaceous layer, which has a thermal conductivity of about 0.42 W/m-K. Whereas in Case 2, the thermal conductivity of 0.84 W/m-K in the carbonaceous section results in a thermal gradient of 0.072 °C/m, which is still much higher than that without carbonaceous layer (0.03 °C/m). Thermal gradient increase (about 0.113 °C/m in Case 1 and 0.042 °C/m in Case 2 compared to Case 0) leads to a significant increment in temperature across the carbonaceous section and the underlying sediments (about 34 °C in Case 1 and 13 °C in Case 2 respectively, Figure 4.7). This has caused the temperature at a depth of 1.5 km to increase to about 100 °C in Case 1 and 80 °C in Case 2. The large, but uniform increment of temperature below the carbonaceous blanket contrasts with a vertically variable temperature increment proportional to the depth of burial which would result from an increase in basement heat flow (Pollack and Cercone, 1994). Thus, without an increase of basal heat flow, the carbonaceous insulation causes high storage of thermal energy in the model basin. The elevated temperatures will persist for as long as the carbonaceous layer remains.

Initial Temperature Variation with Depth
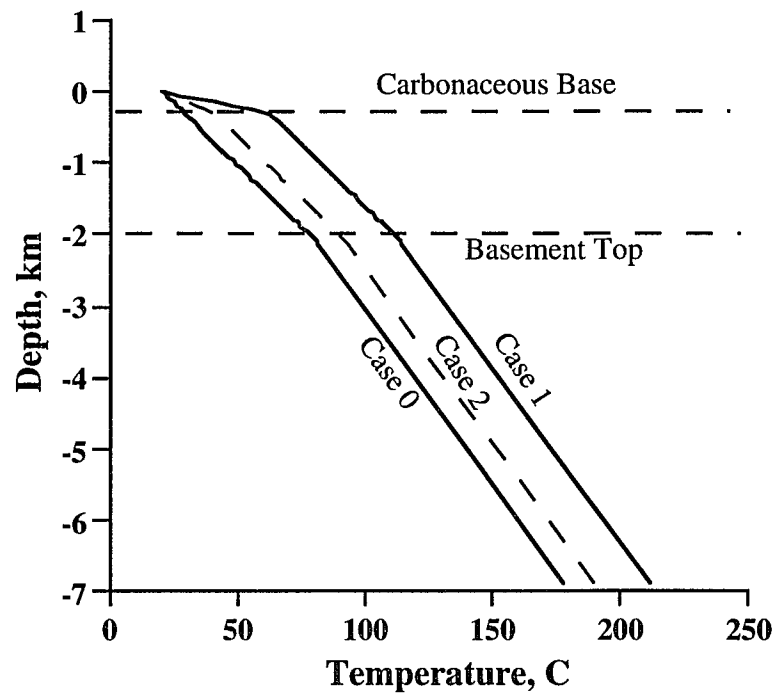
Figure 4.7. Initial temperature vs. depth in Case 0, Case 1, and Case 2. The temperature in Case 3 is the same with Case 2. Case 4 has the same temperature profile with Case 0 on left hand side, where there is no carbonaceous cover. Whereas on the right hand side, the temperature profile is the same with Case 1, with carbonaceous cover.

Evidence documenting the thermal blanket effect were recently obtained by some other workers. Temperature measurements in the Karoo coal (thickness of 100-150 m) of eastern Bostswana, Africa, yielded thermal gradients well in excess of 0.1 °C/m, whereas in the crystalline basement beneath or nearby the coal basins the temperature gradient was typically less than 0.02 °C/m (Pollack and Cercone, 1994). The thermal conductivity of the lithologies present in the Karoo section ranges over a full order of magnitude, from less than 0.5 W/m-K for coal and 1.0 W/m-K for carbonaceous mudstones to greater than 3.0 W/m-K for quartz sandstones. Similarly, a study of Jurassic coal deposits in Australia by Beck (1976) revealed gradients as high as 0.14 °C/m, while Kayal & Christoffel (1982) found gradients through Gondwana coals in India to range from 0.04 to 0.25 °C/m. Blackwell and Steele (1988) also reported low thermal conductivities and associated high thermal gradient of 0.06 °C/m for coal and carbonaceous rocks in a borehole in northwestern Colorado.

4.4.2. Fluid flow in Cases 0, 1, 2 , 3 and 4

Figure 4.8 show the groundwater flow fields of Case 0 through Case 4 at an elapsed model time of 0.2 m.y. The velocity arrows are shown with the same vertical exaggeration as the physical dimensions of the model. Therefore, the arrows represent the true direction of fluid flow in the model basin. Flow fields in these cases all indicate that on the left side of the model, fluids are driven by the topographic gradient downward to recharge the basal aquifers, with a vertical flow rate of a few centimeters per year. Fluid flow is focused along the basal aquifers towards the discharge area on the right of the model, where flow is upward. In the middle region of the model, fluid flow is mainly horizontal. Flow patterns in these cases are basically similar.

The maximum Darcy rate along the basal aquifers in Case 1 can be more than 8.5 m/yr. in the early stage of modeling (Figure 4.9), higher than those in Cases 2 (about 7.2 m/yr.) and 4 (about 6.7 m/yr.). Darcy velocities in Case 0 are similar to
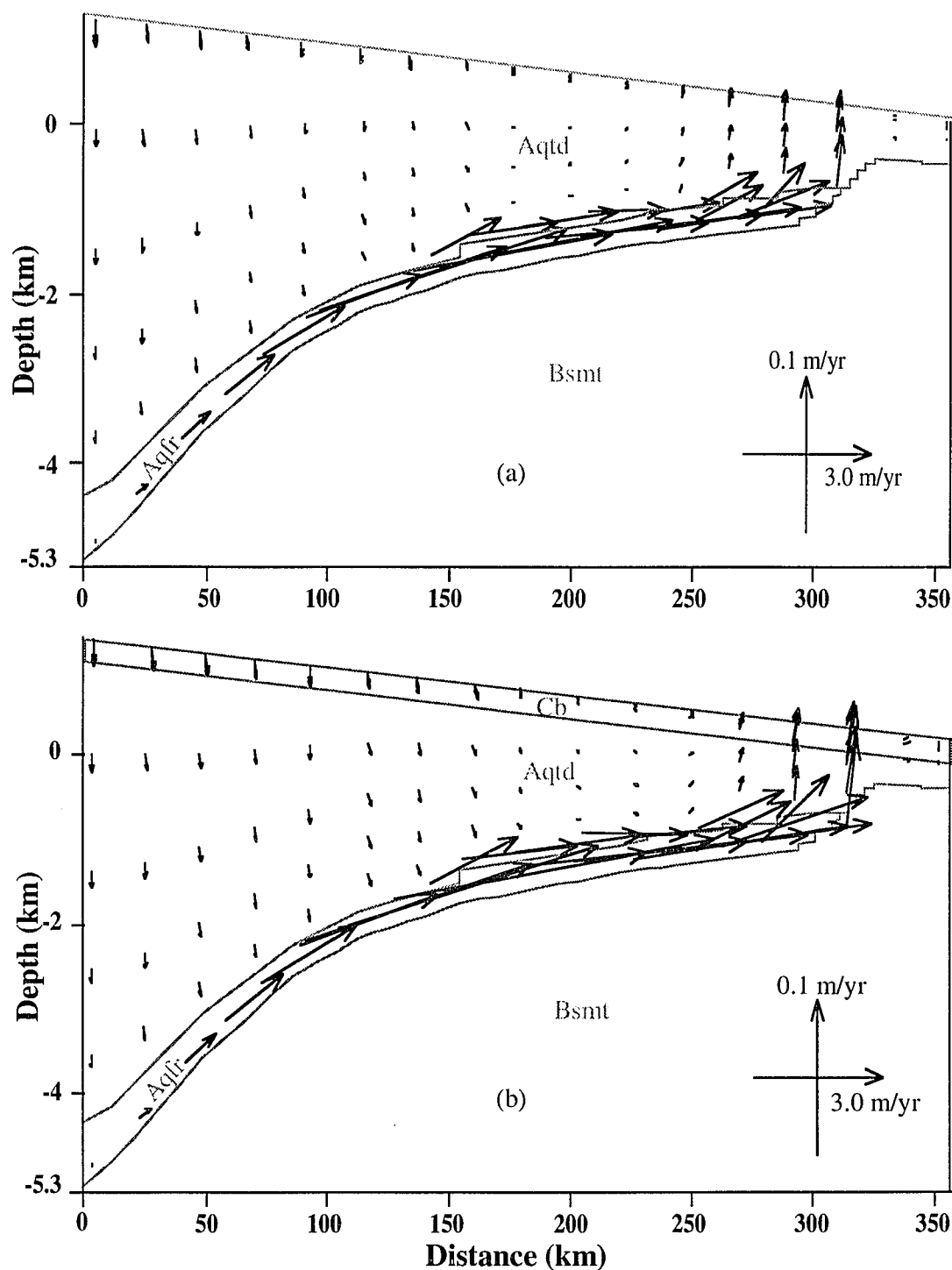
Figure 4.8a-b. Fluid flow fields at 0.2 Ma in Case 0 (a) and in Case 1 (b). The light lines outline the basement (Bsmt), aquifers (Aqfr, Units A and B), aquitards (Aqtd, Units C and D) and carbonaceous layer (Cb). Note both diagrams have the same scale for the arrows. See next page for other cases.
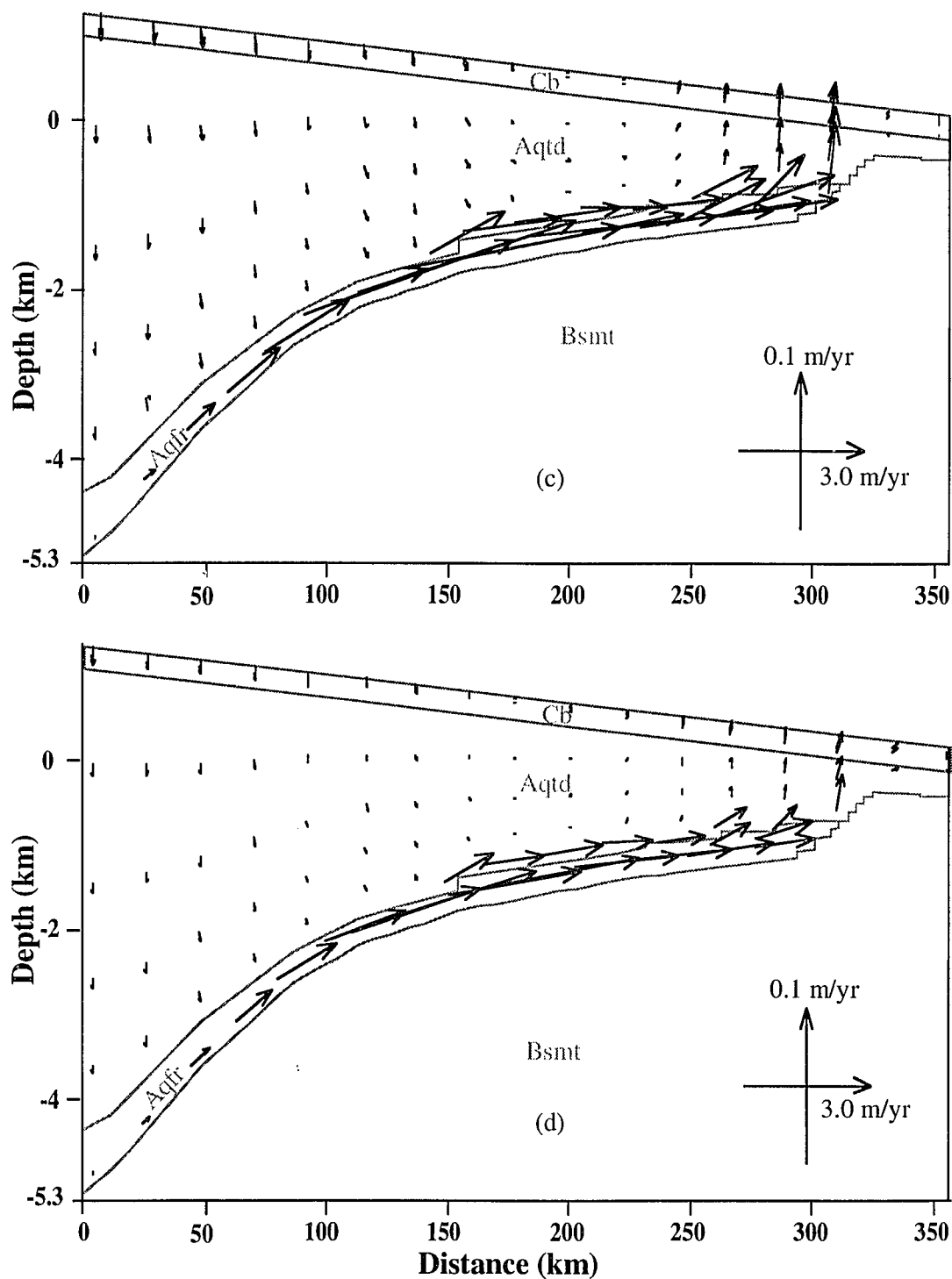
Figure 4.8c-d. Fluid flow fields at 0.2 Ma in Case 2 (c) and in Case 3 (d). The light lines outline the basement (Bsmt), aquifers (Aqfr, Units A and B), aquitards (Aqtd, Units C and D) and carbonaceous layer (Cb). Note both diagrams have the same arrow scale with those in the last page. See next page for Case 4.
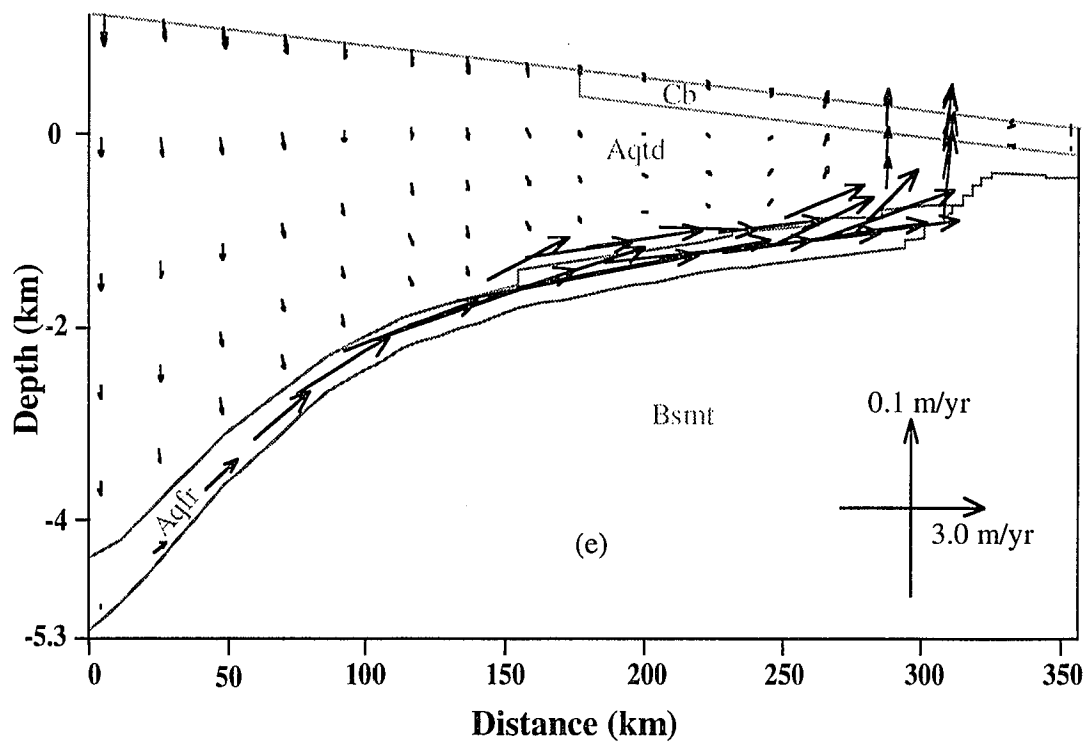
Figure 4.8e. Fluid flow field at 0.2 Ma in Case 4 (e) (half carbonaceous cover). The light lines outline the basement (Bsmt), aquifers (Aqfr, Units A and B), aquitards (Aqtd, Units C and D) and carbonaceous layer (Cb). Note that arrow scaling here is the same with those in the last page.

those obtained by Garven et al. (1993), Deming and Nunn (1991) and those in the last chapter, with a maximum value about 6.3 m./yr. in the early stage of modeling. Darcy velocities in Case 3, in which vertical permeability in the carbonaceous layer is 10 times lower than Case 1, are much lower compared to the other cases. Darcy velocities generally decrease with time (Figure 4.9). In all cases, flow rates decrease quickly in the early stage, but slowly after about 0.5 m.y. of modeling time.

Higher Darcy velocities in Case 1 result from higher basinal temperatures caused by the carbonaceous insulation (Figure 4.7). Higher temperature can cause lower fluid viscosities (Kestin et al., 1981) and thus higher flow rates. Thus, Darcy velocities shown on Figure 4.9 imply that the average temperature in Case 1 is higher than Case 2, which is higher than Case 4. Average temperature in Case 0 is the lowest compared to Case 1, 2 and 4. The reason that Case 4 has lower average temperature and fluid flow rates is because most sediments in the basin do not have carbonaceous coverage.

Lower vertical permeability of the carbonaceous layer in Case 3 resulted in a flow pattern different from that in Case 2 (Figure 4.8). Compared to Case 2, the recharge area in Case 3 is narrower and the discharge area is wider. Higher permeability of the carbonaceous layer in Case 2 caused faster discharge of groundwater in the St. Francois Mountain area, where the basal aquifers end. Thus, it requires a larger area to recharge the same amount of fluids. On the other hand, a decrease in vertical permeability of the carbonaceous layer in Case 3 reduces fluid discharge and hence the recharge area is small.

The major reason for the general decrease in Darcy velocity with time is because uplift of the model basin occurs instantaneously in all of these cases. The decreasing flow rate during the early stage of modeling seems unrealistic for a gradually uplifting foreland basin, which will be discussed later in Case 5. Figure 4.9 also indicates that the flow rates are dependent on the thermal conductivity of the carbonaceous section. Lower conductivity of the carbonaceous layer causes higher velocity of fluid flow.
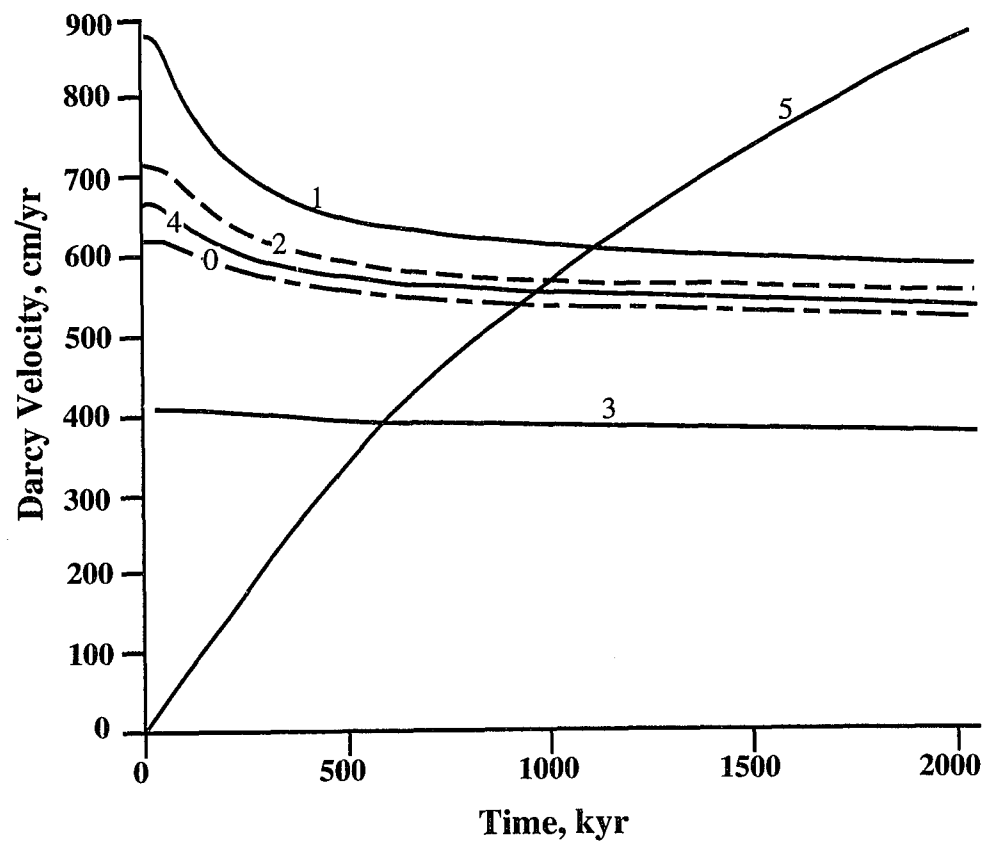
Figure 4.9. Maximum Darcy velocity (along the basal aquifers) versus time for all cases. Curve numbers correspond to the Cases.

4.4.3. Temperature distributions

The temperature fields are dramatically changed by fluid transport in all cases. In general, downward movement of fresh water from the recharge area has cooled the deep sediments and hence pulled down the isotherms on the left side of the model. On the other hand, heat carried up by fluid along the basal aquifers has tremendously increased temperatures in the discharge region in each case. However, different thermal conductivity and permeability of the carbonaceous section have resulted in different thermal histories of the foreland basin.

4.4.3.1. Temperature field in Case 1:

Figures 4.10 and 4.11 present the temperature fields and residual temperatures (current temperature - initial temperature) in Case 1 at elapsed model times of 0.2 and 1.0 Ma respectively. Compared to the initial condition (Figure 4.6), deep sediments in the far left of the basin have cooled down between 90 °C and 110 °C by downward flow of cold fluids from the recharge region (also see Figures 4.12a and 4.12b). Temperatures in the discharge area after an elapsed time of 0.2 Ma have increased about 80 °C (about 30 °C in Case 0) in the shallow sediments above the igneous rocks (see Figure 4.10b and Figure 4.12d), and more than 30 °C in the deep sediments adjacent to the igneous rocks (Figure 4.12c). Figure 4.12 summarizes the temperature variation with time at four locations for all cases. Compared to the temperature variation in the case without coal layer covering (Case 0), thermal insulation has increased the efficiency of heat transport from the deep sediments to the shallow discharge area.

Thermal insulation by the carbonaceous layer also retains heat during discharge of hot fluids by preventing surface heat loss. This is indicated by the even sharper thermal gradient (0.34 °C/m) in the top layer (Figure 4.10a) and the very low thermal gradient (< 10 °C/km) in the underlying sediments. This low thermal gradient is consistent with that obtained from fluid inclusion studies by Rowan and Leach (1989).

Figure 4.10. Temperature distribution (a) and residual temperature (T-To) (b) in Case 1 at 0.2 Ma. The heavy dashed contours represent the approximate temperatures inferred to have existed during the formation of MVT ore deposits. Light lines outline the basement (Bsmt), aquifers (Aqfr, Units A and B), aquitards (Aqtd, Units C and D) and carbonaceous layer (Cb).
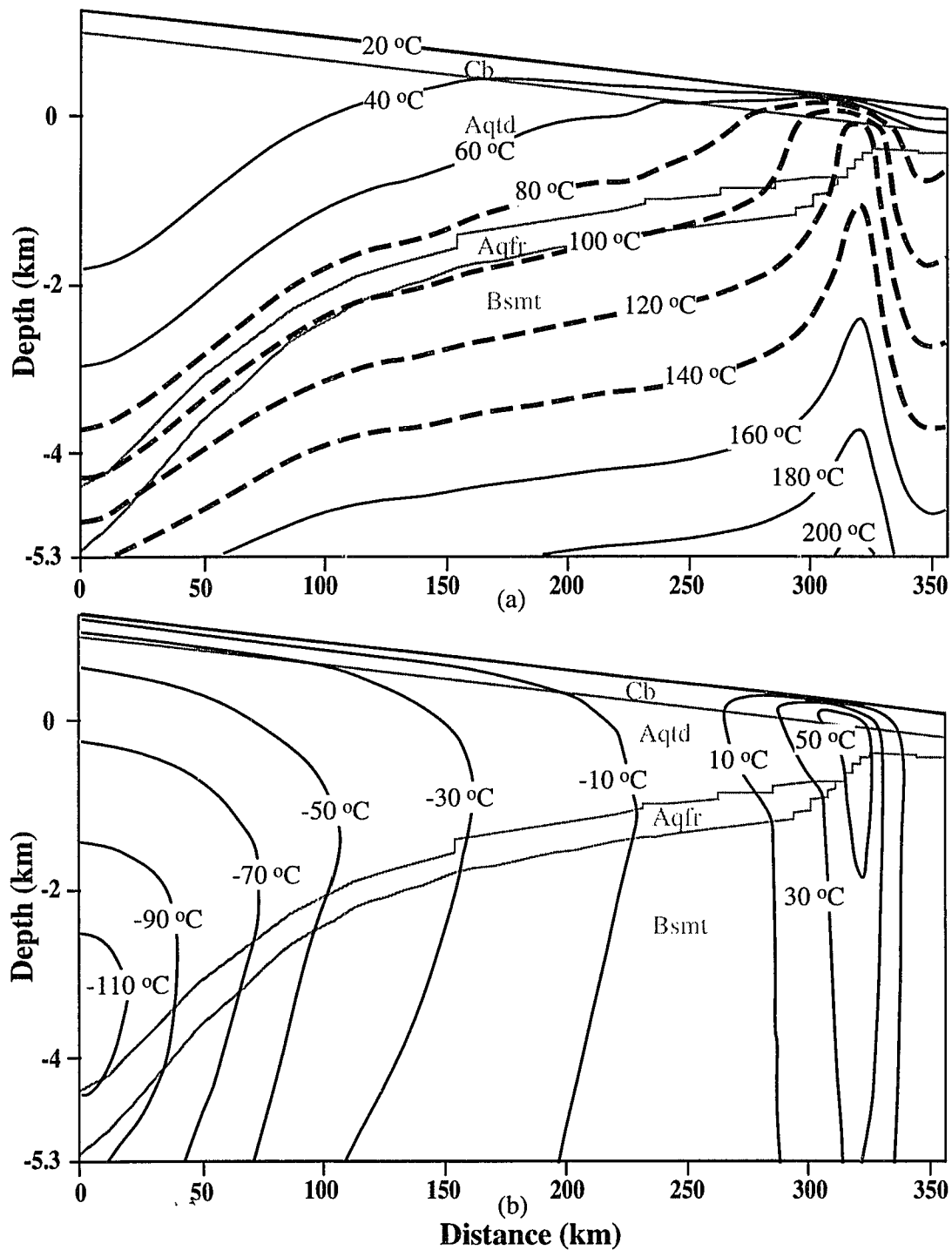
Figure 4.11. Temperature distribution (a) and residual temperature (T-To) (b) in Case 1 at 1.0 Ma. The heavy dashed contours represent the approximate temperatures inferred to have existed during the formation of MVT ore deposits. Light lines outline the basement (Bsmt), aquifers (Aqfr, Units A and B), aquitards (Aqtd, Units C and D) and carbonaceous layer (Cb).
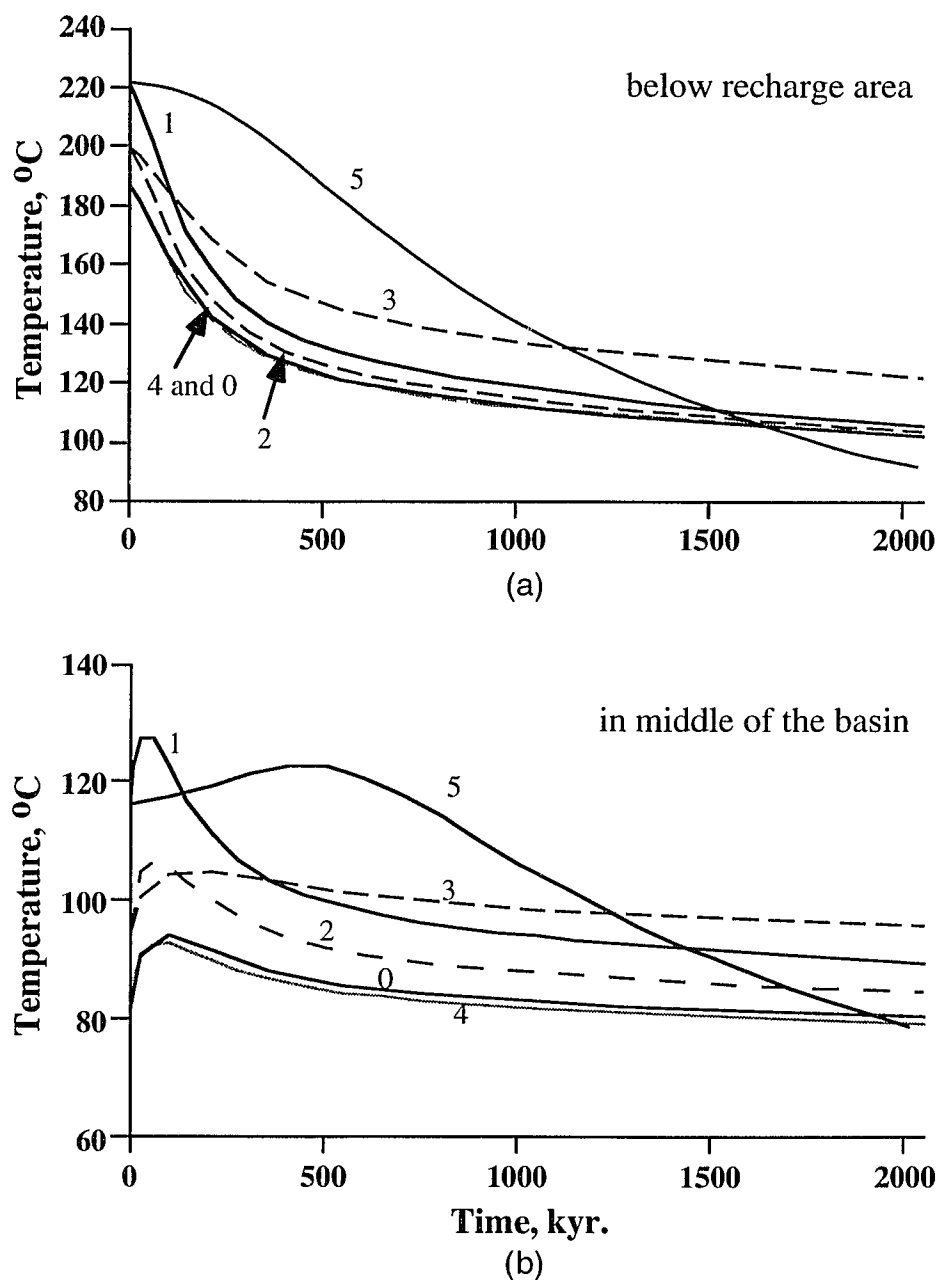
Figure 4.12a-b. Temperature variation with time for sediments below the recharge area (a) and in the middle of the basin (b). Curve numbers correspond to their cases. See Cross-Marks 1 and 2 in Figure 4.5 for the locations of (a) and (b) respectively. See next page for temperature variation in the discharge area.
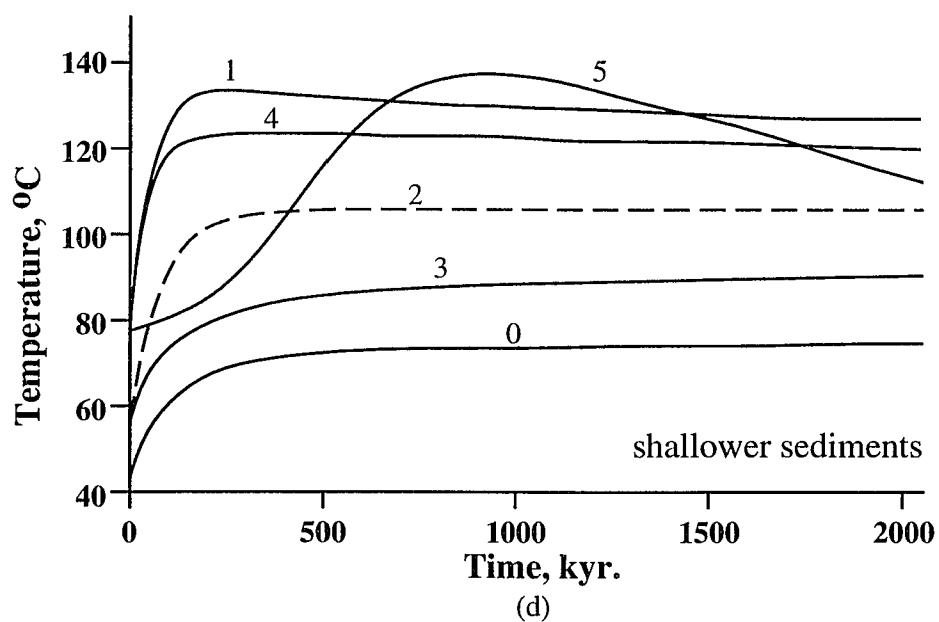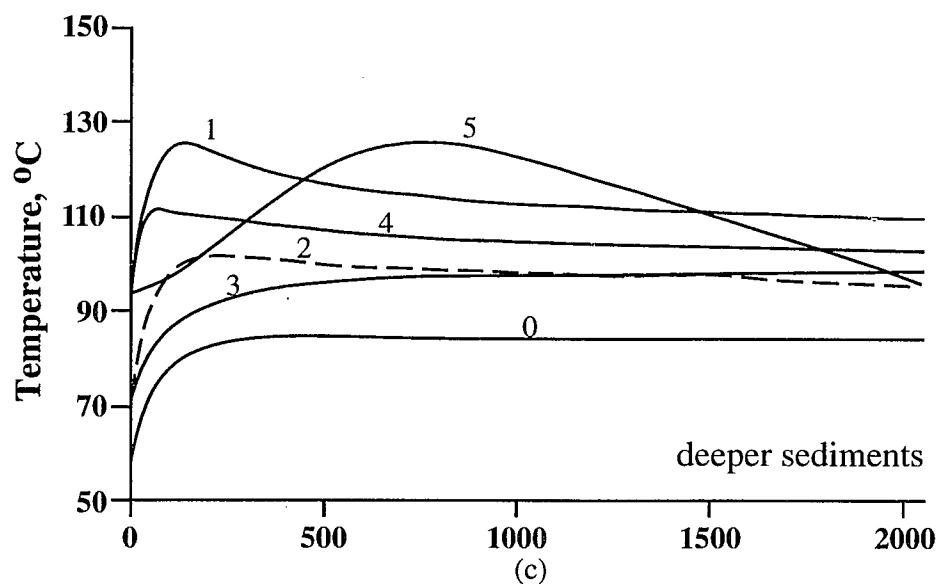
Figure 4.12c-d. Temperature variation with time for the deeper (c) and shallower (d) sediments in the discharge area. Curve numbers correspond to their cases. See Cross-Marks 3 and 4 in Figure 4.5 for the locations of (c) and (d) respectively.

The temperature pattern at 1.0 Ma (Figure 4.10) has been modified by the rapid discharge of groundwater, compared to model results at 0.2 Ma (Figure 4.11). Upwarping of isotherms in the discharge region of Figure 4.11a is much narrow, compared to that in Figure 4.10a. Even there is an increase of temperature in the igneous rocks, temperature generally decreases in the deep sediments adjacent to the igneous rocks after about 0.2 Ma (Figure 4.12).

The above phenomenon can be explained as low thermal conductivity of the carbonaceous layer, which acts as a thermal blanket, has prevented heat loss by conduction. In the early stage of modeling, sediments in the discharge area were subjected to a thermal pulse (see Figure 4.12c) caused by the rapid transport of heat by fluid flow along the basal aquifers. Thus, heat can be stored over a broad area represented by the pulled-up isotherms. In the later stage of modeling, cooling in the deep sediments has caused discharged fluids to be cooler. Thus continuous discharge of hot fluids out of the system, eventually causes the left side of the upwarped isotherms to shift toward the right into the igneous rocks.

The amplitudes of the upwarped isotherms in the sediments remain almost unchanged between 0.2 to 1.0 Ma. Isotherms in the basement have moved upward. Because heat flow at the model base was assumed constant through time, heating by the upward flowing hot fluids along the basal aquifers, has decreased the heat flow at the sediment-basement interface, and forced an increase in temperature in the basement below the discharge region (Figure 4.11b). Cooling of the deep sediments below the recharge region has increased heat flow and decreased temperature in the basement rocks below the recharge area (Figure 4.11b).

4.4.3.2. Temperature field in Case 2:

Increasing the thermal conductivity of the carbonaceous layer results in lower model temperatures in both the discharge and recharge regions. Figures 4.13 and 4.14 show the temperature distribution and residual temperatures at 0.2 and 1.0 m.y., respectively.
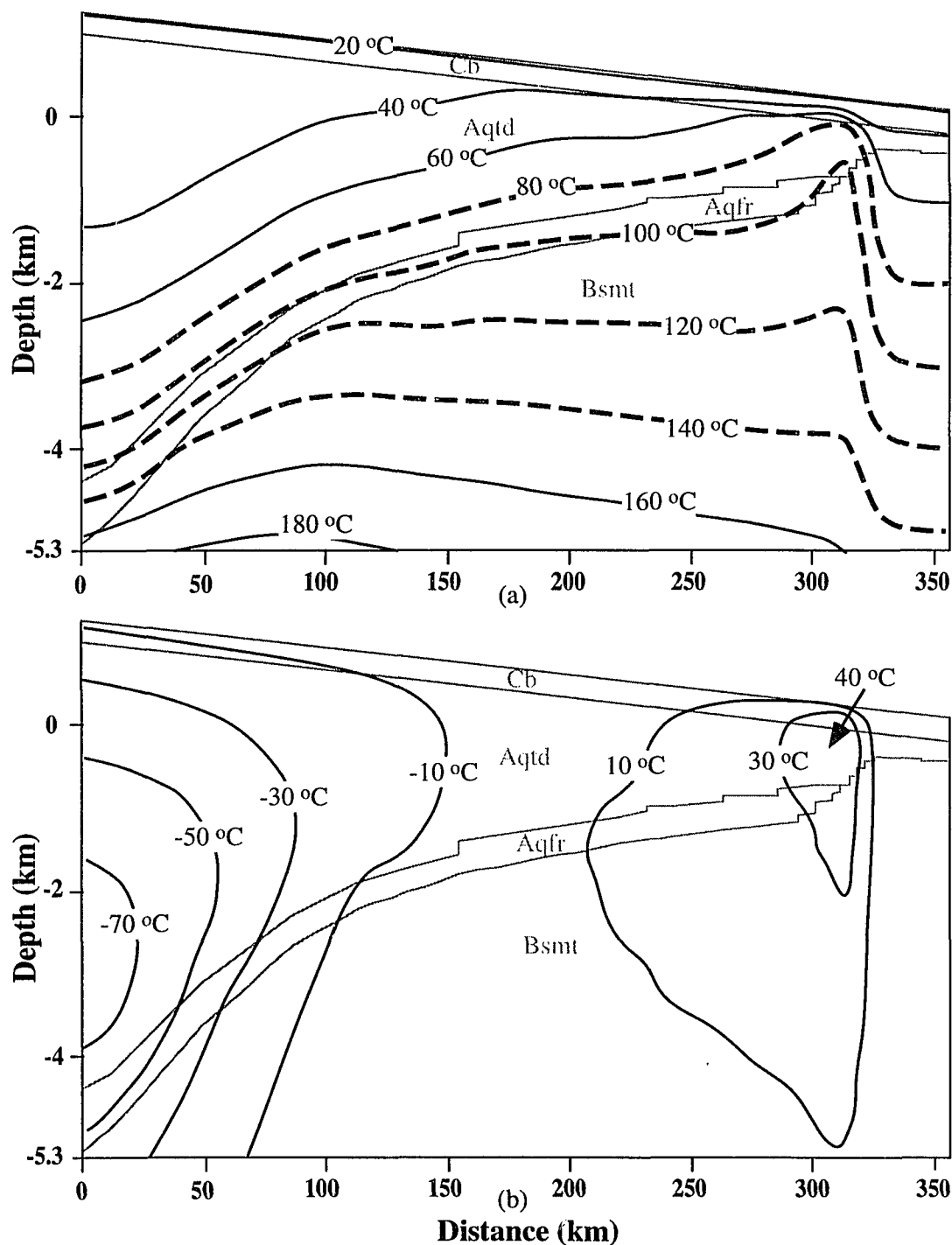
Figure 4.13. Temperature distribution (a) and residual temperature (T-T0) (b) in Case 2 at 0.2 Ma. The heavy dashed contours represent the approximate temperatures inferred to have existed during the formation of MVT ore deposits. Light lines outline the basement (Bsmt), aquifers (Aqfr, Units A and B), aquitards (Aqtd, Units C and D) and carbonaceous layer (Cb).
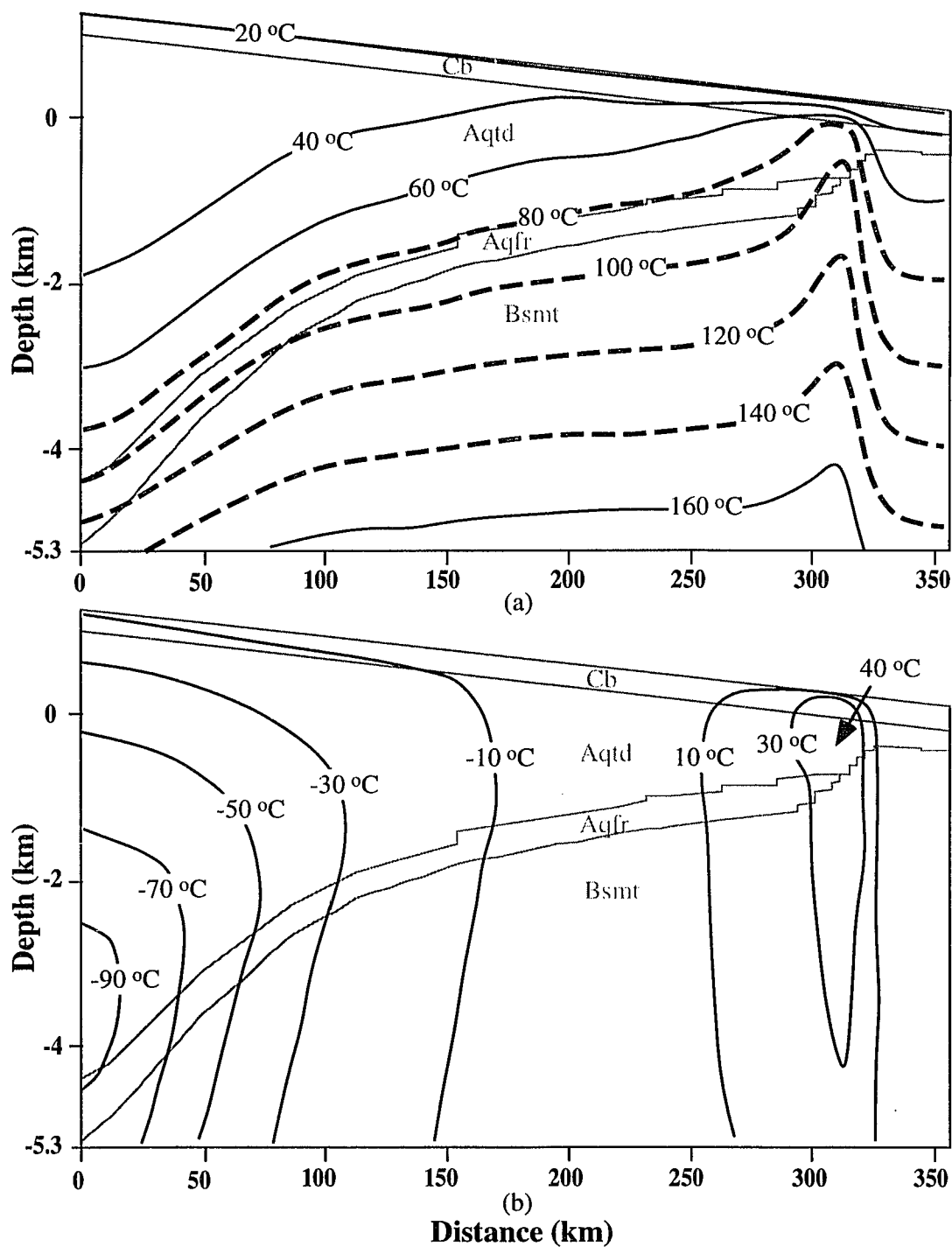
Figure 4.14. Temperature distribution (a) and residual temperature (T-To) (b) in Case 2 at 1.0 Ma. The heavy dashed contours represent the approximate temperatures inferred to have existed during the formation of MVT ore deposits. Light lines outline the basement (Bsmt), aquifers (Aqfr, Units A and B), aquitards (Aqtd, Units C and D) and carbonaceous layer (Cb).

Compared to the initial thermal condition (Figure 4.6b), it is observed that a temperature decrease of about 70 °C (90 °C in Case 1) at 0.2 Ma and 90 °C (110 °C in Case 1) at 1.0 Ma in the deep sediments on the far left of the basin. In the discharge region, temperatures of shallow sediments can increase more than 40 °C (about 80 °C in Case 1) after 0.2 Ma (also see Figure 4.12d), but those of the deep sediments immediately adjacent to the igneous rocks on the left increased about 30 °C at time of 0.2 Ma and then decreased slowly (thermal pulse observed, see Figure 4.12c). These indicate that heat can not be transported in this case as efficiently as in Case 1. However, compared to Case 0 (without coal layer coverage), shallow sediments in the discharge region have been warmed up more than 30 °C (Figure 4.12d). There was generally an increase of temperature in the igneous rocks and within the basement, which is similar to Case 1.

There is almost no shifting in the left side of the upwarped isotherms to the right in the shallow sediments of the discharge region as in Case 1. I interpret this is because there was only a low magnitude transient thermal pulse passing through this region in the early stage of the modeling. The lower value of the thermal pulse was mainly caused by the lower fluid flow rates (Figure 4.9). Less thermal insulation by the higher conductivity carbonaceous layer caused the underlying sediments to decrease in temperature, which in turn increases the fluid viscosity (Kestin et al., 1981). Thermal energy in the transient pulse can be more easily consumed by the basement rocks, when flow rates are low, because there is more time for thermal interaction between the basement rocks and hot fluids moving along the basal aquifers.

Thermal insulation of the carbonaceous layer in this case retained less heat during the discharge, compared to Case 1. This is reflected by the lower thermal gradient of about 0.22 °C/m (about 0.34 °C/m in Case 1) in the top layer and higher thermal gradient of about 0.023 °C/m (0.01 °C/m or less in Case 1) in the underlying sediments. Other phenomena observed in Case 2 are similar to those in Case 1.

4.4.3.3. Temperature field in Case 3:

Lower vertical permeability of the carbonaceous layer has caused fluid flow velocities to decrease (Figure 4.9). Small changes in the temperature field were observed from model time 0.2 to 1.0 Ma (Figures 4.15 and 4.16). Compared to Case 2 (both cases have the same initial temperature, also see Figure 4.13b), temperatures only decreased by about 50 °C (70 °C in Case 2) at 0.2 Ma and about 70 °C (90 °C in Case 2) at 1.0 Ma in the deep sediments on the far left of the basin. Decreased efficiency in heat transport has resulted in a smaller thermal gradient of 0.14 °C/m (about 0.22 °C/m in Case 2) within the top layer and a larger thermal gradient of 0.035 °C/m (0.023 °C/m in Case 2) in the underlying sediments in the discharge area.

In the deep sediments immediately adjacent to the igneous rocks in the discharge region, temperatures generally showed an increase through time and no transient thermal pulse was observed (also see Figure 4.12c); temperatures in these sediments increased by about 20 °C at 0.2 Ma (Figure 4.15b) and 30 °C at 1.0 Ma (Figure 4.16b). After 1.0 Ma, the temperatures in the deep sediments became slightly higher than in Case 2 (Figure 4.12c). In the shallow sediments in the discharge region (Figure 4.12d), temperatures increased even more slowly in the early stage of modeling, but had a trend of continuous increase to 2.0 Ma. At 1.0 Ma, these sediments had a temperature increase of about 35 °C (more than 40 °C in Case 2).

The above results are primarily caused by the low fluid flow rates, which prevented the basin from losing too much heat in the early stage of modeling and allowed the basement rocks a longer time to buffer the changes in the thermal regime caused by fluid flow. Furthermore, compared to Case 2, the lower and higher thermal gradients within the carbonaceous layer and the underlying sediments respectively in the discharge area imply weaker thermal insulation by the carbonaceous sediments. Temperature variations in the igneous rocks and within the basement are similar to those observed in Case 1 and Case 2.
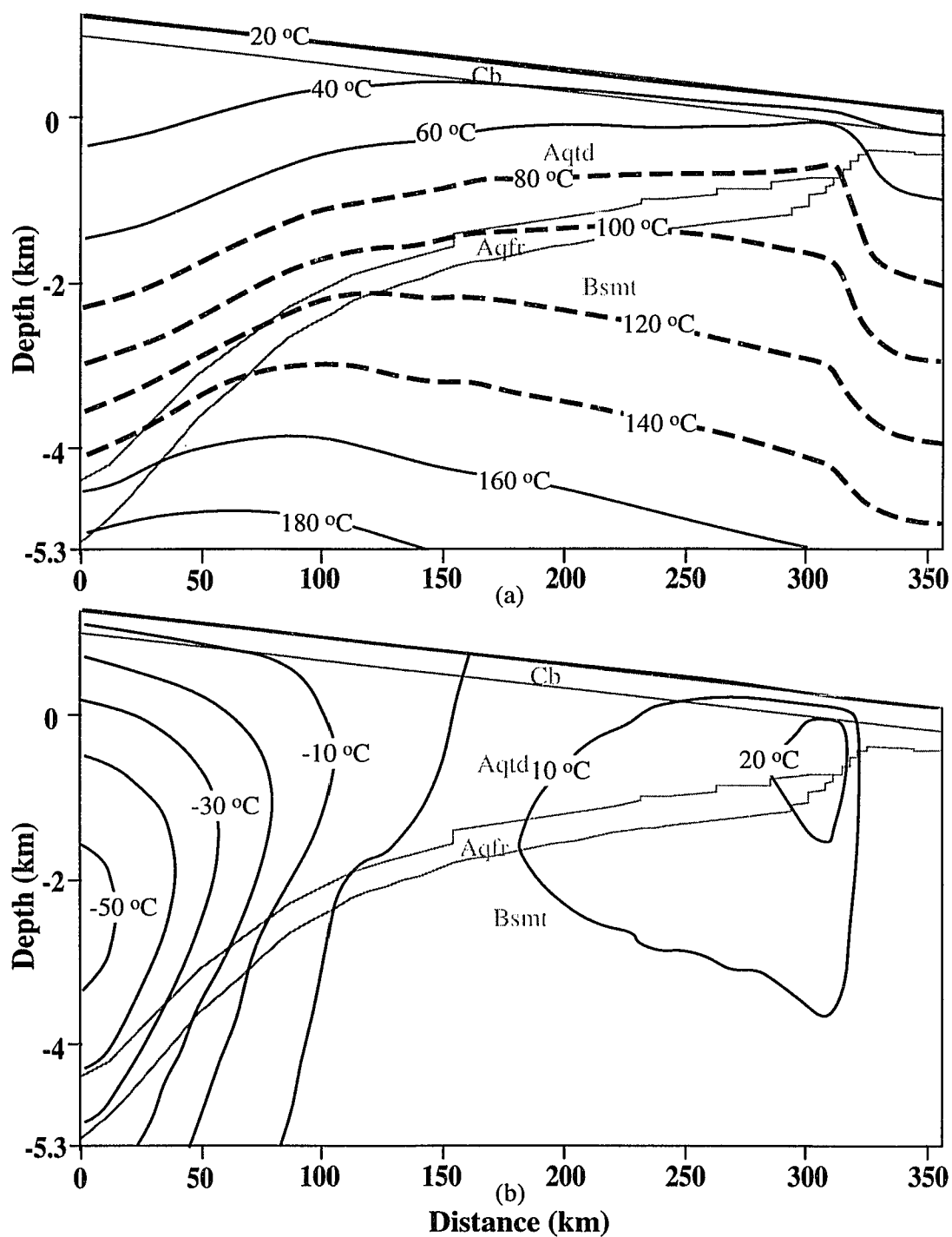
Figure 4.15. Temperature distribution (a) and residual temperature (T-To) (b) at 0.2 Ma. in Case 3. The heavy dash contours represent the approximate temperatures inferred to have existed during the formation of the MVT ore deposits. Light lines outline the basement (Bsmt), aquifers (Aqfr), Units A and B), aquitards (Aqtd, Units C and D) and the carbonaceous layer (Cb).
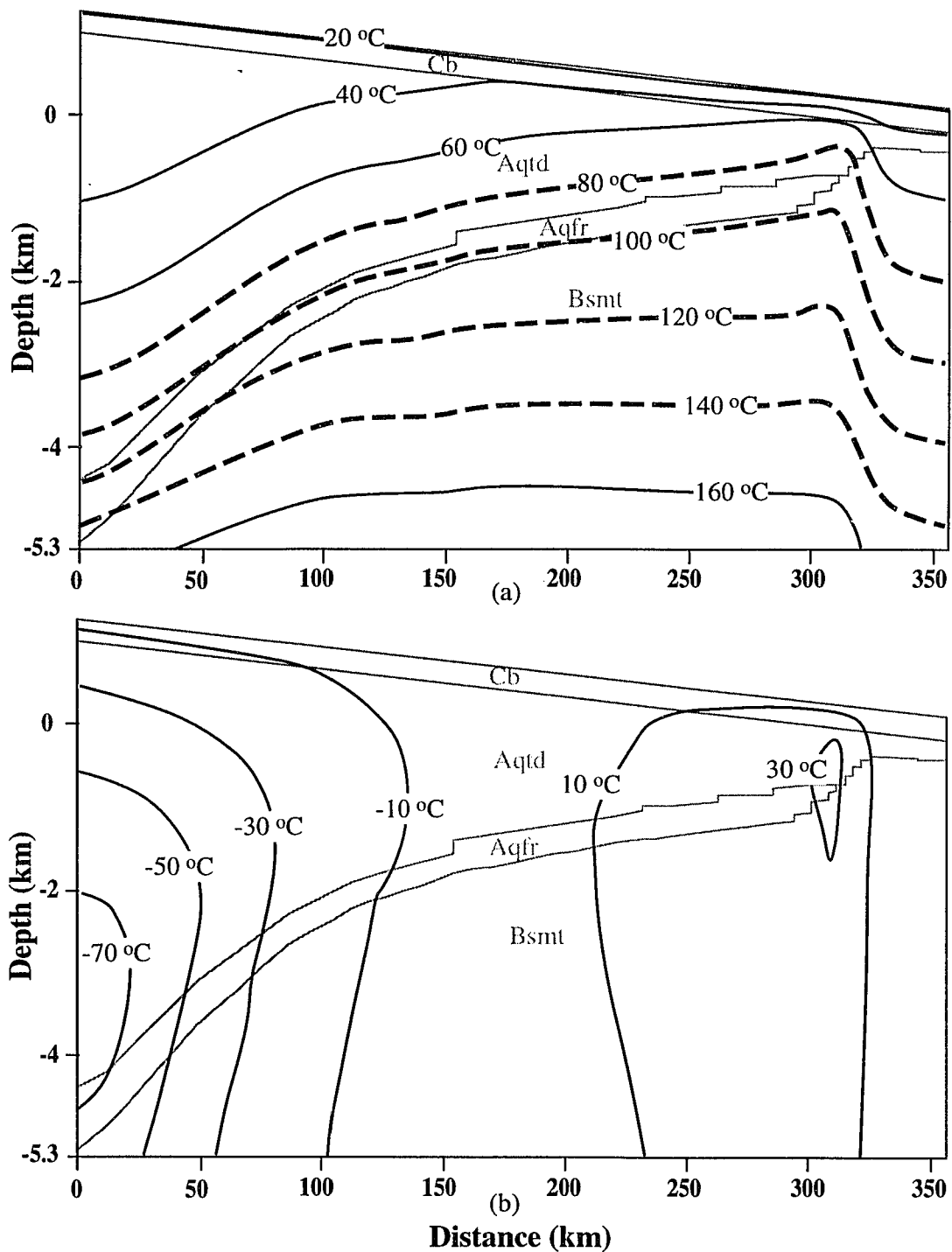
Figure 4.16. Temperature distribution (a) and residual temperature (T-To) (b) in Case 3 at 1.0 Ma. The heavy dashed contours represent the approximate temperatures inferred to have existed during formation of MVT ore deposits. Light lines outline the basement (Bsmt), aquifers (Aqfr, Units A and B), aquitards (Aqtd, Units C and D) and carbonaceous layer (Cb).

4.4.3.4. Temperature field in Case 4:

Figures 4.17 and 4.18 show the model temperature and residual temperature at about 0.2 Ma and 1.0 Ma respectively, in Case 4 (half covering by low conductivity carbonaceous layer). In the deep sediments on the far left of the model, initial temperatures were about 35 °C lower than Case 1 (see Figure 4.6). Compared to the initial conditions, temperatures decreased by about 60 °C (90 °C in Case 1) at 0.2 Ma and about 80 °C (110 °C in Case 1) at 1.0 Ma In the discharge region, sediment temperatures increased about 50 °C (> 60 °C in Case 1) at both 0.2 Ma and 1.0 Ma . In the deep sediments immediately adjacent to the igneous rocks, a small thermal pulse was observed (Figure 4.12c). In the shallow sediments above the igneous rocks of the discharge region, no thermal pulse occurred (Figure 4.12d). Discharge temperatures remained approximately constant at about 120 °C (an increase of more than 40 °C, compared to the initial value) after 0.5 Ma.

Even though Case 4 has only half carbonaceous cover on the right of the model basin which causes lower average temperature and lower Darcy velocities, temperature distribution in the discharge area is similar to that in Case 1 (compare Figures 4.10a and 4.17a). Lower Darcy velocities and lower initial heat storage in Case 4 imply that heat transport is not as efficient as in Case 1. This is why upwarping of isotherms in the discharge region is narrower and lower in amplitude (Figure 4.17a), compared to Case 1 (Figure 4.10a). However, the similarity of temperature distribution in the discharge area between these two cases indicates the importance of heat retention by low thermal conductivity carbonaceous layer.

4.4.4. **Surface heat flow**

Surface heat flow from Cases 1 to 5 were computed, considering only the conductive component. Figures 4.19a and 4.19b show surface heat flow in these cases at 0.2 Ma and 1.0 Ma respectively. These curves generally reflect that groundwater
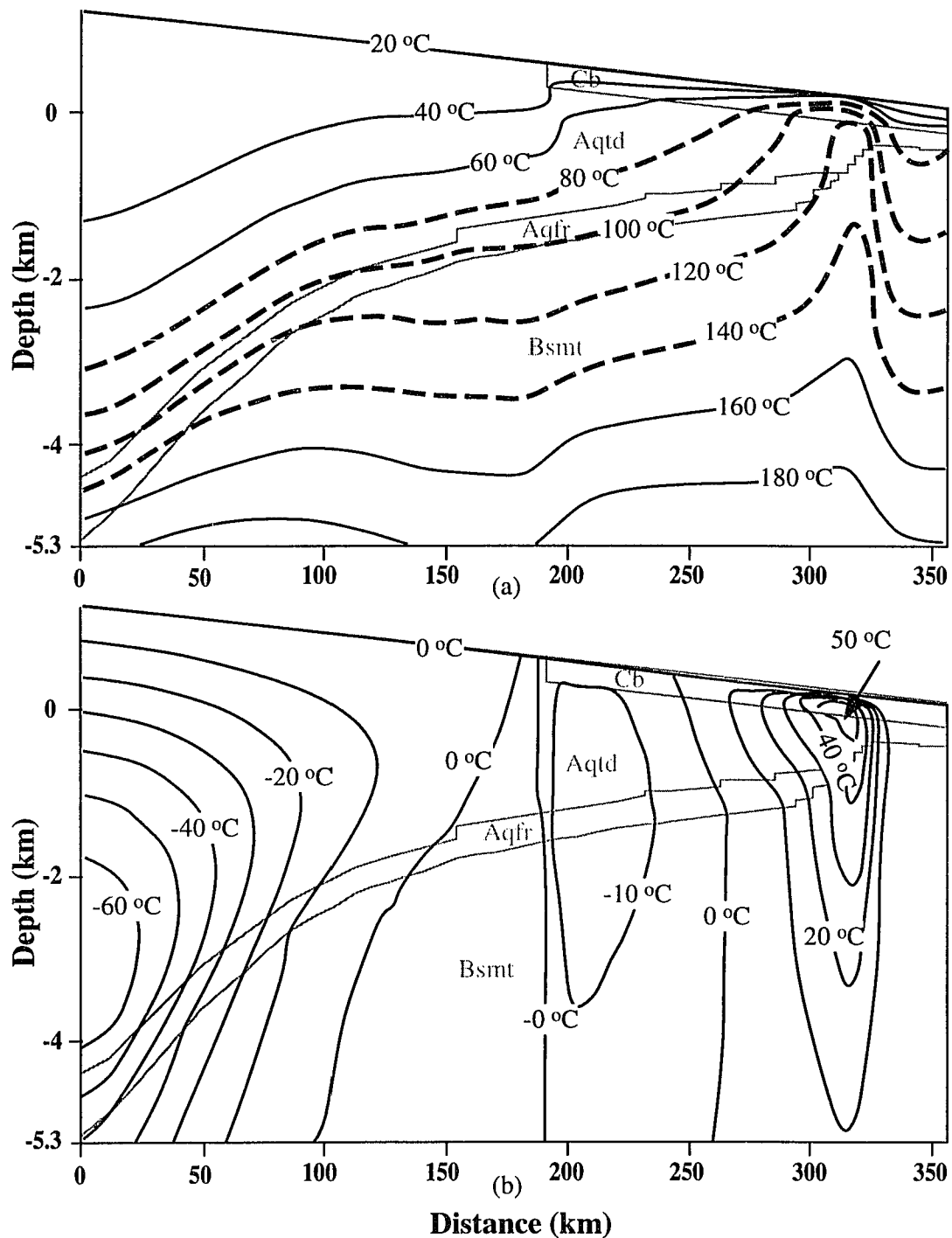
Figure 4.17. Temperature distribution (a) and residual temperature (T-To) (b) in Case 4 at 0.2 Ma. The heavy dashed contours represent the approximate temperatures inferred to have existed during the formation of MVT ore deposits. Light lines outline the basement (Bsmt), aquifers (Aqfr, Units A and B), aquitards (Aqtd, Units C and D) and carbonaceous layer (Cb).
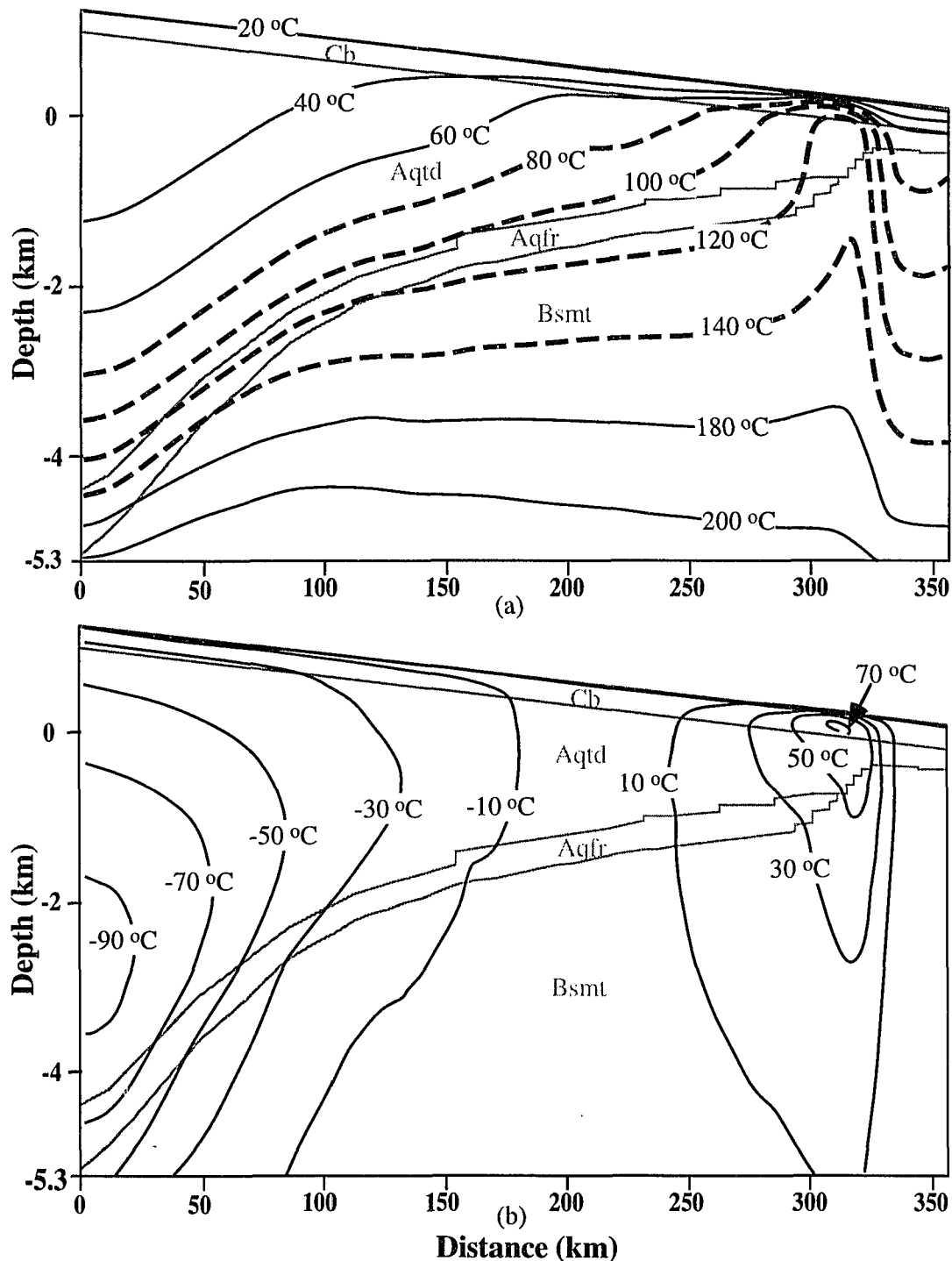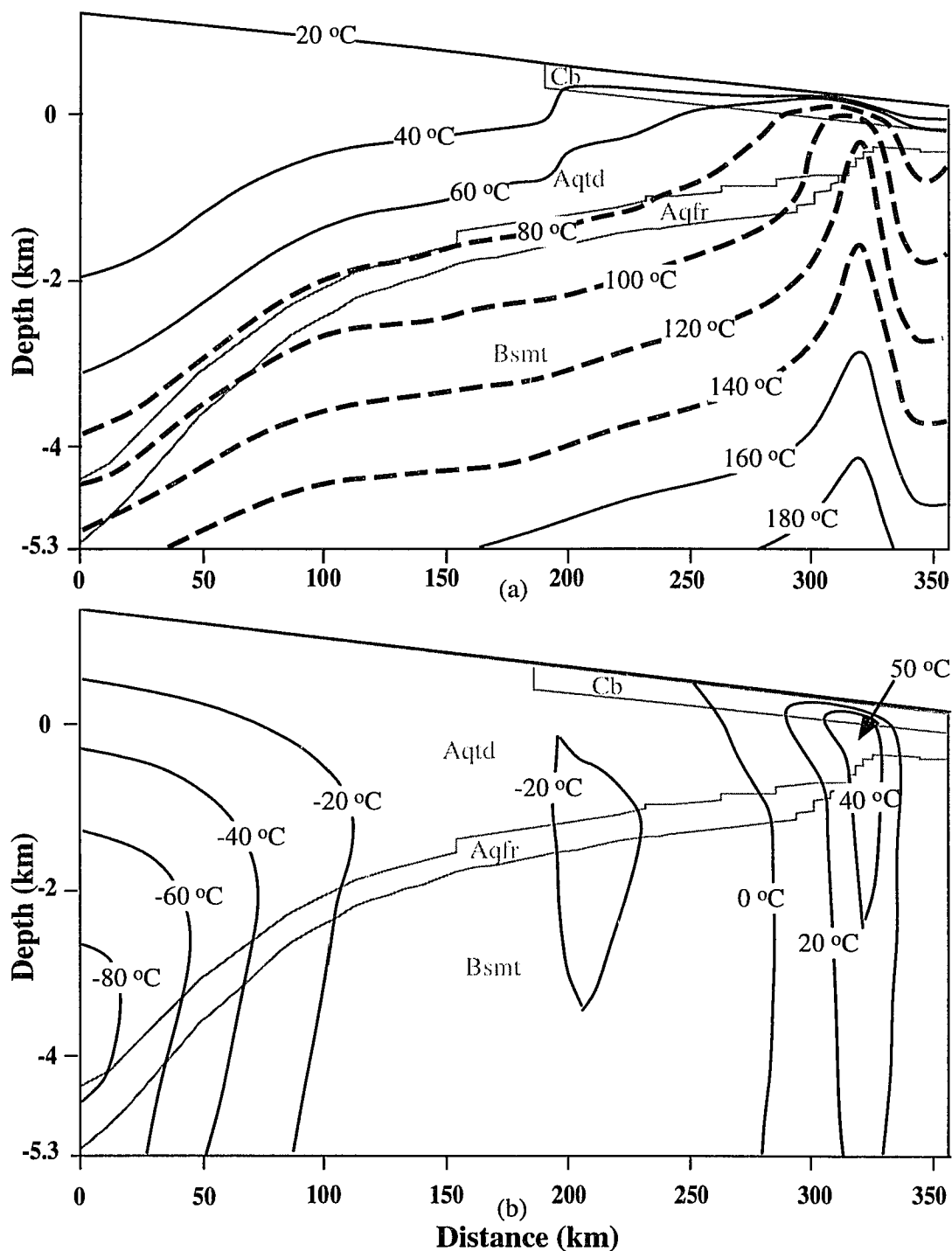
Figure 4.18. Temperature distribution (a) and residual temperature (T-To) (b) in Case 4 at 1.0 Ma. The heavy dashed contours represent the approximate temperatures inferred to have existed during the formation of MVT ore deposits. Light lines outline the basement (Bsmt), aquifers (Aqfr, Units A and B), aquitards (Aqtd, Units C and D) and carbonaceous layer (Cb).
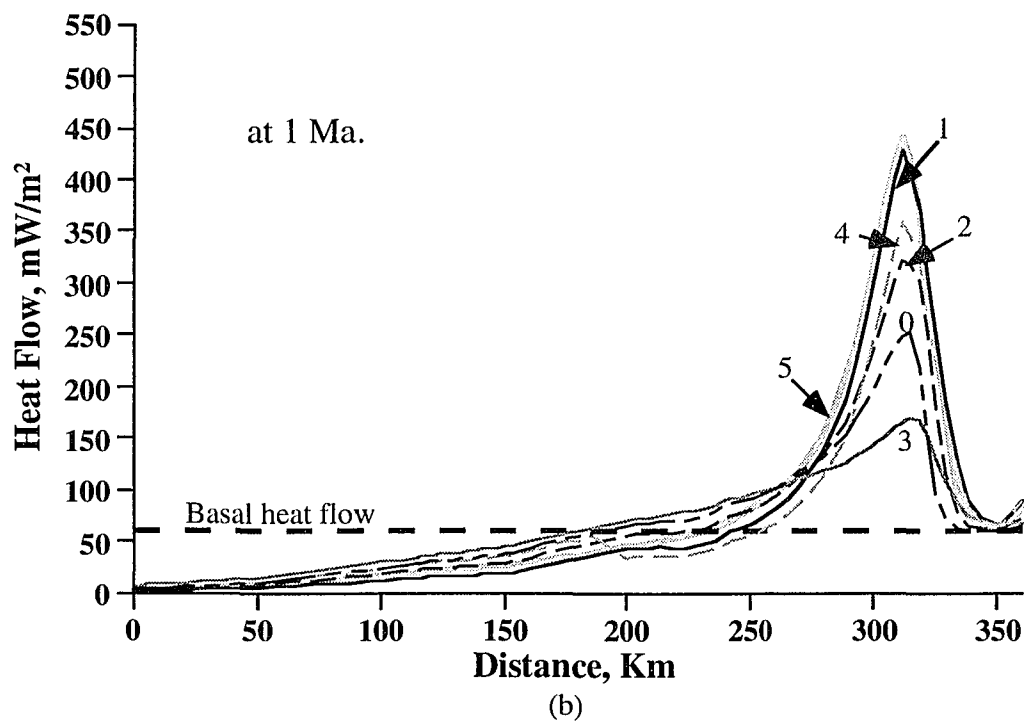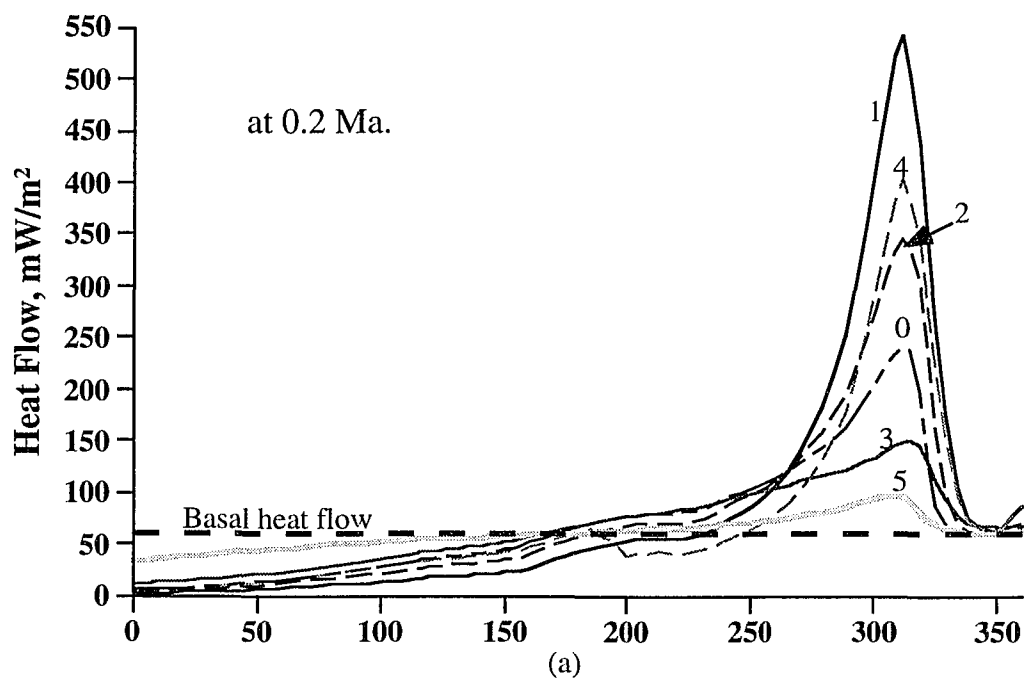
Figure 4.19a-b. Surface heat flow at 0.2 Ma (a) and at 1.0 Ma (b). Curve numbers correspond to the Cases. See next page for the variatons of surface heat flow with time.

Average Surface Heat Flow vs. Time
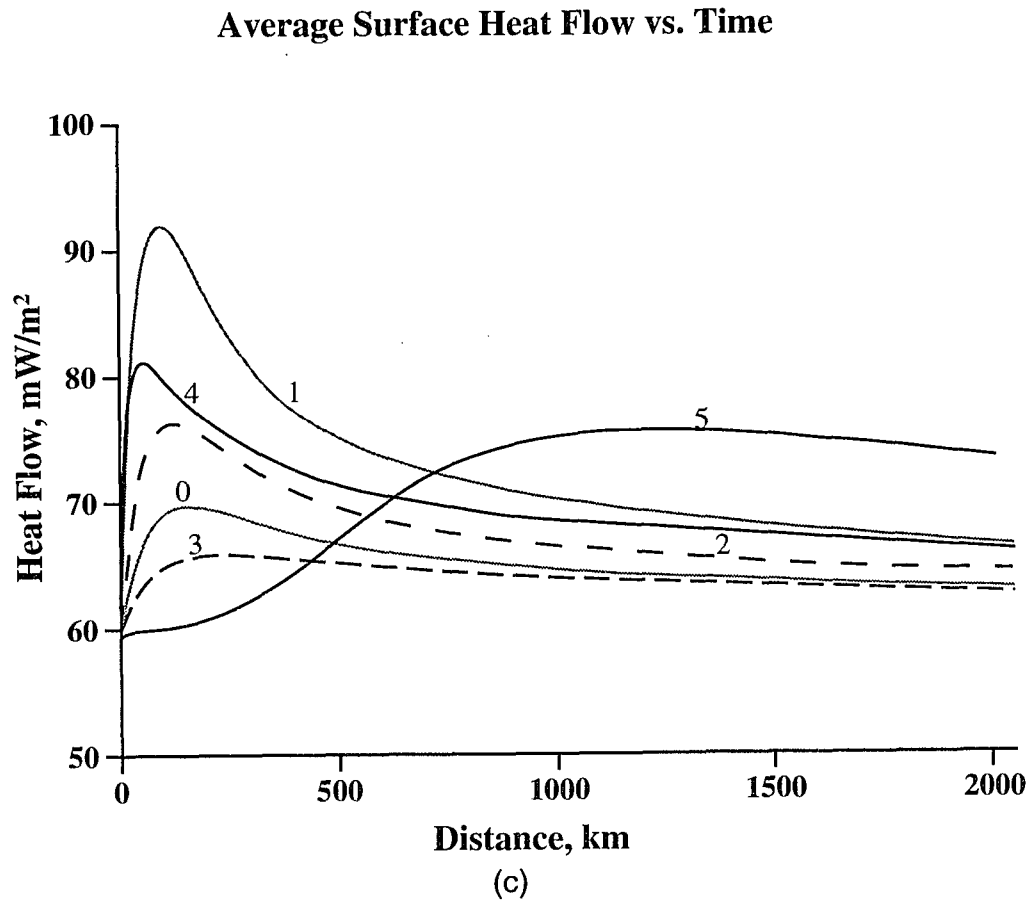
Figure 4.19c. Average surface heat flow vs. time (c) for all cases. The curve numbers correspond to their cases.

flow reduces surface heat flow in the recharge area and tremendously increases surface heat flow in the discharge region. The heat flow patterns here are consistent with those obtained in other numerical simulations associated with the formation of MVT ore deposits (for example, Majorowicz and Jessop, 1981; Kilty and Chapman, 1982; Chapman, 1984; Majorowicz et al., 1984 and 1985b; Gosnold and Fischer, 1986; Gosnold, 1985 and 1990; Garven, 1989; Smith et al., 1989; Meert et al., 1991; Deming and Nunn, 1991).

Figure 4.19 indicates that thermal conductivity and permeability of the carbonaceous rocks are two important factors that control surface heat flow. For example, in the discharge region at 0.2 Ma (Figure 4.19a), the maximum surface heat flow in Case 1 (low conductivity) is about 550 mW/m^2, much higher than 350 mW/m^2 in Case 2 (high conductivity). Lower vertical permeability in Case 3 tremendously reduces the average surface heat flow to 150 mW/m^2 (compared to Case 2), even lower than Case 0 (no carbonaceous cover, see Figure 4.19c). Partial cover by the low conductivity carbonaceous layer (Case 4) also causes high surface heat flow, with a maximum value of about 400 mW/m^2 at 0.2 Ma. In the recharge region, higher conductivity and lower permeability of the carbonaceous sediments caused higher surface heat flow, but differences between the cases are much smaller than in the discharge area.

Figure 4.19c shows that surface heat flow in Cases 1, 2, 3 and 4 decreased after time of 0.1 m.y., but in Case 3 the decrease was much slower than the other cases. This observation is consistent with temperature variations (Figure 4.12c and 4.12d). The decrease in surface heat flow in Case 1, 2 and 4 was primarily caused by the transient thermal pulse, which occurred in the discharge region during the early stage of modeling. In Case 3, however, temperatures in the discharge region generally increased through time and no thermal pulse was observed.

4.4.5. Case 5: Thermal evolution in an uplifting foreland basin

4.4.5.1. Fluid flow in Case 5:

The general flow pattern in Case 5 is similar to the other cases. Figures 4.20a and 4.20b show the flow fields at 0.2 and 1.0 Ma, when maximum elevation was 0.2 and 1.0 km at the left end, respectively. Both velocity arrows and physical dimensions of the model in Figure 4.20 have the same vertical exaggerations as Figure 4.8. Darcy velocities in this case were initially zero everywhere. Continuous uplift (1 mm/yr. at the left end and 0 mm/yr. at the right end) of the model basin gradually increased the topographical gradient of the water table and thus increased fluid flow rates with time. Significant variation in flow velocity have caused the flow pattern to change. For example, the flow field at 0.2 Ma (Figure 4.20a) has more horizontal components in the central part of the model and has a wider recharge area than at 1.0 Ma (higher flow velocity, Figure 4.20b).

The increasing rate of Darcy velocities was about 0.64 cm/yr. per thousand years in the early stage of uplifting, but decreased to about 0.35 cm/yr. per thousand years at elapsed model time of 1.0 Ma (Figure 4.9). The rate of increase in Darcy velocity with time slows because of the cooling of the model basin. Flow velocity is inversely proportional to fluid viscosity, which in turn is dependent on the temperature, as mentioned earlier. At 1.0 Ma the maximum Darcy velocity was about 5.6 m/yr.

4.4.5.2. Temperature distribution in Case 5:

The initial temperature field (Figure 4.21) in Case 5 is approximately identical to that of the instantaneous uplifting case (Case 1) (also see Figure 4.6a). However in Case 5, because fluid flow velocities were initially zero everywhere and were gradually increasing with time, sediment temperatures change more slowly in the early stage of modeling. Compared to the initial condition, deep sediments in the far left of the basin have only been cooled about 6 °C at 0.2 Ma (60 °C in Case 1), but 80 °C at 1.0 Ma (100 °C in Case 1), see Figures 4.22 and 23 for the corresponding temperature fields
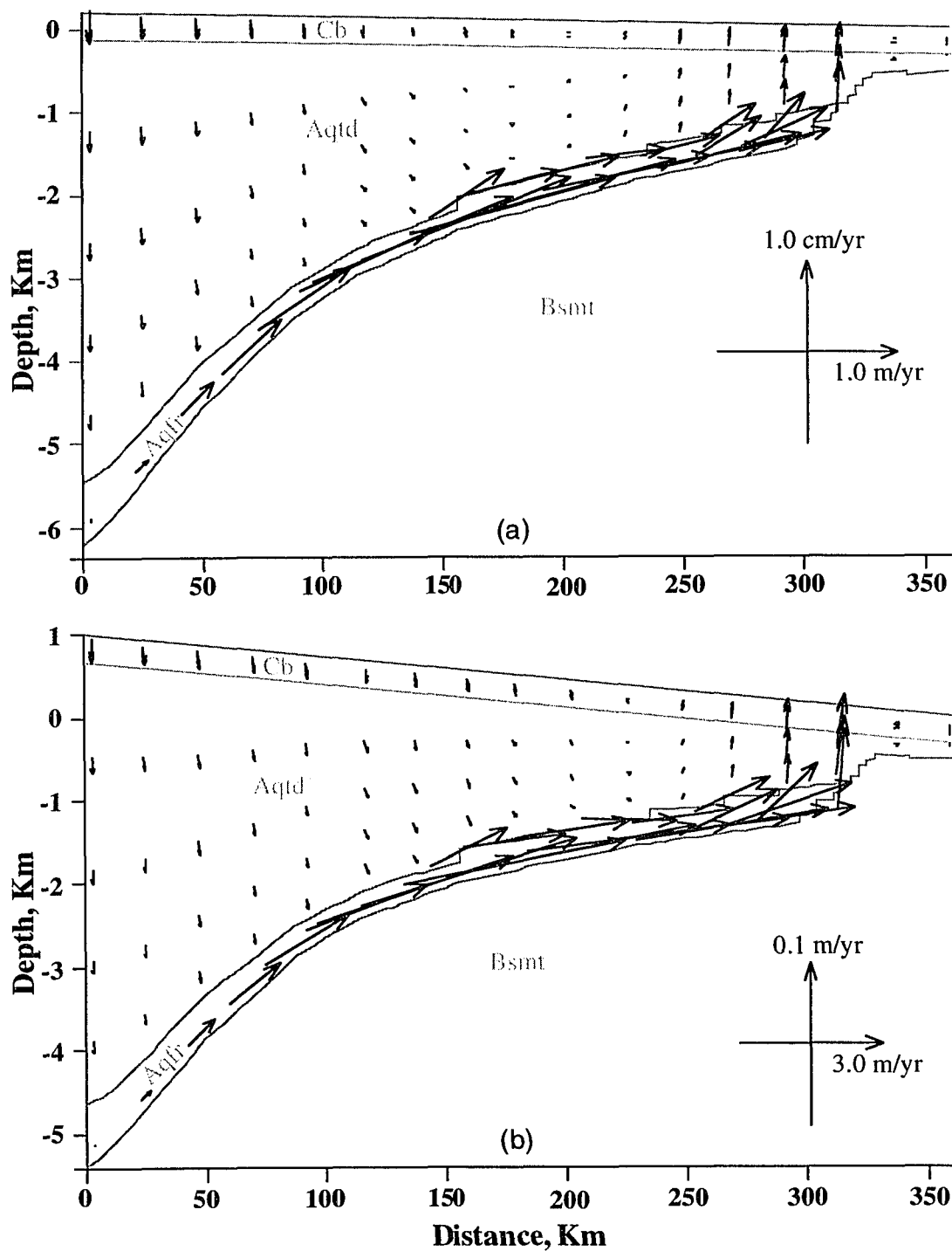
Figure 4.20. Fluid flow fields in Case 5 (uplifting foreland basin) at 0.2 Ma (a) and 1.0 Ma (b). The light lines outline the basement (Bsmt), aquifers (Aqfr, Units A and B), aquitards (Aqtd, Units C and D) and the carbonaceous layer (Cb).
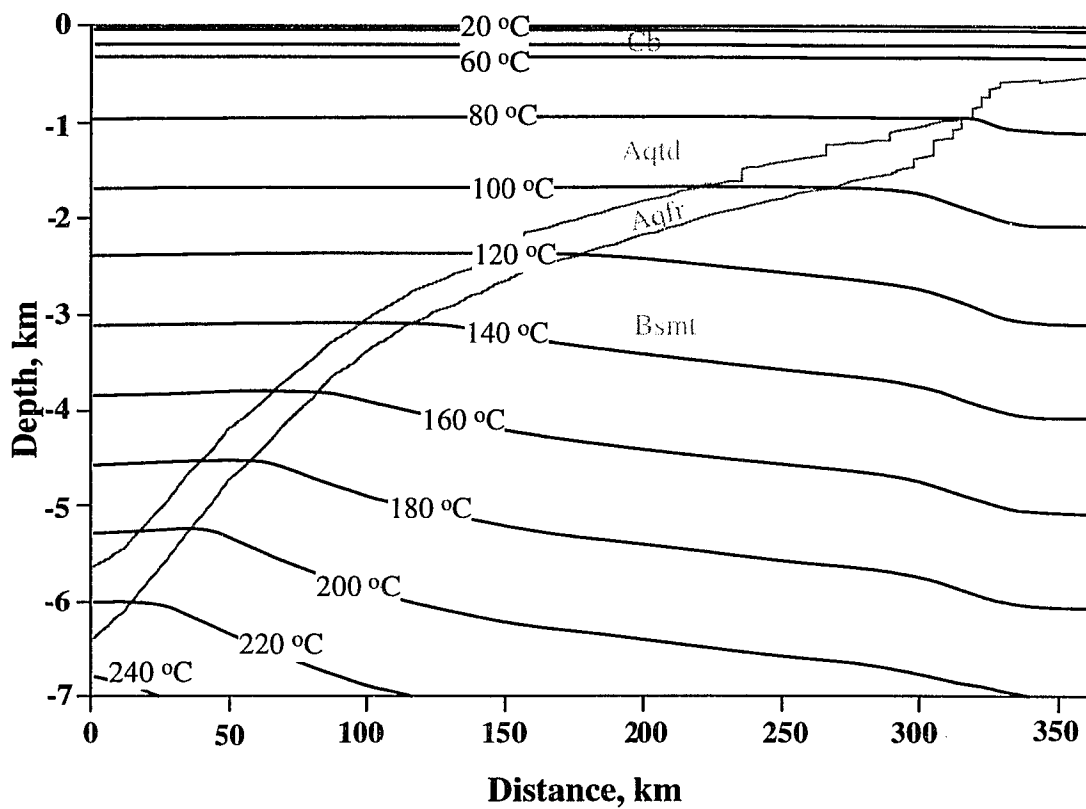
Figure 4.21. Initial temperature field of steady-state heat conduction in Case 5 (an uplifting foreland basin). The light lines outline the basement (Bsmt), aquifers (Aqfr, Units A and B), aquitards (Aqtd, Units C and D) and carbonaceous layer (Cb).
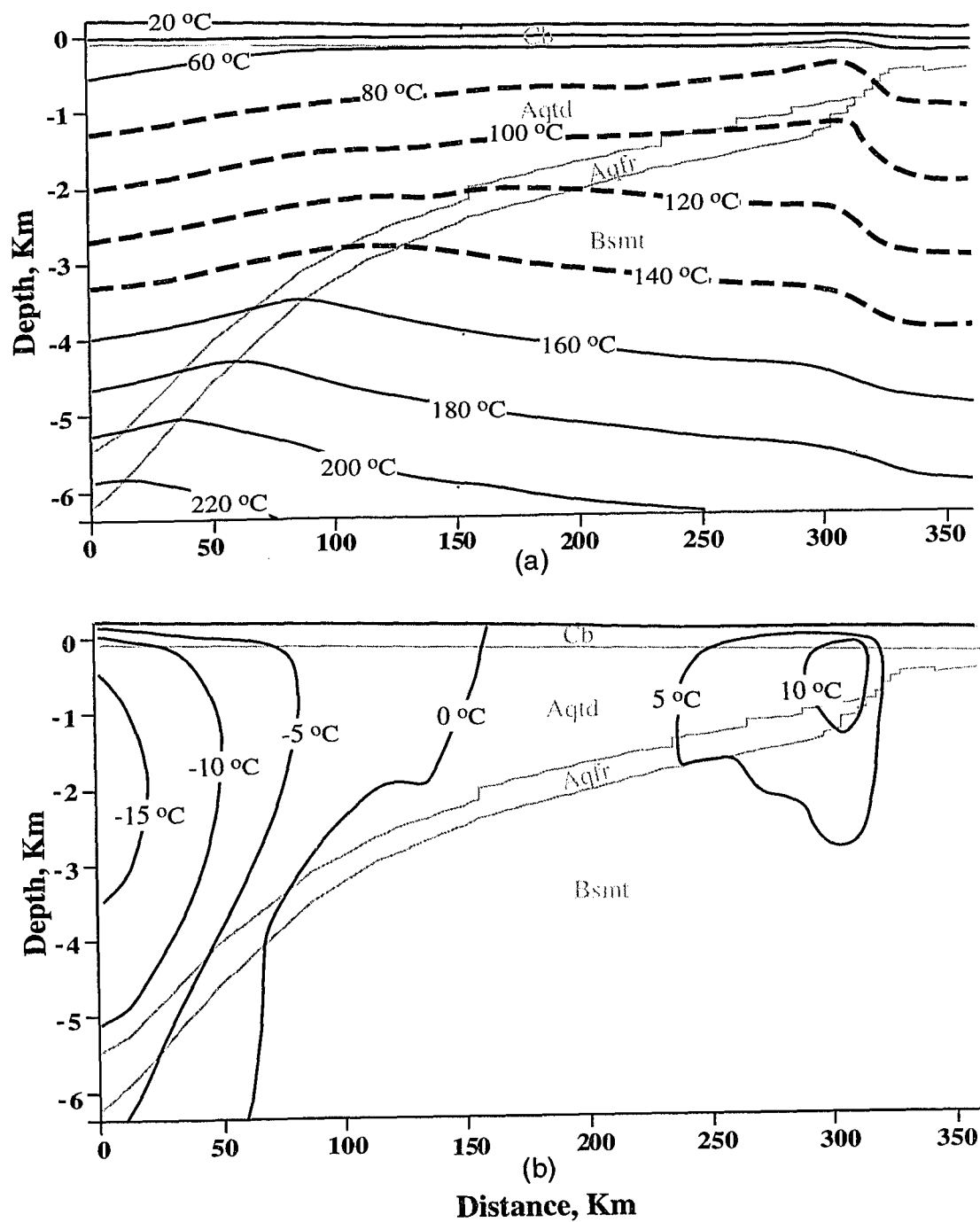
Figure 4.22. Temperature field (a) and residual temperature (b) (T-To) at 0.2 Ma in Case 5 (uplifting case). The heavy dashed contours represent the approximate temperature range inferred to have existed during the formation of MVT ore deposits. The light lines outline the basement (Bsmt), aquifers (Aqfr, Units A and B), aquitards (Aqtd, Units C and D) and carbonaceous layer (Cb).
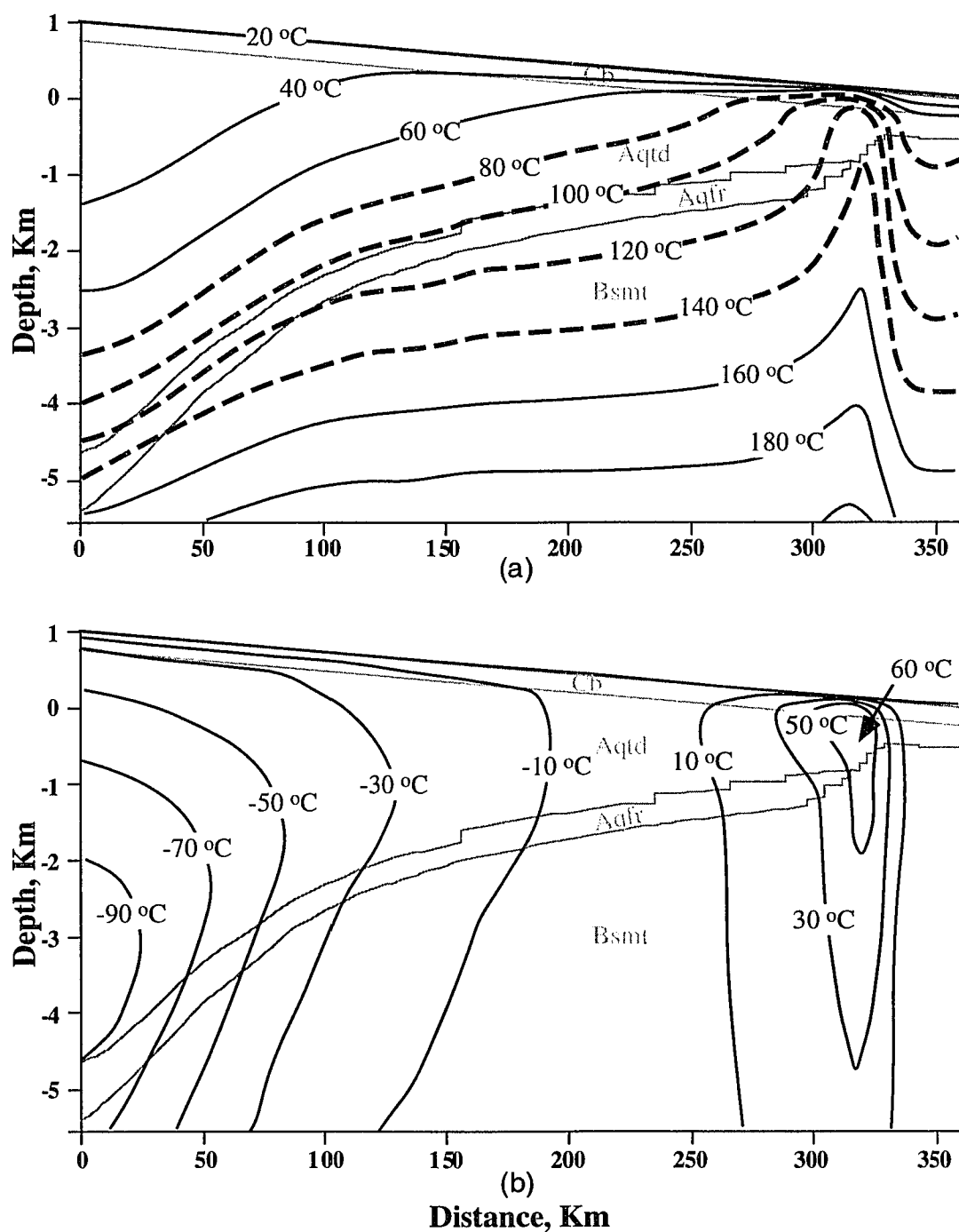
Figure 4.23. Temperature field (a) and residual temperature(b) (T-To) at 1.0 Ma in Case 5 (an uplifting foreland basin). The heavy dashed contours represent the approximate temperature range inferred to have existed during the formation of MVT ore deposits. The light lines outline the basement (Bsmt), aquifers (Aqfr, Units A and B), aquitards (Aqtd, Units C and D) and carbonaceous layer (Cb).

(and residual temperatures). On the other hand, temperatures in the shallow sediments in the discharge region, increased by only 10 °C at 0.2 Ma (80 °C in Case 1), but increased by more than 60 °C at 1.0 Ma. Maximum temperature in the discharge area for this case is a few degree warmer than in Case 1 during the first million years (also see Figure 4.12d), even though the maximum elevation of Case 5 at 1.0 m.y. is 1.0 km, less than that in Case 1 (1.2 km).

The phenomenon that shallow sediments in the discharge region of Case 5 have higher maximum temperature than that in Case 1, can be explained by slowly heating of the shallow sediments and the upper part of the basement by discharged fluids in Case 5, which allows the basement a longer time to store heat energy, in order to maintain constant heat flow at the model base. When the thermal pulse slowly passed through this region at about 1.0 m.y., the upper basement had already been warmed. Whereas in Case 1, high velocity fluid flow in the early stage (< 0.2 Ma) resulted in an earlier thermal pulse appearing in the discharge region, when the upper basement was not as warm as in Case 5 at 1.0 Ma.

High discharge velocities in the early stage of Case 1 also indicates that the system lost heat more quickly, compared to Case 5. However, after about 1.5 Ma, sediment temperatures in Case 5 were generally lower than those in Case 1 (temperature field not shown, but see Figure 4.18 for a comparison of surface heat flux), because after that the topographical gradient in Case 5 (> 1.5 km over 360 km) was significantly larger than that of Case 1 (1.2 km over 360 km).

Other phenomena observed in Case 1 are also found in Case 5, such as high thermal gradients in the top layer, low thermal gradient in the underlying sediments and a rightward shift of the left side of the upwarped isotherms (see 4.4.3.1 for explanations).

Surface heat flow in the discharge region of Case 5 was low in the early stage of modeling (Figure 4.19a), but increased to about 450 mW/m^2 (approximately the value in Case 1) at 1.0 Ma (Figure 4.19b). The increasing heat flow in the discharge area is

consistent with sediments warming by fluid flow. Average heat flow (Figure 4.19c) in Case 5 was also low in the early stage of modeling and became higher (about 7 mW/m^2) than Case 1 after a model time of 0.75 Ma, indicating that the uplifting model basin lost more heat in the later stage. After 1.2 Ma, average surface heat flow started to decrease, due to the cooling of the model basin.

With a partial cover of carbonaceous sediments on the right of the model basin, a gradually uplifting foreland basin also can cause a high temperature field, with its magnitude and pattern similar to that in Case 4, in the discharge area (not shown). The major difference is the phase of temperature variation, which is slower than Case 4. The comparison among the full coverage, half coverage, and no coverage of carbonaceous sediments in an uplifting foreland basin is very similar to that among Cases 0, 1 and 4.

4.5. DISCUSSION

Low thermal conductivity causes the carbonaceous section to have a high thermal gradient, which in turn elevates temperatures of the underlying sediments and basement rocks, even for basal heat flow at about the continental average (60 mW/m^2). Thus, thermal insulation can initially cause high storage of thermal energy in the model basin. For example, with a typical thermal conductivity of 0.4 W/m-K, thermal insulation by a 300 m thick carbonaceous section can cause a temperature increase of about 35 °C in the underlying sediments and the basement rocks. High heat storage requires millions of years for the basin to retain heat. However, according to the observed and model maximum burial (>1400 m) of Pennsylvanian coals that are now near the surface in the study area (Beaumont et al., 1987), the sedimentation of the Pennsylvanian sediments lasted several tens of million years in the study area. This would allow the basin to warm before it was uplifted. Thus, the initial thermal condition used in this study (steady state without fluid flow) is geologically reasonable. Elevated temperatures persist for as long as the carbonaceous layer resides on top of the basin.

Higher average temperature in the model basin significantly decreases fluid viscosity, and greatly increase the fluid flow velocity. According to Kestin et al. (1981), temperature is the most important factor controlling fluid viscosity. Based on my calculation and those by Kestin et al. (1981) using the empirical equations developed by Kestin et al. (1981), an increase of 35 °C can cause at least a 45 % decrease in fluid viscosity at temperatures between 20 and 55 °C, and about a 30 % decrease between 90 and 120 °C. These results indicate that the viscosity difference can result in a Darcy velocity difference as high as 2.5 m/yr. in the early stage of modeling (< 0.2 Ma). Thus, heat can be more efficiently transported, if there is a thermal insulation by low thermal conductivity sediments.

High fluid flow along the basal aquifers driven by topographic differences in an uplifted foreland basin, is a powerful means for developing high temperatures at shallow depths in the discharge region. Even without a carbonaceous layer (Case 0), fluid flow still causes a temperature increase of about 30 °C in the shallow sediments (Figure 4.12d). With a carbonaceous layer, shallow sediments in the discharge area can increase by 70 °C (Case 1, Figure 4.10b).

Carbonaceous sediments also can trap heat transport by fluid flow. This is indicated by a thermal gradient in the carbonaceous layer in the discharge area up to 0.34 °C/m in Case 1, about 2.5 times the initial thermal gradient. However, thermal insulation does not produce large thermal gradient in underlying sediments. For example, most sediments in the discharge area in Case 1 at 0.2 Ma, have a thermal gradient less than 10 °C/km. According to Rowan and Leach (1989), the minor amount of silica in the Viburnum Trend indicates that cooling was not a primary cause of sulfide precipitation. Fluids whose primary aquifer was the Lamotte Sandstone, predominantly a quartz arenite, should have been in equilibrium with quartz. Quartz in the Viburnum Trend occurs as a minor, drusy, vug-lining phase, but the district lacks the intense silicification found in other MVT ore districts such as Tri-State (Rowan and Leach, 1989). Quartz

solubility is strongly temperature dependent and, under equilibrium conditions, a decrease of 10 °C or more should have precipitated at least as many moles of silica as galena (assuming a galena solubility of between 1 and 10 ppm) (Rowan and Leach, 1989). Clearly this is not the case, as galena is far more abundant than quartz in the Viburnum Trend (Rowan and Leach, 1989). Thus, temperature results in this study are consistent with inference drawn by Rowan and Leach (1989). Based on the temperature variations in the discharge area of Cases 1, 2 and 3, relatively low thermal conductivity and high permeability are required for a carbonaceous layer to generate the low thermal gradient seen in the underlying sediments. The higher permeability of the carbonaceous rocks can increase heat transport, and thus, causes higher temperatures at shallow depths in the discharge area (Figure 4.12d).

Thermal insulation of the carbonaceous layer greatly increases heat storage in basement rocks, which have a volume much larger than overlying sediments. This heat storage can continuously replace heat lost to the surface during discharge of hot fluids. For example, in Case 4 which is partially covered by a carbonaceous layer on the right, thermal insulation and heat supplied from the basement rocks can cause temperatures in the discharge area to be higher than that in the deep sediments.

The observed transient thermal pulse at shallow depths is also attributable to the location of the high permeable aquifers, which lie immediately above the basement rocks and connect the discharge area with the deep sediments in the recharge area. This allows the heat from the deep, high temperature sediments to be transported more efficiently to the discharge area.

Fluid flow within the model basin has a greater effect on the lower thermal boundary when thermal insulation is included. If the base of the model is not sufficient deep, rapid variation of the temperature field in the basin sediments can deviate basal heat flow from the assumed boundary condition and cause significant errors in the temperature field of the entire model. It is noted, through this study, that the model

base must be set deeper than 15 km so that the off-set of the basal heat flow is under 1% of the assumed value.

The major limitation in this study is the unavailability of the paleostratigraphic information in the Ozark Dome area, because of the erosion since the Early Mesozoic. It would be nice if we can reconstruct the distributions of carbonaceous sediments formed during the Carboniferous period in the study area. The reconstruction may become possible through studying the stratigraphy and basin history in the surrounding sedimentary basins, such Arkoma, Illinois, and Black Warrior, where the Carboniferous sediments preserved.

4.6. CONCLUSIONS

Low thermal conductivity of a carbonaceous layer, which covers or partially covers an uplifted foreland basin may thermally insulate underlying sediments. Thermal insulation causes a sharp thermal gradient in the carbonaceous section, which in turn elevates temperatures of the underlying sediments and basement rocks basin-wide.

Elevated temperatures and resultant high velocities of regional groundwater flow (Darcy velocity more than 6.0 m/yr.) along basal aquifers driven by topography gradient can result in high temperatures (~140 °C) in the shallow discharge region (<1.0 km), even with a typical continent basal heat flow of 60 mW/m^2. Partial coverage of carbonaceous sediments limited to the discharge areas also results in high temperatures of more than 120 °C in the shallow discharge region. A low thermal gradient (less than 10 °C/km) in the shallow discharge area predicted by the thermal insulation simulation is consistent with results from fluid inclusion studies by Rowan and Leach (1989).

The presence of a transient thermal pulse in the discharge areas is primarily dependent on the thermal conductivity and permeability of the carbonaceous layer. Low thermal conductivity or high permeability of the carbonaceous section results in a large thermal pulse, because fluid flow rates and thermal energy storage are high. Thus the thermal pulse is thermally buffered by basement rocks, as it moves through the basal

aquifers. High thermal conductivity or lower permeability of the carbonaceous section, however, decreases groundwater flow and gives basement rocks more time to interact with the groundwater. Thus, only a small thermal pulse reaches the discharge area.

Thermal conductivity and permeability of the carbonaceous layer also have important effects on the surface heat flow. Lower conductivity and higher permeability increase surface heat flow in the discharge region, but cause lower surface heat flow in the recharge area. Vertical permeability of the carbonaceous layer is sensitive to surface heat flow in the discharge region. For example, a 10 fold decrease in vertical permeability in the carbonaceous layer can cause surface heat flow to drop 200 mW/m^2, and becomes much lower than the case without a carbonaceous cover.

Fluid velocities in a gradually uplifting foreland basin increase with time. Sediment temperatures in such basin vary more slowly with time, compared to the instantaneous uplifting case. An uplifting basin initially loses heat slowly. Slow heating of the shallow sediments in the discharge region allows the upper basement to become warmer when the thermal pulse passes through the region. Thus, shallow sediments in the discharge area can have a maximum temperature about 5 $^\circ$C higher than that in the instantaneous uplift case.

CHAPTER 5
EXPULSION OF GEOPRESSURED FLUIDS AND THE INDUCED THERMOHALINE CONVECTION IN SALT BASINS

5.1. INTRODUCTION

Groundwaters with overpressured pore fluids are common in many sedimentary basins. Hunt (1990) reported that the shallowest hydrogeological zone in many overpressured basins is at normal hydrostatic pressure and frequently extends down to about 10,000 ft (3048 m). Below this, the deeper systems are overpressured (geopressured). The hydropressured and geopressured zones are separated by a pressure transition zone where permeability is low and fluid pressure rapidly increases with depth. The formation and properties of the pressure transition zone is the subject of debate. The overpressured systems are not in hydraulic communication with the overlying hydropressured system, unless the low permeability transition zone is broken, followed by upward vertical migration of geopressured fluids (Hunt, 1990).

In a salt basin such as the Gulf of Mexico basin, deep overpressured pore fluids can have salinities significantly lower than pore fluids in the overlying hydropressured sediments. Hanor et al. (1986) found, through studying electric logs from deep oilfield boreholes in south Louisiana, that salinity increases with depth to a maximum of about 150 g/L between 1 and 3.5 km depth (Figure 5.1). Below this zone of high salinity water, salinity decreases with depth to values less than 50 g/L. This salinity profile occurs across the entire 320 km width of south Louisiana. Hanor et al. (1986) attributed the high salinity zone to the dissolution of NaCl from numerous salt domes. The deeper low salinity, overpressured zone is dominantly shaly. This salinity and pressure distribution is consistent with that reported by Hunt (1990) for many other overpressured basins. However, this salinity inversion does not exist in some interior basins, such as Alberta, Illinois, and Michigan basins (Hanor, 1979). In eastern Texas, overpressured fluids appear to be saline (Hanor, personal communication).

101
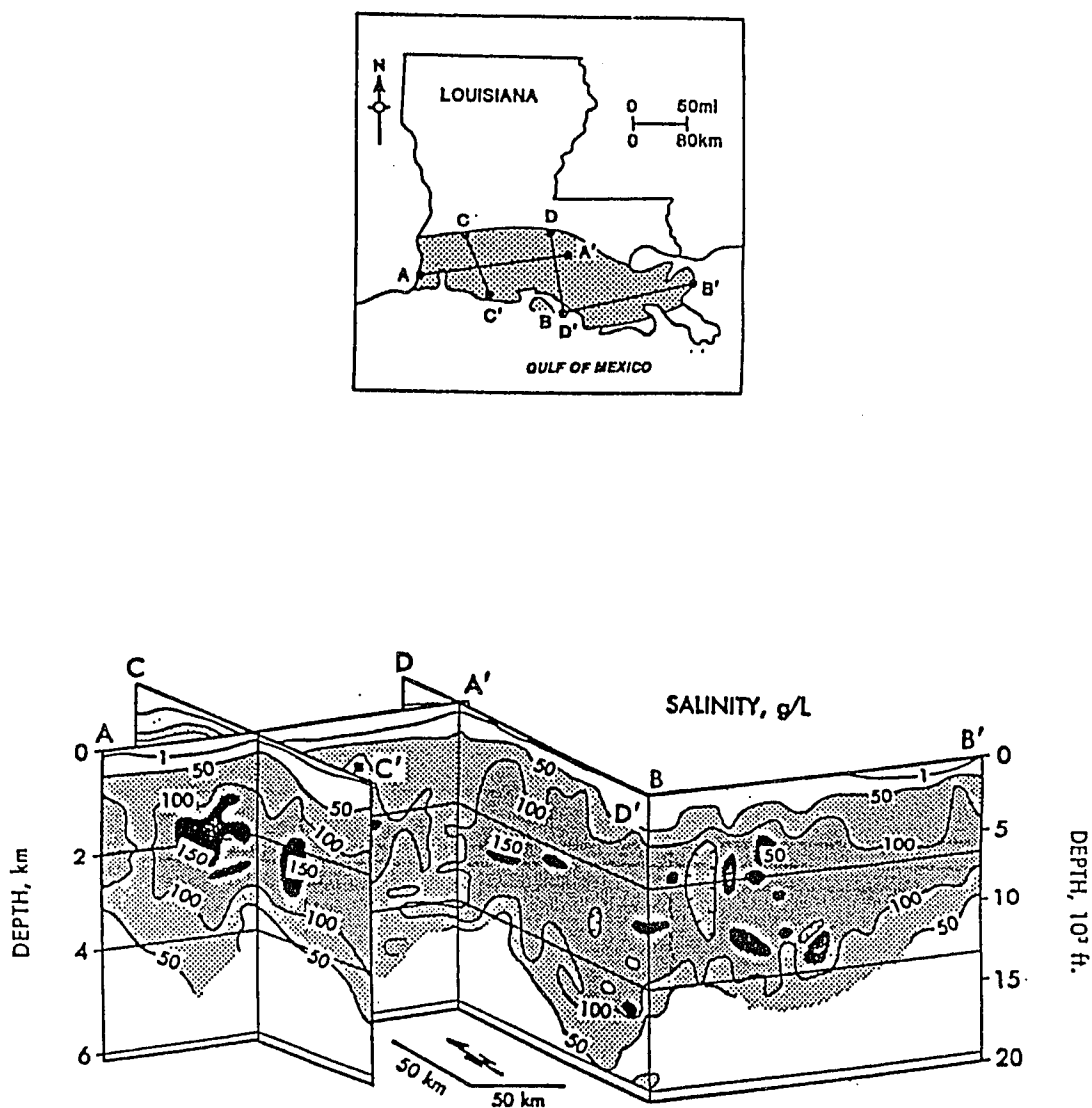
Figure 5.1. Fence diagram showing pore water salinity distribution in South Louisiana salt basin (Hanor, et al., 1986)

When fluid pressure below a seal exceeds the strength of the rock matrix, fractures may form and geopressured fluids are expelled into the overlying sediments. This will cause a pressure drop which leads to the close of the seal by collapse of the fractures or by precipitation of mineral cements. Episodic expulsion of geopressured fluids was first proposed by Cathles and Smith (1983). Hunt (1990) suggested that this episodic process probably occurs over intervals of thousands of years.

There is a variety of evidence for the upward flow of fluids along faults or permeable conduits. For example, Hanor and Sassen (1990) found similarities in carbon isotopic composition of the crude oils between the Lower and Upper Tertiary formations in south Louisiana Gulf Coast. Workman and Hanor (1985) reported that up-welling of volatile fatty acids and $\delta^{18}O$ distributions were consistent with the large-scale vertical mixing of fluids in Iberia Salt Dome in south central Louisiana. Bennett and Hanor (1987) described the perched brine plumes above Welsh Dome in Louisiana. Elevated temperature and pressure conditions also exist in the Gulf of Mexico basin (Cipriani et al., 1994; Cassidy and Ranganathan, 1992). One possible explanation of the above observations is the expulsion of deep hot geopressured fluids into the overlying sediments.

Hanor and Sassen (1990) indicated that in south Louisiana the 2 to 3 km-thick, sand-rich hydropressured zone overlying the geopressured sediments is far more dynamic hydrologically than previously recognized. The dewatering of geopressured sediments into the overlain hydropressured sediments can cause temperature, fluid pressure and salinity anomalies. Furthermore, salt dissolution in the sand-rich hydropressured zone results in high salinity pore fluids of shallow depth which produce pore fluid density inversions sufficient in magnitude to drive large-scale vertical and lateral flow (Hanor, 1987; Hanor and Sassen, 1990), even without the effects of excess fluid pressures.

Because observational data alone can only provide qualitative explanations for driving mechanisms for upward flow of pore fluids, numerical models have been developed to give quantitative answers. Evans and Nunn (1989) modeled the fully coupled effects of heat and solute transport in free thermohaline convection near salt domes. They found that fluid buoyancy can not drive fluids upward along the flank of salt dome, unless the thermal conductivity ratio of salt to sediments is high and buoyancy ratio, the relative effects of concentration and temperature on controlling groundwater density is low, both of which require the porosity of the surrounding sediments to be high (>50%). Evans et al. (1991) further showed that upward ground water flow can occur when the regional background salinity is greater than 15 weight percent and preferential salt dissolution occurs around the top of salt domes. These conditions are typical of many areas in the south Louisiana salt dome province. Ranganathan and Hanor (1988 and 1989) showed by numerical simulation that geopressured waters bleeding upward into the hydropressured zone may affect brine formation in the hydropressured zone, provided the permeability of the geopressured zone is sufficiently high. Roberts and Nunn (1995) proposed from their 1-D modeling studies that compaction of sediments in a seal can close any fractures within a 100 years after they formed. Because geopressured sediments have low permeabilities, it requires 10,000 to 50,000 years for geopressured sediments to develop sufficient high fluid pressures to hydrofracture another episode of fluid expulsion (Roberts and Nunn, 1995).

Qualitative and quantitative studies provide us with some fundamental understanding of the mechanisms driving groundwater flow in salt basins. However, these studies raise further questions such as how much fluid can be expelled from geopressured sediments into overlying hydropressured sediments during a single episode of dewatering, and whether a perched brine plumes above a salt dome can be formed in such a short period of time as proposed by Roberts and Nunn (1995).

Furthermore, It is necessary to understand the long term consequences caused by injection of hot and less saline waters in the hydropressured zone.

In this chapter, I present results from a mathematical model which simulates the expulsion of hot and low salinity fluids from a deep geopressured section, through a permeable fault, into a high salinity hydrostatic section. AKCESS.BASIN, which is a finite element numerical package, is used to couple heat, solute and fluid mass transport. This package allows us to use pore water salinity and temperature as tracers to monitor the migration of geopressured fluid, so that the amount and location of the expelled fluids can be determined during venting. I also describe the long term consequences of short term expulsion of geopressured fluids caused by subsequent thermohaline convection.

5.2. GEOLOGICAL MODEL

There are two major hypotheses for the development of geopressured sediments. One is compaction disequilibrium (e.g. Dickinson, 1953; Bredehoeft and Hanshaw, 1968; Bethke, 1985; Harrison and Summa, 1991) and the other is pressure compartment (Hunt, 1990; Powley, 1990). Some other mechanisms such as dehydration of clay minerals (e.g. Powers, 1967; Bethke, 1986), have also been proposed. The compaction disequilibrium hypothesis holds that the most common cause for overpressuring is rapid accumulation of low permeability sediments, which prevents the escape of enough interstitial fluid to maintain hydrostatic pressure. Bethke (1985, 1988) has shown that development of compaction disequilibrium leading to permanent overpressuring is unlikely to occur unless the sedimentation rate is in excess of 100 m/Ma. This hypothesis best explains those sedimentary basins with clastic sequences and rapid sedimentation rates, such as the northern Gulf of Mexico basin. However, there are several overpressured basins with lower sedimentation rates. This led Hunt (1990) and Powley (1990) to propose the pressured compartment hypothesis which emphasizes that the major causes of overpressuring in many basins are the thermal expansion of pore

fluid and the generation of oil and gas. The pressure compartment hypothesis requires a stratigraphically high layer (or layers) of very low permeability sediments (seal) to prevent excessive fluid from moving upward towards the surface. Examples of these basins are West Siberia rift basin, Williston interior cratonic basin and Uinta lacustrian basin (Hunt, 1990).

Even though these hypotheses are antithetical, it is commonly recognized that over pressures and sharp pressure gradients (e.g. Weedman et al., 1992; Hart et al., 1995) in the transitional zone require that the sediments are either extremely low in permeability or must be capped by permeability barriers (pressure seals) such as shales, tight sandstones, carbonates, and/or evaporites (Weedman et al., 1992). The seals do not necessarily have a unique lithology and they may not conform to conventional geological age, lithology, facies, or structure (Hunt, 1990). What does the seal really consist of is still poorly understood, even though there are several theories regarding the nature of such a seal (Roberts and Nunn, 1995). In the Gulf Coast basin, where shales comprise 85% of the sediments (Bethke, 1986), shales are the most common pressure seals in subsurface (Weedman, et al., 1992), if they are well compacted. Diagenetic reactions that fill open pore spaces, such as the illite-smectite transformation (Bruce, 1984; Freed and Peacor, 1989), or the collapse of secondary porosity after dissolution of grain-supporting cements (Weedman et al., 1992) may decrease the permeability sufficiently to allow overpressures to develop. Alternatively, a seal may form when an immobile gas phase is present in pores, or a shale membrane prevents the passage of saline fluid (Fowler, 1970). The seal will fracture or a fault will form when fluid pressure exceeds the strength of the rock.

The objective of this chapter is to understand the physical processes of the expulsion of warm and low salinity geopressured fluids into the overlying saline hydropressured sediments and its long term consequence on the groundwater system in a salt basin. The geological model used is shown on Figure 5.2. In this model, I do not consider

sedimentation, compaction and mechanisms for overpressure development. I also ignore complicated variations in lithology and physical properties in the fault, sediments and seal. Instead, to emphasize the consequence of the dewatering of geopressured sediments, a seal is considered as a very low permeability layer with thickness of a few tens of meters, as suggested by Weedman et al. (1992) for the rapid vertical transition in fluid pressure in the Tertiary section of Moore-Sams and Morganza fields in Louisiana. The width of the fault or fracture may vary in response to the fluid pressure. To simplify the model, the width of the fault is constant during venting. Additionally, the salinity and pressure distributions in the model are initialized to those observed by Hanor et al. (1986) in the south Louisiana salt basin.

The calculation domain of the model is 30 km by 10 km. The upper section of the model is 3 km thick and initially hydropressured and fluids have a salinity of 15 wt%. The lower section is overpressured with an excess pressure of 24 MPa and a salinity of 0 wt%. The difference in salinity between the two sections represents the maximum difference observed in the Gulf of Mexico salt basin. A thin (50 m) pressure transition zone of very low permeability sediments (10^{-9} mD), which is henceforth referred to as the seal, is located between the hydropressured and geopressured sections. A high permeability fault (25 m wide, 2.5 km high) breaking the seal and connecting the two sections (Figure 5.2). In this study, I present two cases, 1) homogenous and isotropic medium in both hydropressured and overpressured sections; 2) homogenous but anisotropic medium in both sections. Table 5.1 lists physical properties of sediments in Case 1. Sediments in Case 2 have the same properties as Case 1, except that the vertical permeabilities are 10 times smaller.

It may seem controversial to use 0.1 mD for the permeability of overpressured sediments, because overpressured sediments often contain thick shales (e.g. Hanor et al., 1986). However, during expulsion of geopressured fluids, numerous interconnected fractures may be generated. Fractures ranging in width from a few microns to several
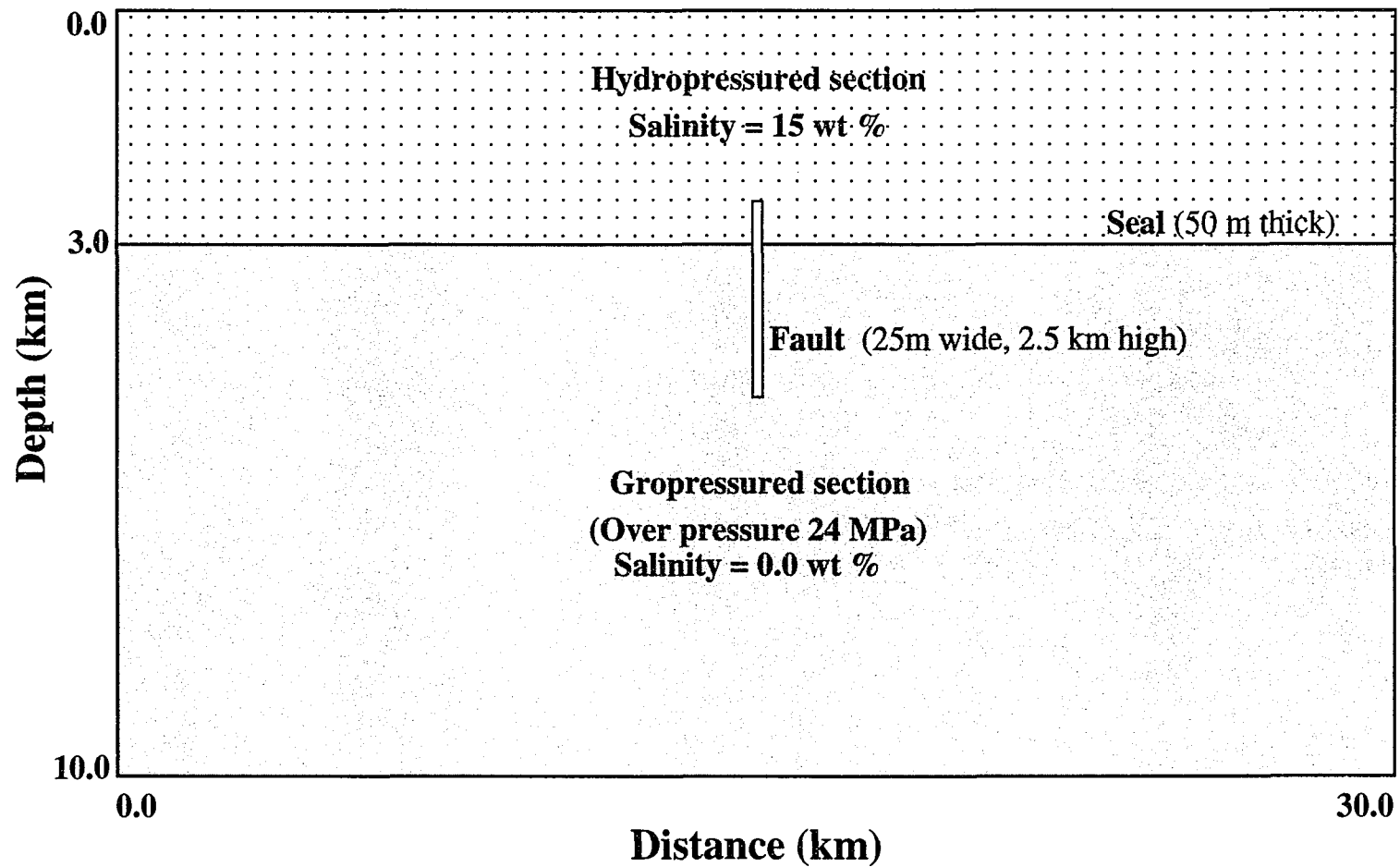
Figure 5.2. Geological model. Fluid pressure and salinity distributions in this model are idealized analogies to those in South Louisiana salt basin (Hanor et al., 1985). See Table 5.1 for the detail of rock properties. Note the fault width is exaggerated about 1000 % horizontally compared to the horizontal domain.

TABLE 5.1. Physical properties of the isotropic model (Case 1)

	Permeability (mDarcy)		Porosity	Thermal conductivity (W/m-K)	Diffusion coefficient (10^{-6} cm²/s)
	Kx	Ky			
Hydropressured section	1.0	1.0	0.25	0.66	0.6
Overpressured section	0.1	0.1	0.2	0.66	0.4
Seal	10^{-9}	10^{-9}	0.0	0.66	0.0
Fault	5.0	10.0	0.2	0.66	0.4

millimeters have been observed in cored rocks in the internal volumes of overpressured

fluid compartments (Hunt, 1990). Pore pressure increases caused by the generation of

oil and gas and the thermal expansion of water could locally induce fractures in pores of

low permeability rocks (e.g. Snarskii, 1964 and 1970). Several authors cited by

Gretener and Feng (1985) have discussed the formation of vertical fractures in

overpressured zones. The choice of 0.1 mD permeability for the geopressured

sediments is also consistent with the range of measured permeabilities for the

geopressured sediments in the Mississippi Fan, 1.0 mD to 10^{-5} m (Bryant et al., 1985)

and the calculations of Bredehoeft and Hanshaw (1968), Magara (1971) and Bethke

(1986). A permeability of 1.0 mD for the hydropressured sediments is consistent with

the permeability used by Ranganathan and Hanor (1989) in the sediments surrounding

West Hackberry Dome, Louisiana.

For both models, I assume fixed temperatures (Dirichlet boundary condition) at the

top and base of the domain, with $T_{top} = 20$ °C and $T_{base} = 220$ °C. There is no lateral

fluid or solute transport at the sides of the domain. In order to emphasize the effect of

the injection of low salinity fluids into the high salinity brine, it is assumed that there is

no vertical flux of fluid at the model top and base.

The following simulations are transient cases. Governing equations used in this study are Eqs (15), (23), (24), (25) and (26) in Chapter 2. Fluid density and viscosity are calculated using Eqs (27) and (28) in Chapter 2, respectively. In order to ensure the accuracy of the simulations, sensitivity tests were conducted to determine suitable grid size and time step for this study. The method for determining the grid size and time step is described in Chapter 2. In the venting case, the average grid size in the area close to the venting fault was set to be 25m x 30m. Time step was 0.1 year in the very early stage of simulation. It was gradually increased to 20 years at 100 years of modeling time and then remained constant. In the post-venting case, the grid size was 30m x 30m. The time step was 0.1 year at the very beginning of simulation and gradually increased to 40 years for the simulation later than 1000 years. Section 5.3.2.4 also discusses the effect caused by the change in grid size and time step in the post-venting isotopic model.

5.3. RESULTS

5.3.1. Venting of geopressured fluids along the fault

5.3.1.1. Fluid pressure variations

According to du Rouchet (1981), hydrofracture occurs when pore fluid pressure reaches 70-90% of lithostatic pressure. In this model, the fluid pressure immediate below the seal (3 km) is initially set to 54 MPa, which is about 78 percent of lithostatic pressure, because the bulk density of sediments is assumed to be 2300 kg/m^3. The value means that the overpressure is 24 MPa, which initially occurs everywhere in the geopressured section.

With the opening of the fault and release of fluids from the overpressured sediments, rapid transport of fluid causes pressures within the high permeable fault zone to depress faster than in the surrounding sediments. The pressure gradient (Figure 5.3) drives fluids toward the fault where are channelized and migrate upward into the hydropressured section. In the hydropressured zone the fluids spread out laterally.
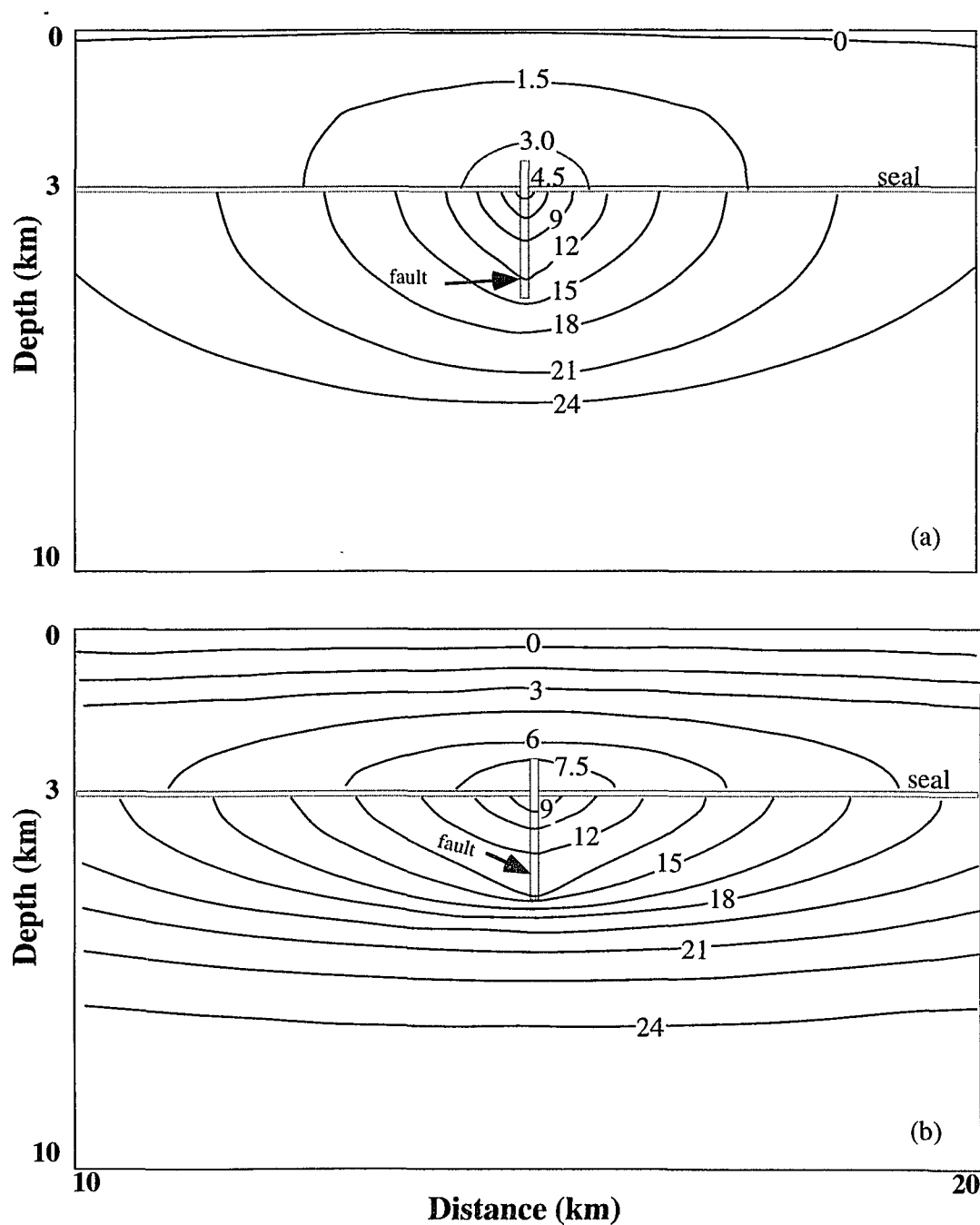
Figure 5.3. Distribution of excess fluid pressure after 680 years of venting in the homgeneous and isotropic model (a) and in the homogeneous and anisotropic model (b). All contour values are in MPa. Note that only the central 10 km of the 30 km wide model is shown and the fault is horizontally exaggerated about 400 % compared to the horizontal domain.

Fluid pressure decreased rapidly in the geopressured sediments around the fault from the initial value of 24 MPa to a value of 6.2 MPa at an elapsed time of 100 years in the isotropic model (Figure 5.4b). After 100 years of expulsion, the pressure decreases very slowly, with a drop of about 1.5 MPa over a period of about 500 years (Figure 5.4b). In the anisotropic model, because the vertical permeability is lower, fluid is more difficult to transport upward. At an elapsed time of less than 100 years, fluid pressure only decreases to about 10 MPa. After 100 years, the decrease rate in fluid pressure is much slower than the isotropic case (Figure 5.4b).

In sediments around the fault in the hydropressured section, fluid pressure quickly increases to a maximum value of 8 MPa in the isotropic model and about 10 MPa in the anisotropic model within the first several years of modeling time (Figure 5.4a). Afterward the pressure in both models starts to decrease. Thus, sediments in the hydropressured section were subjected to a transient pressure pulse in the early stage of modeling. The decrease in fluid pressure in the hydropressured section is related to the decreased fluid transport. Again, the lower vertical permeability of sediments has caused the pressure in the hydropressured zone to decrease more slowly in the anisotropic case. The major difference in pressure distribution (Figures 5.3a and 5.3b) between these two cases is caused by the preferentially horizontal diffusion of fluid pressure in the horizontal direction in the anisotropic case.

Closure of the fault occurs at fluid pressures of about 60% of lithostatic rather than at hydrostatic pressures (43% of lithostatic) (Hunt, 1990). In the isotropic model, fluid pressure at the venting seal dropped to about 57% of the lithostatic pressure 100 years after the opening of the seal (Figure 5.4). In the anisotropic case, because fluid pressure decreases more slowly than in the isotropic case, it takes more than 700 years for the fluid pressure to drop to 60% of the lithostatic pressure. This indicates that the critical fluid pressure for fault closure is strongly dependent on the permeabilities of sediments and the fault under the given hydrogeological conditions. Although more studies are
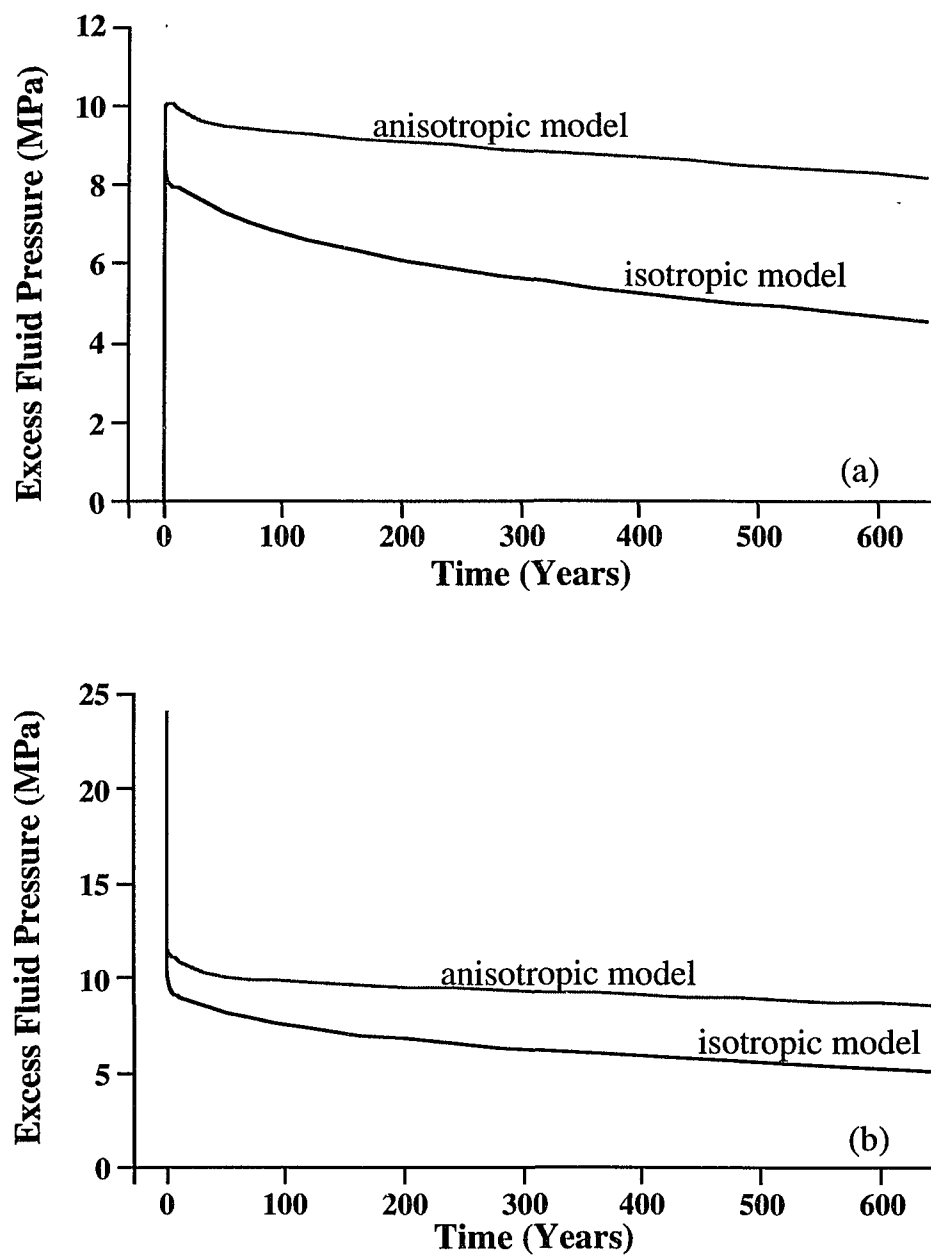
Figure 5.4. Excess fluid pressure variation with time in the sediments immediately above (a) and below (b) the vent.

needed to determine the general relationship between a specific hydrogeological setting and fault closure fluid pressure, the current study suggests that the duration of a single episode of expulsion of geopressured fluids under the conditions of this simulation may be on the order of several hundred years, which is consistent with Hunt (1990), but longer than Roberts and Nunn (1995).

5.3.1.2. Fluid migration along the fault

With the opening of the fault, the large pressure gradient drives fluids up the fault into the overlying hydropressured section (Figures 5.5a and 5.5b). Figure 5.6 shows the variation of vertical Darcy velocity with time at the vent. In the first several years after the opening of the fault, the vertical Darcy velocity is greater than 30 m/yr. in the isotropic model and is about 20 m/yr. in the anisotropic model. Then in the isotropic model, vertical Darcy velocity rapidly decreased to between 7 and 10 m/yr., which last for hundreds of years. In the anisotropic model, Darcy velocity decreased to 5 m/yr. at 100 years. Then the velocity decreased more slowly than in the isotropic model (see Figure 5.6). These results are consistent with decreasing fluid pressures in both cases (Figures 5.4a and 5.4b).

Compared to pressure and temperature, salinity is the best hydrological tracer, because solute diffuses very slowly through porous medium. Hence it is used to monitor the migration of geopressured fluids in the models. Figure 5.5a and Figure 5.5b show the fluid velocity arrows and the precise locations of the hot and low saline plume at the time of 660 years for both cases, respectively. Basically, fluids in the geopressured sediments were flowed toward the fault zone, then were focused upward along the fault zone into the hydropressured section, where they spread out in all directions. Anisotropic permeability of the sediments has resulted in a preferential movement of fluids in the horizontal direction. Thus, the shape of the expelled plume of geopressured fluid is quite different between these two models.
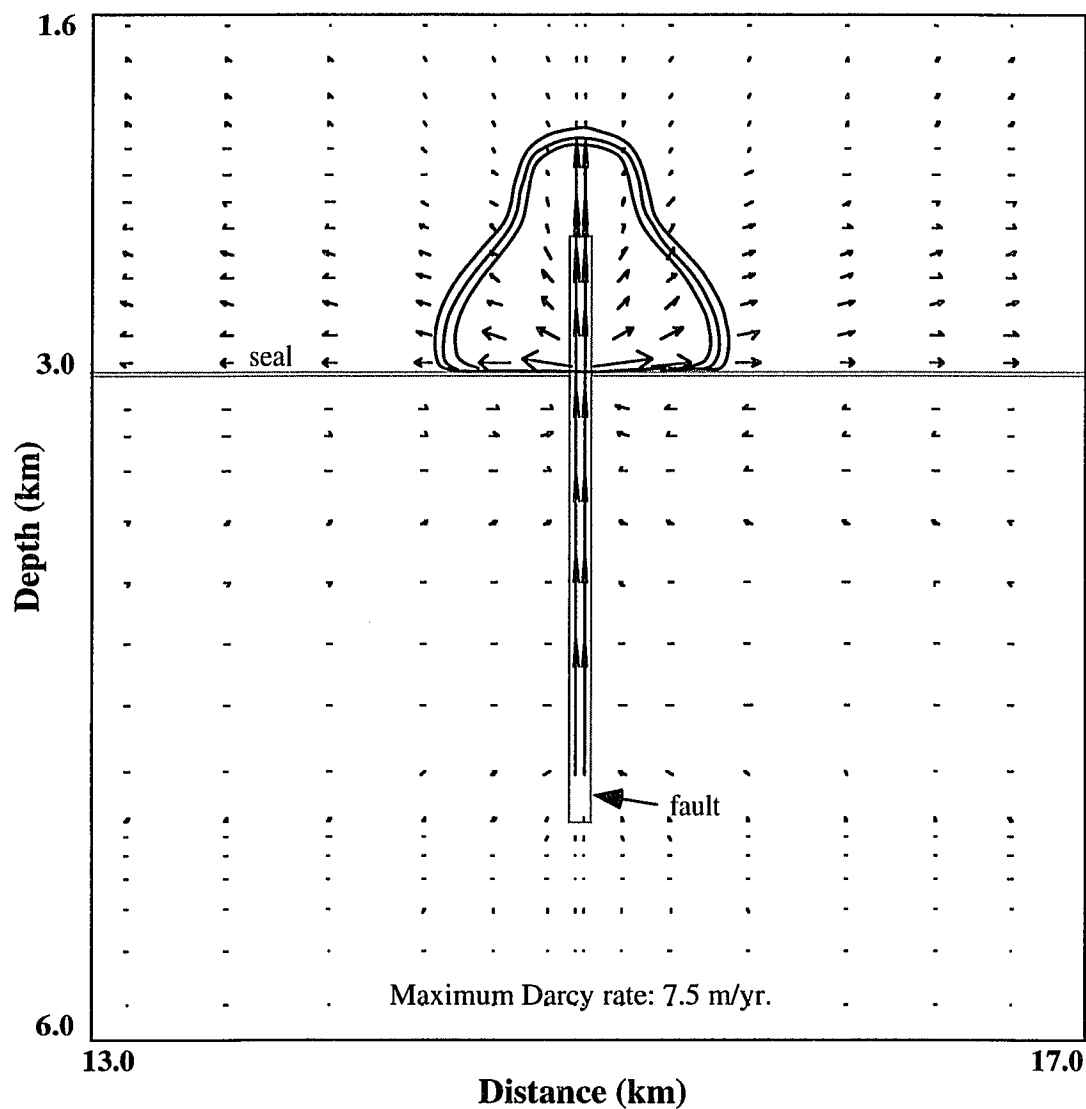
Figure 5.5a. Salinity distribution and flow pattern at 680 years after the fault opens in the homogeneous and isotropic model. The value of the outer contour is 15.0 wt%, the middle is 0.75 wt% and the inner is 0.0 wt%. Note only the central 4 km of the 30 km wide model is shown and the fault has been exaggerated about 400 % horizontally.
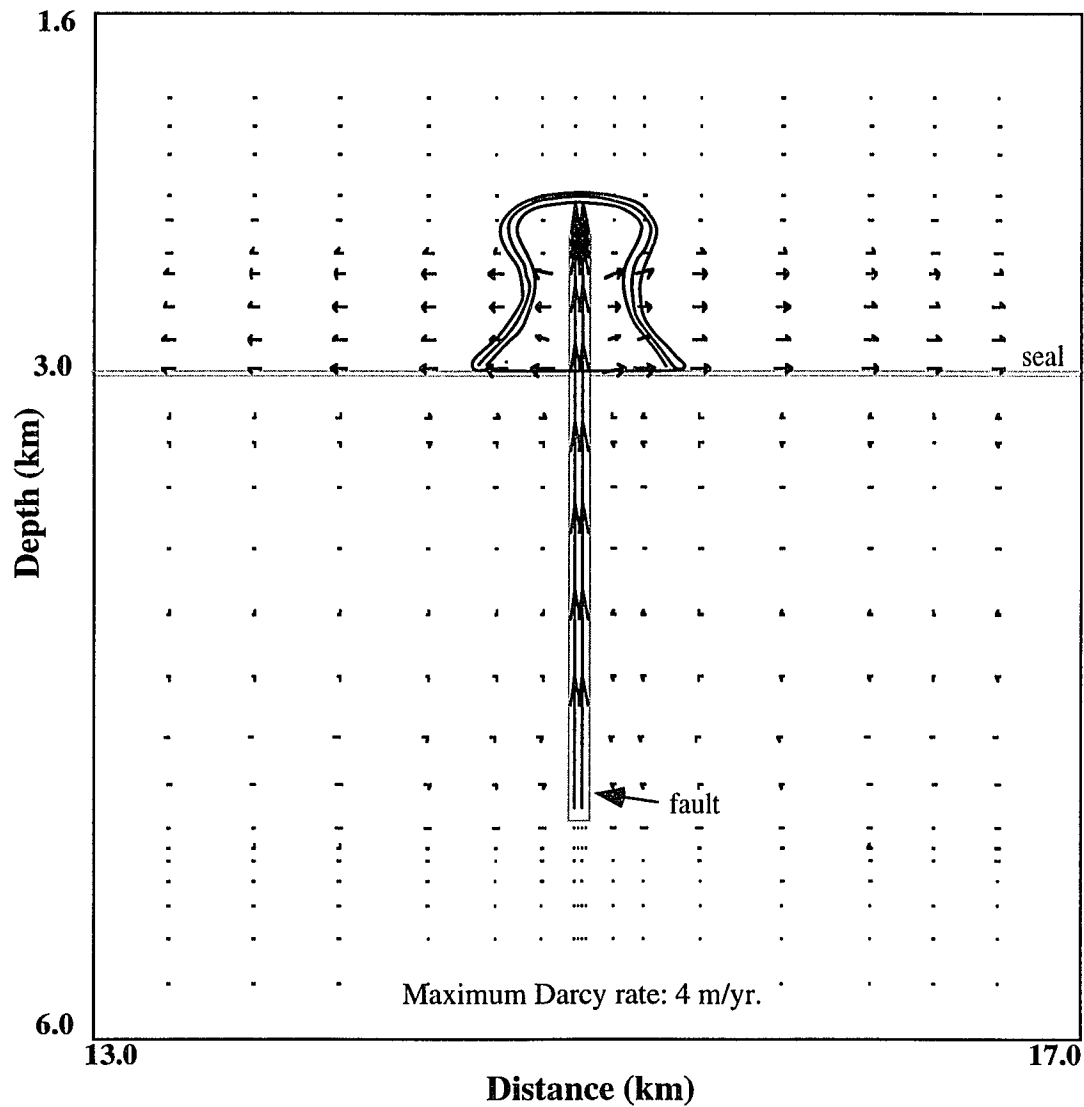
Figure 5.5b. Salinity distribution and flow pattern at 680 years after the fault opens in the homogeneous and anisotropic model. The value of the outer contour is 15.0 wt%, the middle is 0.75 wt% and the inner is 0.0 wt%. Note only the central 4 km of the 30 km wide model is shown, and the fault has been exaggerated about 400 % horizontally.
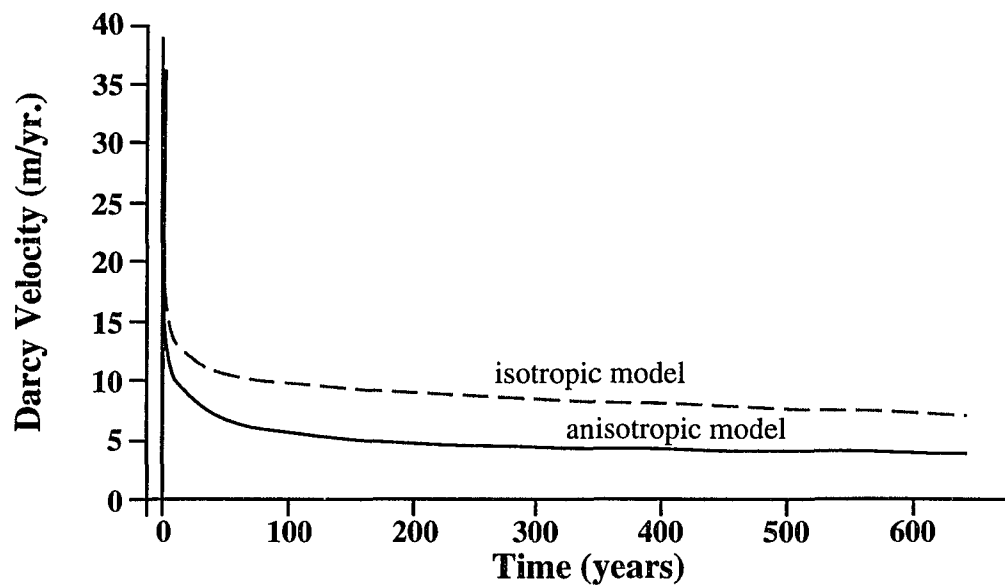
Figure 5.6. Maximum Darcy velocity vs. time after the fault opens at the fault-seal intersection in the homogeneous and isotropic model and in the homogeneous and anisotropic model.
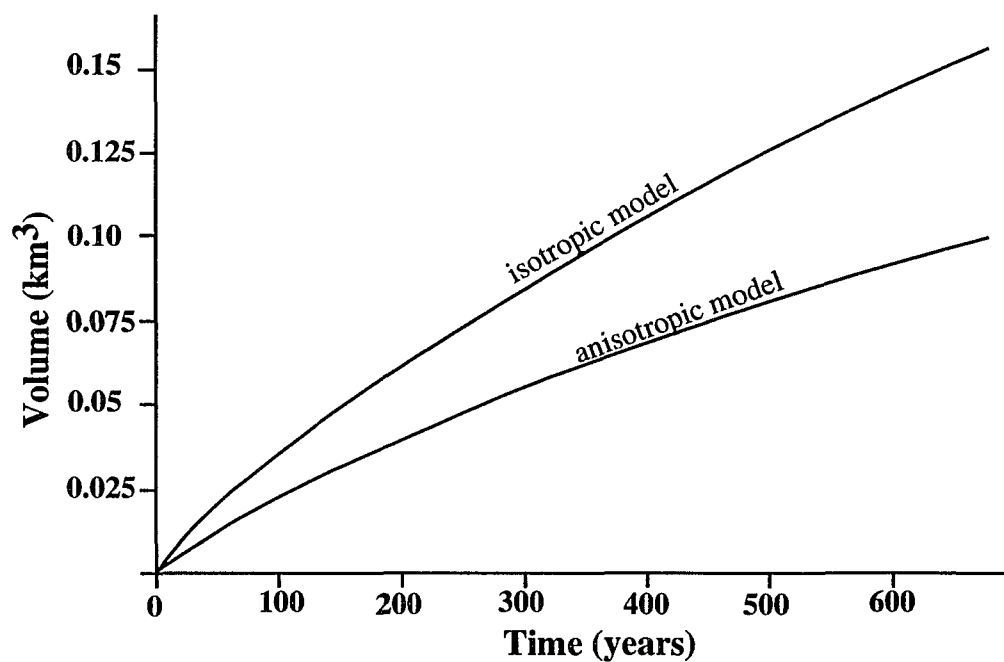
Figure 5.7. Approximate volume of expelled geopressured fluids vs. time in the hydropressured sediments overlying the vent for both isotropic and anisotropic models.

In the isotropic case, because the sediments have isotropic permeability, fluids move uniformly in all directions in the hydropressured sediments, except along the higher permeability fault (Figure 5.5a). Thus, the low salinity plume forms an upward cone-shape (Figure 5.5a). In the anisotropic case, however, fluid migration was dominant in the horizontal direction in the area close fault, because horizontal permeability is ten times higher than vertical permeability (Figure 5.5b). This causes a smaller amount of fluids to be injected into the sediments close to the venting fault, compared to the isotropic case. Fluids continued to migrate along the fault upwards until they reached the top of the fault, where horizontal migration again becomes dominant. Thus, we observe an "I" shape plume at 660 years after the opening of the seal in the anisotropic model (Figure 5.5b).

The volume of the low salinity plume allows us to compute the amount of fluid injected. Figure 5.7 shows the amount of injected fluids with time for both models. A large quantity (25×10^6 m^3) of low salinity fluids has been injected into the hydropressured section after 100 years in the isotropic case, assuming the fault is 1 km long perpendicular to the model profile. This hot, low salinity fluid may cause further disturbance of salinity, temperature, pressure and groundwater flow field by free convection after fluid expulsion stops.

5.3.1.3. Temperature anomalies

Heat can also be efficiently transported by the venting of hot geopressured fluids. The upward movement of hot fluids is reflected by upward deflection of isotherms along the fault. Figure 5.8a and Figure 5.8b show the temperature distribution for both cases at 660 years after the opening of the fault, respectively. Because the upward flow velocity in the isotropic model is much faster than that in the anisotropic model, more heat is brought up along the fault by the flow in the isotropic model. In both models, the maximum upwarping of isotherms occurs around the top of the fault. This implies that decreasing in fluid velocity causes heat to accumulate around the top of the fault.
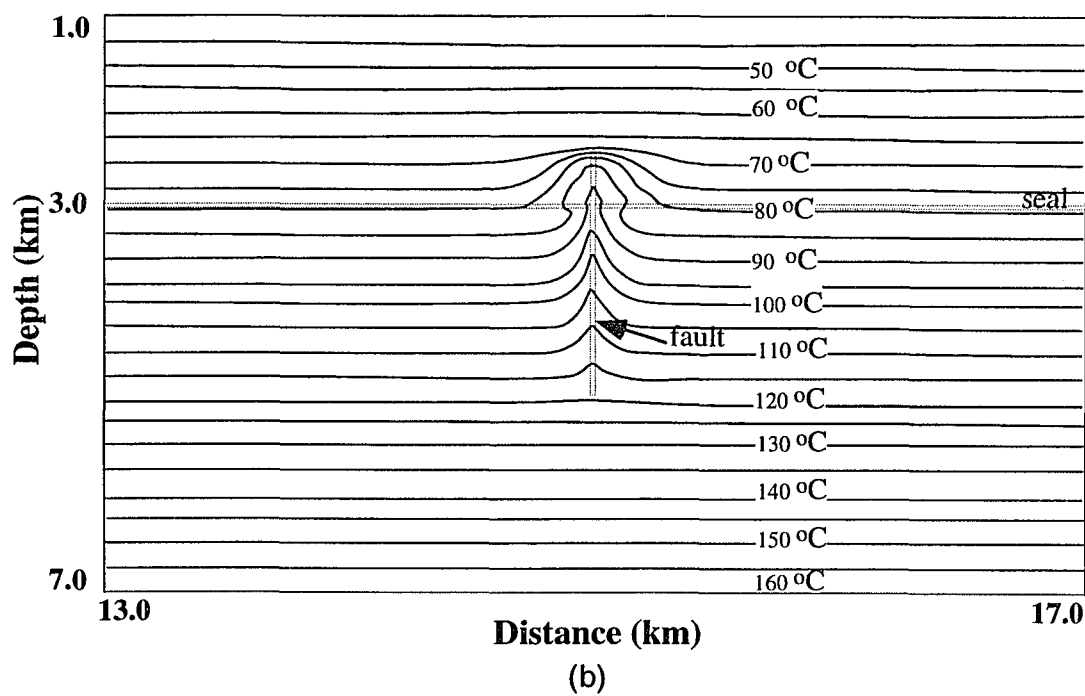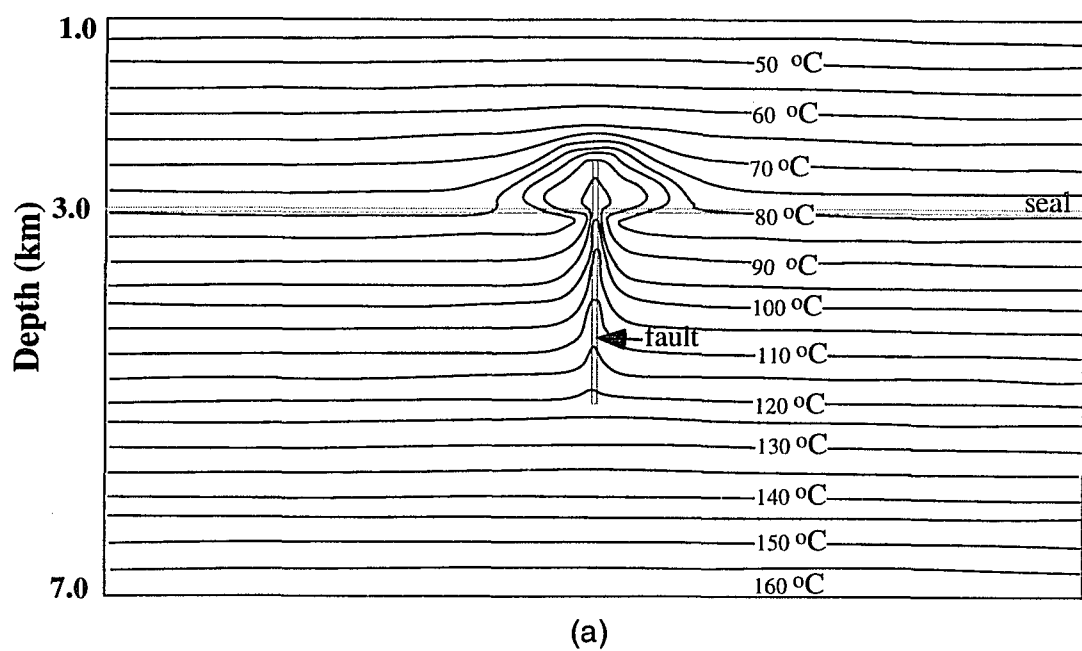
Figure 5.8. Temperature distributions at 680 years after the fault opens in the homogeneous and isotropic model (a) and in the homogeous and anisotropic model (b). Note only the central 4 km of the 30 km wide model is shown.

Anomalous temperatures were as high as 22 °C in the isotropic model and 15 °C in the anisotropic model at 660 years.

5.3.2. Post venting thermohaline convection

5.3.2.1. Fluid pressure variation

It is assumed that the venting of geopressured fluids terminated at an elapsed time of 660 years. Figure 5.9 shows the maximum over-pressure of pore water verses time in the hydropressured section in both isotropic and anisotropic cases after the close of the fault. Excess fluid pressure above the seal dissipated in about one year in the isotropic case. Because of the lower vertical permeability, fluid pressure in the anisotropic case drops more slowly and took about 4 years for the overpressure to disappear. Thus, excess fluid pressure is no longer a driving force for fluid flow.

5.3.2.2. Salinity Rayleigh Number

However, the expelled plume of hot, low salinity fluids is gravitational unstable. Buoyancy is the major mechanism for continuing upward movement of fluids. In order to further understand this free thermohaline convection, salinity Rayleigh Number, which was developed by Sarkar (personal communication), based on analog to thermal Rayleigh number, was used as a convenient way to estimate the strength of convection caused by the salinity difference between the low salinity plume and the surrounding brines. Implicit in this salinity Rayleigh number calculation is that the solute buoyancy is much larger than thermal buoyancy, which is true for my case. As expelled geopressured fluids are not only low in salinity but hot, the salinity Rayleigh number alone underestimates the vigor of convection. AKCESS.BASIN used in these simulations includes both thermal and solute buoyancy effects. AKCESS.BASIN simulations for the post-venting case were computed as described in Section 5.2. The only significant difference between the venting and post-venting case is the closure of the high permeability fault with the resultant hydrologic isolation of the hydrostatic zone from the geopressured sediments.
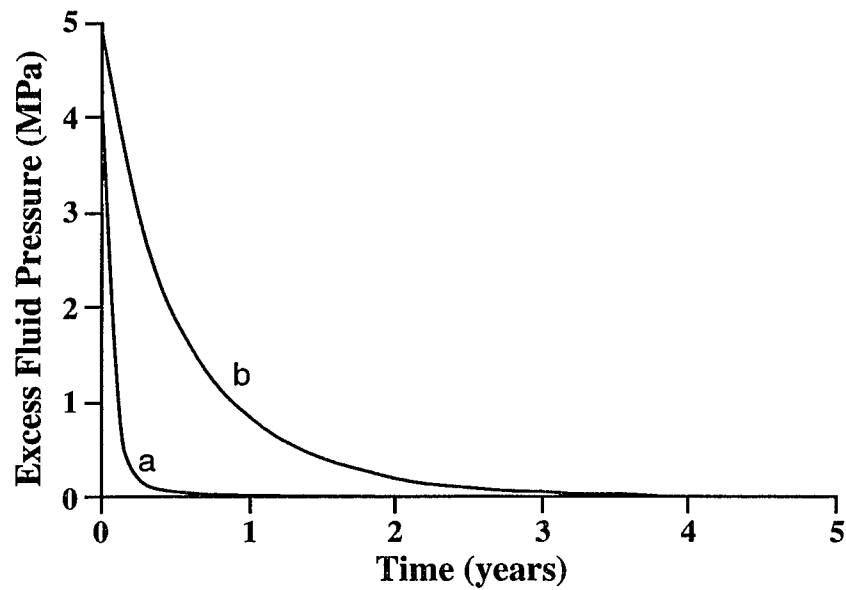
Figure 5.9. Excess fluid pressure variation with time after the fault closes in homogeneous and isotropic model (a) and homogeneous and anisotropic model (b).
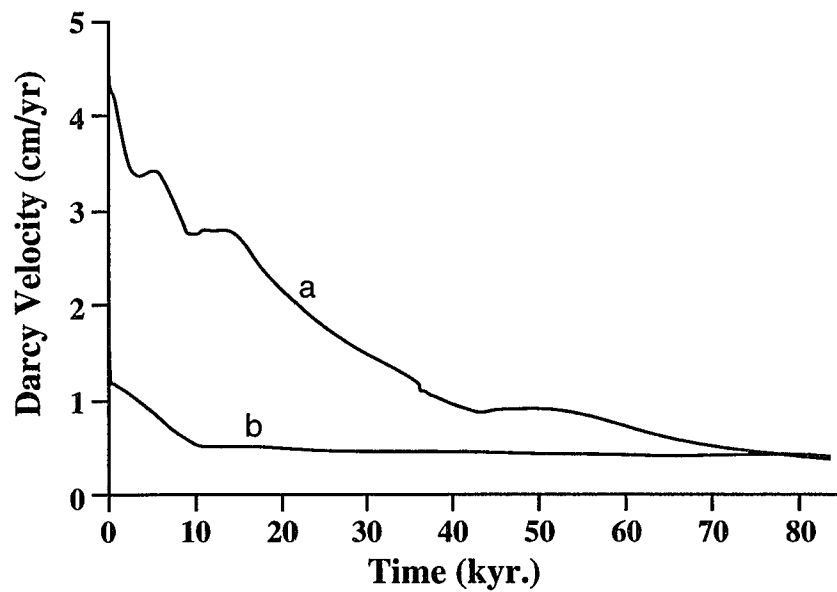
Figure 5.10. Maximum Darcy velocity variation with time in hydropressured section after the fault closes in homogeneous and isotropic model (a) and in homogeneous and anisotropic model (b).

The salinity Rayleigh number, when the plume has an aspect ratio (horizontal diameter divided by vertical diameter) larger than 1 (Sarkar et al., 1995):

$$R = \Delta C \; \beta_C \; H \; K \; g/D\mu; \qquad\qquad (5.1)$$

where R is the salinity Rayleigh number, ΔC is the salinity difference in wt% between the geopressured plume and the surrounding brine, β_C is a constant for converting salinity to fluid density (usually less than 1), H is the height of the plume in centimeters, K is the permeability of the medium in m^2, g is the gravitational acceleration in m/sec^2, D is the diffusion coefficient of the porous medium in m^2/sec and μ is the kinematic viscosity of pore fluid in m^2/sec. When R larger than 40, pore fluids will convect. But when R less than 40 pore fluids will not be able to convect.

When the aspect ratio of a low salinity plume is below 1, equation (5.1) needs to be modified and becomes:

$$R = \Delta C \; \beta_C \; H \; K \; g \; r/D \; \mu; \qquad\qquad (5.2)$$

where r is the aspect ratio of the low salinity plume. As an example, if we take the plume shapes from Figure 5.5a and Figure 5.5b, and calculate the salinity Rayleigh numbers for both isotropic and anisotropic cases at 660 years after the opening of the fault:

$\Delta C = 15$ wt% ;   H = 500 m; $\beta_C = 1$; r = 1;

$K_{isotropic} = 10^{-15}$ m^2 (or 1 mD) and $K_{anisotropic} = 10^{-14}$ m^2 (or 0.1 mD);

$g = 9.8$ m/sec ^{2};

$D = 5 \times 10^{-11}$ m^2/sec; $\mu = 1 \times 10^{-6}$ m^2/sec;

$R_{isotropic} = 14,000$ and $R_{anisotropic} = 1,400$.

Therefore, the salinity Rayleigh number of the expelled low salinity geopressured plume is 14,000 for the isotropic model (Figure 5.5a) and 1,400 for the anisotropic model (Figure 5.5b). The high salinity Rayleigh numbers indicate that pore fluids in the post venting system will convect chaotically, especially in the isotropic model.

5.3.2.3. Free thermohaline convection

High Rayleigh numbers imply vigorous post-venting thermohaline convection. In the hydropressured section of the isotropic model, dissipation of fluid excess fluid pressure has caused a rapid decrease in fluid velocity (Figure 5.10). However, buoyancy created by the density difference between the expelled plume and the surrounding brine has started to develop free thermohaline convection (Figures 5.11a), indicated by the two symmetrical circulation cells on both sides of the former fault. Darcy velocities can be as high as 3.5 cm/yr. in the early stage after the close of the seal (Figure 5.10). An increase in vertical Darcy velocities at elapsed times of 5, 15 and 50 kyr. in the isotropic model (Figure 5.10), indicates that free convection can become stronger. However, Darcy velocities generally decrease with time. For example, at 40 kyr. after the close of the vent, the maximum vertical Darcy velocity has decreased to 1.0 cm/yr. in the isotropic model (Figure 5.10).

One way to explain the decrease in Darcy velocities is that unstable thermohaline system attempts to approach an equilibrium state, by creating smaller circulation cells (Figures 5.12a and 5.13a). In this way, there is extensive mixing between the expelled plume and the surrounding brine. Mixing decreases buoyancy of the plume and thus reduces the flow velocity (Figure 5.10).

In the anisotropic model, because the vertical permeability is lower, thermohaline convection is much weaker (Figure 5.11b, 12b and 13b). After the close of venting, the vertical Darcy velocity quickly decreased to about 0.5 cm/yr., which is then maintained over a long period of time with little change in flow velocity (Figure 5.10).

5.3.2.4. Salinity variations

The shapes of the expelled plumes in the two models change a lot during free thermohaline convection (Figures 5.11 to 5.13). At the beginning of the post-venting simulations, the expelled plume was located immediately above the seal and has an upward cone-shape in the isotropic model, and an "I" shape in the anisotropic model.
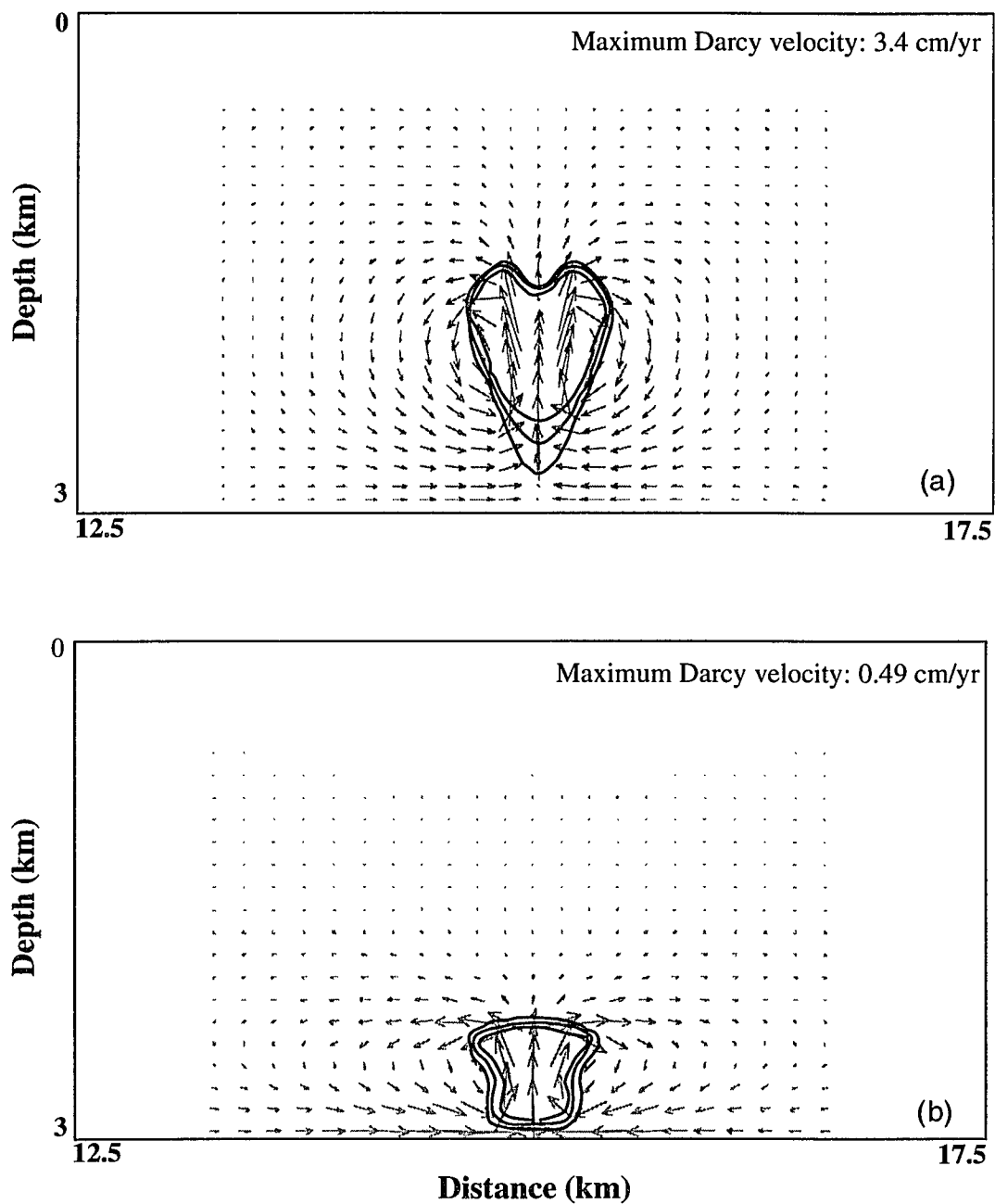
Figure 5.11. Salinity distribution and flow pattern at 7.0 kyr. after the fault closes in the homogeous and isotropic model (a) and anisotropic model (b). In each diagram, the value of the outer contour is 15. wt%; the middle is 7.5 wt% and the inner is 0. wt%. Note arrow scale is different between these two diagrams and only the central 5 km of the 30 km wide model is shown.
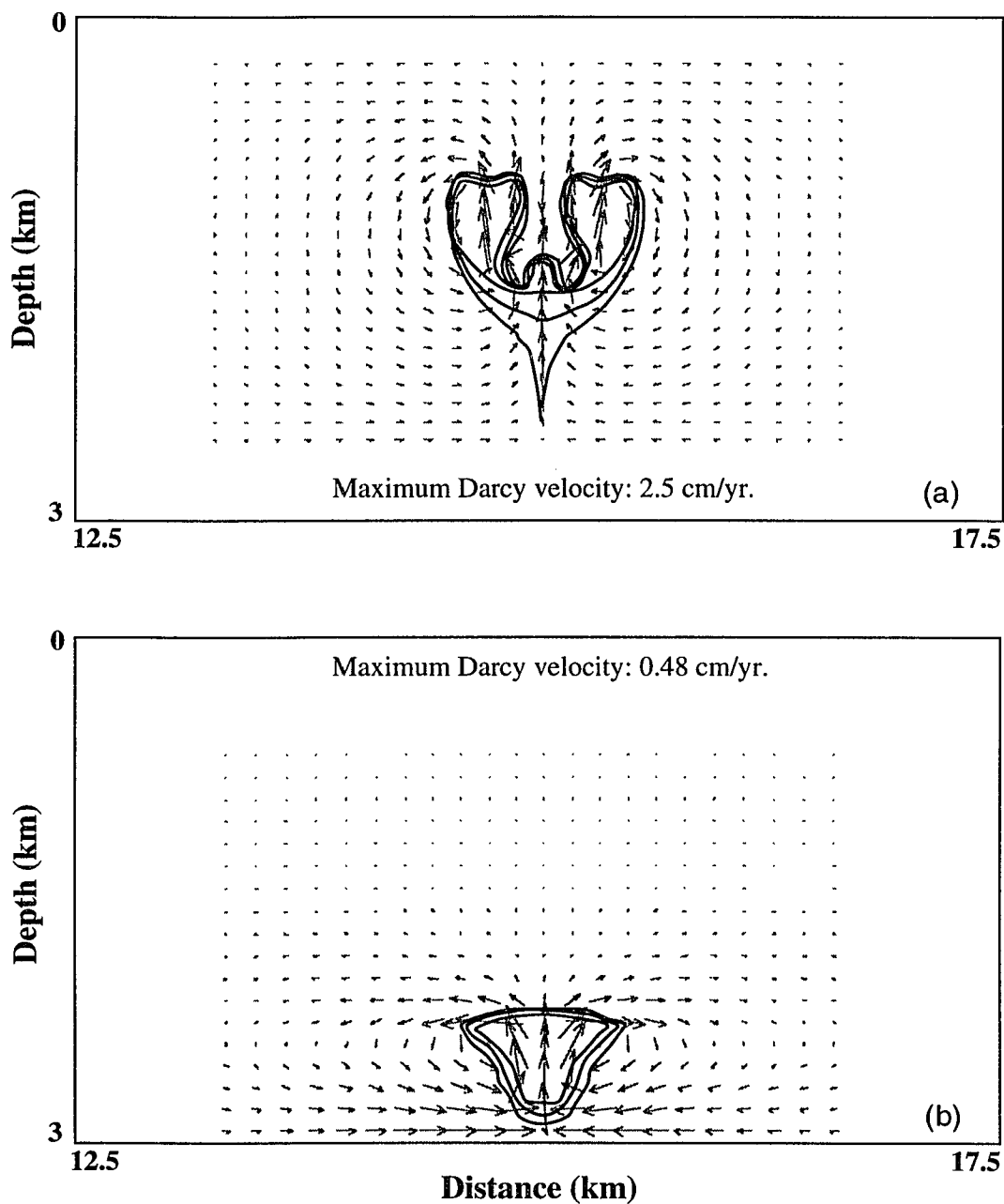
Figure 5.12. Salinity distribution and flow pattern at 15.7 kyr. after the fault closes in the homogeous and isotropic model (a) and anisotropic model (b). In each diagram, the value of the outer contour is 15. wt%; the middle is 7.5 wt% and the inner is 0. wt%. Note arrows have different scale in these two diagrams and only the central 5 km of the 30 km wide model is shown.
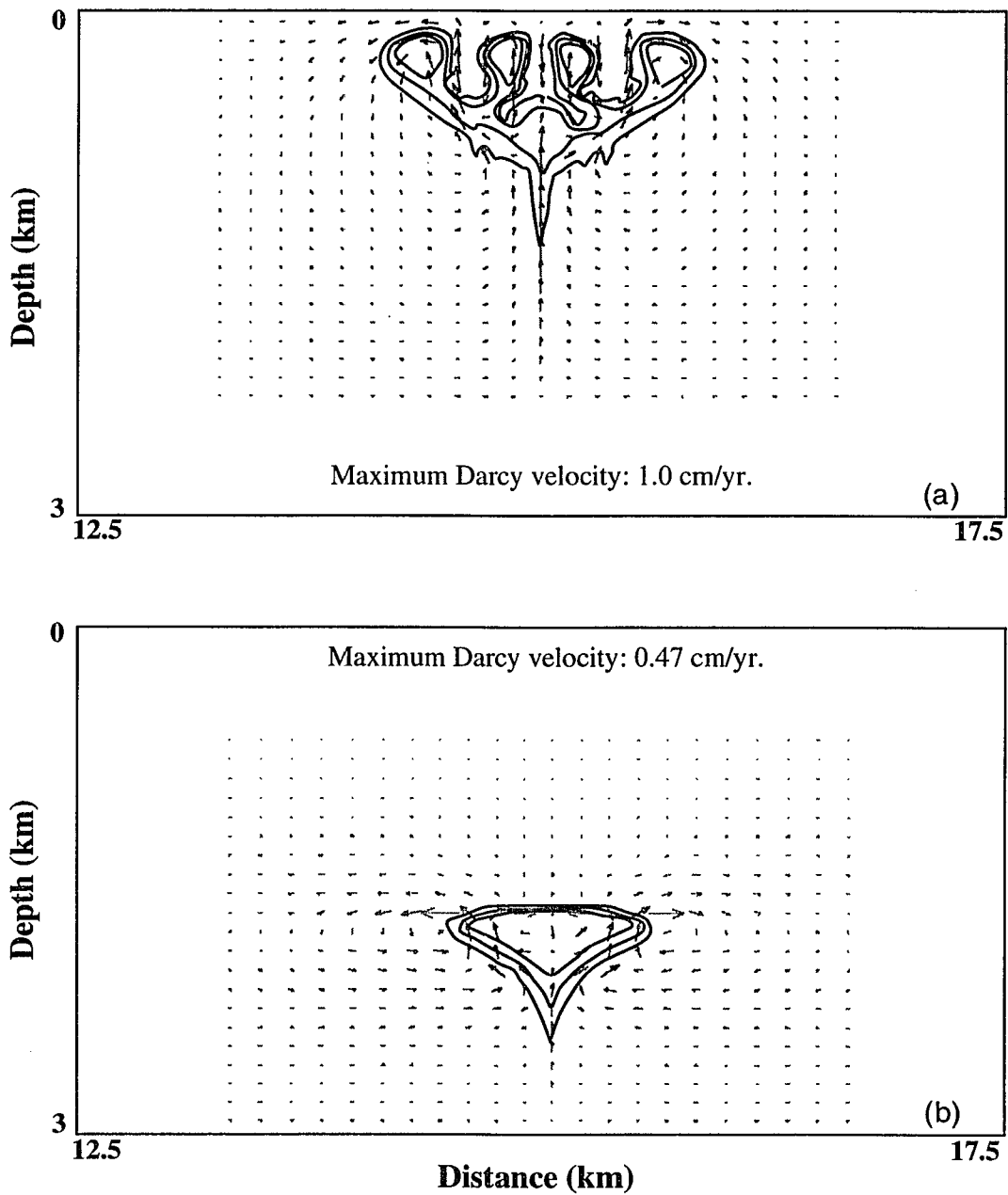
Figure 5.13. Salinity distribution and flow pattern at 36.2 kyr. after the fault closes in the homogeous and isotropic model (a) and anisotropic model (b). In each diagram, the value of the outer contour is 15. wt%; the middle is 7.5 wt% and the inner is 0. wt%. Note arrows have different scale in these two diagrams and only the central 5 km of the 30 km wide model is shown.

After 7.0 kyr., the expelled plume in each of the models has moved upward and become downward cone-shape (Figure 5.11). We also observe that the lower portion of the expelled plume was more saline than the upper part of the plume, and the length of the plume has increased, especially in the isotropic model (Figure 5.11).

Changes in plume shape are controlled by the flow regime, which is dependent on the buoyancy created by the salinity and thermal anomalies. The salinity and thermal anomalies result in changes in hydrostatic pressure along a horizontal plane. Difference of fluid pressure between the plume and the adjacent brine increases with depth. This is because the difference in weight of a water column of a unit area between the plume and the brine along a horizontal plane increases with depth. Thus horizontal movement of brine towards the plume becomes stronger with depth, and the lower portion of the plume becomes compressed. On the other hand, the movement of the low salinity fluids has caused the upper part of the plume to spread out horizontally. Thus, the plume becomes a downward cone-shape (Figure 5.11a).

Brines near the sides and base of the plume also mix with the expelled fluids. This process decreases the density contrast between the plume and the surrounding brines and decreases the upward velocity of the fluids in the lower portion of the plume. On the other hand, in the upper portion of the plume, vertical displacement of fluids dominates and mixing between the plume and brine is weak. Thus, fluid velocities in the upper part of the plume should decrease more slowly than in the lower part of the plume. Thus, the length of the plume gradually increases with time (Figure 5.11a).

Bifurcation is observed in the upper part of the plume as it moves upwards in the isotropic model, but not in the anisotropic model. Figure 5.11a through Figure 5.13a, shows that in the isotropic case, the original plume evolves into two smaller ones, which in turn bifurcate into four even smaller plumes. In this way, the salinity Rayleigh number of the system is decreased and the whole system attempts to become more hydrologically stable. Bifurcation is also consistent with the flow regime, as mentioned

above. My study shows that it may take millions of years for the two systems to reach equilibrium. When the plume reaches the top of the section, the flow pattern becomes complicated because of the downward movement of brine entrapped by the bifurcated plume.

The bifurcation phenomenon is not fully understood. One explanation is that the system is very unstable. This is supported by the observation (Figure 5.11b through 5.13b) that it is more difficult for the plume in the anisotropic model, which has a salinity Rayleigh Number 10 times smaller than the isotropic model, to bifurcate.

It is surprising that the salinity distribution and flow pattern were symmetrical on both sides of the former fault, even for such as unstable system (Rayleigh number >1400). Vigorous convection created by the high contrast of salinity between the plume and the surrounding brines, can significantly disturb the salinity distribution, which in turn changes salinity contrasts and the flow pattern and vice versa. Thus, the flow system should be chaotic. My study also indicates that the chaotic salinity distribution and flow pattern will appear at about one million years after the close of the vent (not shown).

In the isotropic model, because the system is strongly unstable, sensitivity tests indicate that changes in grid size and time step can cause change in the detail of the plume configuration. However, the general feature of bifurcation still can be observed through simulations with different grid size and time step. Similar bifurcation was also observed when a two-dimensional finite difference program, developed by Alok Sarkar, was employed in a simple testing case. In the anisotropic model, because the system is relative stable (salinity Rayleigh number 10 times smaller than the isotropic model), changes in grid size and time step do not significantly affect the results. These results imply that bifurcation is a phenomenon creased by the physical process of thermohaline convection in a strongly unstable system, not by numerical errors.

5.3.2.5. Temperature anomalies

In the post-venting simulation, thermal anomalies still exists in the lower part of the section between 2.5 and 3 km depth long after the fault closes. Temperature anomalies can be more than 10 °C at 7.0 kyr. and as high as 8 °C at 15.7 kyr. in the isotropic model (Figures 5.14a and 5.15a). In the anisotropic model, the maximum temperature anomaly was about 5 °C at 7.0 kyr. and 3 °C at 15.7 kyr. (Figures 5.14b and 5.15b). This indicates that the anomalous temperature distribution influences the sediments for a long time.

Temperature anomalies in the post venting models come from two sources. One is the original thermal anomalies inherited from the injection of hot geopressured fluids. The other is the continuous convection of pore fluids, which pick up heat in the deeper sediments and transport it upwards. Even several thousand years after the vent closes, upward moving fluids still have a maximum vertical velocity of more than ten centimeters per year in the isotropic case. Fluid flow at such high velocities not only can carry sufficient heat to pull up the isotherms along the flow path, but also maintain the thermal anomalies for a long time. Because hydrocarbon generation depends on both the temperature to which the kerogen is heated and the duration of heating (Carter and Leach, 1990), thermal anomalies created by the post venting thermohaline convection can promote thermal maturation of hydrocarbons in the hydropressured zone.

5.4. DISCUSSION

Expulsion of geopressured fluids in a real sedimentary basin should be much more complicated than that obtained from this simplified generic model basin. Thus, it is necessary to keep in mind that results from this study only show some possibilities that may occur in nature.

The results from the venting simulation show that the time required for the pressure in the fault to drop to the level at which the fault closes during an expulsion of
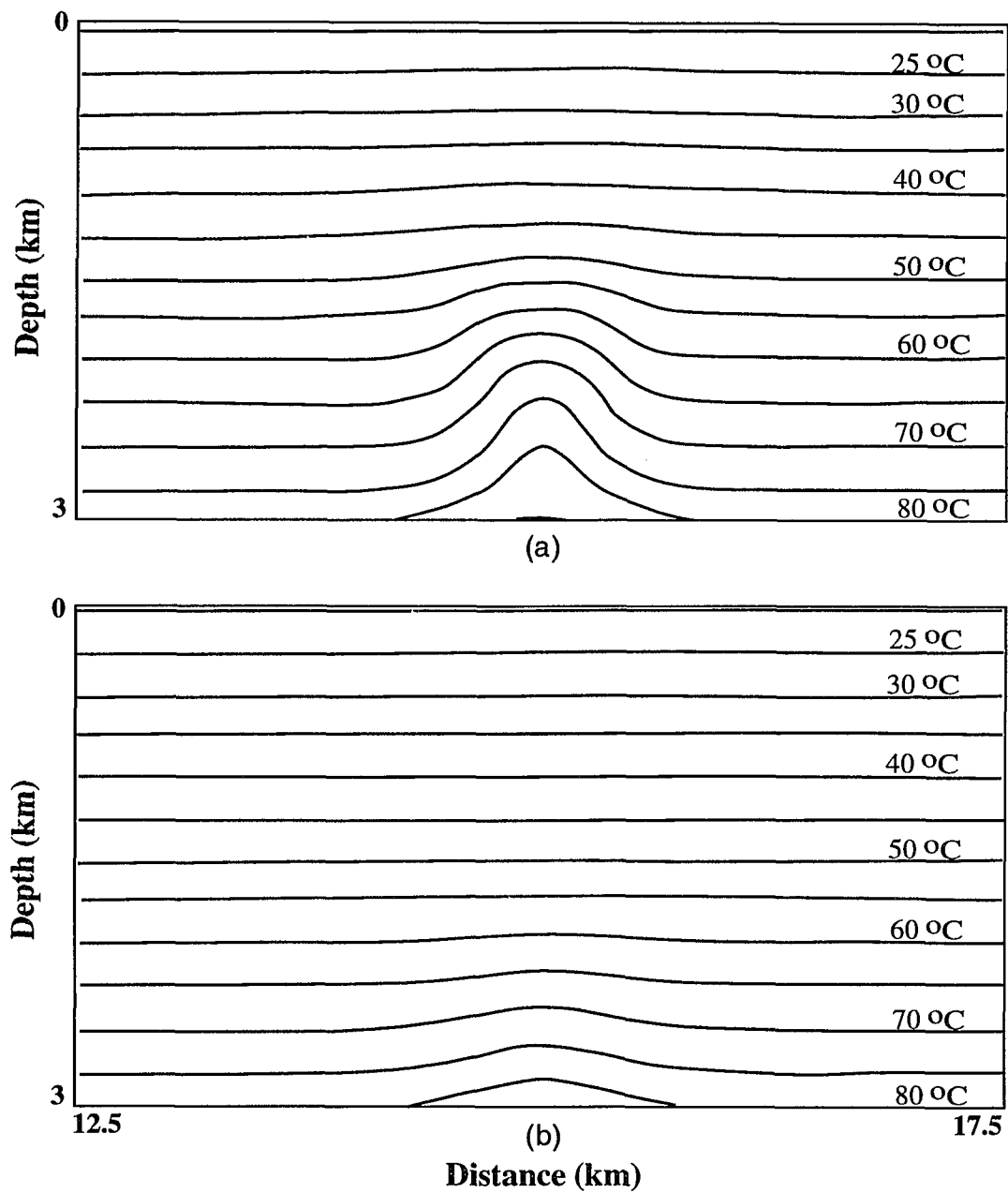
Figure 5.14. Temperature distribution at about 7.0 ky. after the fault closes in the hydropressured section. (a) is the homogeneous and isotropic model, and (b) is the homogeneous and anisotropic model. Note only the central 5 km of the 30 km wide model is shown.
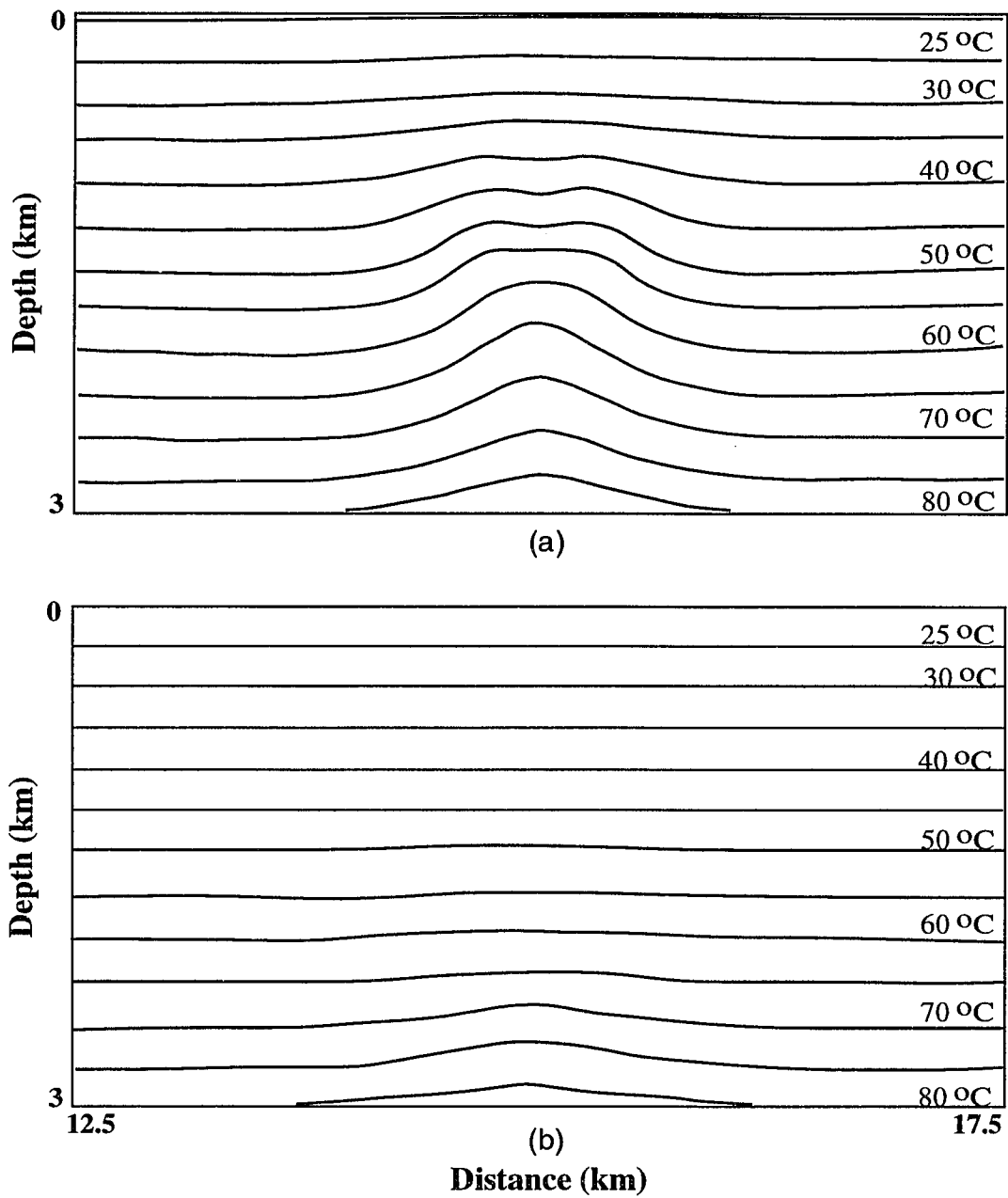
Figure 5.15. Temperature distribution at about 15.7 ky. after the fault closes in the hydropressured section. (a) is the homogeneous and isotropic model, and (b) is the homogeneous and anisotropic model. Note only the central 5 km of the 30 km wide model is shown.

geopressured fluids, is less than 100 years in a homogeneous and isotropic model and may be several hundred years in the anisotropic model. These durations are longer than those (20 - 50 years) predicted by Roberts and Nunn (1995) in their 1-D modeling study. One reason for that may be because the model in this study is two-dimensional. In a two-dimensional model, fluids are supplied from both vertical and horizontal directions in the geopressured section, and focused towards the fault. Thus, the depression in fluid pressure which closes the fault takes longer to develop. In a three-dimensional model, if the fault is short horizontally, then the duration of expulsion can be even longer than that in the two-dimensional model, because it takes longer to draw down fluid pressure near the fault, as fluids are from all directions. Another reason for the longer expulsion in this study is that these models were simplified and did not consider the effects of sediment compressibility and fracture width, which are dependent on fluid pressure. The permeabilities of sediments below and above the seal are important to duration of expulsion. Higher permeability of the sediments below the seal or lower permeability of the sediments above the seal can maintain the high pressure around the sediments immediately below the seal and cause a longer period of expulsion (Roberts and Nunn, 1995). Another reason for the longer expulsion in this study is that we did not consider fault permeability as a function of fluid pressure. Roberts et al. (1996) suggested that the variation of permeability with fluid pressure can significantly decrease the period of expulsion to 20-30 years in the South Eugene Island Block 330 field. Chemical reactions, such as the transformation of solid kerogen into liquid or gaseous hydrocarbons may cause the fluid pressure to rebuild more rapidly than that predicted by from the modeling studies and decreasing the time between expulsion events (Roberts and Nunn, 1995). Sediment anisotropism, heterogeneity and compressibility, which will be discussed further in Chapter 6, are also important for the duration of an expulsion event.

Because the volume of injected hot and less saline fluids can be large, the induced post-venting thermohaline convection will be an important mechanism for transport of heat, fluids and solute in a well developed salt basin. The results from this study indicate that Darcy velocities are as high as 2.5 cm/yr., even at 10,000 years after the termination of expulsion in an homogeneous and isotropic model. Thus, the results of this study strongly support the importance of active, large-scale convective fluid flow, which is believed to be widely occurring in shallower sediments (<2 km) in the Louisiana Gulf Coast (Hanor, 1987).

A real sedimentary basin is rarely homogeneous and isotropic, as used in this study. The heterogeneity and anisotropism can significantly decrease the efficiency of heat, solute and fluid transport by thermohaline convection. However, thermohaline convection may become important when a sand bed has sufficient thickness and permeability. For example, the sand-dominated Wilcox Group of south-central Louisiana can be more than one kilometer thick (e.g. Hanor and Sassen, 1990; Tye et al., 1991). The Wilcox Group dips southward into the shale-dominated geopressured zone (Hanor and Sassen, 1990). Thus, the Wilcox Group is effected by the expulsion of geopressured fluids from the underlain sediments. Observation indicates that strong density overturn exists in this Group, as salinity differences up to 10 wt% between the sediments at a depth of 2.0 km and those below 3.0 km adjacent to the geopressured sediments (Hanor and Sassen, 1990). Thus, vigorous thermohaline convection with Darcy velocity on the order of centimeters per year is expected in this Group, even though when expulsion of geopressured fluids is not active. Other examples of density overturn induced flow near salt domes, include the Iberia Dome (Workman and Hanor, 1985), Welsh Salt Dome (Hanor and Sassen, 1990) and Bay St. Elaine Salt Dome (Cassidy and Ranganathan, 1992) in south Louisiana.

However, heterogeneous and anisotropic sediments in a real sedimentary basin also significantly reduce the likelihood of bifurcation occurring during the upward

movement of a low salinity plume. While it is believed that the bifurcations shown in Figures 11a to 13a are not a numerical problem, bifurcations are unlikely to occur in nature.

The results in this study also indicate that the anomalous temperature (~10 °C) can influences the sediments for a long time (>10,000 years). Thus, thermal anomalies created by the post venting thermohaline convection can result in a higher level of thermal maturation anomaly, because hydrocarbon generation depends on both the temperature to which the kerogen has been heated and the duration of the heating (Cater and Lerche, 1990). My study indicates that the thermal anomaly is stronger if the sediments have higher permeability.

This study also shows that migration of the low salinity plume can become channelized if there is a fault or other vertical high permeability conduit within the sediments (not shown here). This channelized flow may be partially responsible for the many seepages of low density hydrocarbon observed in the Gulf of Mexico continental shelf.

5.5. CONCLUSIONS

When pore fluid pressure exceeds a critical value, sediments hydrofracture to create a high permeable conduit between the geopressured and hydropressured sediments. Pressure gradients drive geopressured fluids into overlying hydropressured sediments. This causes fluid pressure in geopressured sediments to rapidly decrease around the fault. In a hydropressured section, injection of geopressured fluids not only quickly increases fluid pressure in the sediments near the fault, but also creates large salinity and thermal anomalies. It takes a few hundred years for fluid pressure in geopressured sediments to drop to a level, where the fractures collapse and the fault closes. After venting, anomalous fluid pressures in hydropressured sediments dissipate in less than a year.

The injected low salinity plume is gravitationally unstable (salinity Rayleigh Numbers 1400 - 14,000), which can cause free thermohaline convection. The unstable system tries to approach a new equilibrium, by developing smaller circulation cells (bifurcation), which cause extensive mixing between the geopressured fluids and the surrounding brine. Mixing reduces the buoyancy of the plume and decreases flow rates. This study suggests that the bifurcation can only occur when free convection is vigorous (salinity Rayleigh number > 1,000) and the media is homogeneous and isotropic. At these high Rayleigh numbers, groundwater will convect in a chaotic fashion, but it may take a long time (> 1 my.) for an obviously chaotic flow pattern to develop. Migration of the low salinity plume may become channelized if there is a fault or other high permeability conduit within hydropressured sediments.

Even several thousand years after venting, upward moving fluids still have a maximum vertical velocity of several centimeters per year. As long as the sediments have sufficiently high permeability, thermal anomalies persist near the fault for a long time (> 10,000 years), and could result in high organic maturity. Thus, thermohaline convection induced by short term expulsion of hot and low salinity geopressured fluids may be an important mechanism for long term (~10,000 years), kilometer scale vertical and horizontal migration of groundwater in salt basins.

The results of this study support the importance of active, kilometer-scale thermohaline convection induced by density overturn (Hanor, 1987; Workman and Hanor, 1985; Hanor and Sassen, 1990; and Cassidy and Ranganathan, 1992), especially in places with thick sand-dominated sediments, such as the Wilcox Group, in Louisiana Gulf Coast.

CHAPTER 6
EVIDENCE FOR RECENT MIGRATION OF GEOPRESSURED FLUIDS ALONG FAULTS IN SOUTH EUGENE ISLAND, BLOCK 330 FROM ESTIMATION OF PORE WATER SALINITY

6.1. INTRODUCTION

The Eugene Island Block 330 field is located in the Gulf of Mexico, offshore Louisiana, U.S.A., approximately 170 miles (272 km) southwest of New Orleans (Holland et al., 1990) (Figure 6.1a). The field lies near the southern edge of the Outer Continental Shelf (OCS). Water depths in this area of the shelf range from 64 to 81 m (210 to 266 ft). The majority of production is from two large roll-over anticlines abutting a basin-bounding growth fault in GA, HB, JD, KE, LF, MG, OI sandstones (Figure 6.1b). These two anticlines are located mostly within the Shell Block 331 field and the Pennzoil Block 330 field respectively. The Eugene Island Block 330 field was the largest producing field in Federal OCS waters from 1975 to 1980. The field now ranks second in annual hydrocarbon production and fourth in cumulative hydrocarbon production.

Because of its great economic importance, the Eugene Island Block 330 field has been studied extensively (Anderson et al., 1991; Holland et al., 1980 and 1990). Anderson (1993), based on the coupled temperature, pressure, overproduction (low decline rate of production), and seismic amplitude anomalies, suggested the possibility that some oils produced in 1993 may not have been present in the shallow reservoirs at the beginning of production in 1972. This implies that hydrocarbon-bearing fluids have recently been expelled from geopressured sediments into overlying oil and gas reservoirs along the growth fault in the South Eugene Island area (Anderson et al., 1994). 250 temperature measurements from 200 different wells in the Eugene Island Block 330 field indicated an increase in temperature of about 10 °C around the fault zone compared to temperatures away from the fault zone in both foot wall and hanging
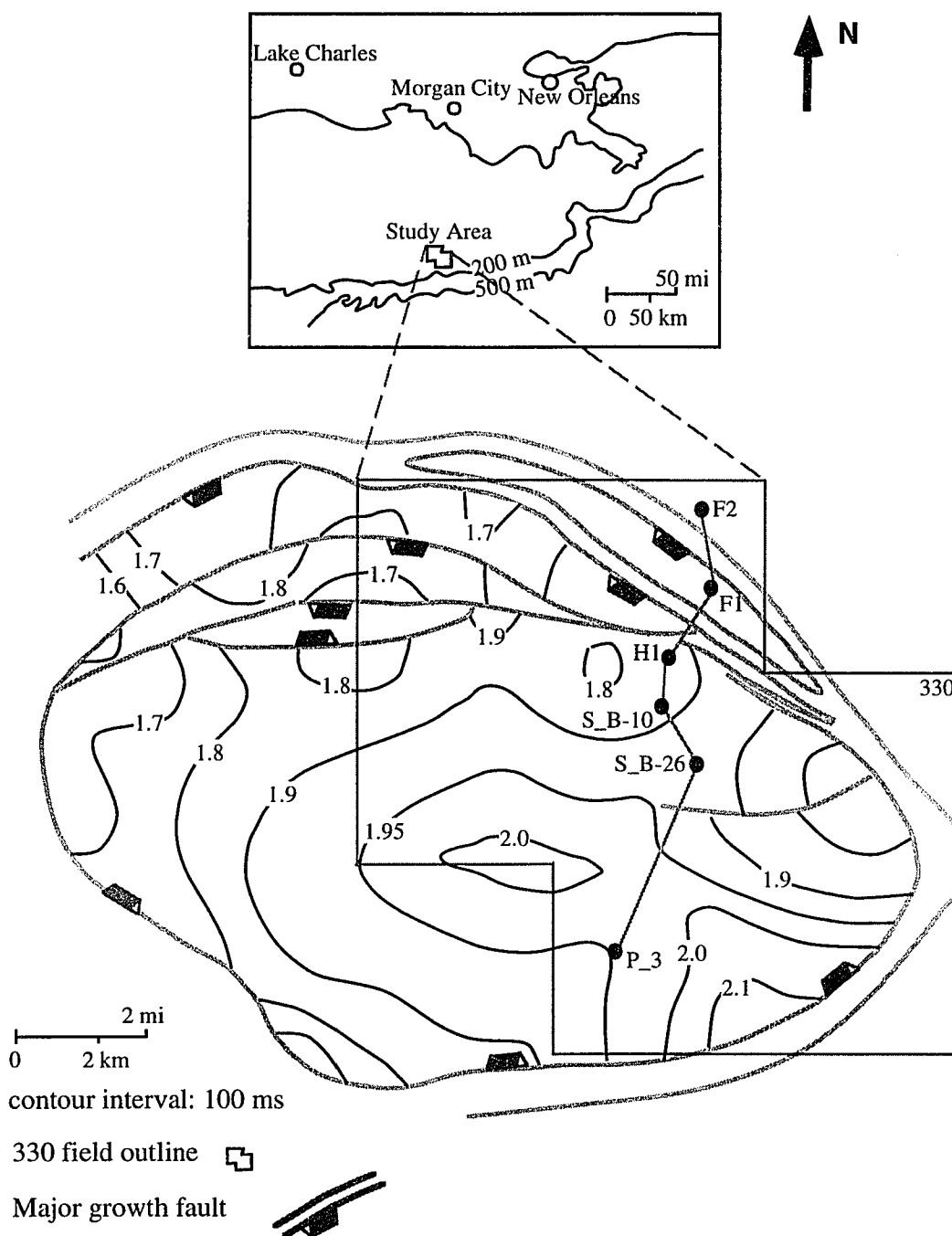
Figure 6.1a. Seismic structure map (lower diagram) of the JD sandstone in Eugene Island Block 330 field vicinity. The contours in the location map (upper diagram) show the water depth of the outer continental shelf. Contour values in the lower diagram are seismic two-way travel time (sec.). F2, F1, H1, S_B-10, S_B-26, and P_3 show the locations of well logs displayed in Figure 6.1b. Both diagrams are from Holland et al., 1990.
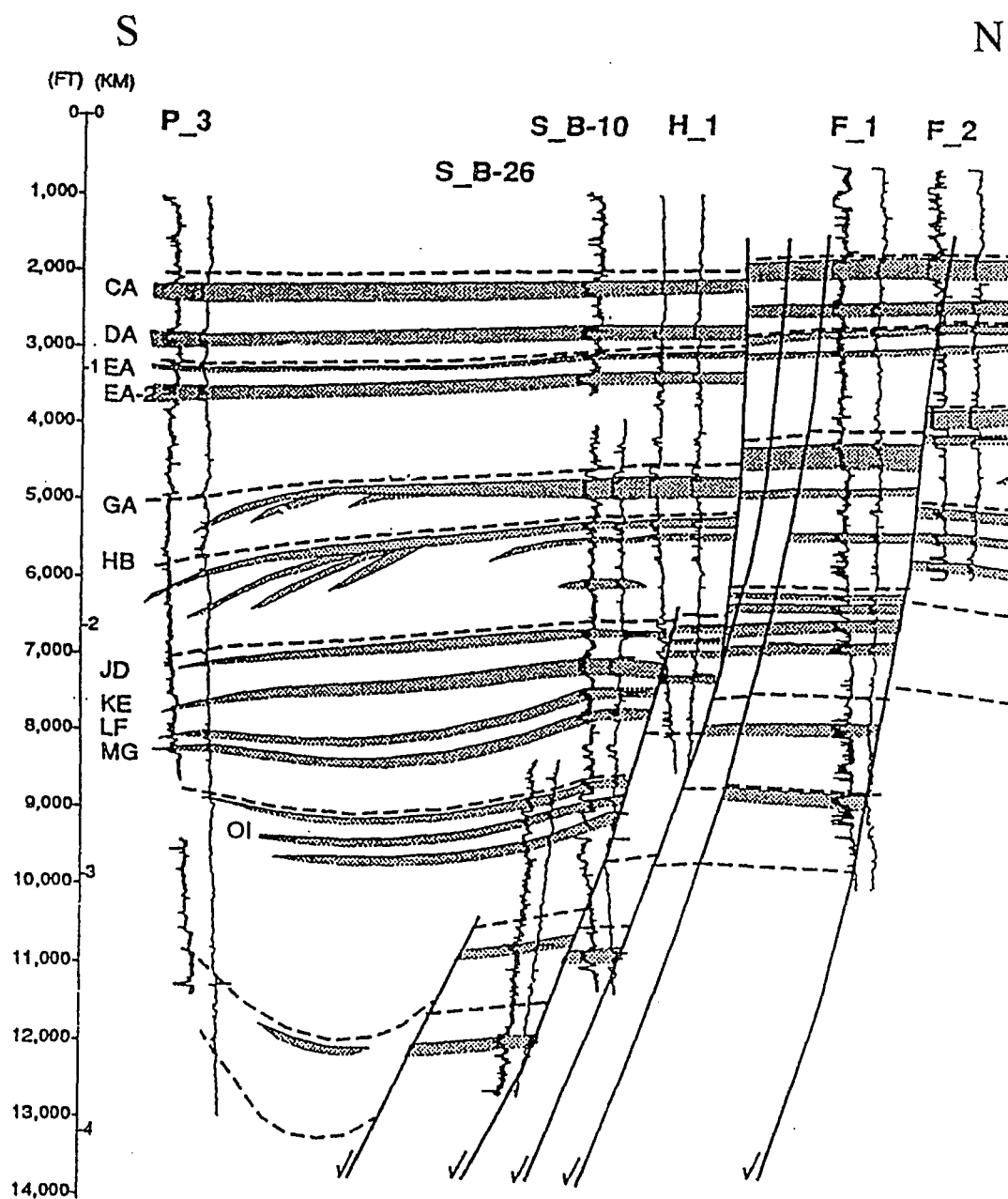
Figure 6.1b. Cross-section based on well log interpretation showing the north-south extent of the prominent sands in the Block 330 field. The logs on the left in the individual wells are either gamma ray or SP logs while the resistivity logs are displayed on the right. Well log correlations are tied to the resistivity logs. See Figure 6.1a for the location of this profile. (Alexander and Flemings, submitted to AAPG Bulletin)

wall (Guerin et al., 1994). It was also observed that fluid pressure is elevated over a broad (~5 km) region around the fault zone (see Figure 6.2 for the fluid pressure variation with depth) (Flemings et al., in prep.; Roberts et al., 1996). Furthermore, changes in geochemistry of hydrocarbons (Anderson et al., 1991; Whelan et al., 1994) and brines (Losh and Wood, 1995) in the area reservoirs suggest significant vertical transport of fluid originated from the deeper overpressured sediments (Cretaceous or older) into their present locations. In fact, active fluid flow was encountered when the Global Basins Research Network (GBRN) took over a Pennzoil-operated development well in the field and extended it through the fault zone. This may indicate that fluids are moving upward along the fault zone from the deep geopressured sediments into the shallow reservoirs.

A number of numerical models have been developed by GBRN workers to simulate the expulsion of geopressured fluids along fault zones from the deep overpressured sediments into the overlying hydropressured reservoirs. Cipriani et al. (1994) constructed finite element fluid flow models, which showed that rapid fluid flow driven by geopressure, could produce temperature anomalies similar to those observed in field measurements. They also pointed out that the flow volume could deliver about 1/4 of the "excess" oil and gas produced from Pennzoil reservoirs over the last 30 years if the fluids were saturated in methane and transported oil in the same proportion to gas as is found today in the Block 330 reservoirs. Roberts and Nunn (1995) integrated structural, stratigraphical and sediment property data in this field into their numerical model, and concluded that temperature and pressure anomalies observed in the South Eugene Island area are consistent with the episodic expulsion of abnormally pressured fluid along the major growth fault, where permeability is strongly dependent on fluid pressure and rock properties in the fault zone.

In a salt basin such as the Gulf of Mexico, pore water in deep sediments (> 3.5 km depth) may have salinities significantly lower than pore water in shallow sediments
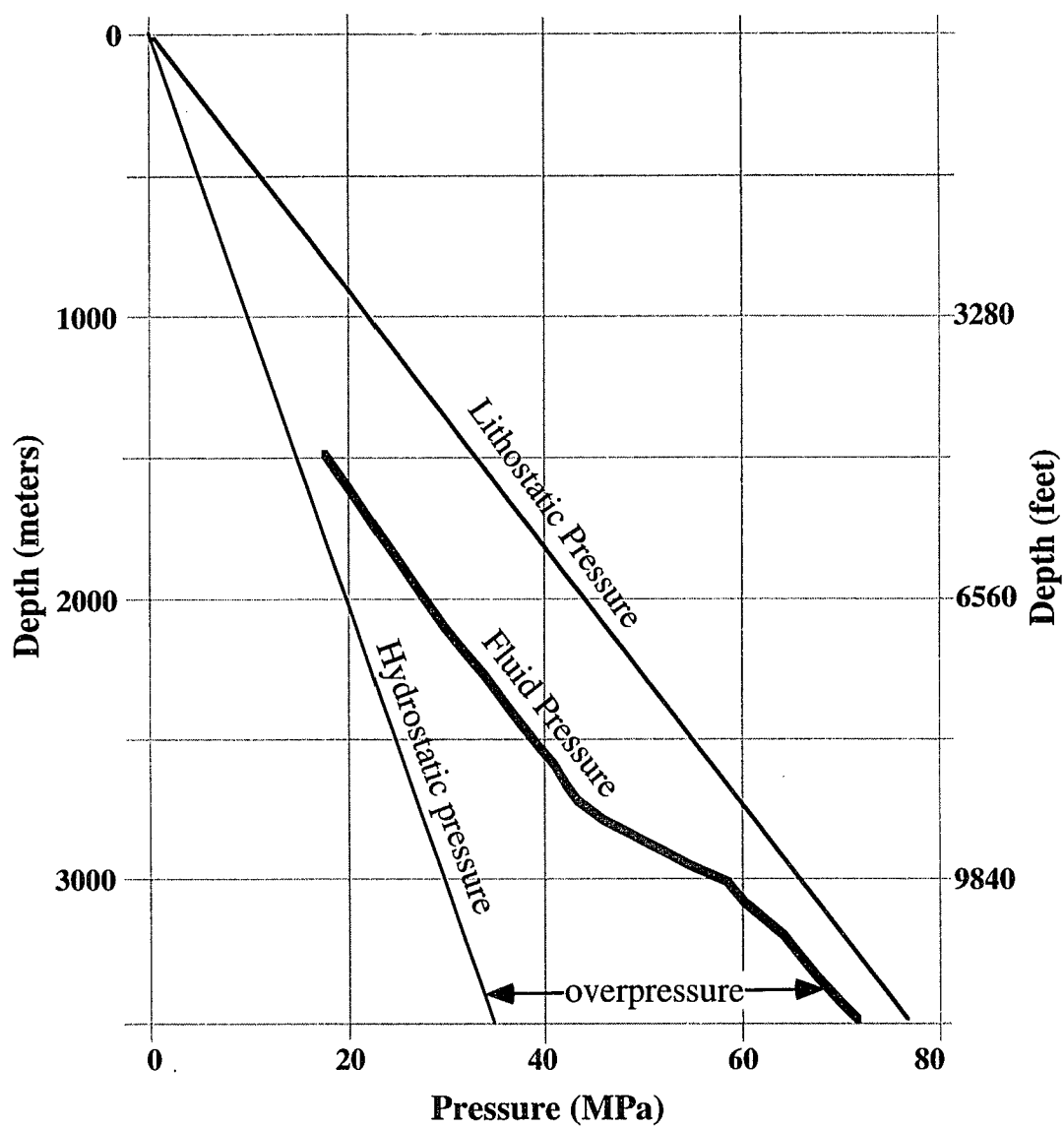
Figure 6.2. Pore fluid pressure in South Eugene Island Block 330 Field and its comparison to hydrostatic and lithostatic pressures. Data are originally from Flemings et al. (in prep).

between 1.0 and 3.5 km depth (Hanor et al., 1986; see Figure 4.1). In addition, deep

sediments are dominantly shaly and their fluids are generally geopressured

(overpressured) (Galloway et al., 1982; Hanor et al., 1986). If geopressured zones have

different pore water salinities compared to the overlying hydropressured sediments,

then salinity can be used as a tracer for monitoring the migration of geopressured fluids

into the hydropressured sediments.

This study is a pore water salinity analysis using SP well logs in the South Eugene

Island Block 330 field. Because NaCl diffuses very slowly through porous media,

salinity is an effective tracer for groundwater flow as demonstrated in Chapter 4. Thus,

salinity analysis allows us to monitor the migration of geopressured fluids along the

fault zone. I also conducted a numerical study which explains the estimated salinity

field and further explores the fluid flow regime.

6.2. GEOLOGICAL SETTING OF THE SOUTH EUGENE ISLAND BLOCK 330 MINI-BASIN

The Gulf of Mexico basin contains siliciclastic sediments from the Sigsbee

escarpment in the south to the northern pinchout of Tertiary sediments on the coastal

plain (Holland et al., 1990), and from the Florida escarpment to the Eastern Mexican

shelf (Martin, 1978). Grabens and down-to-the-basin faulting are present along the

inner coastal plain. These graben and fault systems are related to the formation of the

Gulf of Mexico by early rifting and subsequent sea-floor spreading and subsidence in

the Jurassic through Early Cretaceous (Hall et al., 1982). Since the Mesozoic, there has

been a general basinward shift of the major shelf-margin deltaic depocenters in the Gulf

of Mexico.

During the Plio-Pleistocene, the depocenters shifted from just west of the present

mouth of the Mississippi River to about 160 km south of the present shoreline of the

Texas and Louisiana border (Woodbury et al., 1973). Over 3.65 km of late Pliocene

and Pleistocene age sediments accumulated within the main Pleistocene depocenter

(Woodbury et al., 1973). The high rates of deposition above the underlying salt layer led to salt withdrawal and the development of extensive listric normal faults and salt diapirs at the continental margin (Worall and Snelson, 1989). The salt migration allowed the deposition of thick localized accumulations of sediments which developed into salt-withdrawal mini-basins. Mini-basins are described by Shoup and Karlo (1993) as circular- to elliptical-shaped basins which formed from sediment loading of an underlying salt layer. The downdip margin of a mini-basin is delineated by a counter-regional fault. The updip margin and sides are generally bordered by growth faults and/or salt domes and ridges (Shoup and Karlo, 1993).

The South Eugene Island Block 330 mini-basin is an oblong, approximately 19 by 15 km basin, which comprises part of the larger, Plio-Pleistocene depocenter, and is structurally bounded by four main fault zones (Alexander and Flemings, 1996). The northern and eastern boundaries are defined by arcuate, normal listric growth faults (Figure 6.1a). These faults formed in response to the salt evacuation from the center of the basin and syndepositional subsidence. Counter-regional faults formed at the western and southern margins (Figure 6.1a) of the mini-basin. The counter-regional faults are not considered to be classic growth faults, but as compensation features formed during the lateral withdrawal of salt from salt ridges into adjacent diapirs (Larberg, 1983; Alexander and Flemings, 1996). Along the northern rim of the mini-basin, two anticlines formed by rollover on the downthrown side of the growth fault system (Figure 6.1a) (Holland et al., 1990). The anticlines are separated by a small syncline. The eastern structure is sharply defined and has as much as 1800 ft (549 m) of structural closure. The western anticline has less relief, with 122 to 152 m of structural closure.

The evolution of the mini-basin during the Plio-Pleistocene time has been divided into three phases by Alexander and Flemings (1996): prodelta, stalled-shelf, and bypass. The earliest phase, the prodelta, consists of prodelta shales and turbidites which loaded

and mobilized an underlying salt sill. During the stalled-shelf phase, lowstand shelf margin deltas remained in the regional fault zone, which comprised the northern margin of the mini-basin. A series of deltaic sands, including OI, MG, LF, KE, JD and HB (Figure 6.1b), were deposited adjacent to the fault system over 230,000 years. These sands were capped by transgresssive shales which acted as top seals. All but one (GA sand) of the major exploited reservoirs of the Block 330 field were deposited during this phase (Alexander and Flemings, 1996). During the final phase, the bypass phase, accommodation space within the mini-basin decreased, the deltaic system prograded southward, and lowstand uncomformities formed. During later transgressions, thick deltaic and fluvial sands were deposited on top of the uncomformities. One major reservoir (GA sand) was deposited in the early part of this phase; later-phase sands tend to lack lateral seals and structural closure (Alexander and Flemings, 1996).

Sediments in each of the three phases correspond to a distinct hydrologic regime (Flemings et al., in prep.): the prodelta turbidites are geopressured, the progradational deposits (stalled-shelf) lie in a pressure transition zone, and the coastal plain sediments (bypass) are hydrostatically pressured.

6.3. SALINITY ESTIMATION FROM SP LOGS

The spontaneous potential (SP), is one of the first logging measurements ever made, and has been in continuous use for over 60 years. The SP log has a number of useful functions (Bateman, 1985), including: correlation, lithology indication, porosity and permeability indications, and a means to measure pore water salinity. Spatial variations in pore water salinity derived from SP logs can provide useful information on the degree of hydrologic continuity and compartmentalization of sedimentary sequences, and thus aid in evaluating both local and regional reservoir continuity and determining possible migration pathways for hydrocarbons (Funayama and Hanor, 1995). There is general agreement that the SP curve consists of two major components: the electrofiltration and electrochemical components (Funayama, 1990). The

electrofiltration component is usually negligible for calculation of pore water salinity.

The primary source of the electrochemical component is formed by different ionic

mobilities when two solutions having different ionic activities, such as mud filtrate and

formation water, are in contact and the system tries to restore equilibrium through ionic

diffusion. Thus, the electrochemical potential is of primary importance in the salinity

calculation. The following method for the estimation of salinity follows the work of

Bateman (1985).

6.3.1. Method

The relationship developed by Bateman (1985) between SP response, the

resistivities of the mud filtrate and the formation water was employed to calculate the

pore water salinities (Figure 6.3). The parameters required are SP value, mud filtrate

resistivity (R_{mf}) and its measured temperature, and the formation temperature (T_f). The

relationship among the variations of salinity, absolute SP value, R_{mf} and formation

temperature is non-linear and complicated. Funayama (1990) analyzed the sensitivity

of the salinity calculation at an original SP value of 108 mV, T_f of 183.8 °F, R_{mf} of

0.89 ohm at measured temperature of 76 °F (Figure 6.4). Funayama found that a 10 %

difference in SP deflection will result in a 10 % difference in calculated salinity.

Therefore, SP values are sensitive for the salinity calculations. Resistivity of mud

filtrate is a second order factor for salinity calculations. A 10 % difference of R_{mf} can

cause about a 3 % change in calculated salinity.

6.3.2. SP and related data in South Eugene Island, Block 330

There are 81 wells, which have SP logs in South Eugene Island Block 330. But

only 50 of them were found suitable for this study. Most of the other SP logs do not

cover the depth range in which the reservoir sand beds located. SP logs in the area

usually cover depths of 3,500 ft (1067 m) to 8,000 ft (2439 m).

Most of the SP logs in this area have been interpreted by Peter Flemings and his

Group at Pennsylvania State University and provided tops of the interested sand beds,

initial R_{mf}, T_{mf}

$R_{mf75} = R_{mf} (T_{mf} + 7)/82$

input SP, T_f

Calculate R_w

$K = 60 + 0.133\ T_f$

$R_{mfe}/R_{we} = 10^{-SP/K}$

$R_{mf} > 0.1$

$R_{mfe} = \dfrac{(146\ R_{mf}-5)}{(337R_{mf}+77)}$

$R_{mfe} = 0.85R_{mf}$

$R_{we} = \dfrac{R_{mfe}}{R_{mfe}/R_{we}}$

$R_{we} > 0.12$

$R_{w75} = \dfrac{77\ R_{we} + 5}{146-337R_{we}}$

$R_{w75} = -(0.58 - 10^{(0.69R_{we}-0.24)})$

$x = \dfrac{3.562-\log(R_{w75} -0.0123)}{0.955}$

$ppm(NaCl) = 10^x$

Stop
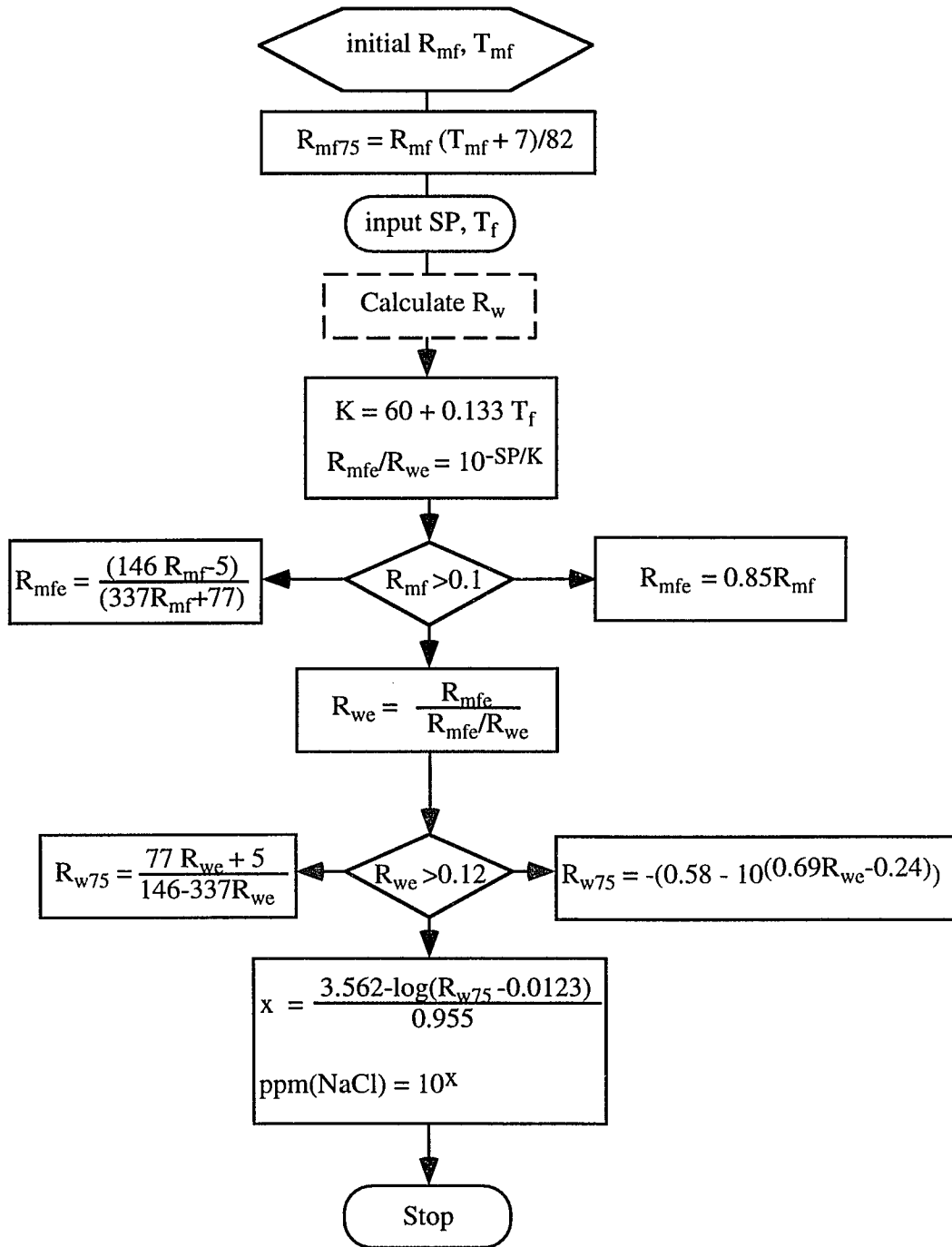
Figure 6.3. Logic flow diagram for salinity estimation from SP logs. Modified from Bateman (1985).
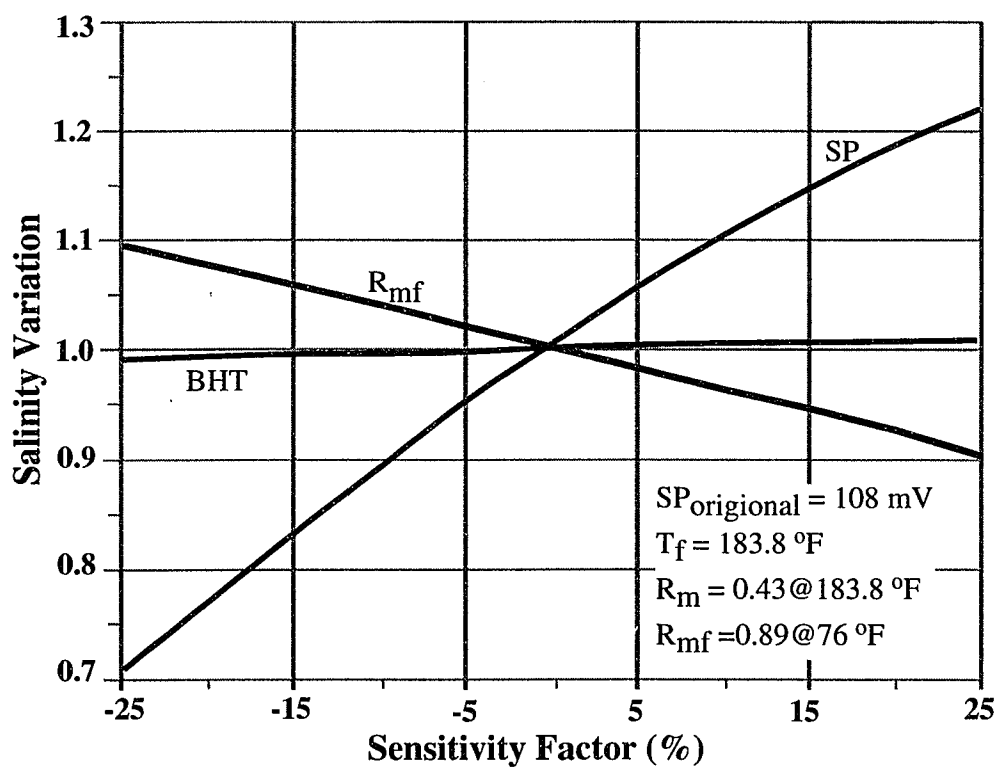
Figure 6.4. Salinity variation with factors: SP, R_{mf} and BHT. SP is the spontaneous potential response, R_{mf} is the resistivity of mud filtrate and BHT is the bottom hole temperature. Parameters at the reference point is shown above. After Funayama (1990).

such as GA, HB, JD, MG and OI are available for this study. Besides these tops of sand beds, the corresponding structure maps and thicknesses (from Holland et al., 1990) were also used to locate the SP responses of the sand layers. In some places, these sand beds may be difficult to recognize from the SP logs, because the pore spaces of the sand beds are filled with low salinity fluids or hydrocarbons, which have high resistivities and can cause SP values to decrease (shift to the right). In these cases, Gamma Ray logs, which are useful for distinguishing sand and shale, were employed. A typical value, which can represent the average SP response for each of the sand beds in each borehole was then selected for the calculation of salinity.

One of the major difficulties in this study is that we do not have enough records of R_{mf}, as this information was not always recorded on the SP log headers. Thus, assumptions for R_{mf} were necessary. I made a simple statistical investigation based on the available R_{mf} records from the wells within the Block 330, and used the following values when necessary:

Depth (ft)	R_{mf} (ohmm)	T_{surf}
<6000	0.18	75 °F (24 °C)
6000 to 7000	0.41	75 °F (24 °C)
>7000	0.48	75 °F (24 °C)

Because a 10 percent difference of R_{mf} can cause about a 3 percent change in calculated salinity (Figure 6.4), salinity results derived from this study are not quantitative. However, the results may qualitatively provide the general pattern of salinity distribution in the Block 330 area. Because salinity calculation is not sensitive to temperature (Figure 6.4), I simply assume formation temperature linearly increases with depth, with a surface temperature of 24 °C and a gradient of 18.23 °C/km.

6.3.3. Results

Pore water salinities in GA-1, HB-1, JD, MG-1 and OI-1 reservoirs (Figure 6.1b) in the South Eugene Island Block 330 have been obtained from the SP log analysis and

displayed on the corresponding structure maps (from Holland et al., 1985) (Figures 6.5 through 6.10). There are 48 control points in both GA-1 and HB-1 sands, 35 control points in JD sand, 31 in MG-1 sand and 18 in OI sand. Some extreme salinity values, such as the one of 24.1 wt% in the southeast of the block (Figure 6.5a), are believed to be caused by the unsuitable assumptions of the R_{mf} values for the calculations. The range of salinity obtained from this study is roughly consistent with that from the brine sample analysis by Losh and Wood (1995), except in HB sand where the sample salinities are twice lower than those from SP logs (Figure 6.6b).

6.3.3.1. Salinities from SP logs produced before 1985

Estimated pore water salinities from SP logs in the shallower GA-1 and HB-1 sands are generally much higher than those in the deeper JD, MG-1 and OI-1 reservoirs. Salinities from SP logs produced before 1985 (most of them from early 1970's) in GA-1 and HB-1 sands also show systematic variations with respect both to the distance from the faults and the structural high (Figures 6.5a, 6.6a and 6.7). Pore fluids nearer the faults and those within the structural high are lower in salinity with an average of about 7.7 wt% in the GA-1 sand and 8.2 wt% in the HB-1 sand; whereas those farther away from the faults have generally higher salinity, with an average of more than 13.0 wt% in both sand beds. The variations of salinity in these two reservoirs also can be observed directly from some SP logs. One example in the GA-1 sand is shown in Figure 6.11. SP responses nearer the faults have less deflection to the left, indicating pore fluids are higher in resistivity for the movement of electrical ions and should be lower in estimated salinity, compared to those further away from the faults.

Pore water salinities from SP logs produced before 1985 in JD, MG-1 and OI-1 sands are generally low and indicate that no systematic variation in salinity with respect to the distance from the faults in each of the reservoirs. The average salinity in the JD sand is about 6.4 wt%, lower than that of 7.2 wt% in MG-1 sand and that of 6.7 wt% in OI-1 sand.

GA-1 Sandstone   **330**

N

10.6
+
10.0
+
+
7.3

A

+ 8.5

Low Salinity

4.1
+

15.6 +
20.4 +
+ 17.5
14.1 +
8.1

+ 6.1
+ 8.5
7.9
+

5.8
+ 8.9
+

11.4+

11.4
13.6
11.3
13.5 + 15.5

10.8
10.8 ++
+8.2
10.3 +

+11.6
11.4 20.0
+ + + 15.0
+8.9
+10.1 +
12.2

7.0
+

4200

+ 24.1

16.0
+
14.8 +
+
11.9

14.5

High Salinity

O/W

4400

4600

|◄——— 1 mile ———►|

O/W   oil/water interface   4400-   Structural contour

     Fault   Low salinity zone
                         (<9.0 wt%)

14.8   Salinity (wt%) from SP logs before 1985

Figure 6.5a. Structural map of GA-1 sandstone in South Eugene Island Block 330, showing the salinity (wt%) distribution, obtained from the SP logs before 1985 (most of them from early 1970's). The light lines outline the structure feature of GA-1 sandstone. Contour values are in feet. The dark area represents the low salinity zone (<9.0 wt%). The structure data are originally from Holland et al. (1986). Also see Figure 6.5b for the salinity distribution after 1985 for comparison. Salinity variation with distance from fault zone along A-A' is displayed in Figure 6.7.

O/W   oil/water interface

Fault

14.8   Salinity (wt%) from SP logs after 1985

10.3   Sample salinity (wt%) from 1994

$_{4400-}$ Structural contour

Low salinity zone
(< 9.0 wt%)

Figure 6.5b. Structural map of GA-1 sandstone in South Eugene Island Block 330, showing the salinity (wt%) distribution obtained from the SP logs produced after 1985 (numbers without underline) and brine sample measurement in 1994 (numbers with underline). The light lines outline the structure feature of GA-1 sandstone. Contour values are in feet. The dark area represents the possible low salinity zone (<9.0 wt%). Compared to Figure 6.5a, low salinity fluids are nearer the fault zone. The structure data are originally from Holland et al. (1986).

O/W	oil/water interface		$_{4400-}$	Structural contour

Fault

Low salinity zone
(<9.0 wt%)

14.8   Salinity (wt %) from SP logs before 1985

Figure 6.6a. Structural map of HB-1 sandstone in South Eugene Island Block 330, showing the salinity (wt%) distribution obtained from the SP logs before 1985 (most of them from early 1970's). The light lines outline the structure feature of HB-1 sandstone. Contour values are in feet. The dark area represents the low salinity zone (<9.0 wt%) before 1985. Also see Figure 6.6b for the salinity distribution after 1985 for comparison. The structure data are originally from Holland et al. (1986). Salinity variation with distance from fault zone along B-B' is displayed in Figure 6.7.

152
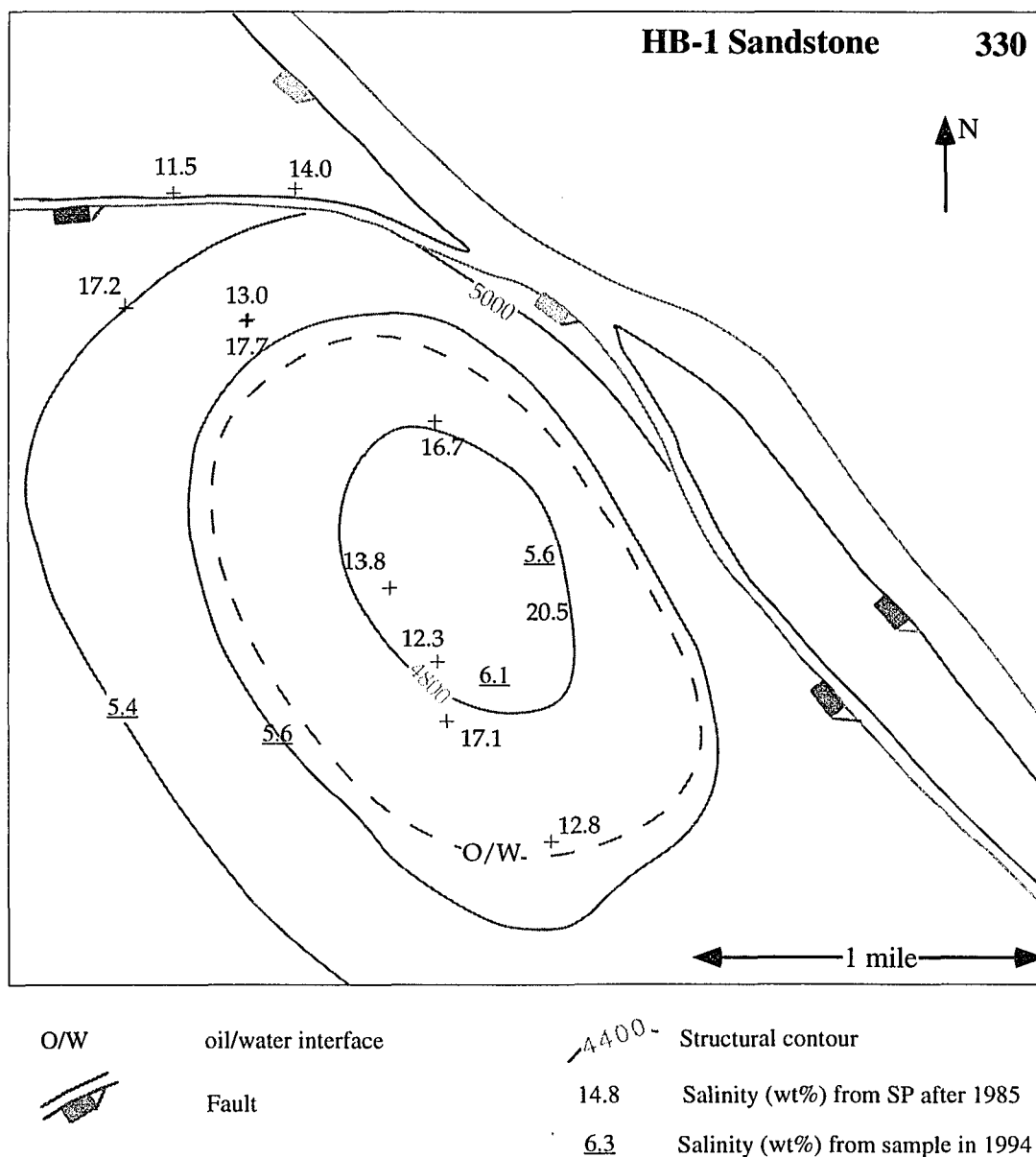
Figure 6.6b. Structural map of HB-1 sandstone in South Eugene Island Block 330, showing the salinity (wt%) distribution obtained from the SP logs after 1985 (numbers without underline) and brine sample measurement in 1994 (numbers with underline). All salinity values from SP logs are higher than 9.0 wt%, much higher than those from brine samples which might be contaminated (see Section 6.3.3.2 for the detail). The light lines outline the structure feature of HB-1 sandstone. Contour values are in feet. Also see Figure 6.6a for the salinity distribution before 1985 for comparison. The structure data are originally from Holland et al. (1986).
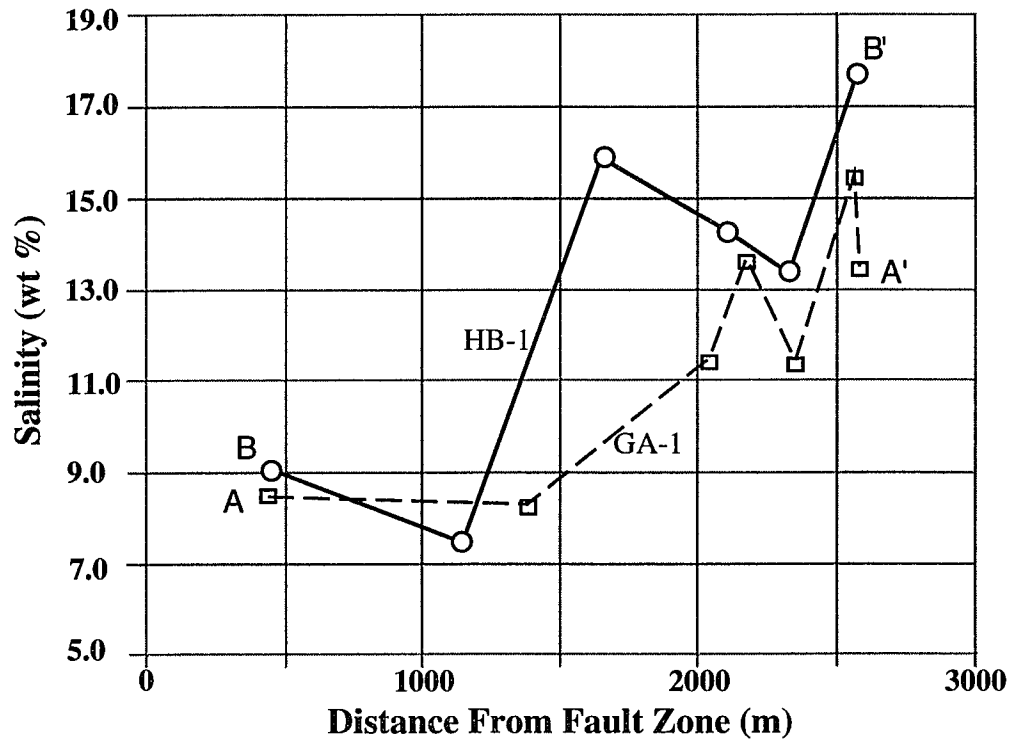
Figure 6.7. Salinity Variation with the distance from the fault zone along A-A' in GA-1 sandstone, and B-B' in HB-1 sandstone. Note only those from the SP logs before 1985 are plotted here. See Figures 6.5a and 6.6a for the locations of A-A' and B-B'.
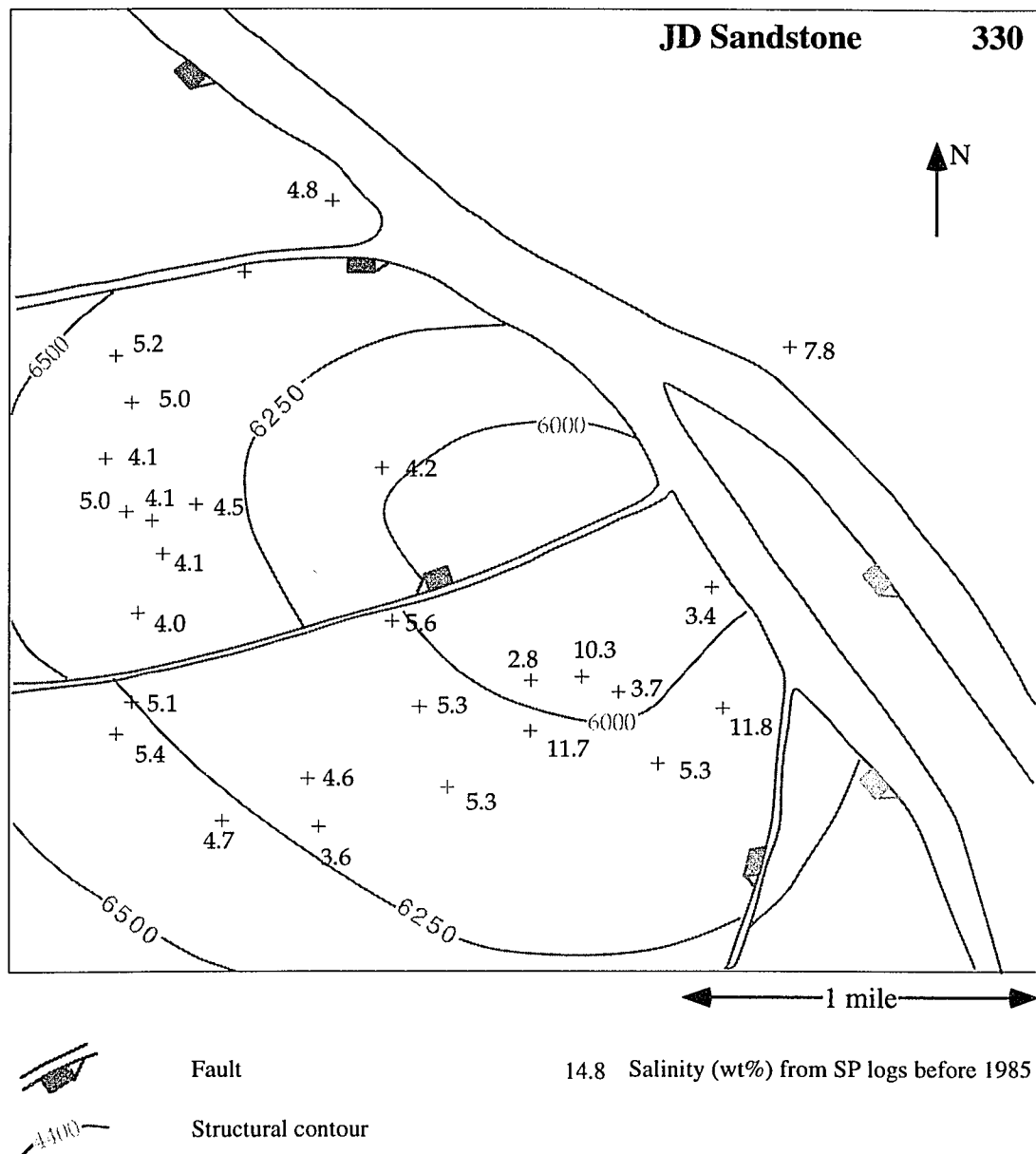
Figure 6.8a. Structural map of JD sandstone in South Eugene Island Block 330, showing the salinity (wt%) distribution obtained from the SP logs produced before 1985 (most of them from early 1970's). These salinity values are significantly lower than those in GA-1 and HB-1 sands. The light lines outline the structure feature of JD sandstone. Contour values are in feet. The structure data are originally from Holland et al. (1986).

JD Sandstone   **330**

Fault   11.8   Salinity (wt%) from SP logs after 1985

Structural contour   6.3   Sample salinity (wt%) from 1994

Figure 6.8b. Structural map of JD sandstone in South Eugene Island Block 330, showing the salinity (wt%) distribution obtained from the SP logs produced after 1985 (numbers without underline) and from brine sample measurement (number with underline) in 1994. There is no significant difference between the values shown here and those in Figure 6.8a. The light lines outline the structure feature of JD sandstone. Contour values are in feet. The structure data are originally from Holland et al. (1986).

MG-1 Sandstone   **330**

Fault   14.8   Salinity (wt%) from SP logs before 1985

_4400_-   Structural contour
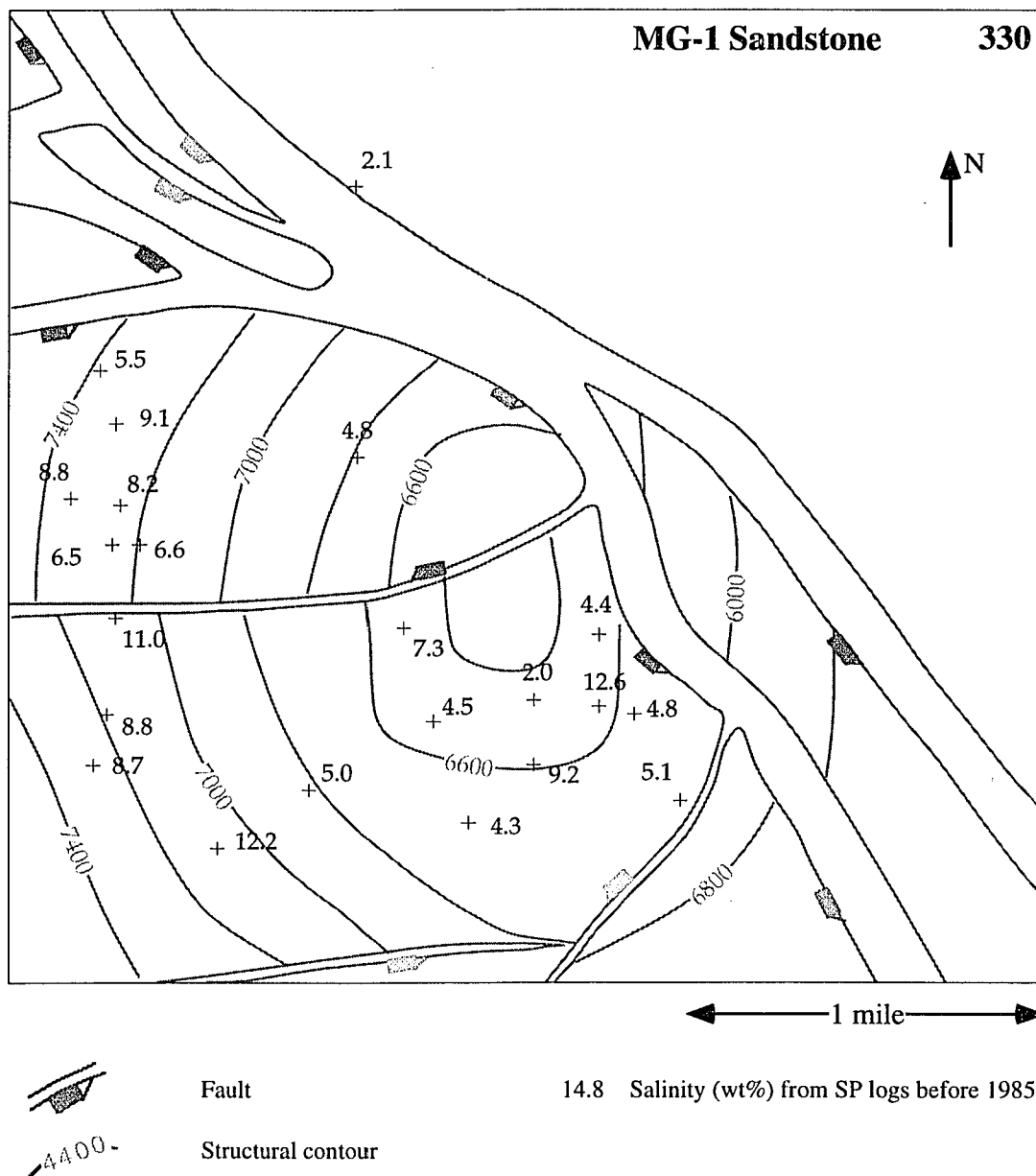
Figure 6.9a. Structural map of MG-1 sandstone in South Eugene Island Block 330, showing the salinity (wt%) distribution obtained from the SP logs before 1985 (most of them from early 1970's). These salinity values are relatively lower than those in GA-1 and HB-1 sands. The light lines outline the structure feature of MG-1 sandstone. Contour values are in feet. The structure data are originally from Holland et al. (1986).
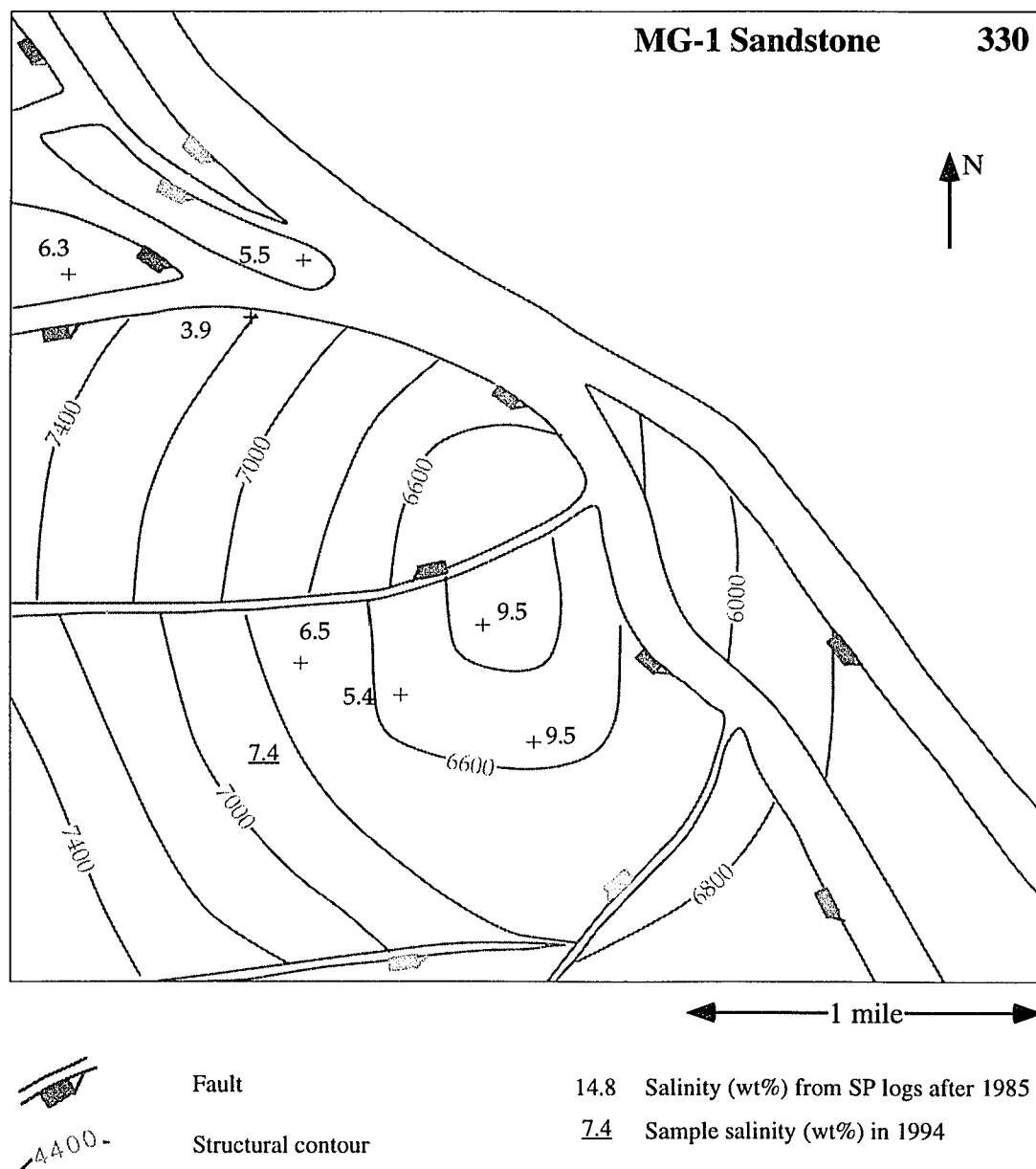
Figure 6.9b. Structural map of MG-1 sandstone in South Eugene Island Block 330, showing the salinity (wt%) distribution obtained from the SP logs produced after 1985 (numbers without underline) and from brine sample measurement (number with underline) in 1994. There is no significant difference between the values shown here and those in 6.9a. The light lines outline the structure feature of MG-1 sandstone. Contour values are in feet. The structure data are originally from Holland et al. (1986).

OI-1 Sandstone **330**

N

+ 3.5

8200 4.2
+

7800

+3.3

7400

7000

8.4
+
7000

O/W -

6600

+
11.2

O/W
7400

5.1
+

5.5
+
7000

8.0
+

+
4.4

7800

8200

7000
O/W +
5.1

7000

+8.7

+ 8.3

O/W

+
5.9
7400

1 mile

Fault   14.8   Salinity (wt%) from SP logs before 1985

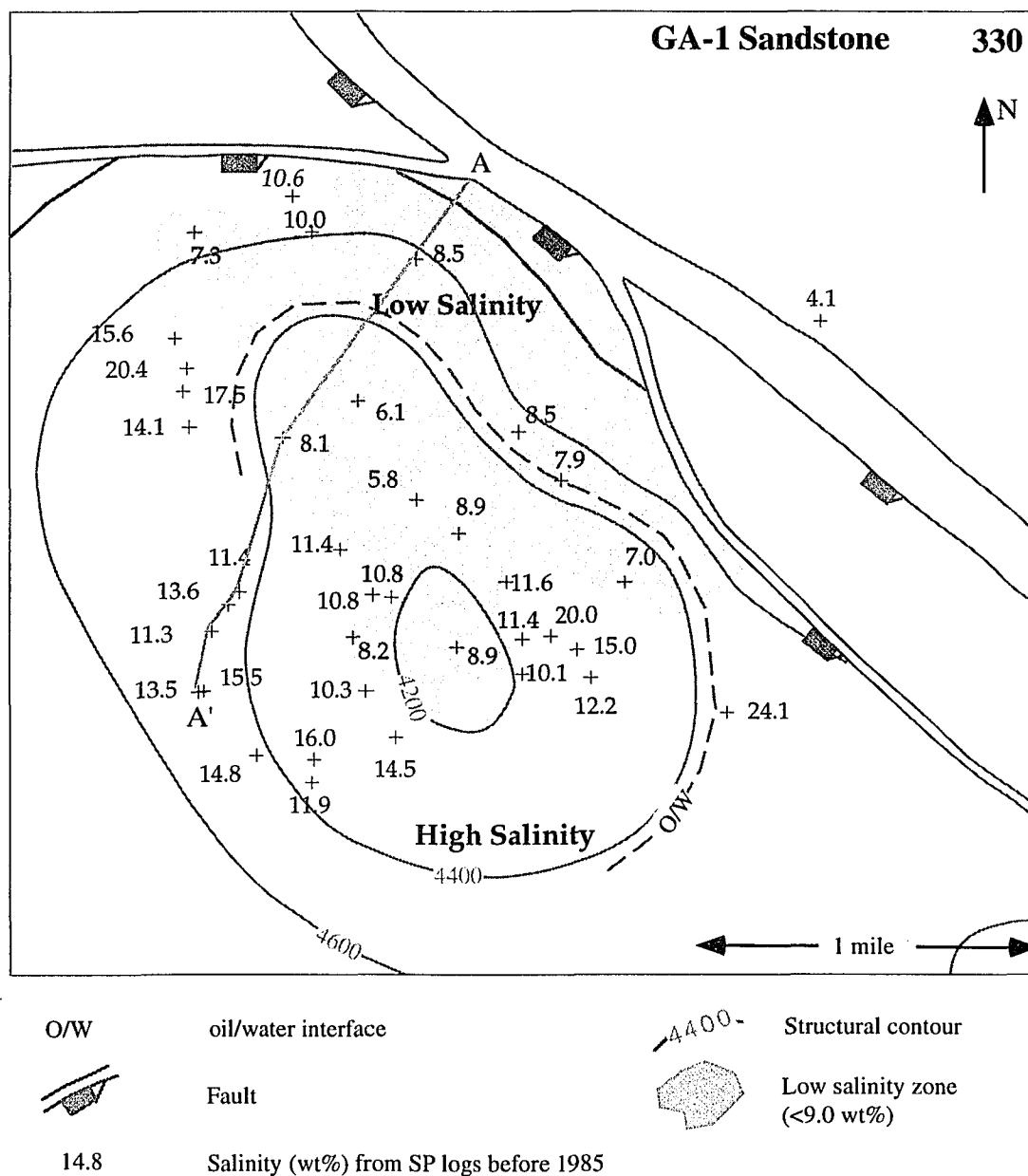4400 -   Structural contour
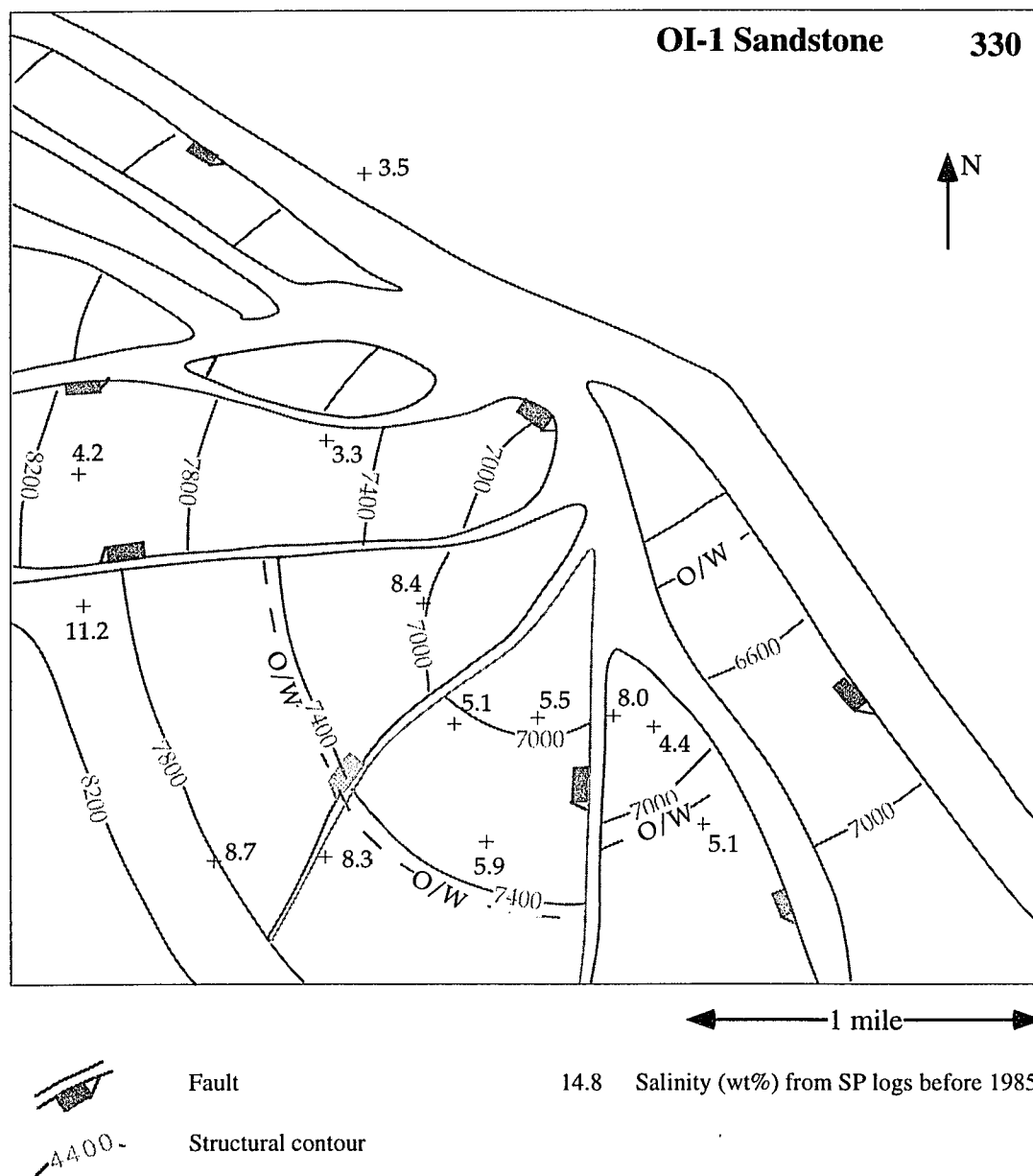
Figure 6.10a. Structural map of OI-1 sandstone in South Eugene Island Block 330, showing the salinity (wt%) distribution obtained from the SP logs before 1985 (most of them from early 1970's). These salinity values are relatively lower than those in GA-1 and HB-1 sands. The light lines outline the structure feature of OI-1 sandstone. Contour values are in feet. The structure data are originally from Holland et al. (1986).

OI-1 Sandstone   **330**

N

6.4 +4.3
7.8 +
8200
7800
7400
7000
7000
8.9 +
O/W
8.0 +
10.4 + 3.3
9.0
O/W
7000
6600
7000
O/W
7000
8200
7800
O/W 7400

—1 mile—

Fault   14.8   Salinity (wt%) from SP logs after 1985

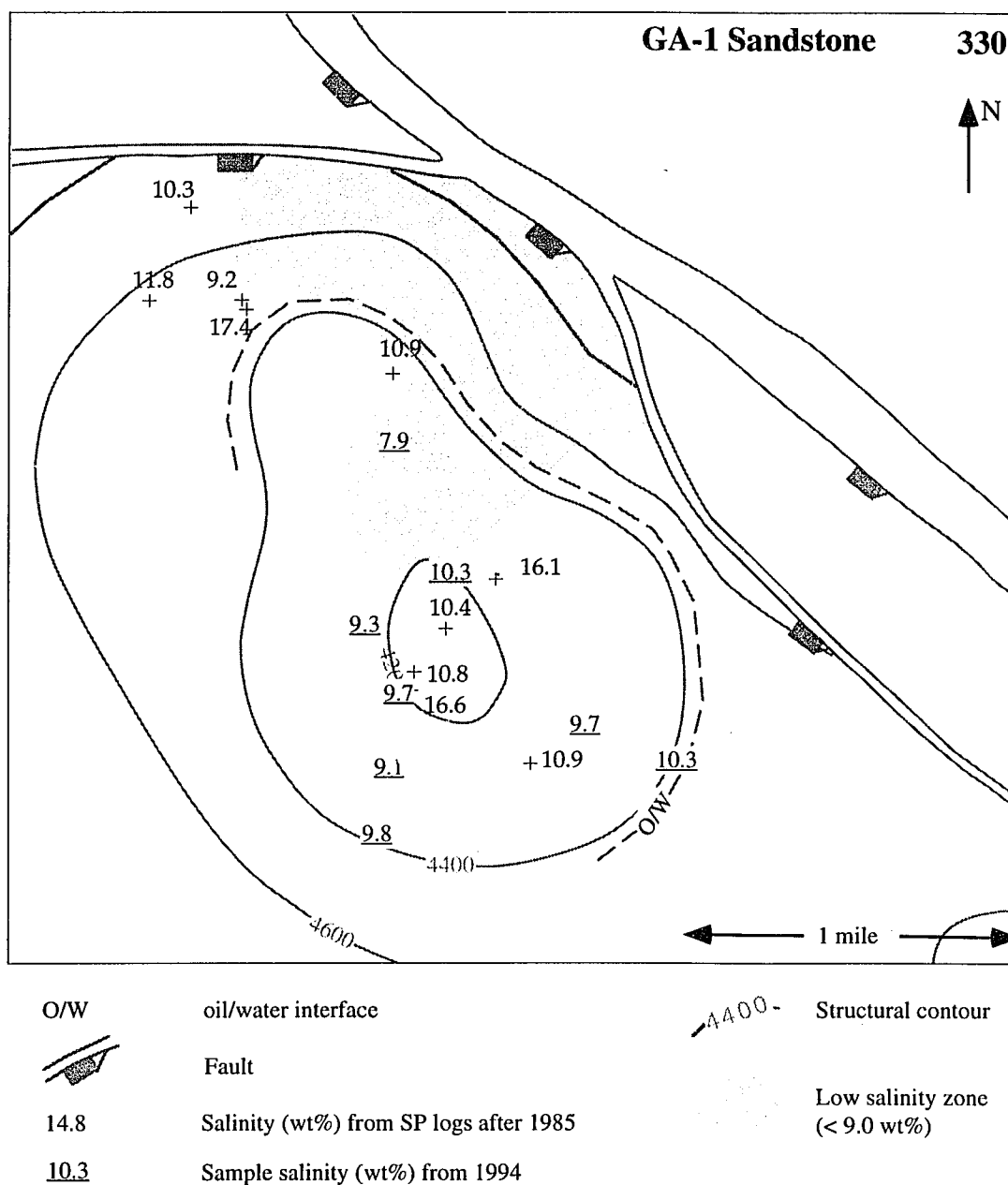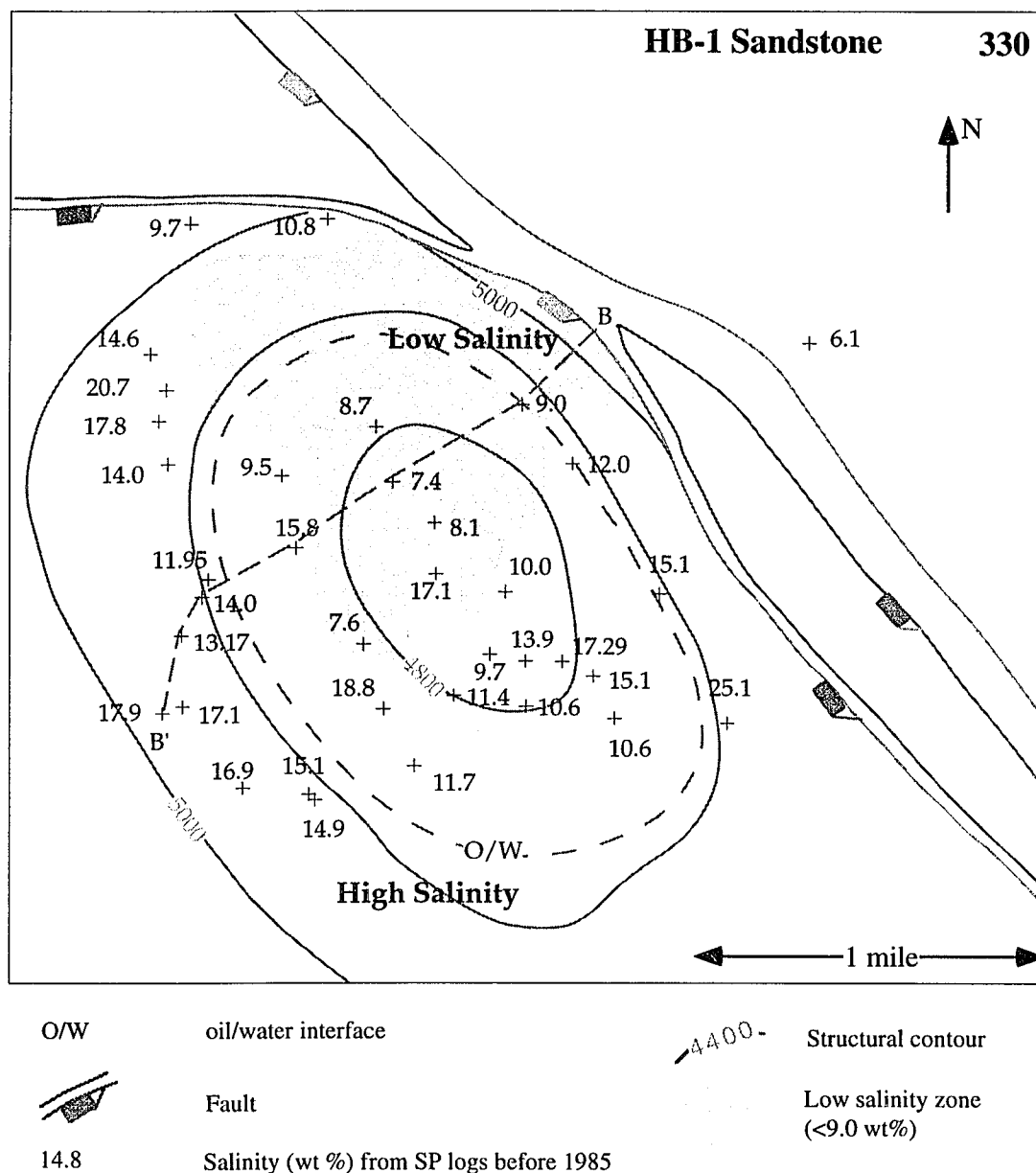Structural contour   6.4   Sample salinity (wt%) in 1994
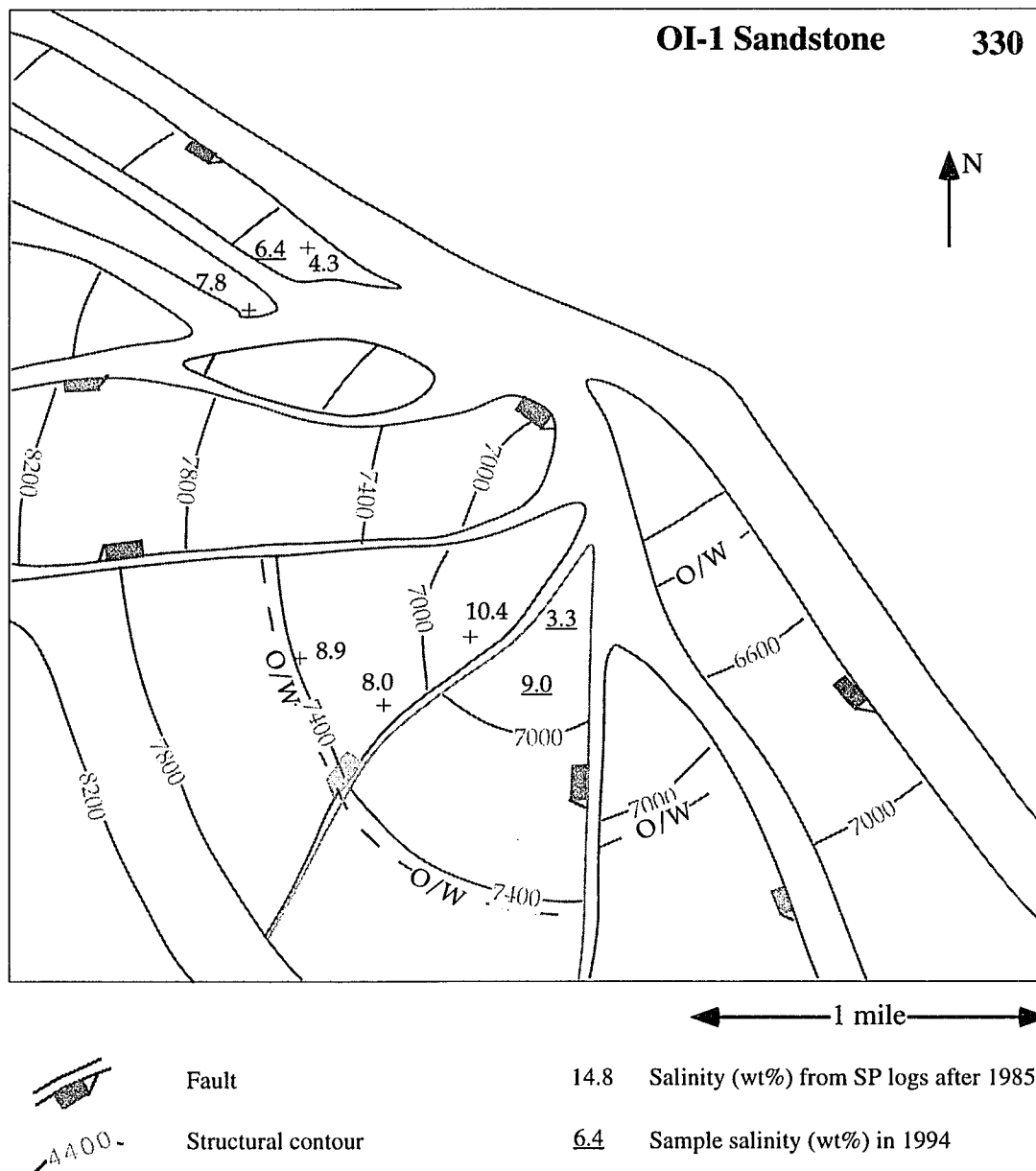
Figure 6.10b. Structural map of OI-1 sandstone in South Eugene Island Block 330, showing the salinity (wt%) distribution obtained from the SP logs produced after 1985 (numbers without underline) and from brine sample measurement (numbers with underline) in 1994. There is no siginificant difference between the values shown here and those in Figure 6.10a. The sample with salinity 3.3 could be contaminated (see Section 6.3.2.2. for the detail). The light lines outline the structure feature of OI-1 sandstone. Contour values are in feet. The structure data are originally from Holland et al. (1986).
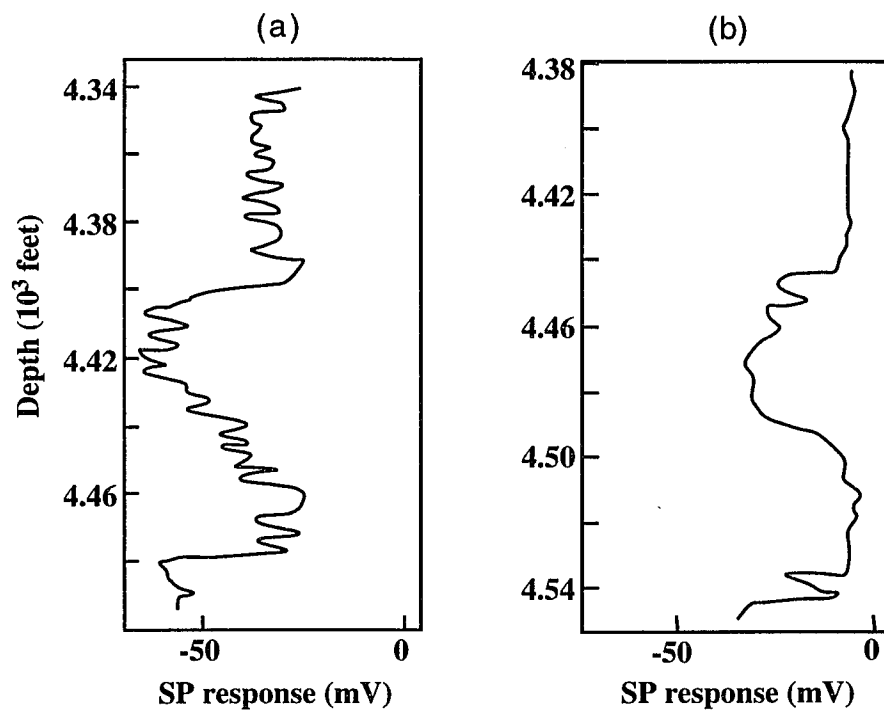
Figure 6.11. Comparison of SP response in GA-1 sand between high salinity zone (a), which is far away from the fault zone, and low salinity zone (b), which is close to the fault zone.

It is quite common to find fresher water in shallow sands and increasingly saline water with depth in many sedimentary basins (Bateman, 1985). Such a progression is shown in Figure 6.12a, where the SP appears deflected to the left deep in the well but is reversed nearer the surface. However, in the South Eugene Island Block 330 area, pore water salinity increases up to depths of 4,000 ft (1220 m) and then starts to decrease below 5,000 ft (1524 m); except at depths around 6,600 ft (2012 m), where the JD sand (hydrocarbon gas dominant) is located (Figure 6.12b). The decreasing SP deflection with depth is believed to be caused by decreasing pore water salinity.

6.3.3.2. Salinities from SP logs produced after 1985 and from sample measurement

Salinity estimation from the SP logs measured after the middle of 1980's is found to be significantly higher than those measured in the early 1970's in the shallower reservoirs GA and HB (see Figures 6.5b and 6.6b). Whereas in the deeper reservoirs JD, MG and OI, salinity does not vary much with time (see Figures 6.8b, 6.9b and 6.10b). Salinities obtained from the new SP logs also does not show systematic variations with respect to the distance from the fault zone.

Estimated salinities in GA-1, JD, MG, and OI sands are basically consistent with the observation from Losh and Wood (1995), 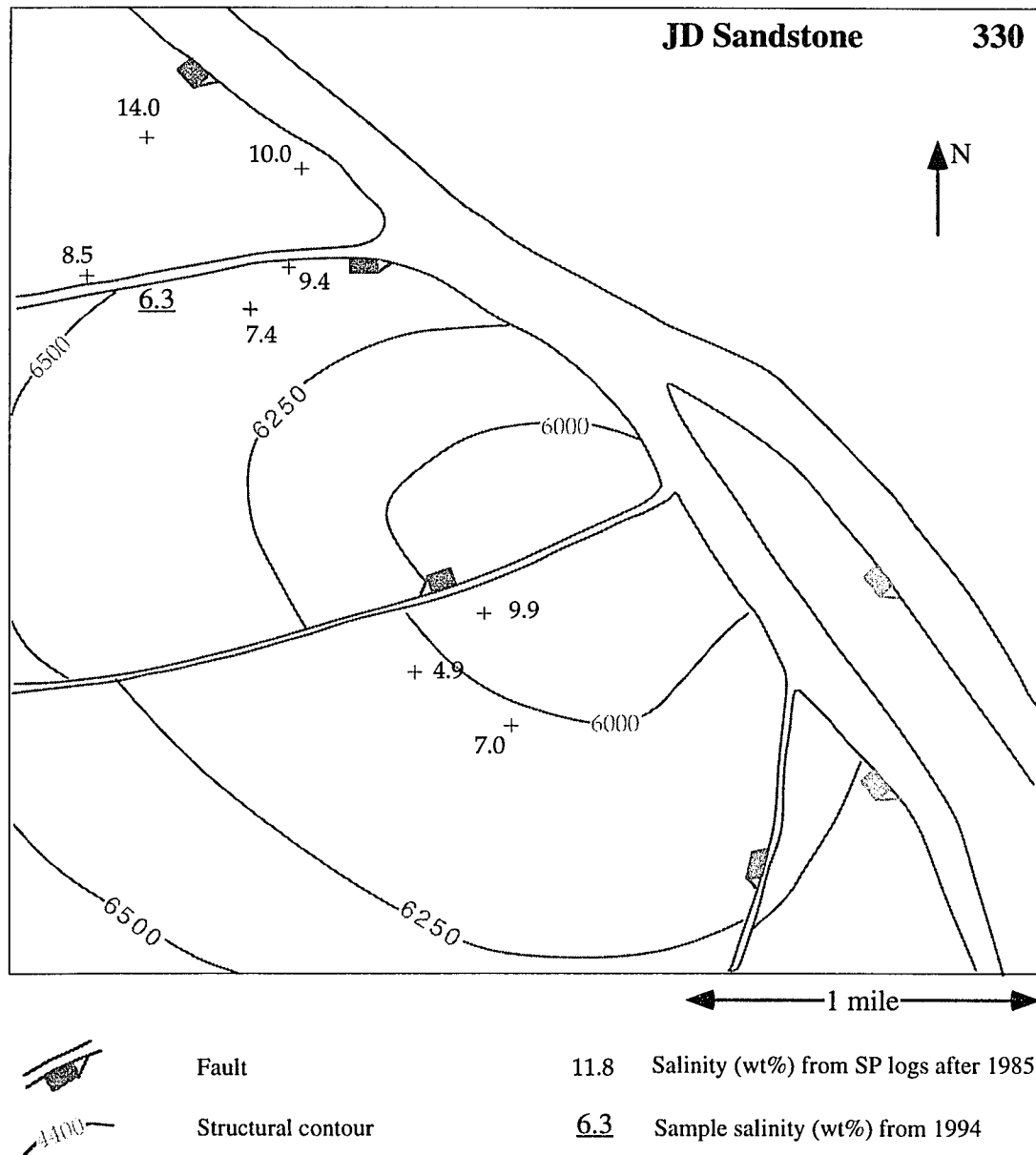who used samples that were collected from producing wells in South Eugene Island Block 330 and 316 in January of 1994 (see Figures 5.6b, 6.8b, 6.9b and 6.10b). However, the average chloride concentration from the four samples in HB sand is about 56825 ppm, at least twice lower than those from the SP log analysis (Figure 6.6b). This difference can be explained by the sample contamination during the collection or by completion fluid. Reasons supporting this explanation are (1) the average ^{129}I age from these four samples is about 38.5 Ma, much younger than the 48 Ma in GA-1 sand and 49.2 Ma in OI sand (other sand beds do not have sufficient age data); (2) Na^+ and Cl^- relationship in these four samples fits the seawater evaporation trend; (3) the average Ca^{++} concentration from these four samples is about 2118 ppm, much lower than that (about 3500 ppm) from other samples;
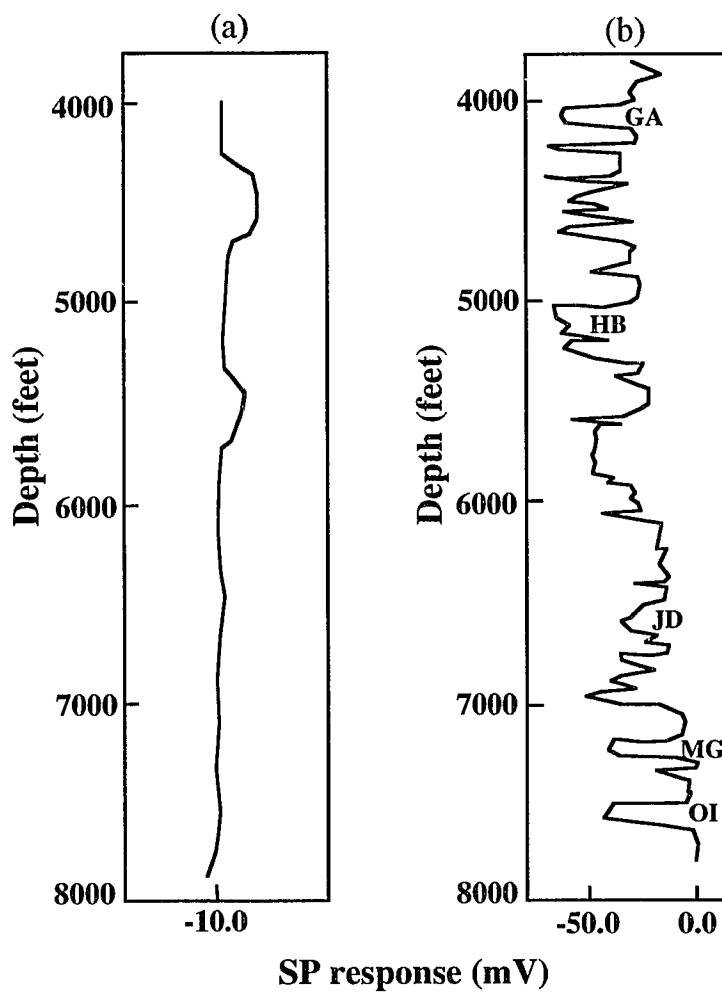
Figure 6.12. (a) shows a typical SP response in a sedimentary basin, where pore water salinity increases with depth. (b) diagram shows the characteristics of SP logs in South Eugene Island Block 330. Note that negative deflection to the left increases with depth in (a), whereas that in the (b) decreases with depth below the 5,000 ft. This may indicate that low salinity pore waters exist in deep sediments in South Eugene Island Block 330 field. (a) diagram is originally from Bateman (1985).

(4) the average Sr^{++} concentration from these four samples is about 90 ppm, also much higher than that (>170 ppm) from other samples. The present day seawater has Cl^- concentration of about 20000 ppm, Ca^{++} around 400 ppm, Sr^{++} about 8 ppm (Broecker and Peng, 1981). Losh and Wood (1995) also recognized some of their samples were contaminated by completion fluid. Thus, I suggest that these four sample values in HB sand are not suitable for this study. Another sample in OI sand, which has Cl^- concentration of 33100 ppm, Ca^{++} of 1550 ppm, Sr^{++} of 43.8 ppm, might also be contaminated and should not be used.

6.3.4. Discussion

Because the errors in the salinity distribution obtained from this study are high, owing to the insufficient records of mud filtrate resistivity, the results of this study only can be qualitatively used to explain the possibility of the migration of geopressured fluids along the fault zone. It is also necessary to remember that the hydrocarbon component in the reservoir sands can significantly effect the SP deflection and result in under-estimation of the pore water salinity. The quantitative relationship between the hydrocarbon content and its effect on the SP deflection is beyond the scope of this study. However, the results of this study indicate that the distribution of pore fluid salinity is not consistent with the hydrocarbon phases in GA-1, HB-1, MG-1 and OI-1 sands (compare especially the oil-water interface and salinity field in Figures 6.5 and 6.6). This suggests that the hydrocarbon phases do not produce a dominant erroneous effect on salinity calculation in these reservoir sands. Sand thickness and shale percentage of the reservoir also can result in the variation of SP deflection. Thick and clean sand beds are favorable for the movement of electrical ions and result in larger SP deflections than the thin and high percentage shale sand beds. However, the net sand isopath of each of the reservoirs (Holland et al., 1990) is quite different from the estimated salinity fields. Thus, thickness and shale percentage of the sand bed can not explain the salinity variation in this area either.

The deeper reservoirs (OI, MG and JD) received geopressured fluids earlier; so they should store more low salinity fluids than the shallower reservoirs (HB and GA). This can explain why the MG-1 and OI-1 sands are all filled with low salinity fluids (and hydrocarbon components) within the Block 330 (Figures 6.9 and 6.10); whereas GA-1 and HB-1 are only partially filled with low salinity fluids (Figures 6.5 and 6.6). The distribution of salinity in each of the reservoir sand is also believed to be significantly affected by pumping of production wells, which draw fluids towards them.

The invariant salinity with age in the deep GM and OI sands may be explained as resulting from the present fault zone acting as a hydrological conduit to the deeper sediments, which are close to the geopressured sediments. Whereas, the shallow reservoirs GA and HB may be recently fault-sealed or partially fault-sealed, because they show an increase in salinity with time in the area close to the fault zone. If the fault zone is sufficiently permeable, then fresher geopressured fluids can continuously supply the loss caused by production pumping, and maintain a low salinity zone in the area close to the fault. The fault-seal mechanism in the shallow reservoirs is consistent with the hydrostratigraphy study of Flemings et al. (in prep.). However, Flemings et al. suggest that the MG and OI sandstones also are in a fault-sealed environment.

Hydrocarbon reservoirs in the present day fault-sealed zone must have been filled during the time when faulting was more active and generated sufficient fractures within the fault zone. A critical question is what is the average permeability that a present fault-sealed zone can maintain during venting of geopressured fluids. Roberts et al. (1996) suggested from their numerical study that fractures within the fault zone must initially be wide enough to increase the permeability to at least 10 mD and that adjacent sediments must be incompressible enough to maintain permeability above 1 mD approximately 20 to 30 years after expulsion begins to transport sufficient fluids across the seal to form temperature and pressure anomalies similar to those observed in the South Eugene Island area.

The following numerical study uses salinity equations to demonstrate the possibility that the geopressured fluids are able to reach the shallow reservoirs during a single episode of expulsion and generate the salinity anomalies as observed in the above SP log analysis, given the hydrogeological conditions suggested by Roberts et al. (1996.). I will also conduct a post-venting case to understand the long term consequence of the expulsion and explore additional mechanism for active fluid migration in the hydropressured sediments.

6.4. NUMERICAL SIMULATION OF MIGRATION OF LOW SALINITY GEOPRESSURED FLUIDS ALONG THE FAULT ZONE IN SOUTH EUGENE ISLAND BLOCK 330.

6.4.1. Model description

The geological model used in this numerical study is shown in Figure 6.13. This is a north-south cross section through the South Eugene Island mini-basin, constructed based on stratigraphic data obtained from seismic lines (Alexander and Flemings, 1996). Roberts et al. (1996) originally used this model profile for modeling the expulsion of abnormally pressured fluids along the faults. Because Roberts et al. (1996) did not consider the solute transport in their simulation, their results can not be used to explain the estimated salinity distribution. Roberts et al. (1996) placed a thin (~25 m) seal on the top of geopressured zone (Figure 6.13). Sediments beneath the seal are shale rich, with the exception of a single thin sand layer immediately below the seal. The overlying hydropressured zone contains 11 sand layers, denoted as CA, DA, EA, GA, HB, JD, K, LF, MG, OI and Lentic from top to bottom, separated by shale. The fault zone cuts through all but the uppermost three sand layers and has a constant permeability. Material properties used in the simulations are shown in Table 6.1. According to Domenico and Schwartz (1990), porosity can be assumed to vary with the change of fluid pressure:

$$\phi = \phi' + (1 - \phi')\rho_w \, g \, \beta \, (P - P') \qquad (6.1)$$

where ϕ is the porosity, P is the fluid pressure, ϕ' and P' are the porosity and fluid
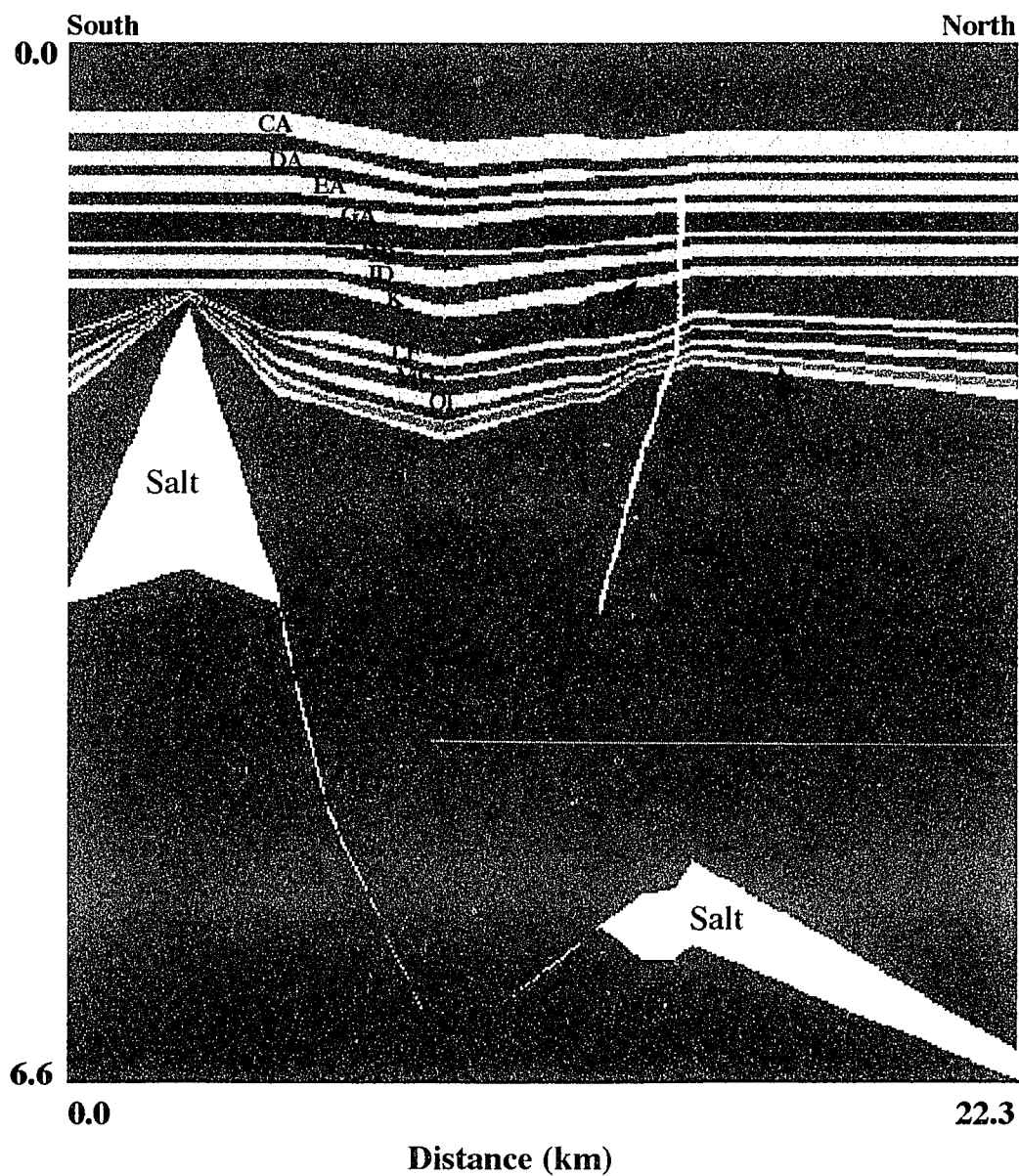
Figure 6.13. Geological model. This is an approximate south-north section across the South Eugene Island, Block 330 Mini-basin. CA, DA, EA, GA, HB, JD, K, LF, MG and OI label the major sand beds in this area. Note that the actual model used in this simulation has a base extended to a depth of 10 km.

pressure in the last time step, ρ_w is the fluid density, g is the gravitation, and β is the vertical compressibility of sediments.

All sediments beneath the seal are assumed to be initially overpressured by 22 MPa and have a uniform salinity of 3.0 wt%; sediments above the seal are hydrostatically pressured and have a salinity of 13.0 wt%. The model mesh contains 86 columns and 91 rows. I used an initial porosity (on surface) of 0.4 for the sand and 0.5 for the shale based on Domenico and Schwartz (1990). Sediments in Gulf of Mexico basin are relatively under-compacted. Thus, according to Domenico and Schwartz (1990), sand and shale beds may have vertical compressibilities of 1.0×10^{-8} m²/N and 1.5×10^{-8} m²/N respectively. These values are similar to those obtained by Hart et al. (1995) in the south Eugene Island Block 330 field based on the measurement of porosity. All the boundary conditions and other initial conditions and parameters are the same as Roberts et al. (1996).

TABLE 6.1. Physical properties

	Permeability (mDarcy) Kx	Ky	Initial porosity	Thermal conductivity (W/m-K)	Diffusion coefficient (10^{-6} cm²/s)	Vertical compressibility (Pa)$^{-1}$
Sand layers	1.0	0.1	0.4	6.0	2 x porosity	1.0×10^{-8}
Shale layers	0.1	0.01	0.5	6.0	2 x porosity	1.5×10^{-8}
Seal	0.0	0.0	0.0	6.0	0.0	
Fault	10.0	10.0		6.0	2 x porosity	
Salt	0.0	0.0	0.0	6.0	0.0	0

The following simulations are transient cases. Governing equations used in this study are Eqs (15), (23), (24), (25) and (26) in Chapter 2. Fluid density and viscosity are calculated using Eqs (27) and (28) in Chapter 2, respectively. In order to control the perturbations caused by the high contrasts in salinity between the geopressured and hydropressured sediments and between the fault zone and the surrounding sediments

when venting begins, the nodes adjacent to the fault zone and the seal are closely spaced (about 25 m by 15 m), compared to those (about 40 m by 15 m) used by Roberts et al. (1996), who did not consider solute transport in their modeling studies. Time step was 0.1 year in the very early stage of simulation, and it was gradually increased to 10 years at 100 years of modeling time and then remained constant. The method to determine a suitable grid size and time step is described in Chapter 2.

6.4.2. Results from the expulsion of geopressured fluids

With the opening of the seal, overpressured fluid is free to move rapidly along the fault zone into the overlying sediments. The consequence of such an event can be described by the anomalies of fluid pressure, porosity, temperature and salinity.

6.4.2.1. Fluid pressure and porosity variation

Initial model fluid pressure right below the seal is about 42 MPa and is about 90 % of lithostatic pressure, consistent with Hart et al. (1995). Thus, the seal should be easily ruptured under such a high pressure condition (du Rouchet, 1981). Rapid release of fluids results in a decrease in fluid pressure in the overpressured sediments around the fault zone (see Figure 6.14). At an elapsed model time of 50 years, excess fluid pressure right below the venting seal has deceased to 10 MPa (Figure 6.15), about 66 % of lithostatic pressure. However, the drop in fluid pressure slows down after an elapsed model time of 50 years. It takes at least 300 years for the model fluid pressure to reach 60% of the lithostatic pressure, at which I assume the vent reseals (Hunt, 1990).

In the sediments around the fault zone above the seal, the migration of fluids from the underlying geopressured sediments has caused fluid pressure to increase quickly in the first 50 years. Afterward, fluid pressure continued to increase but at a very slow rate (Figure 6.15). At 200 years, the maximum excess fluid pressure anomaly in the sediments above the seal is about 8 MPa. In Chapter 5, I mentioned that the sediments above the seal were subjected to a transient pressure pulse in the early stage of expulsion for both isotropic and anisotropic models. It is interesting to note that there is

Excess fluid pressure at 25 years (venting case)
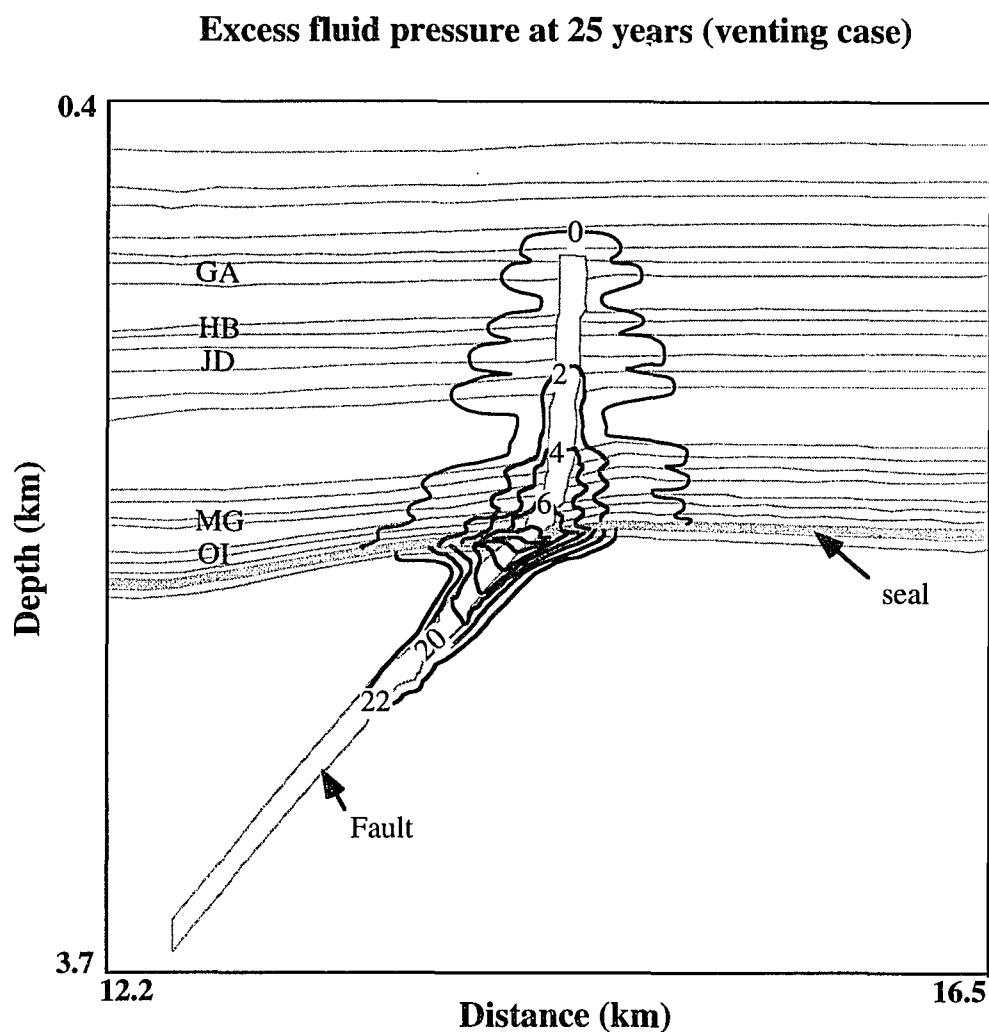
Figure 6.14a. Excess fluid pressure after 25 years of venting. Contour interval is 2.0 MPa. The light lines outline the stratigraphy and fault. GA, HB, JD, MG and OI are the names of sand beds. Note the depth and distance refer to those in model profile in Figure 6.13.

Excess fluid pressure at 300 years (venting case)

Figure 6.14b. Excess fluid pressure after 300 years of venting. Contour values are in MPa. The light lines outline the stratigraphy and fault. GA, HB, JD, MG and OI are the names of sand beds. Note the depth and distance refer to those in the model profile in Figure 6.13.
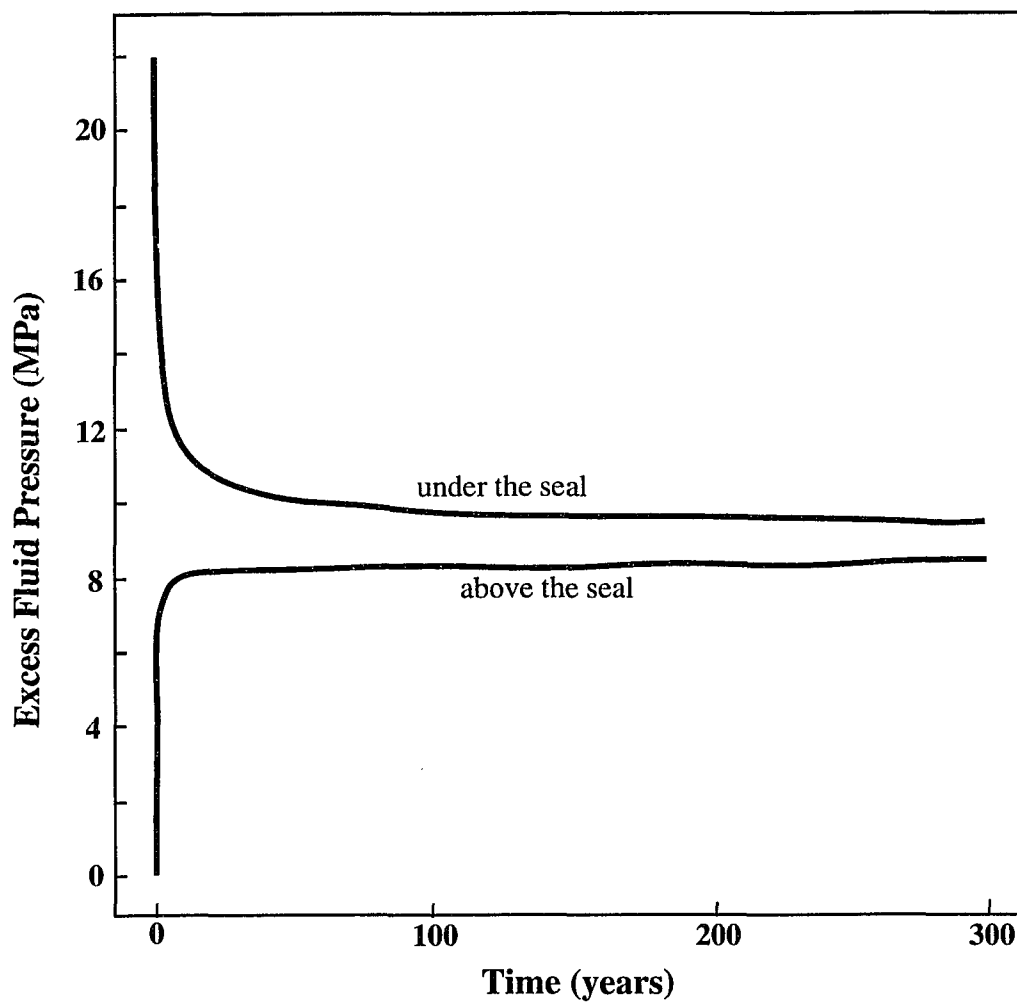
Figure 6.15. Excess fluid pressure variation with time after venting begins for sediments immediately under (upper curve) and above (lower curve) the vent respectively.

no transient pressure pulse in the first 300 years in the current model. Even though results was not obtained after 300 years because the vent was assumed to reseal at that moment, it is believed that fluid pressure above the seal would eventually decrease with time, as the pressure in the geopressured sediments is decreasing. The reason for the difference between the current results and those in Chapter 5 is because the current model considers the compressibility of sediments, and sediments above the seal are not only anisotropic, but strongly heterogeneous.

The expulsion of geopressured fluids can increase the porosity (Figure 6.16) in the hydropressured sediments. For example, porosity in the OI sand bed rapidly increased from its initial value of 0.247 to about 0.29 in the first 10 years and the increase was flow during the remaining period of expulsion, consistent with fluid pressure variation in these sediments (Figure 6.15).

The reason for the porosity increase is that fluid pressure has increased, causing the pore space to expand significantly in the sediments above the seal (Eq. 6.1). The expansion of pore space caused by increase in fluid pressure implies that the efficiency of fluid pressure transport can be significantly reduced because more fluid is stored in the media. In other words, the pressure anomaly can be maintained in the hydropressured sediments for a long time. This also implies that the expulsion of geopressured fluids could last longer in a realistic overpressured sedimentary basin.

The fluid pressure anomaly in the sediments above the seal indicates the preferential movement of fluid and pressure along the permeable sand beds and the fault zone (Figure 6.14). The pressure anomaly is also extremely sensitive to shale permeability. As the permeability of shales in the simulation decreases, flow of geopressured fluid towards the fault zone is severely restricted (also see Roberts et al., 1996).

6.4.2.2. Temperature distribution

The rapid transport of fluids along the fault zone also carries heat, which can generate a thermal anomaly (Figure 6.17). The maximum thermal anomaly is 17 °C at
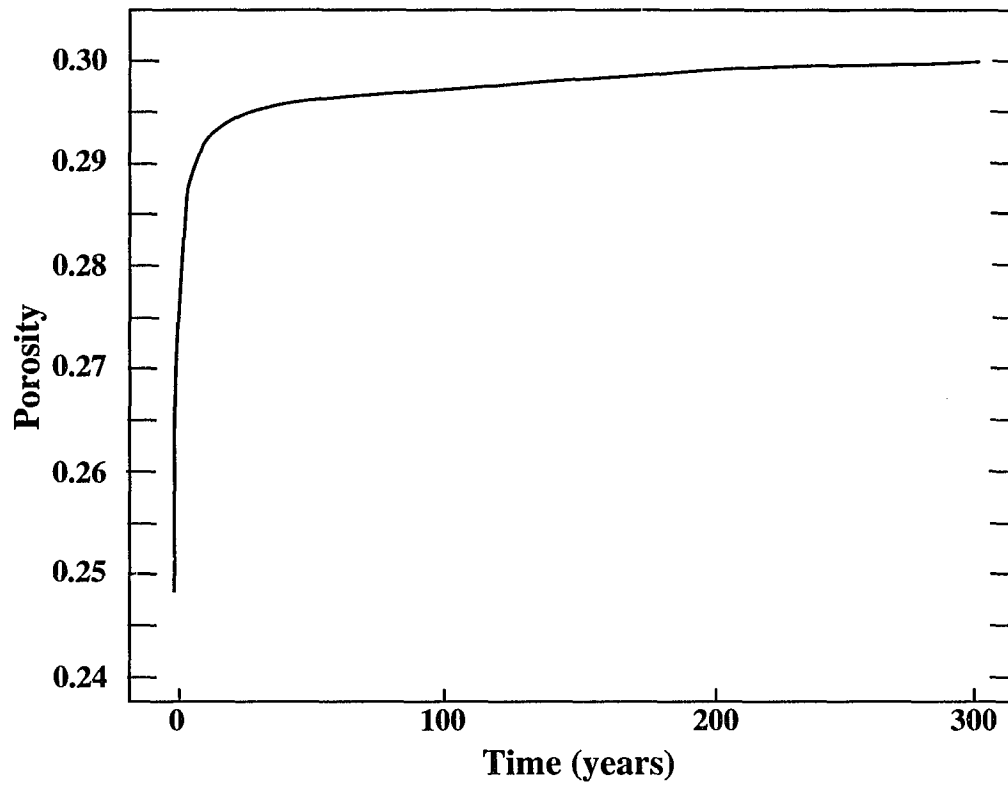
Figure 6.16. Porosity variation with time at sediments immediately above the vent, during the expulsion of geopressured fluids.

Temperature field at 25 years (venting case)
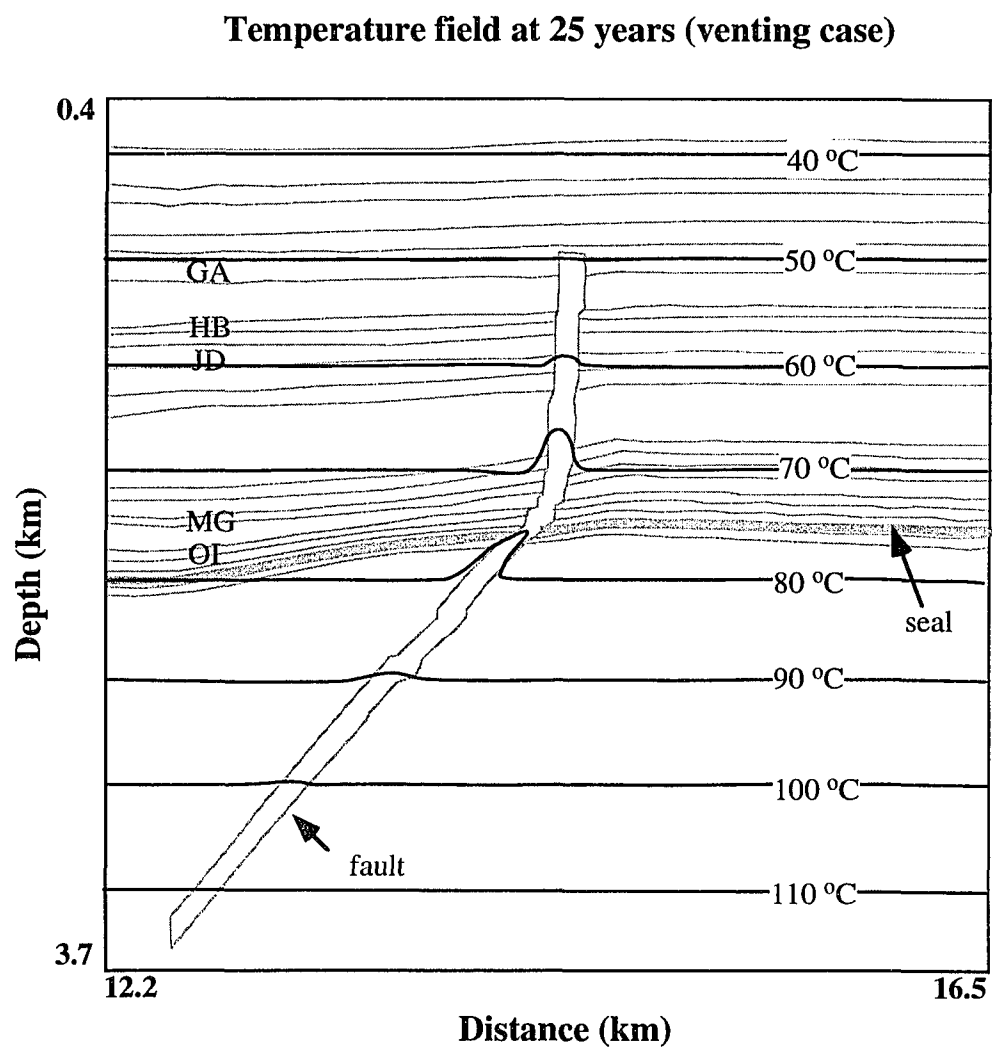
Figure 6.17a. Temperature field after 25 years of venting. The light lines outline the stratigraphy and fault. GA, HB, JD, MG and OI are the names of sand bed. Note that the depth and distance refer to those in Figure 6.13.

Temperature field at 300 years (venting case)

0.4

40 °C

GA

50 °C

HB

JD

60 °C

70 °C

MG

OI

80 °C

seal

90 °C

100 °C

fault

110 °C

3.7

12.2   16.5

Distance (km)

Depth (km)

Figure 6.17b. Temperature field after 300 years of venting. The light lines outline
the stratigraphy and fault. GA, HB, JD, MG and OI are the names of sand beds.
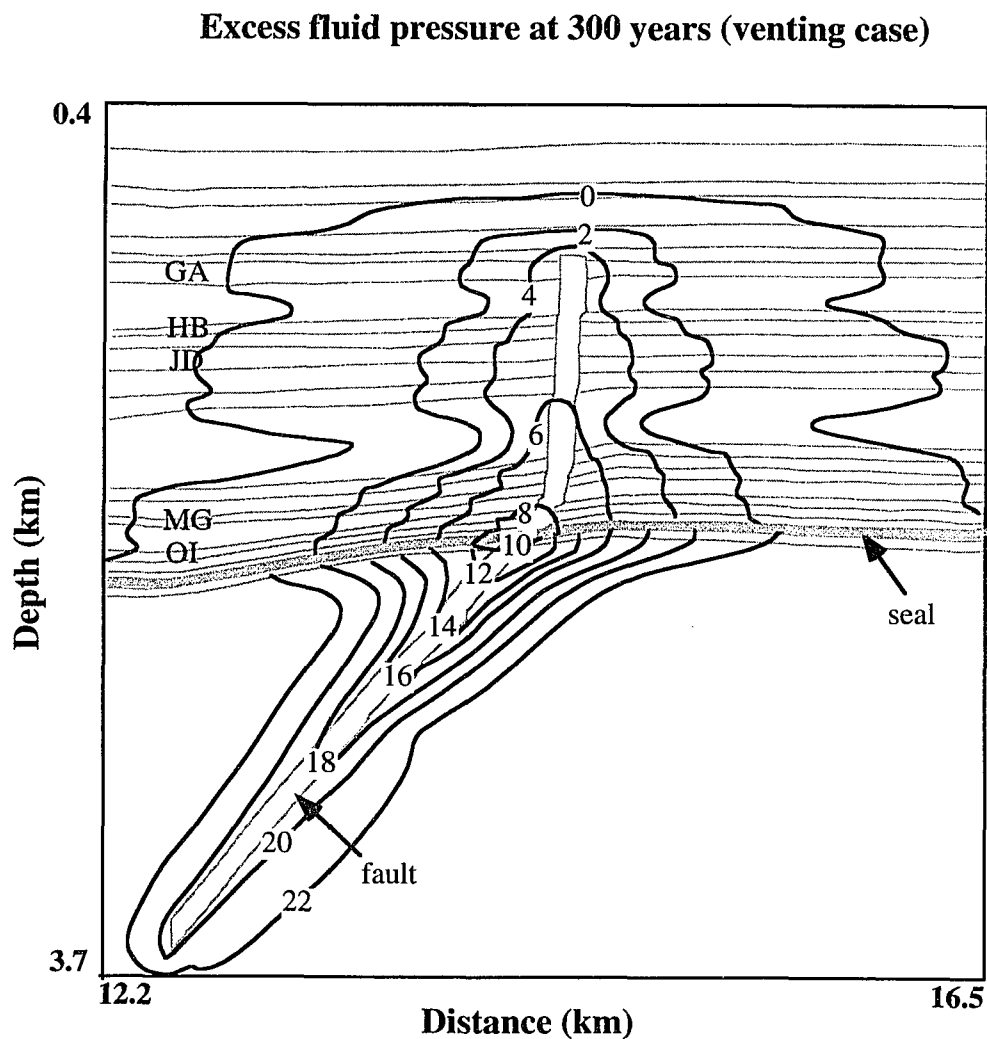Note that the depth and distance refer to those in Figure 6.13.

200 years. Although this thermal perturbation grows as expulsion continues, it is essentially confined to those sediments immediately adjacent to the fault zone. After 300 years of expulsion, isotherms in the upper 0.75 km of the model section are undisturbed and the thermal anomaly extends less than 0.5 km into the sediments on either side of the fault zone. Heat transport is only efficient when fluid is moving vertically in the fault zone.

6.4.2.3. Fluid flow and salinity anomaly

Figure 6.18 shows the fluid flow field at 200 years after the seal ruptures. The pattern of the flow field is similar to that at other time steps. Darcy velocities in the fault are more than 110 m/year in the very early stage of expulsion (Figure 6.19). But they drop quickly to about 20 m/year within the first 20 years. Then the rate of decrease becomes very slow, consistent with the decrease in the fluid pressure in the overpressured sediments. At an elapsed time of 200 years, the maximum Darcy velocity was still as high as 10 m/year.

As mentioned in Chapter 5, pore water salinity can be used as a hydrological tracer to monitor migration of geopressured fluids. Figures 6.20a and 6.20b show the salinity distribution at elapsed times of 25 and 300 years respectively. When the low salinity fluids are expelled into the hydropressured section, the lower sands layers (such as MG and OI) are recharged sooner than the stratigraphically higher sands (such as GA, HB and JD). Thus, the lower sand reservoir sands can receive more low saline fluids than the higher ones during a single episode of expulsion. This phenomenon is consistent with the salinity distributions obtained from the SP analysis. The salinity fields also demonstrates that the geopressured fluids are preferentially migrating along the reservoir sands with sharp fronts.

It is interesting to note that the deeper sand layers on the hanging wall side of the fault zone received more expelled fluids than those on the foot wall side (Figures 6.20a and 6.20b). The sand beds adjacent to the fault zone have a slope of about 4 degree
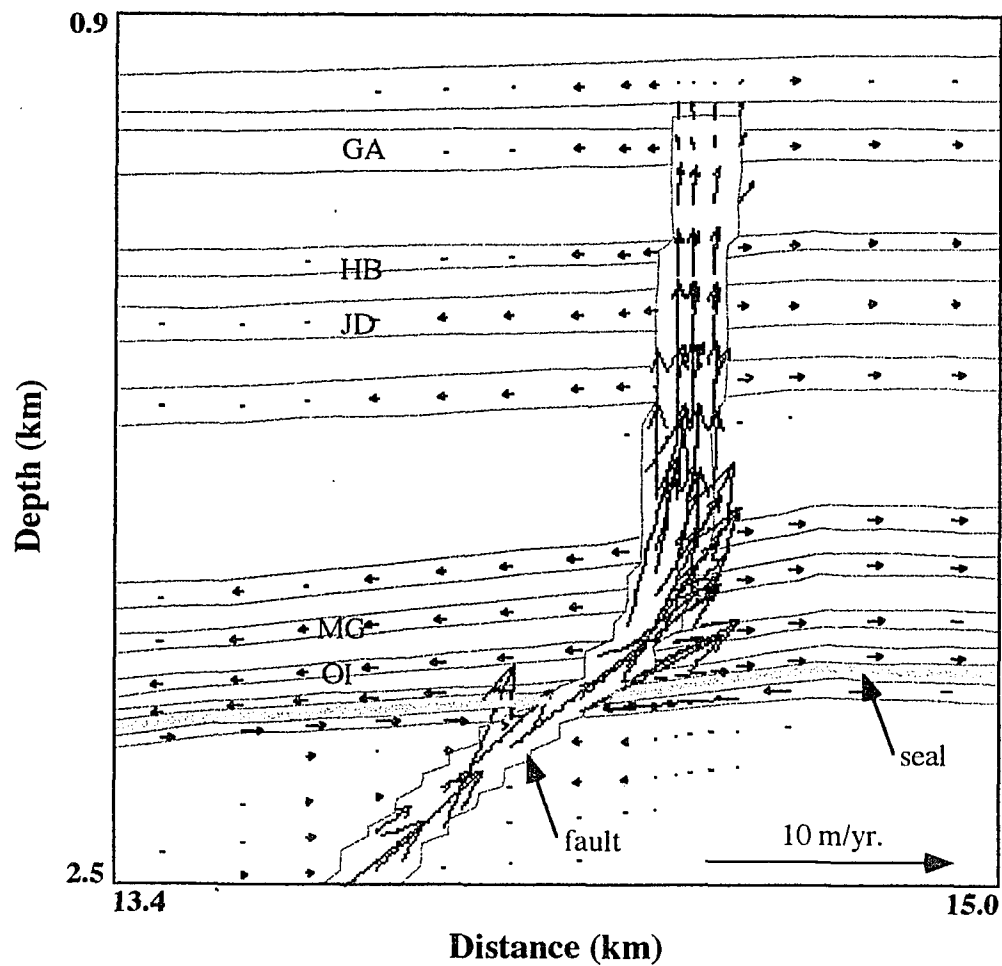
Figure 6.18. Fluid flow field at 200 years after the seal ruptures. Fluids in the sediments under seal are mainly flowing toward the fault zone; whereas those in the sand beds above the seal are moving laterally away from the fault zone. The light lines outline the stratigraphy and the fault. GA, HB, JD, MG and OI and the names of sand bed.
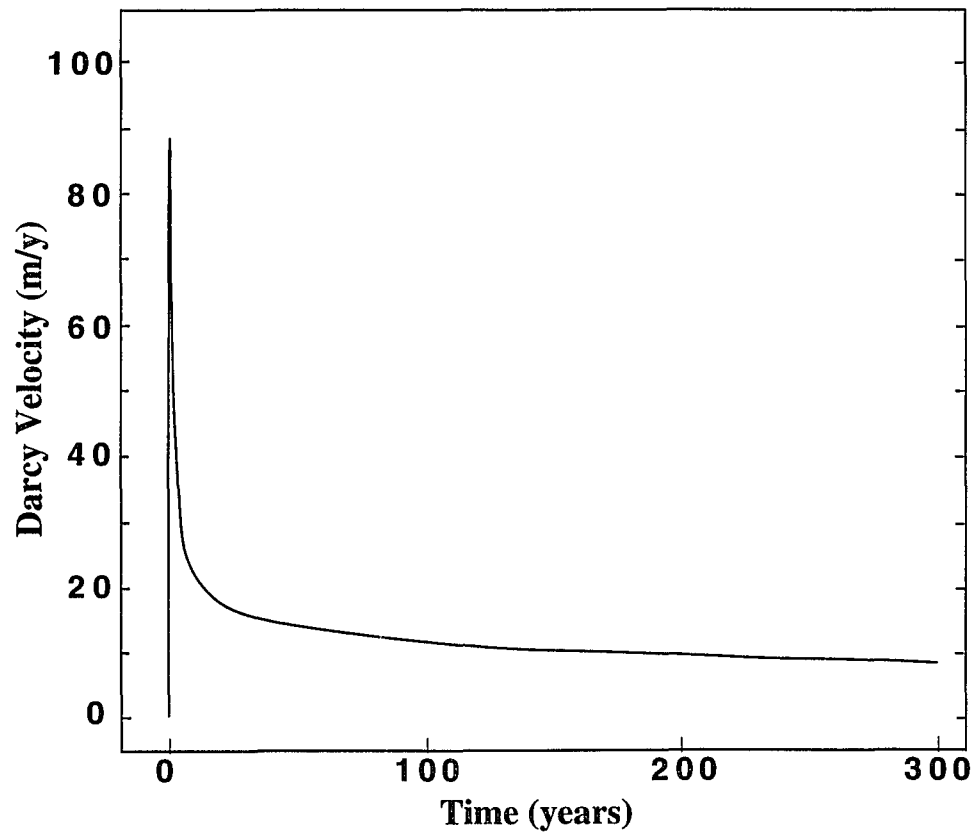
Figure 6.19. Darcy velocity variation with time at the fault/seal intersection after the venting begins.

Salinity distribution at 25 years (venting case)
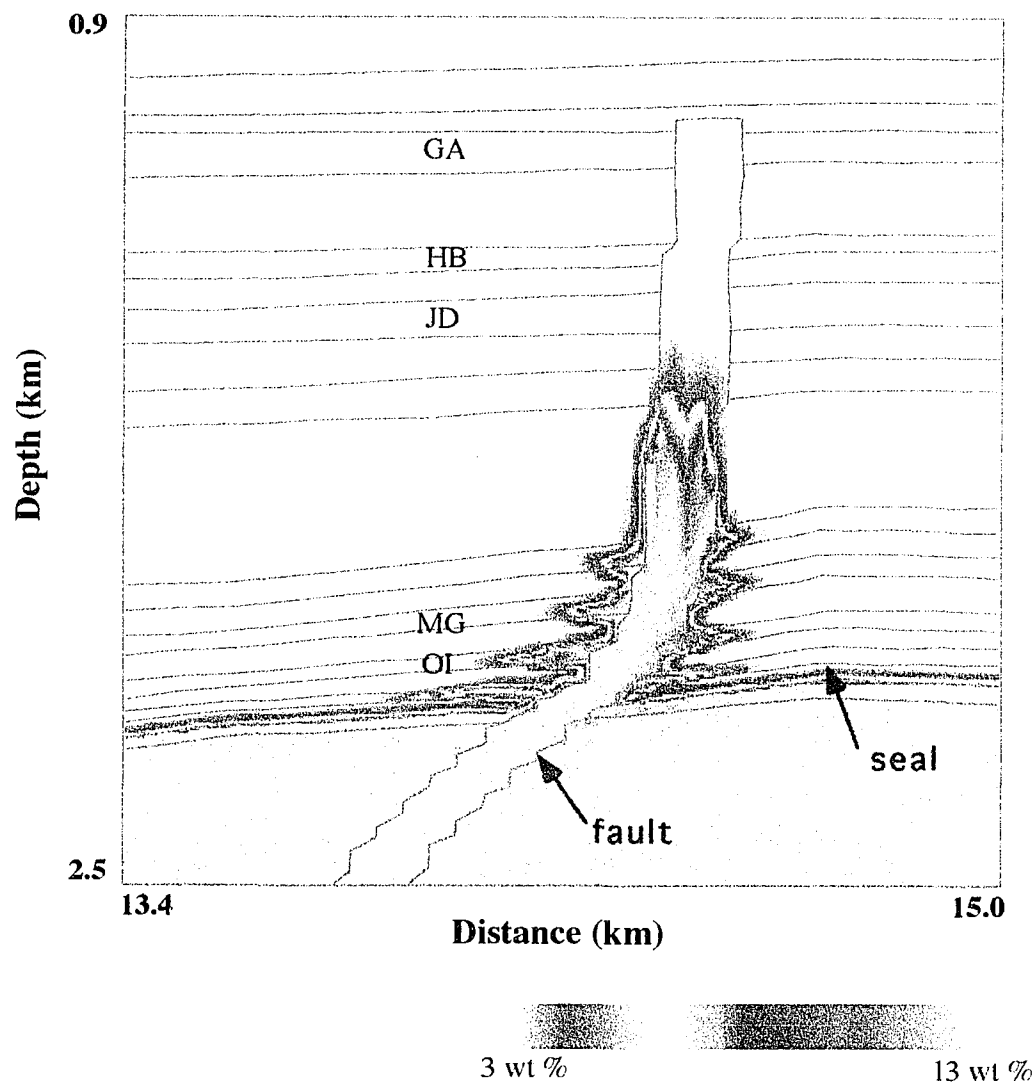
Figure 6.20a. Salinity distribution after 25 years of venting See the above color bar for the salinity scale. The light lines outline the stratigraphy and the fault. GA, HB, JD, MG and OI are the names of sand bed.

Salinity distribution at 300 years (venting case)
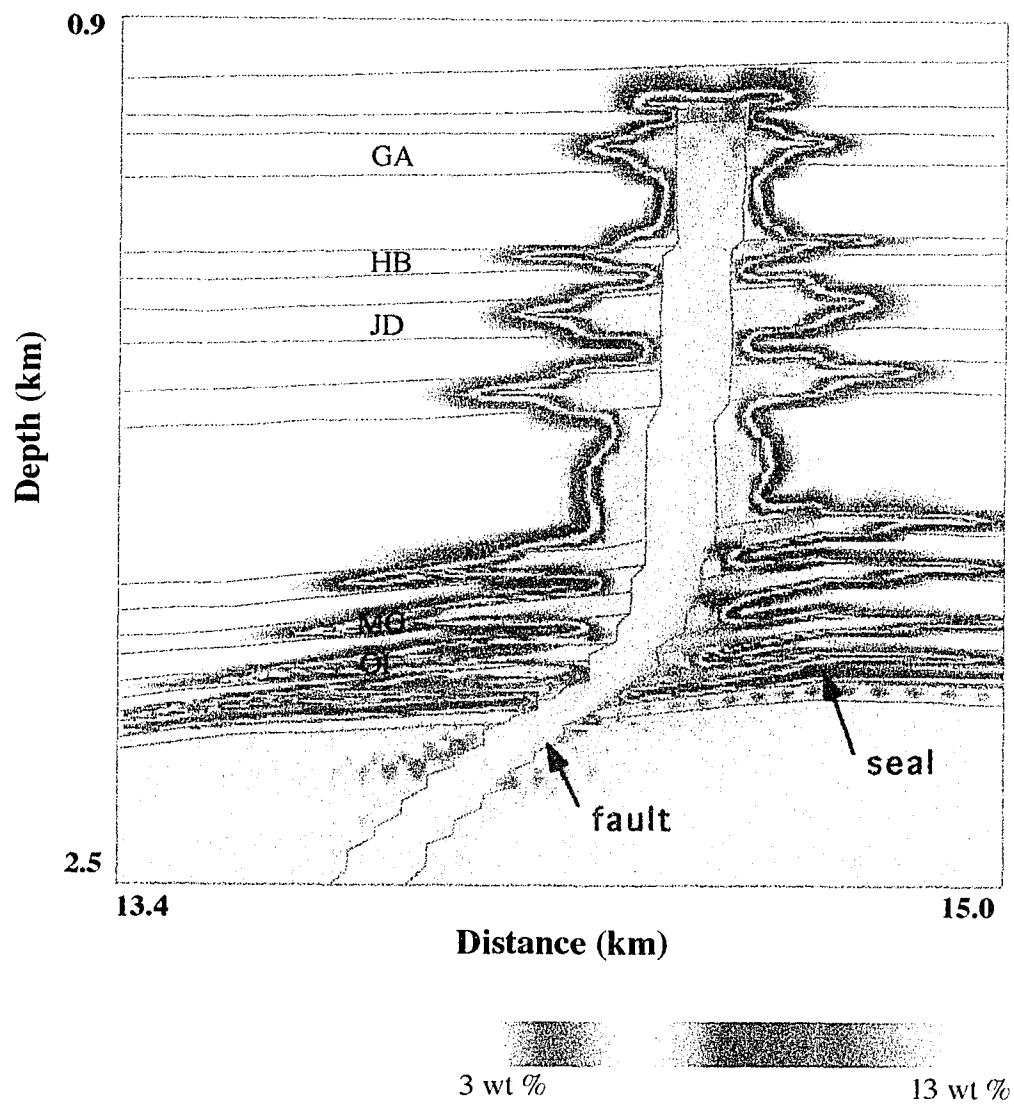
Figure 6.20b Salinity distribution after 300 years of venting. See the above color bar for the salinity scale. The light lines outline the stratigraphy and the fault. GA, HB, JD, MG and OI are the names of sand bed.

toward the south (Figures 6.20a and 6.20b). When the geopressured fluids are expelled into the overlying hydropressured sediments, it is much easier for the fluids to move down-dip. In the up-dip direction, gravitational forces of the original saline water (denser) must be partially overcome. This phenomenon is not obvious in the stratigraphically higher sands (e.g. GA, HB) where the slopes are much smaller.

The results of this study indicates that it takes about 150 years for the new expelled fluids to reach the top of the fault zone and recharge the shallow GA sand. As mentioned earlier, my model results indicate the duration of expulsion can be more than 300 years. Thus, it is reasonable for the shallow reservoirs (GA and HB) to be filled by geopressured fluids during the current expulsion.

Fluids, which initially move into the reservoir sands, especially the shallow ones, are from the fault zone, instead of directly from the geopressured zone. These fault zone fluids may be old geopressured fluids, which were expelled during previous expulsion episodes. This suggests that episodic expulsion events are a possible mechanism for the deep geopressured fluids to migrate a long distance into shallow reservoirs, even though a single expulsion is short (<150 years).

6.4.3. Results from post-venting case

It was previously assumed that the seal closed after an elapsed time of 300 years and no fluid mass and pressure were transported from the geopressured zone into the overlying sediments. At 1000 years in this post-venting simulation, excess fluid pressure in the original hydropressured sediments still can be as high as 2.5 MPa in the deep OI reservoir sand and about 1.0 MPa in the shallow GA reservoir sand (compare Figure 6.21 and Figure 6.14b). Because there is no fluid supply from underlying geopressured sediments, fluid pressure decreases, but at a slow rate (Figure 6.22) after a few hundred years. It takes more than 10,000 years for the excess fluid pressure to completely dissipate. The decrease in fluid pressure causes porosities to decrease (Figure 6.23). High excess fluid pressures continuously drive expelled fluids out of the

Excess fluid pressure at 1000 years (post-venting)
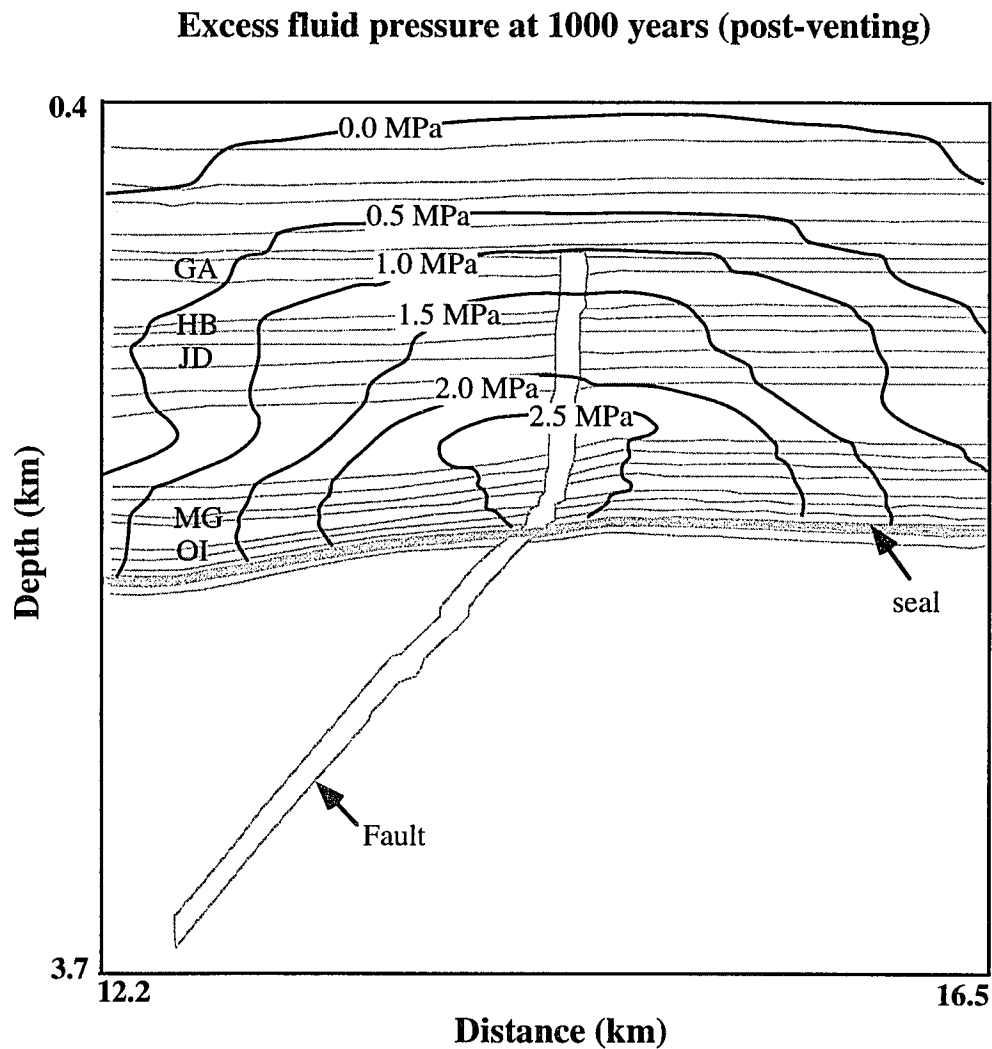
Figure 6.21. Excess fluid pressure at 1000 years after the vent closes. Only the section above the seal is calculated in this post-venting case. See Figure 5.14b (right before the seal closes) for comparison. The light lines outline the stratigraphy and fault. GA, HB, JD, MG, OI are the names of sand bed. Note that the depth and distance refer to those in Figure 6.13.
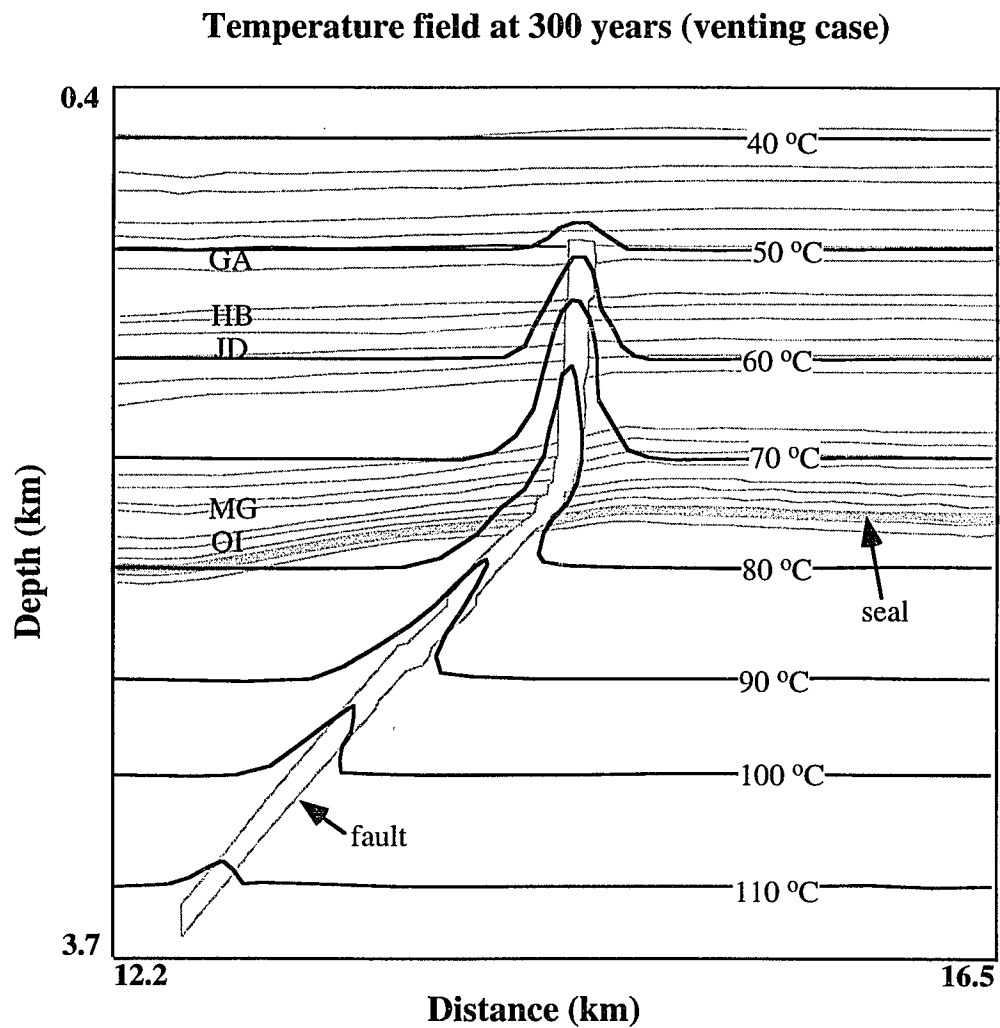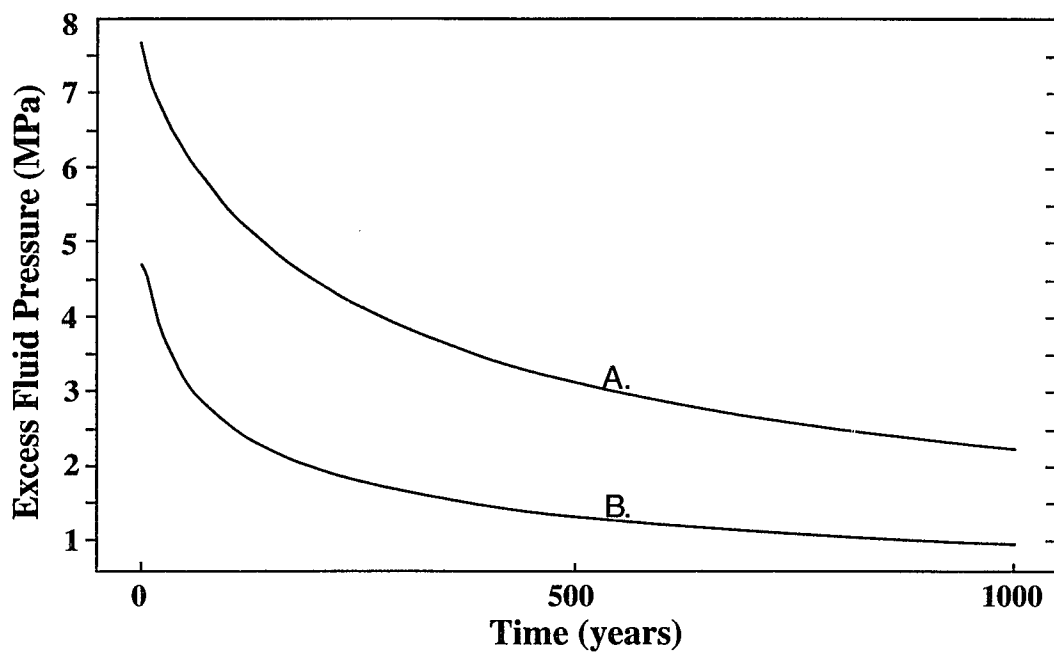
Figure 6.22. Variation of excess fluid pressure with time after the fault closes in sediments immediately above the seal (A) and near the top of the fault (B).
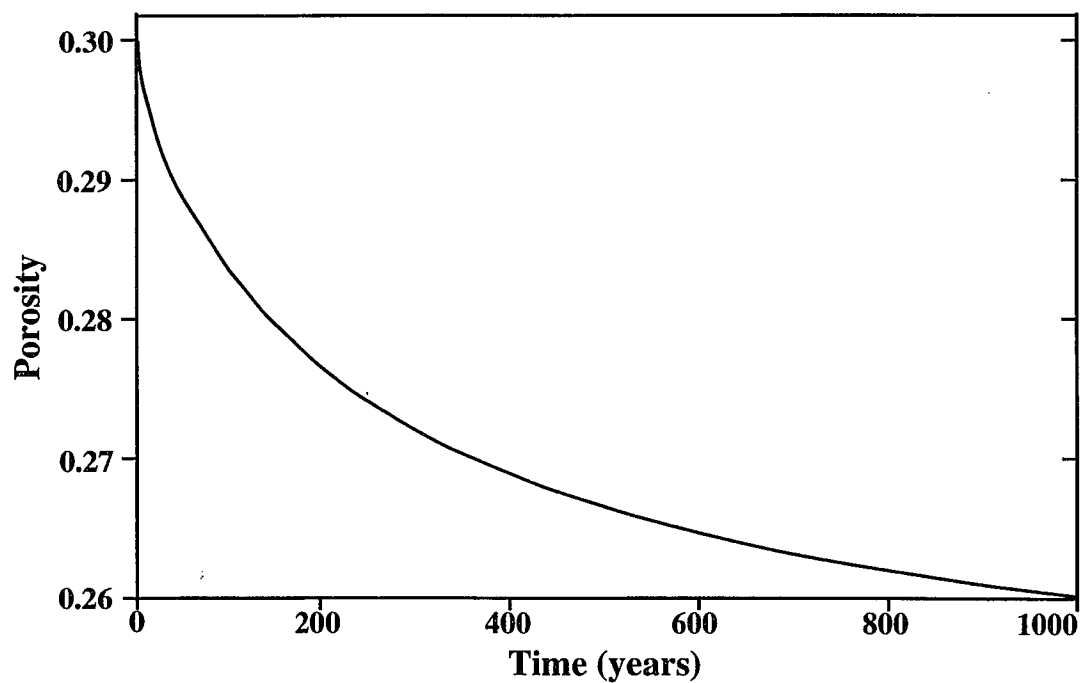
Figure 6.23. Computed porosity variation with time in OI-1 reservoir around the former fault zone after the fault closes.

fault zone, as indicated by the expansion of the low salinity plume (Figure 6.24). Flow rates are as high as 0.1 m/yr. at 1,000 years after the end of fluid expulsion from the geopressured zone.

Without heat transport by convection from the geopressured sediments, the temperature anomaly in the hydropressured zone starts to decline, as indicated by the slowly decreasing amplitudes of the upwarped isotherms along the former fault zone (Figure 6.25). At an elapsed time of 1,000 years, the temperature anomaly is still more than 10 °C. Lateral movement of fluids also carries heat away from the fault zone and produces broadly upwarped isotherms.

6.5. DISCUSSION

The permeability of the fault zone is the most important factor controlling the transport of fluid, pressure, and thermal energy from the geopressured sediments into the overlying hydropressured sediments (Roberts et al., 1996). Only when the fault zone is sufficiently permeable, can expelled fluids reach the shallower reservoirs (GA and HB) during a single episode of expulsion. High fault zone permeability might be generated by fault movement caused by local salt tectonics during the last 3 Ma.

The results of this study show that if the upper part of the fault zone is sufficiently permeable (~10 mD), the maximum excess pressure in the GA sand should be about 4.5 MPa during the expulsion. However, the GA sand is only slightly overpressured (~1 MPa) and has a broad elevation around the fault zone at the present time in the South Eugene Island Block 330 (see Flemings et al., in press). Thus, the field observation is consistent with those results from the above post-venting simulation. The temperature anomalies observed in the field indicate a maximum temperature of about 10 °C in both foot wall and hanging wall of the fault zone (Guerin et al., 1994), also consistent with the above post-venting simulation. Therefore, the observed pressure and temperature anomalies may not necessarily indicate the active vertical migration of geopressured fluids in the shallower reservoirs GA and HB. Thus, the model results
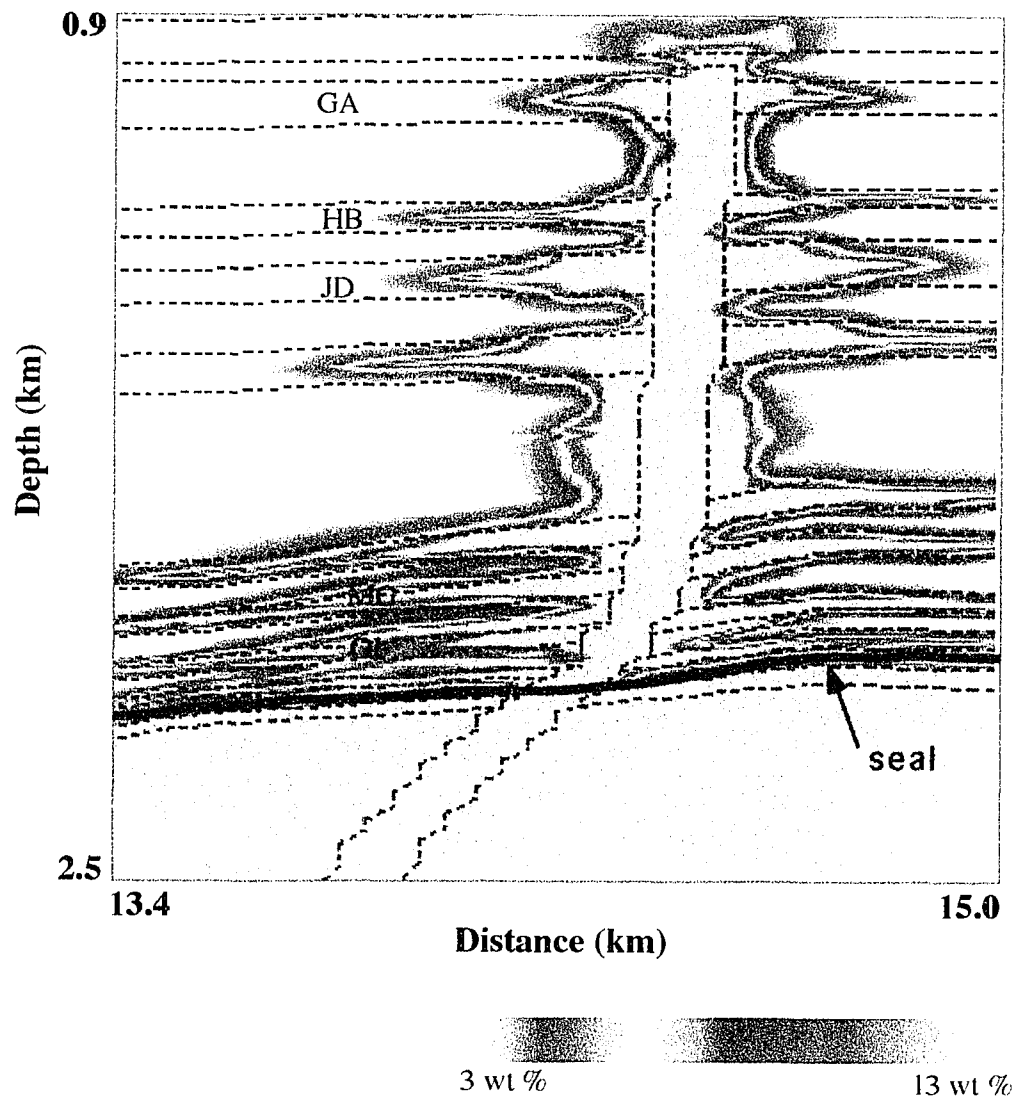
Figure 6.24. Salinity distribution at 1000 years after the vent closes. Note that the low salinity fluids have been spreading out laterally away from the fault zone along the sand beds (see Figure 5.20b for the comparison). See the above color bar for the salinity scale. The dash lines outline the stratigraphy and the fault. GA, HB, JD, MG and OI are the names of sand beds.

186
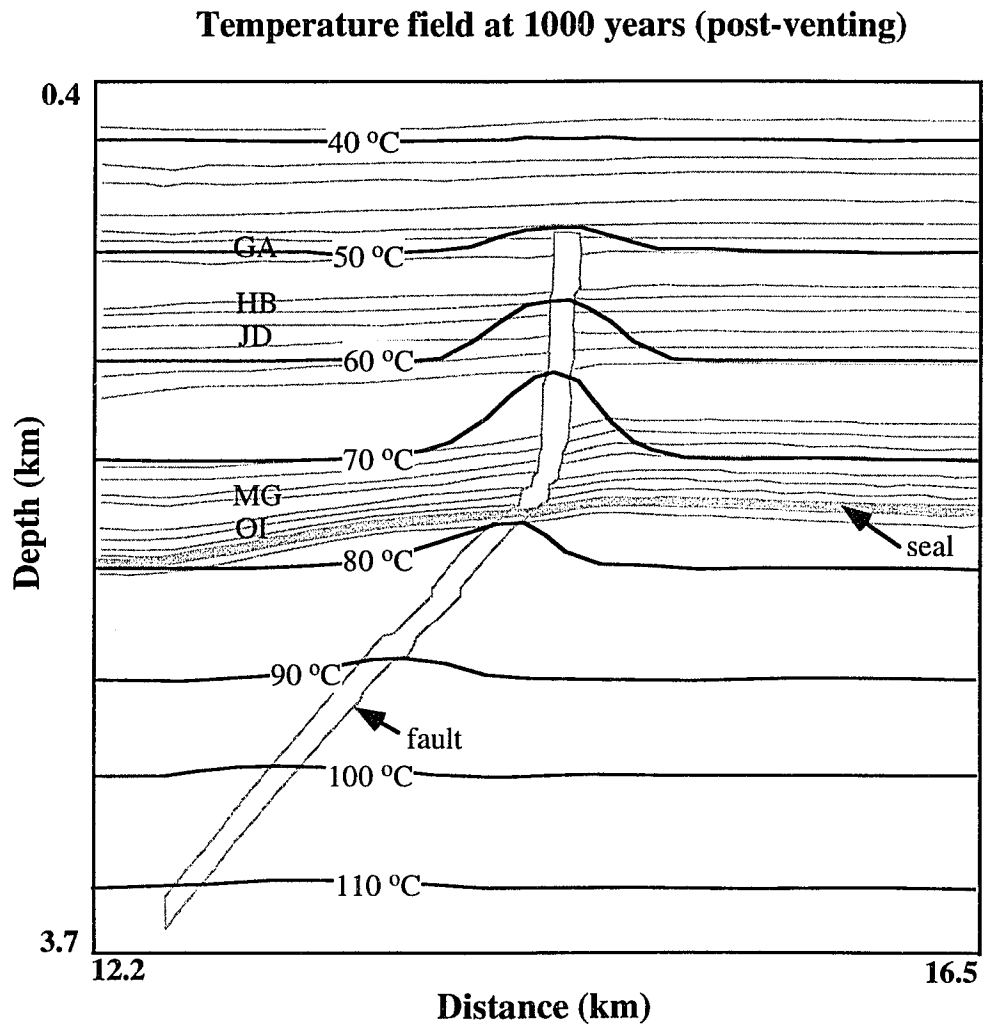
Figure 6.25. Temperature distribution at 1000 years after the vent closes. See
Figure 5.17b (temperature when the vent closes) for comparison. The light lines
outline the stratigraphy and fault. GA. HB. JD. MG and OI are the names of sand
beds. Note that the depth and distance refer to those in Figure 6.13.

support the suggestions made from the earlier salinity analysis that the shallower reservoirs must have been recharged by geopressured fluids in a recent expulsion event, which may no longer exist.

On the other hand, field measurements (Flemings et al., in prep) found that deep reservoirs (OI, MG) are strongly overpressured (about 20 MPa), which is much higher than the maximum value predicted by the model in the deeper reservoirs during the expulsion. This is because that in this model, we assumed the geopressured sediments initially had a uniform excess pressure of only 22 MPa, instead of 40 MPa found in the sediments below the OI sand (Flemings et al., in prep). If we use an excess pressure of 40 MPa for the geopressured sediments, we will expect to have a maximum excess pressure close to 20 MPa in these deeper reservoirs during venting.

The observed excess pressure (20 MPa) in the deeper reservoirs suggest that they are being recharged by fluids expelled from the underlying geopressured sediments along the fault zone. This suggestion is also supported by the difficulty in maintaining such high excess fluid pressure (20 MPa) in a post-venting simulation, even when the initial excess fluid pressure is set to 40 MPa. Active migration of geopressured fluids can explain the uniform low salinity distribution and its invariability with time in these deeper reservoirs. Another explanation for the salinity distribution in these deeper sands is that they are also fault-sealed, as suggested by Flemings et al. (in prep), but the storage of geopressured fluids during the last episode of expulsion is so plentiful that they can continuously supply the fluid lost through pumping.

The persistent fluid pressure anomaly and compressibility of the sediments in the hydropressured section are very important mechanisms for fluid flow, especially in the horizontal direction in shallow sediments. These mechanisms may be important for the recharge of structural or stratigraphical hydrocarbon reservoirs far away from the fault zone. Because the fluid pressure anomaly can exist in the originally hydropressured sediments for such a long time, it actually becomes a secondary geopressured (or

transitional) zone. Drilling through these sediments may further disturb the fluid pressure distribution and change the flow pattern.

Compressibility of the sediments is a critical mechanism for the fluid supply, even thousands of years after the close of the venting seal. When excess pressures and fluids are transported from the underlying geopressured sediments, the original hydropressured sediments may not be compacted during sediment loading. The total volume of the sediments under the excess fluid pressures may not be able to expand significantly because of the tremendous overlying load. However, increasing fluid pressure decreases the effective stress of the sediments so that solid grains can more easily be re-arranged. This process can provide pore spaces as large as possible for storing the expelled fluids (see Figures 6.16 and 6.23 for the examples). Fluid storage caused by compressibility of liquid phases may also become significant under high pressures (Domenico and Schwartz, 1990). Thus, ignoring fluid compressibility will discount the capability of fluid flow induced by the expulsion of geopressured fluids following venting.

Here, the materials are assumed to be elastic and have constant compressibilities. The pore space varies depending on the change in fluid pressure (Equation 6.1). However, the sediments in Gulf of Mexico basin are uncompacted. The sediments may not be as elastic as those described by Domenico and Schwartz (1990). Thus, the pore space increase caused by the increase in fluid pressure in this study may represent a maximum possibility in the study area. Sediment compressibility caused by expulsion of geopressured fluids is still not fully understood. Thus, more work is needed to further determine the quantitative relationship between pore expandability and induced fluid pressure anomalies.

6.6. CONCLUSIONS

The salinities from the SP log analysis are basically consistent with those from brine sample measurement by Losh and Wood (1995), except those in HB sand, which were

possibly contaminated during sample collection. Further brine sample collection and measurement are needed to conform that the four samples in HB sand were contaminated.

Both salinity analysis and numerical study indicate that the present fault zone may act as a hydrological conduit to the deeper reservoirs (depth > 2000 m), which immediately overlies the frictional failure zone in the Eugene Island Block 330. Shallow reservoirs (depth < 1600 m) are believed to be currently fault-sealed. However, shallow reservoirs must have been recharged in the past when the fault zone was more permeable, caused by more extensive faulting activity. The numerical study shows that geopressured fluids can reach shallow reservoirs in about 150 years, if the permeability of the fault zone is sufficient high (>10 mD). The shallow reservoirs might also have been gradually recharged through many episodes of expulsion or by free thermohaline convection.

The compressibility or expandability of the sediments is a critical mechanism to supply fluid and maintain excess fluid pressure for continuous migration of expelled fluids, even thousands of years after the fault closes. Compressibility of sediments may play an important role in the low decline rate of the production history in this area.

In those reservoir sands with relative high dipping slopes (e.g. 3° to 4°), the hanging wall can receive more expelled fluid than the foot wall.

CHAPTER 7
SUMMARY

The results from this dissertation research are helpful to understand the important role that the basement rocks play in thermal evolution of an uplifted foreland basin, how thermal insulation by carbonaceous sediments effect the formation of MVT ore deposits, and the expulsion of warm, low salinity geopressured fluids along a fault zone and its effects on the groundwater system in salt basins. In this dissertation, I have also present the salinity evidence showing the possibility of recent migration of geopressured fluids along the faults, based on pore water salinity estimation from SP logs in the south Eugene Island Block 330.

Thermal buffering by basement rocks strongly effects the transient temperature field in an uplifted foreland basin, where topographical driven recharge is a major driving mechanism for regional groundwater flow. It is impossible in nature to maintain a constant heat flow along the sediment-basement contact, as used by many other modelers in their numerical simulations. This is because rapid fluid flow can significantly change the thermal gradient between sediments and basement rocks along the sediment-basement interface. Furthermore, in some places, where the slope of sediment-basement interface is large, additional heat transported by the fast flowing groundwater along the basal aquifers, can be conducted laterally back into the basement.

Ignoring basement buffering can cause serious errors, such as production of a spurious transient thermal pulse in the groundwater discharge region and incorrect prediction of fluid flow velocity in different stages of modeling. Without considering basement rocks as part of the model, temperatures can be significantly over-estimated in the discharge area. This means that there is serious error in the temperature predictions by Garven et al. (1993), especially during the early stage of modeling in the discharge

area. Relative model errors in temperature histories (~10 °C) can generate very large errors in predicted diagenesis or organic maturation of basin sediments.

Therefore it is important to seek other mechanisms that can generate high temperatures (100 to 150 °C) at shallow depths (<1.5 km) in sedimentary basins. In Chapter 4, thermal insulation by a low thermal conductivity carbonaceous layer was examined in an instantaneously uplifted basin and a gradually uplifting basin. It was found that thermal insulation initially elevates the temperatures of the underlying sediments and basement rocks even for a conduction dominated system. This means that thermal insulation results in a larger heat source for the formation of MVT ore deposits.

Because of thermal insulation, high temperatures (>130 °C) in the shallow discharge region (<1.0 km) can be produced by high velocities of regional groundwater flow (Darcy velocity more than 6.0 m/yr.), driven by topographic gradient along basal aquifers in an instantaneously uplifted basin, even under a typical continent basal heat flow of 60 mW/m². Partial coverage of carbonaceous sediments limited to the discharge areas, can also result in temperatures of more than 120 °C in the shallow discharge region. A low thermal gradient (less than 10 °C/km) in sediments underlying the carbonaceous layer in the shallow discharge area is consistent with fluid inclusion studies by Rowan and Leach (1989).

A transient thermal pulse observed in the discharge areas is primarily dependent on the thermal conductivity and permeability of the carbonaceous layer. Lower conductivity and higher permeability of the carbonaceous section can result in a large thermal pulse, because these parameters increase fluid flow rates and retention of thermal energy. Thus, the thermal pulse is not strongly buffered by basement rocks. High thermal conductivity and lower permeability of the carbonaceous section, however, slows down the groundwater flow and gives basement rocks more time to interact with the groundwater. As a result, less heat is transported to the discharge area.

Thermal conductivity and permeability of the carbonaceous layer are also important for the surface heat flow. Lower conductivity and higher permeability increase surface heat flow in the discharge region, but cause lower surface heat flow in the recharge area. Surface heat flow in the discharge region is sensitive to vertical permeability of the carbonaceous layer. For example, a 10 fold decrease in vertical permeability in the carbonaceous layer can cause surface heat flow to drop 200 mW/m^2.

In a gradually uplifting model, which is closer to a real foreland basin, sediment temperatures vary more slowly and the basin loses less heat in the early stage of uplift, compared to an instantaneous uplifting basin. Slow heating of the shallow sediments in the discharge region allows the upper basement to become warmer when the thermal pulse passes through the region. Thus, shallow sediments in the discharge area have a maximum temperature about 5 ^{o}C higher than that in the instantaneous uplifting model.

In Chapter 5, I studied the short term expulsion of low salinity geopressured fluids into high salinity hydropressured sediments and its long term effects in a salt basin. The expulsion of geopressured fluids not only quickly increases fluid pressure in the hydropressured sediments near the fault, but also creates large salinity and thermal anomalies. The anomalous fluid pressures in hydropressured sediments dissipates in a few years after the expulsion terminates, if the compressibility of sediments under these anomalous pressures is ignored.

An injected low salinity plume is gravitationally unstable (salinity Rayleigh Numbers >10,000), which can cause free thermohaline convection. The unstable system tries to approach equilibrium by developing smaller circulation cells (bifurcation), which cause extensive mixing between the geopressured fluids and the surrounding brine. Even several thousand years after venting ends, upward moving fluids can have a maximum vertical velocity of several centimeters per year. As long as the sediments have sufficiently high permeability, thermal anomalies persist in the sediments near the fault for a long time (> 10,000 years), and could result in higher

organic maturity. Thus, thermohaline convection induced by the short term expulsion of hot and low salinity geopressured fluids may be an important mechanism for long term (~10,000 years), kilometer scale vertical and horizontal migration of groundwater in salt basins. A real salt basin is generally heterogeneous and anisotropic, and the induced free thermohaline convection may not be as strong or have the same circulation pattern as described in this model (Chapter 5).

Compressibility of the sediments can supply fluid and maintain excess fluid pressure for continuous migration of expelled fluids, even thousands of years after the seal closes (Chapter 6). Compressibility of sediments may play an important role in the low decline rate of the production history in the South Eugene Island Block 330 area.

A fault zone may not always act as a hydrological conduit. Salinity analysis from SP logs and numerical study (Chapter 6) indicate that the present fault zone in the Block 330 area may only provide a permeable conduit to the deeper reservoirs (about 2000 m deep), which immediately overly the frictional failure zone. Shallow reservoirs (depth<1600 m) are believed to be currently fault-sealed. Therefore, shallow reservoirs must have been recharged in the past when the fault zone was more permeable, caused by more extensive faulting activity. The numerical study shows that geopressured fluids can reach shallow reservoirs in about 150 years, if the permeability of the fault zone is sufficient high (>10 mD). The shallow reservoirs might also have been gradually recharged through many episodes of expulsion or by free thermohaline convection.

The above studies have general implication to other geological processes. For example, the thermal buffering by basement rocks is applicable to any near surface process that generates rapid changes in temperature, such as sedimentation, uplift and erosion, and tectonic denudation during continental extension. The thermal insulation by carbonaceous rocks can generate elevated temperatures associated with the formation of MVT ore deposits, and increase the thermal maturity of organic matters at

shallow depths. Results from the simulation of expulsion of geopressured fluids implies that the hydrocarbon in an overpressured basin can be efficiently transported from the deep sediments into shallow reservoirs within a few hundred years. The rapid migration of geopressured fluids also significantly increases the thermal maturity anomalies of organic matters in shallow sediments near the fault conduits.

Most of the above results are based on geological models which simplify or omit some geological processes. Thus, more work needs to be done to test these hypotheses in geologically realistic conditions. For example in Chapter 4, it is important to seek the possibility to reconstruct the distribution of Pennsylvanian coal swamps, carbonaceous sediments and coal in the Ozark dome area. The reconstruction may be done through studying the sedimentary basins where the Pennsylvanian strata are preserved in the Mid-continent region. It is also necessary to see how well a single layer with averaged thickness and thermal conductivity works, compared to a sediment section in which thinner coal beds are frequently and discontinuously distributed, as observed in many sedimentary basins. In this way, a more realistic situation of the "real world" will be simulated. In Chapter 5, more work needs to be done to determine the permeabilities of a seal, geopressured sediments and the width and permeability of a fault zone. In Chapter 6, it is necessary to further study the expandability of sediments subjected to the expulsion of geopressured fluids, especially in basins such as Gulf of Mexico where sediments are strongly under-compacted. Another valuable future study would be to collect fluid samples from major production reservoirs, especially from HB sand, to monitor the temporal variation of pore water salinity, so that the conclusions from this study can be tested. It is also necessary to conduct more sensitivity tests, such as variable permeability and thermal conductivity in the models, to improve our understanding of the current results.

BIBLIOGRAPHY

Alexander, L. L. and Flemings, P. B., Geological evolution of a Plio-Pleistocene salt withdrawal mini-basin: Block 330, Eugene Island, South Addition, offshore Louisiana: AAPG Bull., March, 1996?

Anderson, R. N., He, W., Hobart, M. A., Wilkinson, C. R., and Nelson, H. R., Active fluid flow in the Eugene Island area, offshore Louisiana: Geophysics: the Leading Edge of Exploration, 12-17, 1991.

Anderson, R. N., Recovering dynamic Gulf of Mexico reserves and the U. S. energy future: Oil and Gas Journal, 85-91, 1993.

Anderson, R. N., Flemings, P., Losh, S., Austin, J. and Woodhams, R., Gulf of Mexico growth fault drilled, seen as oil, gas migration pathway: Oil and Gas Journal, 97-102, 1994.

Archer, P. L. and Kirr, J. N., Geological overview, coal, and coalbed methane resources of the Illinois Basin-Illinois, Indiana, and Kentucky, in: Rightmire, C. T., Eddy, E. G., and Kirr, J. N., eds, Coalbed methane resources of the United States: AAPG studies in Geology, series 17, 105-134, 1984.

Atwood, G. I., and Foman, M.J., Nature and growth of southern Louisiana salt domes and its effect on petroleum accumulation: AAPG Bull., 43, 2595-2622, 1959.

Bateman, R. M., Open-Hole Log Analysis and Formation Evaluation, International Human Resources Development Corporation, Boston, P. 647, 1985.

Beaumont, C., Quinlan, G. M., and Mamilton, J., The Alleghanian orogeny and its relationship to the evolution of the eastern interior, North America: Canadian Society of Petroleum Geologists, Memoir, 12, 425-445, 19487.

Beer, J., Dynamics of fluids in porous media, America Elsevier Pubilishing Company, Inc., 1972.

Bennett, S. C. and Hanor, J. S., Dynamics of subsurface salt dissolution at the Welsh dome, Louisiana Gulf Coast. In: I. Lerche and J.J. O'Brien, eds., Dynamical Geology of salt and related structures: Academic Press, London, 653-667, 1987.

Berg, R. R. and Habeck, M. F., Abnormal Pressure in the Lower Vicksburg McAllen Ranch Field, South Texas: Trans. Gulf Coast Assoc. Geol. Soc., 32, 247-253, 1982.

Bethke, C. M., A numerical model of compaction-driven ground-water flow and heat transfer and its application to the paleohydrology of intracratonic sedimentary basins: J. Geophys. Res., 90, 6817-6828, 1985.

Bethke, C. M., Inverse hydrologic analysis of the distribution and origin of Gulf Coast geopressured zones: J. Geophys. Res., 91, 6535-6545, 1986.

Bethke, C. M., Hydrologic constraints on the genesis of the Upper Mississippi valley district from Illinois Basin brines: Econ. Geol., 81, 233-249, 1986.

Bethke, C. M., Reply to Palciauskas, V. V.: J. Geophys. Res., 93: 3500-3504, 1988.

Bethke, C. M., and Marshak, S., Brine migrations across North America - The plate tectonics of groundwater: Annu. Rev. Earth Planet. Sci., 18, 287-315, 1990.

Blackwell, D. D. and Steele, J. L., Thermal conductivity of sedimentary rocks-- measurement and significance, in: Naeser, N. D. and McCulloh, D., eds, Thermal history of sedimentary, 1988.

Blackwell, D. D. and Steele, J. L., Thermal conductivity of sedimentary rocks; measurement and significance, in: Naeser, N. D., McCulloh, D. and Thane, H., eds, Thermal history of sedimentary basins; methods and case histories, 13-36, 1989.

Bodner,D. P. and Sharp, J.M., Jr., Temperature variations in South Texas subsurface: AAPG Bull., 72, 21-32, 1988.

Bodner,D. P., Blanchard, P.E and Sharp, J.M., Jr., Variations in Gulf Coast heat flow created by groundwater flow: Trans. Gulf Coast Assoc. Geol., 35, 19-27, 1985.

Bredehoeft, J. D., and Hanshaw, B.B., On the maintenance of anomalous fluid pressures: 1. Thick sedimentary sequences: Geol. Soc. America Bull., 79, 1097-1106, 1968.

Broecker, W. S. and Peng, T. H., Tracers in the sea: a publication of the Lamont-Doherty Geological Observatory, Columbia University, New York, 1982.

Bryant, W. R., and DSDP Leg 96 shipboard Scientists, Consolidated characteristics and excess pore water pressures of Mississippi Fan sediments, Chapter 43 in: Bouma, A., Normark, W.R., and Barnes, N.E., eds., Submarine fans and related turbidite systems, 299-309, 1985.

Carter, K. and Lerche, I.: Trans. Gulf Coast Assoc. Geol. Soc., 40, 73-86, 1990.

Cassidy, D. P. and Ranganathan, V., Groundwater upwelling, near Bay St. Elaine Salt Dome in southeastern Louisiana, as inferred from fluid property variations: AAPG Bull., 76, 1560-1568, 1992.

Cathles, L. and Smith, A. T., Thermal constraints in the formation of Mississippi Valley-Type lead-zinc deposits and their implications for episodic basin dewatering and deposit genesis: Econ. Geol., 78, 983-1002, 1983.

Cathles, L. M., and Smith, A. T., Thermal constraints on the formation of Mississippi Valley-Type lead-zinc deposits and their implications for episodic basin dewatering and deposit genesis: Econ. Geol., 78, 983-1002, 1983.

Cathles, L. M., Scales and effects of fluids flow in the upper crust: Science, 248, 323-248, 1990.

Chapman, D. S., Keho, T.H., Bauer, M. S. and Picard, M. d., Heat flow in the Uinta basin determined from bottom hole temperature (BHT) data: Geophysics, 49,. 453-466, 1984.

Cipriani, F. D., Coehlo, D., Cathles, L., Roberts, J. S and Nunn, J. A.,
    Temperature and pressure anomalies near the Red Fault; South Eugene Island
    Block 330, Gulf of Mexico: Annual-Meeting-Abstract-AAPG-and-Society of
    Economic Paleontologists and Mineralogists, 122, 1994.

Conveney, R. M., Goebel, R. D. Jr., and Ragan, V. M., Pressures and temperatures from
    aqueous fluid incluisions in sphalerite from midcontinent country rocks: Econ.
    Geol., 82, 740-751, 1987.

Cook, P. J., Geochemistry and diagenesis of interstitial fluids and associated
    calcareous oozes: Deep Sea Drill. Proj., 27, 463-480, 1974.

Daniels, E. J., Altaner, S. P., Marshak, S., and Eggleston, J. R., Hydrothermal alteration
    in anthracite from eastern Pennsylvania: Implications for mechanisms of
    anthracite formation: Geology, 18, 247-250, 1990.

Davis, M. W., and Ehrlich, R., Late Peleozoic crustal composition and dynamics in the
    southeastern United States, in: Briggs, G., ed., Barboniferous of hte southeastern
    United States: GSA Special Paper, 148, 171-185, 1974.

Demaison, G., The generative basin concept, in: Demaison, G. and Murris, R. J., eds.,
    Petroleum geochemistry and basin evaluation: AAPG Memoir 35, 1-14, 1984.

Deming, D. and Nunn, J. A., Numerical simulations of Brine Migration by
    Topographically driven recharge: J. Geophys. Res., 96, 2485-2499, 1991.

Deming D., Nunn, J. A. and Evans, D. G., Thermal effects of compaction driven
    groundwater flow from overthrust belts: J. Geophys Res., 95, 6669-6683, 1990.

Deming D., Nunn, J. A. and Jones, S., Some problems in thermal history studies, in:
    Nuccio, V. F. and Barker, C. E., eds., Applications of thermal maturity studies
    to energy exploration, 61-80, 1990.

Dickinson, G., Geological aspects of abnormal pressures in Gulf Coast Louisiana:
    AAPG Bull., 37, 410-432, 1953.

Domenico, P. A. and Schwartz, F. W., Physical and chemical hydrogeology, Hohn
    Wiley & Sons, Inc., 1990.

Dorobeck, S., Migration of orogenic fluids through the Siluro-Devonian Helderberg
    Group during Late Paleozoic deformation: Constraints on fluid sources and
    implications for thermal histories of sedimentary basins: Tectonophysics, 159,
    24-45, 1989.

du Rouchet, J., Stress fields, a key to oil migration: AAPG Buletin, 65, 74-85, 1981.

Elliot, W. C., and Aronson, J. L., Alleghenian episode of K-bentonite illitization in the
    southern Appalachian basin: Geology, 15, 735-739, 1987.

Evans, David G., Theoretical and numerical modes for coupled heat and mass
    transport and groundwater flow near salt domes, Ph.D. Dissertation, Department
    of Geology and Geophysics, Louisiana State University, 1989.

Evans, D. G. and Nunn, J. A., Free thermohaline convection in sediments surrounding a salt column: J. Geophys.l Res., 94, 12413-12422, 1989.

Evans, David G. and Nunn, Jeffrey A., Free Thermohaline Convection in Sediments Surrounding a Salt Column: J. Geophys. Res, 94, 12413-12422, 1989.

Evans, David G., Nunn, Jeffrey A. and Hanor, Jeffrey S., Mechanisms driving groundwater flow near salt domes: Geophys. Res. Let., 18, 927-930, 1991.

Fertl, W. H., Chilligarian, G. V. and Riecke, H. H.,III, Abnormal formation pressures, Elsevier, Amsterdam, 328, 1976.

Flemings, P. B., Alexander, L. L. and Anderson, R. N., The hydrostratigraphy of a Plio-Pleistoncene growth fault: the Eugene Island 330 Field: in prep.

Funayama, M., Distribution and migration patterns of subsurface fluids in the Wilcox Group in central Louisiana, a master thesis, Department of Geology and Geophysics, Louisiana State University, 1990.

Galloway, W. E., Bebout, d. G., Fisher, W. L., Dunlap, J. B. Jr., Cabrera-Castro, R., Lugo-Rivera, J. E. and Scott, T. M., Cenozoic, in: Salvador, A., ed., The Gulf of Mexico Basin: GSA, The Geology of North America, J, 245-324, 1991.

Garven, G., and Freeze, R. A., The role of regional groundwater flow in the formation of ore deposits in sedimentary basins: A quantitative analysis, in Proceedings of the Second Annual Canadian National Hydrogeology Conference, Winnipeg, Manitoba, Canadian Chapt., Int. Assoc. Hydrogeologists, Edmonton, Canada, 66-67, 1982.

Garven, G., The role of regional fluid flow in the genesis of the Pine Point Deposit, Western Canada Sedimentary Basin, Econ. Geol., 80, 307-324, 1985.
Garven, G., and Freeze, R. A., Theoretical analysis of the role of groundwater flow in the genesis of stratabound ore deposits, 1, Mathematical and numerical model: Am. J. Sci., 284, 1085-1124, 1984a.

Garven, G., and Freeze, R. A., Theoretical analysis of the role of groundwater flow in the genesis of stratabound ore deposits, 2, Quantitative results: Am. J. Sci., 284, 1125-1174, 1984b.

Garven, G., a hydrogeologic model for the formation of the giant oil sands deposits of t he western Canadian sedimentary Basin: Am. J. Sci., 289, 105-166, 1989.

Garven, G., and Sverjensky, Hydrogeology of regional flow systems associated with the formation of Mississippi Valley-type ore deposits in the Mid-continent (abstract): Geol. Soc. Am. Abstr. Program, 21, A9, 1989.

Garven, G., Ge, S., Person, M. A., and Sverjensky, D. A., Genesis of stratabound ore deposits in the Mid-continent basins of North America. 1. The role of regional groundwater flow: Am. J. Sci, 293, 497-568, 1993.

Ge, S., and Garven, G., Tectonically induced transient groundwater flow in foreland basins, in: Price, G. R., ed., Origin and evolution of sedimentary basins and their energy and mineral resources: Geophys. Mongr. Ser., 48, 145-157, 1989.

Gosnold, W. D., Heat flow and groundwater flow in the Great Plains of the United States: J. Geodyn., 4, 247-264, 1985.

Gosnold, W. D. and Fischer, D. W., Heat flow studies in sedimentary basins. In: J. Burus (editor), Thermal Modeling in Sedimentary Basins. Gulf Publishing, Houston, TX, 199-218, 1986.

Gosnold, W. D., Heat flow in the Great Plains of the United States: J. geophys. Res., 95, 353-374, 1990.

Graham, S A., Ingersoll, R. V., and Dickinson, W. R., Common provenance for lithic grains in Carboniferous sandstones from Ouachita Mountains and Block Warrior Basin: Journal of Sedimentary Petrology, 46, 3, 620-632, 1976.

Gretener, P. E., and Feng, Z., Three decades of geopressures--insights and enigmas: Vereinigung Schweizerischer Petroleum-Geologen und-Ingenieure Bulletin, 51(120), 1-34, 1985.

Guerin, G., R. N, Anderson and He, W. 3-D temperature distribution and heat flow analysis for the Eugene Island 330 Area, Offshore Louisiana: AAPG Annual Meeting Abstracts, 160, 1994.

Halbouty, Michel T., Salt dome: Gulf Region, United States and Mexico, Gulf Pulishing Company, Houston, Texas, 1967.

Hall, D. J., Cavanaugh, T. D., Watkins, J. S. and McMillen, K. J., The rotational origin of the Gulf of Mexico based on regional gravity data, in J. S. Watkins and C. L. Drake, eds, Continental margin geology: AAPG Memoir 34, 115-125, 1982.

Hanor, J. S., Kilometre-scale thermohaline overturn of pore waters in the Louisiana Gulf Coast: Nature, 327, 11, 501-503, June, 1987.

Hanor, J. S., Bailey, J. E., Rogers, M. C. and Milner, L. R., Regional variations in physical and chemical properties of South Louisiana oil field brines: Trans. Gulf Coast Assoc. Geol. Soc., 36, 143-149, 1986.

Hanor, J. S. and Sassen, R., 1990, Evidence for large-scale vertical and lateral migration of formation waters, dissolved salt, and crude oil in the Louisiana Gulf Coast. Reprinted from: D. Schumacher and B.F. Perkins (eds), Gulf Coast Oil and Gases: Their Characteristics, Origin, Distribution, and Exploration and Prodution Significance: Proc. 9th Ann. Res. Conf. Gulf Coast Sec. Soc. of Econ. Paleo. Mineral. Foundation, 283-296, 1990.

Harrison, W. J. and Summa, L. L., Paleohydrology of the Gulf of Mexico Basin: Am. J. Sci., 291, 109-176, 1991.

Hay, R. L., Lee, M., Lolata, D. R., Matthews, J. C., and Morton, J. P., Episodic potassic diagenesis of Ordovician tuffs in Mississippi Valley area: Geology, 16, 743-747, 1988.

Hearn, P. P., Sutter, J. F. and Belkin, H. E., Evidence for late-Paleozoic brine migration in Cambrian carbonate rocks of the central and southern Appalachians:

Implications for Mississippi Valley-type sulfide mineralization: Geochim. Cosmochim. Acta, 51, 1323-1334, 1987.

Hearn, P. P., Jr., and Sutter, J. F., Authigenic potassium feldspar in Cambrian carbonates: Evidence of Alleghenian brine migration: Science, 228, 1529-1531, 1985.

Hewitt, J. L., Geological overview, coal, and coalbed methane resources of the Warrior Basin-Alabama and Mississippi, in: Rightmire, C. T., Eddy, E. G., and Kirr, J. N., eds, Coalbed methane resources of the United States: AAPG studies in Geology, series 17, 73-104, 1984.

Holland, D. S., Leedy, J. J. and Lammlein, D. R., Eugene Island 330 field-U.S.A. offshore Louisiana, in E. A. Beaumont and N. H. Foster, eds., Structural Traps III: Tectonic Fold and Fault Traps: AAPG Treatise of Petroleum Geology, 103-143, 1990.

Holland, D. S., Nunan, W. E., Lammlein, D. R. and Woodhams, R. L., Eugene Island Block 330 field, offshore Louisiana, in M. T. Halbouty, ed., Giant oil and gas fields of the decade: 1968-1978: AAPG Memoir, 30, 253-280, 1980.

Hunt, J. M., Generation and Migration of Petroleum from abnormally pressured fluid compartments. AAPG Bull., 74, 1-12, 1990.

Hsu, K. J., Origin of saline giants: A critical review after the discovery of the Mediterranean evaporite: Earth Science Reviews 8, 371-396, 1972.

Jackson, M., McCabe, C. Ballard, M. M., and Van der Voo, R., Magnetite authigenesis and diagenetic paleotemperatures across the northern Appalachian Basin: Geology, 16, 592-595, 1988.

Johnsson, M. J., Distribution of maximum burial temperatures across northern Appalachian basin and implications for Carboniferous sedimentation patterns: Geology, 14, 384-387, 1986.

Keith, L. and Rimstidt, J. P., A numerical compaction model of overpressuring in shales: Math. Geol., 17, 115-135, 1985.

Kestin, J., Khalifa, H. E., and Correia, R. J., Table of the dynamic and kinematic viscosity of aqueous NaCl solutions in the temperature range 20-150 °C and the pressure range 0.1-35 MPa: J. Phys. Chem. Ref. Data, 10(1), 1981.

Kisvarsanyi, E. B., Granitic ring complexes and Precambian hot-spot activity in the St. Francois terrane, Midcontinent region, United States: Geology, 8, 43-47, 1980.

Kilty, K. and Chapman, D. S., Convective heat transfer in selected geologic situations: Groundwater, 18, 386-394, 1982.

Larberg, G. M. B., Contra-regional faulting: salt withdrawal compensation; offshore Louisiana, Gulf of Mexico, in Bally, A. W., ed., Seismic expression of structural styles: AAPG Studies in Geology Series, 15, 2.3.2.42-2.3.2.44, 1983.

Leach, D. L., Temperature and slinity of hte fluids responsible for minor occurrences of sphalerite in the Ozark region of Missouri: econ. Geol., 74, 931-937, 1979.

Leach, K. L., and Rowan, E. L., Genetic link between Ouachita foldbelt tectonism and the Mississippi Valley-type Lead-zinc deposits of the Ozarks: Geology, 14, 931-935, 1986.

Lopatin, N. W., Temperature and geologic time as factors in coalification: Akad. Nauk SSSR Izvestia Serie Geologie, 3, 95-106, 1971.

Losh, S. and Wood, J., Brine Chemistry, Block 330 and 316, communication within the Global Basins Research Network.

Lorenz, John, Haas, J. L. Jr., Clynne, M.A., Potter, R. W. II, and Schafer, C. M., Geology, mineralogy, and some geophysical and geochemical properties of salt deposits, in: Physical properties data for rock salt, 1981.

Lu, G., Marshak, S., Kent, D. V., Characteristics of magnetic carriers responsible for late Paleozoic remagnetization in carbonate strata of the midcontinent, U. S. A.: Earth Planet. Sci. Lett., 99, 351-361, 1990.

Mackenzie, A. S., and Quigley, T. M., Principles of geochemical prospect appraisal: AAPG Bull., 72, 399-415, 1988.

Magara, K., Permeability considerations in generation of abnormal pressures: Soc. Pet. Eng. J., 11: 236-242, 1971.

Magara, K., Reevaluation of montmorillonite dehydration as a cause of abnormal pressure and hydrocarbon migration: AAPG Bull., 59, 292-302, 1975.

Majorowicz, J. A. and Jessop, A. M., Regional heat flow patterns in the western Canadian sedimentary basin: Tectonoophysics, 74, 209-238, 1981.

Majorowicz, J. A., Jones, F. W., Lam, H. L. and Jessop, the variability of heat flow both regional and with depth in southern Alberta, Canada: Effect of groundwater flow?: Tectonophysics, 106, 1-29, 1984.

Majorowicz, J. A., Jones, R. W., Lam, H. L. and Jessop, A. M., Terrestrial heat flow and geothermal gradients in relation to hydrodynamics in the Alberta Basin, Canada: J. Geodyn., 4, 265-283, 1985a.

Majorowicz, J. A., Jones, R. W., Lam, H. L. and Jessop, A. M., Regional variations of heat flow differences with depth in Alberta, Canada: Geophys. J. Astron. Soc., 81, 479-487, 1985b.

Manheim, F. T., Waterman, L. S., Lee, S., Woo, C. C. and Sayles, F. M., Interstitial waters on small core samples, Leg 23, red Sea. in: Init. Rep. Deep. Sea. Drill. Proj., 23, 955-967, 1974.

Marshak, S., Lu, G., and Kent, D. V., Reconnaissance investigation of remagnetizations in Paleozoic limestones from the Mid-continent of North America (abstract): Eos Trans. AGU, 70, 310, 1989.

Martin, R. G., Northern and eastern Gulf of Mexico continental margin: stratigraphic and structural framework, in A. H. Bouma et al., eds., framework, facies, and oil trapping characteristics of the upper continental margin: AAPG Studies in Geology, 7, 21-42, 1978.

McCabe, C. and Elmore, R. D., The occurrence and origin of Late Paleozoic remagnetization in the sedimentary rocks of North America: Rev. Geophys., 27, 471-494, 1989.

McCabe, C., Jackson, M. and Saffer, B., Regional patterns of magnetite authigenesis in the Appalachian Basin: Implications for the mechanism of Late Paleozoic remagnetization: J. Gephys. Res., 94, 10429-10443, 1989.

McDuff, R. E., Gieskes, J. M., and Lawrence, J. R., Interstitial water studies, Leg 42A, in: init. Rep. Deep Sea Drill. Project, 42, 561-568, 1978.

McKee, E. D., and Crosby, E. J., Paleotectonic investigations of the Pennsylvanian System in the United States: United States Geological Survey, Professional Paper, 853, 541 p., 1975.

McManus, K. M. and Hanor, J. S., Diagenetic evidence for massive evaporite dissolution, fluid flow, and mass transport in the Louisiana Gulf Coast: Geology, 21, 727-730, 1993.

Meert, J. G., Smith, D. L., and Fishkin, L., Heat flow in the Ozark Plateau, Arkansas and Missouri: relationship to groundwater flow: Journal of Volcanology and Geothermal research, 47, 337-347, 1991.

Nunn, J. A. and Sassen, R., The framework of hydrocarbon generation and migration, Gulf of Mexico continental slope: Trans. Gulf Coast Assoc. Geol. Soc., 36, 257-262, 1986.

O'Brien, J. J., and Lerche, I., Impact of heat flux anomalies around salt diapirs and salt sheets in the Gulf Coast on hydrocarbon maturity: models and observations: Trans. Gulf Coast Assoc. Geol. Soc., 38, 231-243, 1988.

Ochsenius, C., Die Bildung der Steinsalzlager und ihrer Mutterlangensalze, C.E.M. Pfefer, Halle, 1978.

Ode, Helmer, Review of Mechanical Properties of Salt Relating to salt dome Genesis: GSA Special Paper, 88, 544-595, 1968.

Oliver, J., Fluids expelled tectonically from orogenic belts: Their role in hydrocarbon migration and other geologic phenomena: Geology, 14, 99-102, 1986.

Person, M. and Garven, G., Hydrologic constraints on petroleum generation within continental rift basins: Theory and application to the Rhine Graben: AAPG Bull., 76, 468-488, 1992.

Person, M. and Garven, G., A sensitivity study of the driving forces on fluid flow during continental-rift basin evolution: GSA Bull., 106, 461-475, 1994.

Phillips, S. L., Ozbek, H. and Silvester, L. F., Density of sodium chloride solutions at high temperatures and pressures, Lawrence Berkeley Laboratory Report #16275, University of California, 11, 1983.

Pollack, H. N. and Cercone, K. R., Anomalous thermal maturities caused by carbonaceous sediments: Basin Research, 6, 47-51, 1994.

Powers, M. C., Fluid release mechanisms in compacting marine mudrocks and their importance in oil exploration: AAPG Bull., 51, 1240-1254, 1967.

Powley, D. E., Pressures and hydrogeology in petroleum basins: Earth-Science Reviews, 29, 215-226, 1990.

Pryor, W. A., and Sable, E. G., Carboniferous of the eastern interior basin, in: Briggs, G., ed., Carboniferous of the southeastern United State: GSA Special Paper, 148, 281-313, 1974.

Quinlan, G. M. and Beaumont, C., Appalachian thrusting, lithospheric flexure, and the Paleozoic stratigraphy of the Eastern Interior of North America: Canadian Journal of Earth Sciences, 21, 973-996, 1984.

Ranganathan, V. and Hanor, J. V., Density-driven groundwater flow near salt domes: Chem. Geol. 74, 173-188, 1988.

Ranganathan, V. and Hanor, J. V., Perched brine plumes above salt domes and dewatering of geopressured sediments: J. Hydro., 110, 63-86, 1989.

Ranganathan, V., Basin dewatering near salt domes and formation of brine plumes: J. Geophys. Res, 97, 4667-4683, 1992.

Rieke, H. H., and Kirr, J. N., Geological overview, coal, and coalbed methane resources of the Arkoma Basin-Arkansas and Oklahoma, in: Rightmire, C. T., Eddy, E. G., and Kirr, J. N., eds, Coalbed methane resources of the United States: AAPG studies in Geology, series 17, 135-162, 1984.

Roberts, S. J. and Nunn, J. A., Episodic fluid expulsion from geopressured sediments: Mar. and Pet. Geol. 12, 195-204, 1995.

Roberts, S. J. and Nunn, J. A., Cathles, L. and Cipriani, F. D., Expulsion of abnomally pressured fluids along faults: J. Geophys. Res. March, 1996?

Rowan, E. L., and Leach, D. L., Constraints from fluid inclusions on sulfide precipitation mechanisms and ore fluid migraion in the Viburnum trend lead district, Missouri: Economic Geology, 84, 1948-1965, 1989.

Saunders, J. A., and Swann, C. T., Mineralogy and geochemistry of a cap-rock Zn-Pb-Sr-Ba occurrence at the Hazlehurst salt dome, Mississippi: Econ. Geol., 89, 381-390, 1994.

Sayles, F. M., Waterman, L. S., and Manheim, F. T., Interstitial water studies on small core samples from the Mediterranean Sea: Init. Rep. Deep Sea Drill. Proj., 13, 801-808, 1973.

Sclater, J. G., Parsons, B. and Jaupart, C., Oceans and continents: similarities and differences in the mechanisms of heat loss: J. Geophys. Res., 86, 11535-11552, 1981.

Sharp, J. G., Energy and momentum transport model of the Quachita Basin and its possible impact on formation of economic mineral deposits: Econ. Geol., 73, 1057-1068, 1978.

Sharp, J. M., Jr. and Domenico, P. A., Energy and momentum transport in thick sequences of compacting sediment: Geol. Soc. Am., 87, 390-400, 1976.

Sharp, J. M., Jr., Energy and momentum transport model of the Ouachita basin and its possible impact on formation of economic mineral deposits: Econ. Geol., 73, 1057-1068, 1978.

Shoup, R. C., and Karlo, J. F., Structural systems of the northwestern Gulf of Mexico: AAPG Student Course, 1993.

Smith, L., and Chapman, D. S., On the thermal effects of groundwater flow, 1, Regional scale systems: J. Geophys., Res., 88, 593-608, 1983.

Smith, L., Forster, C. and Woodbury, A., Numerical simulation techniques for modeling advectively disturbed thermal regimes. In: a. E. Beck, G. Garven and Stegena, L., eds, Hydrogeologic Regimes and Their Subsurface Thermal Effects: Am. Geophys. Union, Geophys. Monog., 47, 1-6, 1989.

Snarskii, A. N., Relationship between primary migratin and compaction of rocks: Petroleum geology, 5, 362-364, 1964.

Snarskii, A. N., The nature of primary oil migratin, in Izvestiya Vsysskikh Uchebnykh Zavedeniy, Neft'i Gaz, translated by Associated Technical Services, 13, 11-15. 1970.

Stevart, F. H., Marine Evaporites: United States Geological Survey Professional Paper 440-Y, 52, 1963.

Sverjensky, D. A., Genesis of Mississippi Valley-type lead-zinc deposits: Annu. Rev. Earth Planet. Sci., 14, 177-199, 1986.

Thacker, J. L., and Anderson, K. H., The geologic setting of the southeast Missouri lead district-regional gelogic history, structure, and stratigrahy: Econ. Geol., 72, 339-348, 1977.

Tissot, B., first data on the mechanisms and kinetics of the formation of petroleum in sediments: Revue de I'Institut Francais du Petrole, 24, 470-501, 1969.

Toth, J., Gravity-induced cross-formational flow of formation fluids. Red fault region, Alberta, Canada: Analysis, patterns, evolution: Water Resources Research. 14, 805-843, 1978.

Tye, R. S., Moslow, T. F., Kimbrell, W. C and Wheeler, C. W., Lithostrotigraphy and Production Characteristics of the Wilcox Group (Paleocene-Eocene) in Central Louisiana: AAPG Bull., 75, 1675-1713, 1991.

Waples, D. W., Time and temperature in petroleum formation: application of Lopatin's method to petroleum exploration: AAPG Bull., 64, 1033-1040, 1980.

Waples, Douglas W., Generation and Migration of Petroleum from abnormally Pressured Compartments: Discussion1: AAPG Bull., 75, 326-327, 1991.

Whelan, J. K., Kennicutt , M. C. II, Brooks, J. M., Schumacher, D. and Eglington, L. B., Organic geochemical indications of dynamic fluid flow processes in petroleum basins: Org. Geochem., 22, 587-615, 1994.

Whitmarsh, R. B., and the shipboard scientific party, Site 225: Init. Rep. Deep Sea Drill. Proj., 23, pt. 2, 539-553, 1974a.

Whitmarsh, R. B., and the shipboard scientific party, Site 228: Init. Rep. Deep Sea Drill. Proj., 23, pt. 2, 677-692, 1974b.

Willman, H. C., et al., 1979, Handbook of Illinois stratigraphy: Illinois State Geological Survey Bull. 95, 261.

Workman, A. L., and Hanor, J. S., Evidence for large-scale vertical migration of dissolved fatty acids in Louisiana oil field brines: Iberia field, south-cental Louisiana: Trans. Gulf Coast Assoc. Geol. Soc., 35, 293-300, 1985.

Wood, D. A., Relationships between thermal maturity indices calculated using Arrhenius equation and Lopatin method: implications for petroleum exploration: AAPG Bull., 72, 115-134, 1988.

Woodbury, H. O., Murray, I. B. Jr., Pickford, P. J. and Akers, W. H., Pliocene and Pleistocene depocenters, outer continental shelf. Louisiana and Texas: AAPG Bulletin, 57, 2428-2439, 1973.

Woodbury, A. D., and Smith, L., On the thermal effects of three-dimensional groundwater flow: J. Geophys. Res., 90, 759-767, 1985.

Worrall, D. M., and Snelson, S., Evolution of the northern Gulf of Mexico, with emphasis on Cenozoic growth faulting and the role of salt, in Bally, A. W., and A. R. Palmer, eds., The geology of North America an overview: GSA Decade of North American Geology, A, 97-138, 1989.

VITA

Guichang Lin was born in Guangdong Province, the People's Repulic of China in 1962. He got his B.S. in geophysics from Jianghan Petroleum Institute in 1983. He then worked for four years, doing seismic exploration for the Jianghan Geophysical Corporation, Jianghan Oil-Field, Hubei Province, the P. R. of China. From 1987 to 1989, he was a graduate student, involving in an integrated exploration program at the University of Petroleum of China. In 1989, he went to Landmark Graphics Corporation in Texas for a further study. In 1990, he moved to the Colorado School of Mines, where he received a Professional Degree in Geophysics in 1992. At present, he is working on his Ph.D. at the Department of Geology and Geophysics of Louisiana State University at Baton Rouge, Louisiana.

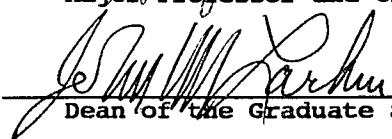# DOCTORAL EXAMINATION AND DISSERTATION REPORT

Candidate: Guichang Lin

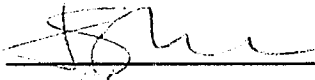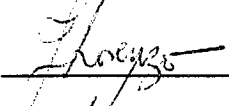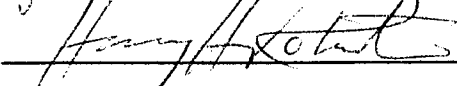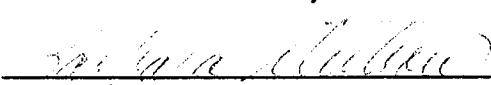**Major Field:**   Geology

Title of Dissertation: Groundwater Flow With Heat and Solute Transport
in Sedimentary Basins

Approved:

_____
Major Professor and Chairman

_____
Dean of the Graduate School

EXAMINING COMMITTEE:

_____

_____

_____

_____

_____

_____

_____

Date of Examination:

March 18, 1996